

Durham E-Theses

Assessment of high resolution SAR imagery for mapping floodplain water bodies: a comparison between Radarsat-2 and TerraSAR-X

AL-ALI, MOHAMED,SAIF,MOHAMED,QASIM

How to cite:

AL-ALI, MOHAMED,SAIF,MOHAMED,QASIM (2011) *Assessment of high resolution SAR imagery for mapping floodplain water bodies: a comparison between Radarsat-2 and TerraSAR-X*, Durham theses, Durham University. Available at Durham E-Theses Online: <http://etheses.dur.ac.uk/3347/>

Use policy

The full-text may be used and/or reproduced, and given to third parties in any format or medium, without prior permission or charge, for personal research or study, educational, or not-for-profit purposes provided that:

- a full bibliographic reference is made to the original source
- a [link](#) is made to the metadata record in Durham E-Theses
- the full-text is not changed in any way

The full-text must not be sold in any format or medium without the formal permission of the copyright holders.

Please consult the [full Durham E-Theses policy](#) for further details.

Assessment of high resolution SAR imagery for mapping floodplain water bodies: a comparison between Radarsat-2 and TerraSAR-X

Mohamed Saif Al-Ali

Abstract

Flooding is a world-wide problem that is considered as one of the most devastating natural hazards. New commercially available high spatial resolution Synthetic Aperture RADAR satellite imagery provides new potential for flood mapping. This research provides a quantitative assessment of high spatial resolution RADARSAT-2 and TerraSAR-X products for mapping water bodies in order to help validate products that can be used to assist flood disaster management. An area near Dhaka in Bangladesh is used as a test site because of the large number of water bodies of different sizes and its history of frequent flooding associated with annual monsoon rainfall. Sample water bodies were delineated in the field using kinematic differential GPS to train and test automatic methods for water body mapping. SAR sensors products were acquired concurrently with the field visits; imagery were acquired with similar polarization, look direction and incidence angle in an experimental design to evaluate which has best accuracy for mapping flood water extent.

A methodology for mapping water areas from non-water areas was developed based on radar backscatter texture analysis. Texture filters, based on Haralick occurrence and co-occurrence measures, were compared and images classified using supervised, unsupervised and contextual classifiers. The evaluation of image products is based on an accuracy assessment of error matrix method using randomly selected ground truth data. An accuracy comparison was performed between classified images of both TerraSAR-X and Radarsat-2 sensors in order to identify any differences in mapping floods. Results were validated using information from field inspections conducted in good conditions in February 2009, and applying a model-assisted difference estimator for estimating flood area to derive Confidence Interval (CI) statistics at the 95% Confidence Level (CL) for the area mapped as water. For Radarsat-2 Ultrafine, TerraSAR-X Stripmap and Spotlight imagery, overall classification accuracy was greater than 93%. Results demonstrate that small water bodies down to areas as small as 150m² can be identified routinely from 3 metre resolution SAR imagery. The results further showed that TerraSAR-X stripmap and spotlight images have better overall accuracy than RADARSAT-2 ultrafine beam modes images. The expected benefits of the research will be to improve the provision of data to assess flood risk and vulnerability, thus assisting in disaster management and post-flood recovery.

**Assessment of high resolution SAR imagery for mapping floodplain
water bodies: a comparison between Radarsat-2 and TerraSAR-X**

Thesis submitted for the Degree of Doctor of Philosophy

Department of Geography

Durham University

Mohamed Saif Al-Ali

December, 2011

Declaration

The material contained in this thesis has not been previously submitted by the candidate for a degree in this or any other University.

Statement of Copyright

The copyright of this thesis rests with the author. No quotation from it should be published without the prior written consent and information derived from it should be acknowledged.

Acknowledgements

First and foremost, I would like to express my sincere gratitude to his Highness General Sheikh Mohamed bin Zayed Al Nahyan, the Crown Prince of Abu Dhabi and Deputy Supreme Commander of the United Arab Emirates Armed Forces for his personal encouragement and support.

I am most grateful to my family and parents, without their support I would have never been able to complete this PhD.

Many thanks to my PhD supervisors, Prof. David Petley and Prof. Danny Donoghue for their guidance and advice. Also many thanks to people who helped me in any way.

Thanks are due to the Canadian Space Agency for providing RADARSAT-2 data via the SOAR Program (project 2041). Thanks also go to the German Aerospace Centre (DLR) for providing TerraSAR-X data at a reduced price for scientific use (Proposal ID: HYD0480).

Table of Contents

Abstract	i
Title Page	ii
Declaration	iii
Statement of Copyright.....	iii
Acknowledgments.....	iv
Table of Contents.....	v
List of Figures.....	ix
List of Tables.....	xiii

Chapter 1: Introduction

1.1 Background.....	1
1.2 Aim and Objectives.....	4
1.3 Research Questions.....	5
1.4 Thesis Structure.....	5

Chapter 2: Earth Observation for Disaster Risk Management

2.1 Introduction.....	7
2.2 Flood Disasters.....	9
2.3 Earth Observation for Flood Disaster Management Cycle.....	11
2.4 Initiatives for Using Remote Sensing for Disaster Management.....	15
2.4.1 The International Charter on Space and Major Disasters	16
2.4.2 UN-SPIDER.....	18
2.4.2.1 UN-SPIDER Global Network and Activities.....	18
2.4.2.2 UN-SPIDER Knowledge Portal	19
2.5 The Need for Detailed Flood Area Mapping.....	20
2.6 Summary.....	23

Chapter 3: Principles of Mapping Using Synthetic Aperture Radar

3.1 Background.....	24
3.2 SAR System Parameters.....	28
3.2.1 SAR Frequency.....	28
3.2.2 Polarization and Spatial Resolution.....	29
3.2.3 Incidence Angle and Look Direction.....	30
3.2.4 Backscatter.....	32
3.2.5 Speckle Filtering.....	35
3.3 Development in SAR Technology.....	36
3.4 Mapping Floods and Water Bodies.....	37
3.5 SAR Data Interpretation.....	44
3.6 Limitations of Using SAR Data to Detect Flooded Areas.....	45
3.7 Evaluation of SAR Frequency and Polarization.....	46
3.8 Radarsat-2 and TerraSAR-X Remote Sensing Systems.....	48
3.8.1 Radarsat-2.....	48

3.8.1.1	Radarsat-2 Instrument System.....	49
3.8.1.2	Satellite Orbit.....	51
3.8.1.3	Beam Modes and Polarizations.....	52
3.8.2	TerraSAR-X.....	53
3.8.2.1	TerraSAR-X Instrument System.....	54
3.8.2.2	Satellite Orbit.....	56
3.8.2.3	Beam Modes and Polarizations.....	56
3.9	SAR Data Accuracy Assessment.....	58
3.9.1	Sampling Design.....	60
3.9.2	Accuracy Assessment methods.....	60
3.9.3	Accuracy Assessment Applications in SAR Remote Sensing.....	63
3.10	Conclusion.....	65

Chapter 4: Description of the Study Area

4.1	Introduction.....	67
4.2	Justification of the Study Area.....	67
4.3	Geographic Location of the Study Area.....	70
4.4	Climate.....	71
4.5	Floodplain and Drainage Network.....	76
4.6	Soil.....	79
4.7	Hydrology and Water Resources.....	80
4.7.1	Groundwater.....	81
4.7.2	Floods in Bangladesh.....	82
4.7.3	Water Bodies.....	84
4.8	Agriculture.....	87
4.9	Built-up Areas.....	91
4.10	Synthesis.....	92

Chapter 5: Methodology

5.1	Introduction.....	93
5.1.1	Data Collection Methodology.....	94
5.1.2	Data Processing.....	94
5.1.3	Data Evaluation.....	94
5.2	Data Description.....	95
5.2.1	SAR Data Description.....	96
5.2.2	Radarsat-2 Data.....	97
5.2.3	TerraSAR-X Data.....	98
5.2.4	Field Data Description and Organization.....	98
5.2.4.1	GPS Equipment and Data Collection.....	99
5.2.4.2	ProMark3-RTK Base/Rover Configuration.....	100
5.2.4.3	Water Body Information and Field Visits.....	101
5.2.4.4	Surveying Water Bodies.....	104
5.3	Remote Sensing and GIS Software Used.....	104
5.3.1	ArcGIS.....	105
5.3.2	ERDAS Imagine.....	105
5.3.3	ENVI.....	105
5.3.4	Definiens Professional (eCognition software).....	105

5.4	Data Preparation.....	106
5.4.1	Data Pre-processing.....	106
5.4.1.1	Georeferencing and Resampling.....	107
5.4.1.2	Geocorrection by dGPS Ground Control Points.....	107
5.4.1.3	Geocorrection via Google Earth.....	108
5.4.2	Textural Analysis.....	109
5.4.2.1	Density Slicing.....	110
5.5	Water Body Mapping.....	111
5.5.1	Unsupervised Classification.....	112
5.5.2	Supervised Classification.....	112
5.5.2.1	Maximum Likelihood.....	113
5.5.3	Object-Oriented Image Processing.....	114
5.6	Remote Sensing Data Accuracy Assessment.....	115
5.6.1	Sampling Design for Mapping Accuracy Assessment.....	115
5.6.1.1	Response Design.....	116
5.6.1.2	Sampling Design.....	118
5.6.1.3	Analysis Design.....	119
5.7	Conclusion.....	120

Chapter 6: Data Preparation

6.1	Introduction.....	121
6.2	Data Pre-Processing.....	122
6.2.1	Fieldwork Data.....	122
6.2.2	Rectification of SAR Data.....	124
6.2.3	Geometric Correction.....	125
6.2.4	Geocorrection by dGPS GCPs.....	126
6.2.5	Geocorrection via Google Earth.....	129
6.2.6	Spatial Subset for SAR Images.....	132
6.3	SAR Images Texture Analysis.....	133
6.3.1	Speckle Noise Reduction.....	136
6.3.2	Analysis of Texture Measures.....	137
6.3.2.1	Occurrence Measures.....	139
6.3.2.2	Co-Occurrence Measures.....	145
6.3.3	Texture Analysis with a Combination of Texture Measures.....	153
6.4	Conclusion.....	156

Chapter 7: Water Body Mapping

7.1	Introduction.....	157
7.2	Water Body Mapping Using Backscatter Density Slicing.....	158
7.2.1	Density Sliced Radarsat-2 Products.....	159
7.2.2	Density Sliced TerraSAR-X Products.....	161
7.2.3	Comparison of Density Slice Assessment between the Tow Sensors.....	163
7.2.4	Analysis of Polarization.....	164
7.3	Water Body Mapping Using Image Classification.....	165
7.3.1	Unsupervised Classification.....	165
7.3.2	Supervised Classification.....	167
7.3.2.1	Analysis of Training Data.....	167

7.3.3	Supervised Classification of Radarsat-2 Data.....	170
7.3.3.1	Classified Occurrence Texture Images.....	172
7.3.3.1.1	HH Polarization.....	172
7.3.3.1.2	VV Polarization.....	175
7.3.3.2	Classified Co-occurrence Texture Images.....	177
7.3.4	Supervised Classification of TerraSAR-X Data.....	180
7.3.4.1	Classified Occurrence Images.....	180
7.3.4.1.1	HH Stripmap Polarization.....	180
7.3.4.1.2	VV Stripmap Polarization.....	182
7.3.4.1.3	HH Spotlight Image.....	184
7.4	Contextual Analysis.....	186
7.4.1	Segmentation.....	187
7.4.1.1	Radarsat-2 HH Image Segmentation.....	189
7.4.1.2	TerraSAR-X HH Image Segmentation.....	191
7.4.2	Image Object-Oriented Classification.....	193
7.4.2.1	Object-Oriented Classification of Radarsat-2 HH and TerraSAR-X HH Images.....	194
7.5	Comparison between Radarsat-2 and TerraSAR-X.....	198
7.6	Area Estimation.....	200
7.6.1	Flood Area Estimates.....	202
7.6.1.1	Radarsat-2 HH Data and TerraSAR-X HH Data.....	203
7.7	Summary.....	205
Chapter 8: The Potential Applications of New SAR Data for Flood Disaster Management		
8.1	Introduction.....	209
8.2	Current Operational Applications of SAR Satellite Data for Flood Risk Management.....	210
8.2.1	Current Capacity of Using SAR Satellites for Flood Disaster Management by Space-Based Initiatives.....	212
8.3	The Potential Operational Applications of the Developed Methods in the Phases of Flood Disaster Cycle.....	217
8.3.1	Pre-Flood Mitigation and Preparedness.....	219
8.3.2	Response to Floods.....	221
8.3.3	Post-Flood Recovery.....	226
8.4	Summary.....	226
Chapter 9: Conclusions		
9.1	Conclusions.....	229
9.2	Main Findings.....	230
9.3	Directions for future study.....	231
References	234
Appendices	256

List of Figures

Figure 1.1	Natural disaster impacts by sub-group: 2010 versus 2000-2009 annual Average.....	2
Figure 1.2	Percent share of reported victims by disaster sub-group and continent in 2010.....	2
Figure 2.1	2010 human impact by disaster types compared to decade average.....	10
Figure 2.2	Disaster management cycle.....	14
Figure 2.3	UN-SPIDER Space Application Matrix.....	20
Figure 2.4	An example of a damaged bridge - Pakistan flood-2010.....	22
Figure 2.5	An example of houses surrounded by floods - Pakistan flood-2010.....	22
Figure 3.1	Electromagnetic spectrum.....	25
Figure 3.2	Short and long wavelengths reflected from a surface.....	29
Figure 3.3	Schematic diagrams of geometry of radar image acquisition system and incidence angles.....	31
Figure 3.4	Typical radar backscatter curves for smooth, moderate and rough surfaces at different incidence angles.....	33
Figure 3.5	Radar energy scattering from different surfaces.....	34
Figure 3.6	Backscatter from smooth surfaces.....	35
Figure 3.7	Imaging different types of surface with radar.....	35
Figure 3.8	Reflectance significance comparison and flooding map.....	40
Figure 3.9	Radarsat-2 configuration.....	51
Figure 3.10	Radarsat-2 SAR beam modes of operation.....	52
Figure 3.11	TerraSAR-X system components.....	55
Figure 3.12	TerraSAR-X SAR modes of operation.....	57
Figure 3.13	Possible sources of error in remotely sensed data.....	59
Figure 3.14	The Error Matrix.....	61
Figure 3.15	The general concept of producer's and user's accuracy.....	62
Figure 4.1	Flood prone areas of Bangladesh.....	68
Figure 4.2	Maximum flooded area in Bangladesh 1969–2009.....	69
Figure 4.3	Location of the study area within Bangladesh.....	71
Figure 4.4	Climate map of Bangladesh.....	72
Figure 4.5	Average temperature of the study area.....	74
Figure 4.6	Average mean monthly rainfall in millimetre of the study area.....	74
Figure 4.7	Average wind speed (m/s) in Bangladesh at surface level from January to December.....	75
Figure 4.8	Main and regional rivers' map showing the location of the study area within a basin of rivers' network.....	78
Figure 4.9	General soil map of Bangladesh.....	80
Figure 4.10	Hydrological regions of Bangladesh.....	81
Figure 4.11	Causes of floods in Bangladesh.....	83
Figure 4.12	Examples of typical water-body types of various sizes in rural Bangladesh.....	86
Figure 4.13	Importance of small bodies of water in everyday life in Bangladesh.....	87
Figure 4.14	Crop fields during the fieldwork in January 2009.....	88

Figure 4.15	Examples of two types of wetlands: (A) irrigated newly transplanted fields; (B) rice field ploughing.....	89
Figure 4.16	Some types of trees adjacent to water bodies.....	90
Figure 4.17	Water hyacinth floating on a water body.....	90
Figure 4.18	Typical rural road made of asphalt, showing planted trees on both sides.....	91
Figure 5.1	An overall workflow of the data processing methodology.....	95
Figure 5.2	Radarsat-2 product acquired with HH polarization for the study area before Geocorrection.....	97
Figure 5.3	Using a small local boat carrying dGPS-Rover equipment to avoid access limitation and steep areas.....	99
Figure 5.4	ProMark3-RTK dGPS equipment - Base station (A) and Rover (B)....	100
Figure 5.5	Setting up the ProMark3 equipment (base and rover) during fieldwork in Bangladesh.....	101
Figure 5.6	Study area extracted from Radarsat-2 HH image.....	102
Figure 5.7	A water body (scale: 14mx24m) photographed during fieldwork.....	104
Figure 5.8	Methodology workflow of data preparation.....	106
Figure 5.9	An example of a GCP extracted from a water body for both dGPS-reference and SAR-input data.....	108
Figure 5.10	Co-occurrence matrix.....	110
Figure 5.11	General methodology flowchart for mapping flood.....	111
Figure 5.12	Discriminant functions calculated for each pixel.....	113
Figure 5.13	Methodology flow chart of the contextual classification.....	115
Figure 6.1	Methodology flow chart of data preparation.....	121
Figure 6.2	An example of training and test data.....	123
Figure 6.3	An example of the buffering process.....	124
Figure 6.4	Radarsat-2 and TerraSAR-X data before and after projection.....	125
Figure 6.5	GCPs and dGPS data distributed over the study area.....	128
Figure 6.6	Radarsat-2 HH and TerraSAR-X HH products extracted before and after geocorrection.....	129
Figure 6.7:	The spatial distribution of the GCPs over the study area extracted from the Google Earth.....	131
Figure 6.8	Distance of distortion of a water body extracted from Google Earth....	132
Figure 6.9	Image subset corners.....	132
Figure 6.10	Imaging SAR sensor-HH polarization for various types of land cover.....	134
Figure 6.11	A water body used as test scene showing surrounding features.....	135
Figure 6.12	A comparison between 3×3 and 5×5 window sizes of median filter.....	137
Figure 6.13	Reflectance profiles of specific sample pixel for the original SAR images.....	139
Figure 6.14	Reflectance profiles of occurrence data-range texture measure.....	140
Figure 6.15	Reflectance profiles of occurrence mean texture measure.....	141
Figure 6.16	Reflectance profiles of occurrence variance texture measure.....	142
Figure 6.17	Reflectance profiles of occurrence entropy texture measure.....	143
Figure 6.18	Reflectance profiles of occurrence skewness texture measure.....	144

Figure 6.19	Reflectance profile of co-occurrence mean texture measure.....	146
Figure 6.20	Reflectance profile of co-occurrence variance texture measure.....	147
Figure 6.21	Reflectance profile of co-occurrence homogeneity texture measure.....	148
Figure 6.22	Reflectance profile of co-occurrence contrast texture measure.....	149
Figure 6.23	Reflectance profile of co-occurrence dissimilarity texture measure.....	150
Figure 6.24	Reflectance profile of co-occurrence entropy texture measure.....	151
Figure 6.25	Reflectance profile of co-occurrence second-moment texture Measure.....	152
Figure 6.26	Reflectance profile of co-occurrence correlation texture measure.....	153
Figure 6.27	Texture analysis for products of both sensors data - HH and VV polarizations.....	154
Figure 6.28	Texture analysis for Radarsat-2 data - HH and VV polarizations.....	155
Figure 6.29	Comparison between occurrence and co-occurrence combined texture measures with Radarsat-2 HH.....	155
Figure 6.30	Comparison between occurrence and co-occurrence using density slice technique with Radarsat-2 HH.....	155
Figure 7.1	Methodology flow chart of water body mapping and accuracy assessment.....	157
Figure 7.2	Defining density slice ranges for <i>water</i> class using co-occurrence and occurrence <i>mean</i> variable - Radarsat-2-HH image.....	159
Figure 7.3	Example of density sliced results of co-occurrence and occurrence <i>mean</i> variable - Radarsat-2 HH and VV.....	160
Figure 7.4	Statistical results of density slicing for <i>water</i> class with co-occurrence <i>mean</i> variable - Radarsat-2 HH.....	160
Figure 7.5	Statistical results of density slicing for <i>water</i> class with occurrence mean variable - Radarsat-2 HH.....	161
Figure 7.6	Defining density slice ranges for <i>water</i> class with occurrence <i>mean</i> variable - TerraSAR-X.....	162
Figure 7.7	Example of density sliced results of TerraSAR-X HH and VV occurrence <i>mean</i> texture variable.....	162
Figure 7.8	Statistical results of density slicing for <i>water</i> class of TerraSAR-X HH occurrence <i>mean</i> variable.....	163
Figure 7.9	A visual comparison of SAR sensor polarizations between Radarsat-2 and TerraSAR-X.....	165
Figure 7.10	Unsupervised classification ISODATA and K-Means comparison between Radarsat-2 and TerraSAR-X images.....	166
Figure 7.11	Land cover classes with fieldwork photographs.....	168
Figure 7.12	Supervised classification of occurrence data-range and mean texture image for Radarsat-2 HH.....	173
Figure 7.13	Supervised classification of occurrence data-range and mean texture image for Radarsat-2 VV.....	176
Figure 7.14	Supervised classification of Radarsat-2 HH produced after applying co-occurrence variables.....	178
Figure 7.15	Supervised classification of occurrence data-range and mean texture image for TerraSAR-X HH.....	181

Figure 7.16	Supervised classification of occurrence data-range and mean texture image for TerraSAR-X VV.....	183
Figure 7.17	Supervised classification of occurrence data-range and mean texture image for TerraSAR-X HH Spotlight.....	185
Figure 7.18	Methodology flow chart of the contextual classification used for segmentation and object-oriented classification.....	187
Figure 7.19	Radarsat-2 HH texture image before and after segmentation.....	190
Figure 7.20	Radarsat-2 HH original image before and after segmentation.....	190
Figure 7.21	TerraSAR-X HH texture image before and after segmentation.....	192
Figure 7.22	TerraSAR-X HH original image before and after segmentation.....	193
Figure 7.23	Checking signatures separability using Definiens 2D feature space plot for training classes.....	194
Figure 7.24	Comparison of object-oriented classification between original image and texture image of Radarsat-2 HH.....	196
Figure 7.25	Comparison of object-oriented classification between original image and texture image - TerraSAR-X HH.....	197
Figure 8.1	Number of activations by hazard type for year 2009.....	213
Figure 8.2	SAR data consumption during 2009 by quantity of archive and new-acquisition data.....	213
Figure 8.3	Colombia flood 2010.....	215
Figure 8.4	Phases of flood disaster management cycle.....	218
Figure 8.5	Potential use of TerraSAR-X spotlight HH for mapping very small water bodies.....	220
Figure 8.6	An example of discrimination between permanent water bodies and flooding.....	221
Figure 8.7	Outline of the water area mapping proposed methods for operational flood disaster applications for flat topography areas.....	223
Figure 8.8	Changes detection using TerraSAR-X HH.....	224
Figure 8.9	An example of <i>water</i> class layer of the study area produced from the developed methods and mashup in the Google Earth.....	225

List of Tables

Table 2.1	Applications of different wavebands for disaster management.....	11
Table 2.2	Characteristics of some current satellite sensors used in mapping and monitoring hazards and disasters.....	13
Table 2.3	Members of the Disaster Charter and available satellite resources.....	17
Table 3.1	Highlights of SAR history – from radar to SAR technology.....	26
Table 3.2	Current and near future commercial earth observation SAR sensors.....	27
Table 3.3	Characteristics of some current SAR satellite bands.....	29
Table 3.4	Some features of Radarsat-2 and their benefits.....	49
Table 3.5	Radarsat-2 spacecraft and Antenna general characteristics.....	50
Table 3.6	Radarsat-2 orbit characteristics.....	51
Table 3.7	Radarsat-2 beam modes and products.....	53
Table 3.8	TerraSAR-X system parameters.....	55
Table 3.9	TerraSAR-X orbit and attitude parameters.....	56
Table 3.10	TerraSAR-X beam modes and products specifications.....	57
Table 3.11	Characteristic parameters of stripmap mode.....	58
Table 4.1	Regional Rivers and their lengths across areas of Bangladesh included Dhaka Division.....	77
Table 4.2	Bangladesh severe floods in the last three decades.....	84
Table 4.3	Characteristics of various sizes of small water bodies.....	85
Table 4.4	Percentage of land area planted by crop in 2004–5 in Bangladesh.....	89
Table 5.1	Parameters of SAR product acquisitions.....	96
Table 5.2	Fieldwork timetable.....	103
Table 5.3	Overview of water body numbers and sizes surveyed during fieldwork.....	103
Table 5.4	Class description for reference data evaluation protocol.....	118
Table 5.5	Specifications of validation data used.....	119
Table 6.1	Number of water bodies surveyed by dGPS during fieldwork according to water body type.....	122
Table 6.2	Number and size of training and test data.....	123
Table 6.3	Comparison of control point error for Radarsat-2 and TerraSAR-X products based on dGPS data.....	128
Table 6.4	An example of the total RMS error for Google Earth imagery.....	132
Table 7.1	A comparison of mapped area of four example water bodies extracted from Radarsat-2 HH and TerraSAR-X HH imagery compared with dGPS data.....	164
Table 7.2	Comparison of Density values and water area estimation of HH and VV between Radarsat-2 and TerraSAR-X.....	164
Table 7.3	Jeffries–Matusita distance separability matrix of land cover training samples for pairs of classes.....	171
Table 7.4	Confusion matrix of classified image of Radarsat-2 HH occurrence data-range and mean variables without median 3x3 window.....	175

Table 7.5	Confusion matrix of classified image of Radarsat-2 HH with occurrence <i>data-range</i> and <i>mean</i> variables with median 3x3 window applied.....	175
Table 7.6	Confusion matrix of classified image of Radarsat-2 VV with occurrence <i>data-range</i> and <i>mean</i> with median 3x3 window.....	176
Table 7.7	Confusion matrix of classified image of Radarsat-2 HH with <i>co-occurrence mean</i> , <i>variance</i> and <i>dissimilarity</i> with median 3x3 window applied.....	178
Table 7.8	Confusion matrix of classified image of Radarsat-2 HH with <i>co-occurrence mean</i> , <i>variance</i> and <i>contrast</i> with median 3x3 window.....	179
Table 7.9	Comparison of accuracy assessment (percentage) between classified images using occurrence and co-occurrence variables for Radarsat-2.....	179
Table 7.10	Confusion matrix (percentage) of classified image of TerraSAR-X HH <i>occurrence data-range</i> and <i>mean</i> with median 3x3 window applied.....	182
Table 7.11	Confusion matrix (percentage) of classified image of TerraSAR-X HH <i>occurrence data-range</i> and <i>mean</i> with no median 3x3 window applied.....	182
Table 7.12	Confusion matrix (percentage) of classified image of TerraSAR-X VV <i>occurrence data-range</i> and <i>mean</i> with median 3x3 window applied.....	183
Table 7.13	Confusion matrix (percentage) of TerraSAR-X spotlight HH <i>occurrence data-range</i> and <i>mean</i> texture image without median 3x3 window applied.....	185
Table 7.14	Confusion matrix (percentage) of TerraSAR-X spotlight HH <i>occurrence data-range</i> and <i>mean</i> texture image with median 3x3 window applied.....	186
Table 7.15	Segmentation parameters for Radarsat-2 HH occurrence <i>data-range</i> and <i>mean</i> texture image.....	190
Table 7.16	Segmentation parameters for Radarsat-2 HH non-texture image.....	190
Table 7.17	Segmentation parameters of TerraSAR-X HH texture image (<i>data-range</i> and <i>mean</i>) variables.....	192
Table 7.18	Confusion matrix comparison between texture image and non-texture image contextual classification - Radarsat-2 HH.....	196
Table 7.19	Confusion matrix comparison between texture image and non-texture image contextual classification - TerraSAR-X HH.....	197
Table 7.20	A brief comparison between images of Radarsat-2 and TerraSAR-X for water detection using HH polarisation, 3m, and high incidence angles.....	200
Table 7.21	Error matrix for Radarsat-2 HH ultrafine Data.....	201
Table 7.22	Error matrix for TerraSAR-X Stripmap Data.....	201
Table 7.23	Error matrix for TerraSAR-X spotlight Data.....	218
Table 7.24	Summary of water area estimates for the 204 km ² study area comparing mapped areas and areas estimated from a model-assisted difference	

	Estimator.....	204
Table 7.25	Comparison of sensors for water area estimation.....	205
Table 7.26	Comparison of accuracy assessment (in percentage) of Maximum-Likelihood classified image between both SAR sensors.....	206
Table 8.1	Potential ways of using remote sensing to support disaster management phases.....	211

Chapter One:

INTRODUCTION

1.1 Background

Natural disasters are defined as events not brought about by human activity that have significant negative on people, infrastructure, and the environments (see Figure 1.1). In year 2010 alone, 385 natural disasters worldwide are reported to have killed more than 297000 people, affected over 217.0 million others and caused US\$ 123.9 billion of economic damages (Guha-Sapir et al., 2011). Amongst the various types of disasters, flooding and other hydrological events (such as tropical cyclones) are devastating and frequent. Flood disasters were the most frequently occurring disasters on average annually for the years 2000 to 2009, and also for the year 2010, in terms of occurrence and victims (i.e. numbers affected) (Figure 1.1).

The Asian continent has the most hydrological disasters that affected people. For example in 2010 95% of the global disaster victims were located in Asia (see Figure 1.2). Bangladesh is one of those countries most seriously impacted by floods. Floods caused by a combined effect of the annual monsoon and a direct hit by cyclone Sidr in November 2007 affected around 15 million people, including damaging 1,088,120 households, and 2,472,944 acres of crops (CERF, 2008). The 2010 Pakistan flood inundated one-fifth of that country and affected over 20 million people along the Indus River (Guha-Sapir et al., 2011). The large number of affected people from flood disasters in such Asian countries suggests that a key factor for these impacts may be a lack of resilience to cope with the event in terms of infrastructure, properties, adaptation, awareness, and preparation.

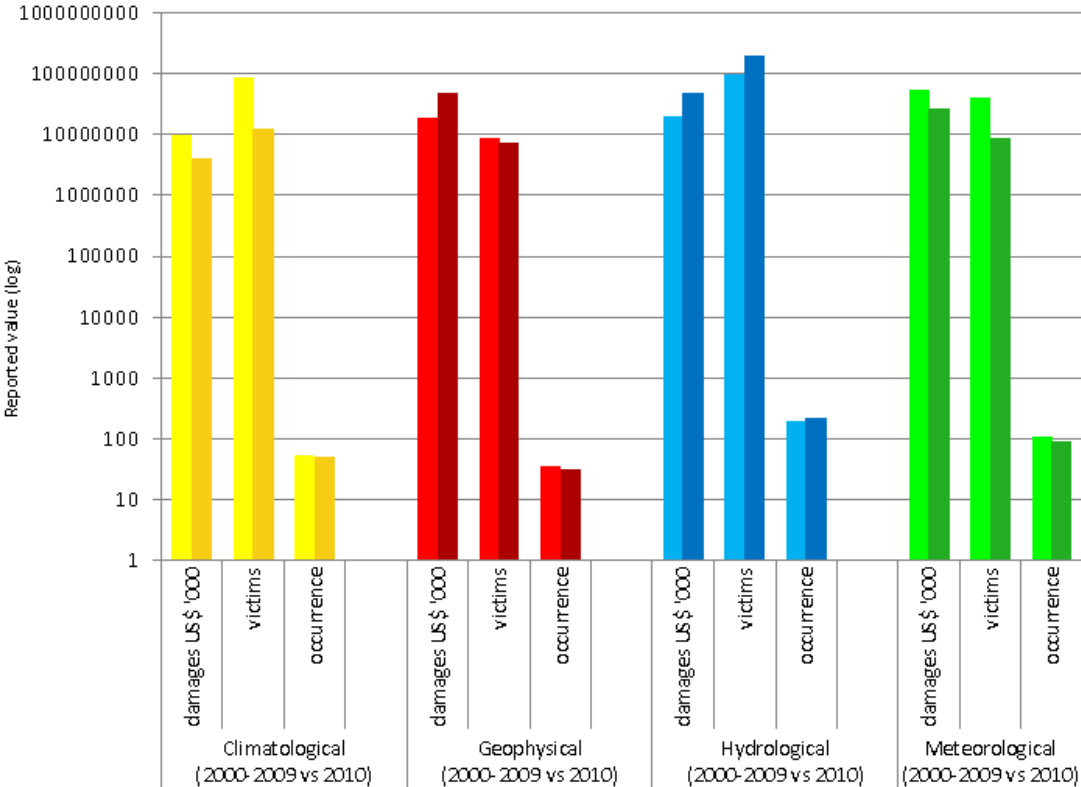
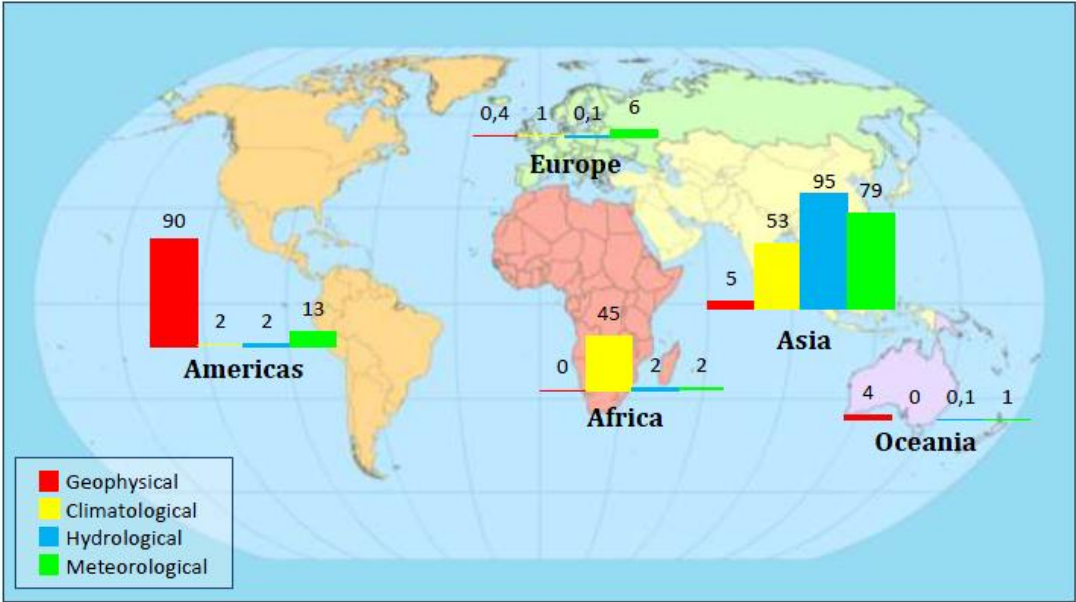


Figure 1.1: Natural disaster impacts by sub-group: 2010 versus 2000-2009 annual average (Guha-Sapir et al., 2011).



*Percentages ≤ 0.05 are displayed as zeros

Figure 1.2: Percent share of reported victims by disaster sub-group and continent in 2010 (Guha-Sapir et al., 2011).

The extent to which the impacts of a disaster can be reduced depends on the speed and effectiveness of managed response activities (Kerle & Oppenheimer, 2002). Different civil protection authorities, non-governmental organizations and international organizations have observed that there is a need for up-to-date spatial information to facilitate the management of disasters (i.e. floods) to help reduce their consequences and minimize the extent of affected areas in terms of material and human impact (Allenbach et al., 2005; Luscombe and Hassan, 1992). Remote sensing is a technology that is potentially well-suited to the provision of spatial information in a timely fashion that can assist disaster risk management.

Mapping and monitoring hazards and disasters using remote sensing imagery has proven successful, with applications for a range of disaster types, including floods, earthquakes, volcanic activity, wildfire, landslides and urban heat islands (Joyce, et al., 2009; Nichol, 2005; Tralli et al., 2005; Voigt et al., 2007). This success has been achieved as a result of a range of factors, such as improvements in spatial resolution; development in communication and networking for satellite-based disaster response; and the establishment of a number of international scientific and technical coordination bodies in the area of space-based information (Voigt et al., 2007).

The potential of optical remote sensing for monitoring several of these applications with regard to different disasters is well known. However, one of the big limitations is cloud cover during flood events, which prevents the collection of optical data. Radar satellite systems operate independently of light and weather conditions, making radar systems more appropriate for operational monitoring of flood events (see Nico et al., 2000). However, the resolution constraint has limited the usefulness of SAR imagery in the monitoring and evaluation of flood events. A number of studies have been conducted into the use of SAR data for mapping water bodies and the extent of flood events; however those studies have in general been based on lower resolution SAR imagery. For example, Huda (2004) assessed Radarsat-1, ERS-1, and SIR-C data for mapping small water bodies in Bangladesh, and found that not all sizes of water bodies can be identified (the limit being so-called *jolas* and *beels*, which have surface areas of 1000 m² or more). Therefore, and particularly in relation to the new availability of high resolution radar data (i.e. ultrafine Radarsat-2 and stripmap TerraSAR-X), previous studies based on lower resolution SAR systems are now not applicable. Accordingly,

there is a pressing need to evaluate the applicability of the new, high resolution SAR satellite data, and the associated image processing techniques, for supporting flood management.

1.2 Aim and Objectives

This study aims to evaluate the capabilities of high spatial resolution, space-borne Synthetic Aperture Radar data products in order to identify and accurately delineate water area extent. This will be accomplished by investigating the capabilities of Radarsat-2 and TerraSAR-X data products.

The main objectives of the research are as follows:

1. To investigate the capabilities of two satellite imaging radar sensors, namely Radarsat-2 (launched in December 2007) and TerraSAR-X (launched in June 2007). High spatial resolution data products from these sensors have been studied to assess their potential application to water area mapping, and in particular to establish the most appropriate system characteristics (spatial resolution, frequency, polarizations, and incidence angles) for the mapping of flood inundation in South Asian floodplains. The assessment has been implemented using a test site in Bangladesh, where floodplains typically consist of a complex patchwork of agricultural field systems, settlements and a large number of natural and man-made water bodies with different sizes and shapes. Ground data has been collected from the test site simultaneously with the acquisition of SAR imagery. Each SAR instrument has its own system capabilities - spatial resolution, polarisation and other system parameters - that can be evaluated in terms of adjusting each parameter to arrive at the most appropriate system for flood detection.
2. To determine effective image processing and spatial analysis methods for separating water bodies from other ground features. The study has applied different methods and techniques for pre-processing, enhancing, classifying and correlating ground truth data. This research process has been used to evaluate the most appropriate methods to delineate water surfaces in SAR imagery.

3. To perform a comparative empirical evaluation of Radarsat-2 and TerraSAR-X data products using imagery from both satellites acquired simultaneously (or at near simultaneous points) in order to establish which performs best for the detection of different water bodies by combining visual interpretation with ground-surveyed “truth” data.

1.2 Research Questions

The proposed research project has been implemented to answer the following indicative research questions:

1. Is it possible to automate water body detection so that such techniques can be transferred for application in other areas and environments?
2. What is the minimum size of water body or flood event that can confidently be identified from SAR imagery?
3. What is the optimum image processing sequence for separating water bodies from other ground features?
4. What are the effects of SAR system variations (e.g. polarization, spatial resolution and wavelength) for mapping water areas?
5. What are the effects of environmental factors such as land cover type on the detection of water bodies?
6. How precisely can flood extent (or area) be mapped using SAR data?

1.4 Thesis Structure

Chapter Two of the thesis presents an overview of the use of Earth observation techniques for flood risk management, and in particular the use of SAR remote sensing in the various phases of the flood disaster cycle (mitigation, preparedness, response, and recovery). Examples of initiatives that have used earth observation data for disaster management have been reviewed, including the international charter on space and major disasters and the United Nations platform for space-based information for disaster management and emergency response (UN-SPIDER). In the end of this chapter, the need for detailed flood area maps in local scale has been emphasized.

Chapter Three reviews the existing literature on the principles of mapping using synthetic aperture radar in terms of:

- SAR system parameters;
- Satellite image processing techniques for mapping hazards and disasters;
- Mapping floods and water bodies;
- SAR data interpretation;
- Evaluation of SAR frequency and polarization;
- Radarsat-2 and TerraSAR-X systems;
- SAR data accuracy assessment.

Chapter Four presents a detailed description of the study area. This includes a justification of the study area selection, geographic location, climate, floodplain and drainage network, hydrology and water resources, agriculture, and built-up areas. Chapter Five describes the methodology used in this study. The data used in this study, (Radarsat-2, TerraSAR-X, and dGPS field data) are described. This chapter also includes methods conducted for data preparation, flood mapping and accuracy assessment. The following chapter (Six) discusses the data preparation in terms of the data pre-processing and the SAR imagery texture analysis results. Results of the flood mapping are described in Chapter Seven, which includes four main sections: flood mapping using backscatter density slicing; flood mapping using image classification; contextual analysis; and evaluation of SAR products and processing and area estimation and quantification of confidence intervals on water area mapping. Chapter Eight discusses the potential applications of the methods developed in this thesis for flood area mapping. Chapter Nine is the final chapter and presents the main conclusions and gives the recommended directions for future research.

Chapter Two:**EARTH OBSERVATION FOR DISASTER RISK MANAGEMENT****2.1. Introduction**

As disaster risk reduction is a global concern, the International Strategy for Disaster Reduction (ISDR) was adopted by United Nations (UN) member states in 2000. The ISDR aims to reduce disaster losses by coordinating international efforts through the implementation of the Hyogo Framework (2005–2015). The goal of the Hyogo Framework is to guide states and organizations to reduce disaster risk (UNISDR, 2005). Disaster risk reduction requires a continuous process to prevent or reduce the impacts of natural and technological disasters. This involves establishing and implementing strategies, policies and programmes, including structural and non-structural measures at all levels of government and non-government involvement, in all phases of the disaster cycle: mitigation, preparedness, response and recovery (UNISDR, 2002).

Various attempts have been made to define disaster, but most definitions are either too broad or too narrow (Songer, 1999). However, the glossary of the UNISDR (2009) provides a comprehensive definition, where it is described as “a serious disruption of the functioning of a community or a society involving widespread human, material, economic or environmental losses and impacts, which exceeds the ability of the affected community or society to cope using its own resources”. The origin of natural disasters falls into two general types: geophysical disasters, such as earthquakes, landslides and volcanic eruptions; and climatic disasters, such as floods, droughts, cyclones and forest fires.

The term “disaster management”, also known as “emergency management” (UNISDR, 2009), can be defined as “the managerial function charged with creating the framework within which communities reduce vulnerability to hazards and cope with disasters” (FEMA, 2011a). The general goals of disaster management are to avoid or minimize losses from hazards; to provide urgent assistance to affected communities; and to assure short- and long-term recovery (GDRC, 2008). Although there is no tailored emergency management system appropriate for all countries, it is believed that specialist

knowledge and experience can guide authorities and organizations towards better solutions in managing emergencies (Unlu et al., 2010).

Effective emergency management requires appropriate planning and an integrated emergency plan at all levels of government and non-government involvement. Emergency management planning is a process of establishing arrangements and strategies that enable risks to be managed effectively by governments, organizations and communities (Abrahams, 2001). The planning process should deal with several components, such as assessing the likely effects of hazards, vulnerabilities and risks on communities; preparing strategies in relation to mitigation, preparedness, response and recovery; understanding the roles and responsibilities of all agencies; and establishing a strong emergency management network and preparing a comprehensive plan (Abrahams, 2001).

The most important aspect in emergency management, particularly in response and recovery planning, is a rapid and appropriate response to a disaster or crisis situation (Perry and Lindell, 2003). When planning for response operations, there must be a shared understanding in multiagency management of the concepts of command, control, coordination and communication (Abrahams, 2001). Command, which operates vertically within an organization, is defined as the direction of the organization's members and resources to perform specific tasks towards disaster management. Control relates to the responsibilities taken for tasks, and the horizontal coordinating activities across organizations, with the needs of emergency management activities. Coordination brings together all available resources and operates them vertically within the organization in order to ensure an effective disaster management response. Communication is essential for implementing command, control and coordination. A lack of communication often adversely affects the effectiveness of the response to disasters. Therefore, where appropriate communication should be strengthened in terms of better understanding roles and responsibilities and ensuring regular meetings are held between the personnel of all organizations that deal with disasters and participate in training and exercises (Abrahams, 2001).

Developing a policy for efficient emergency management requires an understanding of management principles. The International Association of Emergency Managers (IAEM) have proposed eight principles for emergency management (IAEM, 2007):

- Comprehensive – taking into account all types of hazards and all phases of disasters.
- Progressive – planning for mitigation and preparedness based on predicted future disasters.
- Risk-driven – assigning priorities and resources according to risk analysis.
- Integrated – focusing on unity of effort within all levels of government and all elements of a community.
- Collaborative – creating and maintaining genuine relationships and communication among individuals and organizations.
- Coordinated – harmonizing the activities of all relevant stakeholders.
- Flexible – using creative approaches.
- Professional – exploiting science and knowledge based on education, training, experience, ethical practice, public stewardship and continuous improvement.

2.2 Flood Disasters

A flood is the inundation of land that may cause damage, or loss of, land (WFP, 2011). Flood disasters impact on humans, infrastructure and the environment. As part of international efforts related to flood risk management, the International Flood Initiative (IFI) was launched in January 2005 during the World Conference on Disaster Reduction in Kobe, Japan. The overall aim of the IFI is to strengthen capacity in countries to better respond to floods and minimize the risks that result from floods by focusing on research, information networking, awareness, education, training and the provision of technical assistance and guidance (IFI, 2008). This recognises that flooding is a worldwide problem and is considered to be one of the most devastating natural hazards. Statistics from the Centre for Research on the Epidemiology of Disasters (CRED), as shown in Figure 2.1, compared to other natural disasters, demonstrate that floods have the largest impact on people. For example, the average annual number of affected people in the period 2000–2009 was more than 94 million, whilst in 2010 alone, flood disasters affected more than 178 million people (CRED, 2011). Moreover, the UN

predict that by 2050 two billion people will be vulnerable to floods; this figure is expected to double or more in two generations because of climate change and other factors (UNU, 2004). For these reasons, the emphasis of this thesis has been on evaluating new emerging remote sensing technologies for mapping areas inundated by water and also on assessing the extent to which SAR systems could provide reliable data in flood area inundation that could assist with disaster management given the day-night all weather capabilities of SAR.

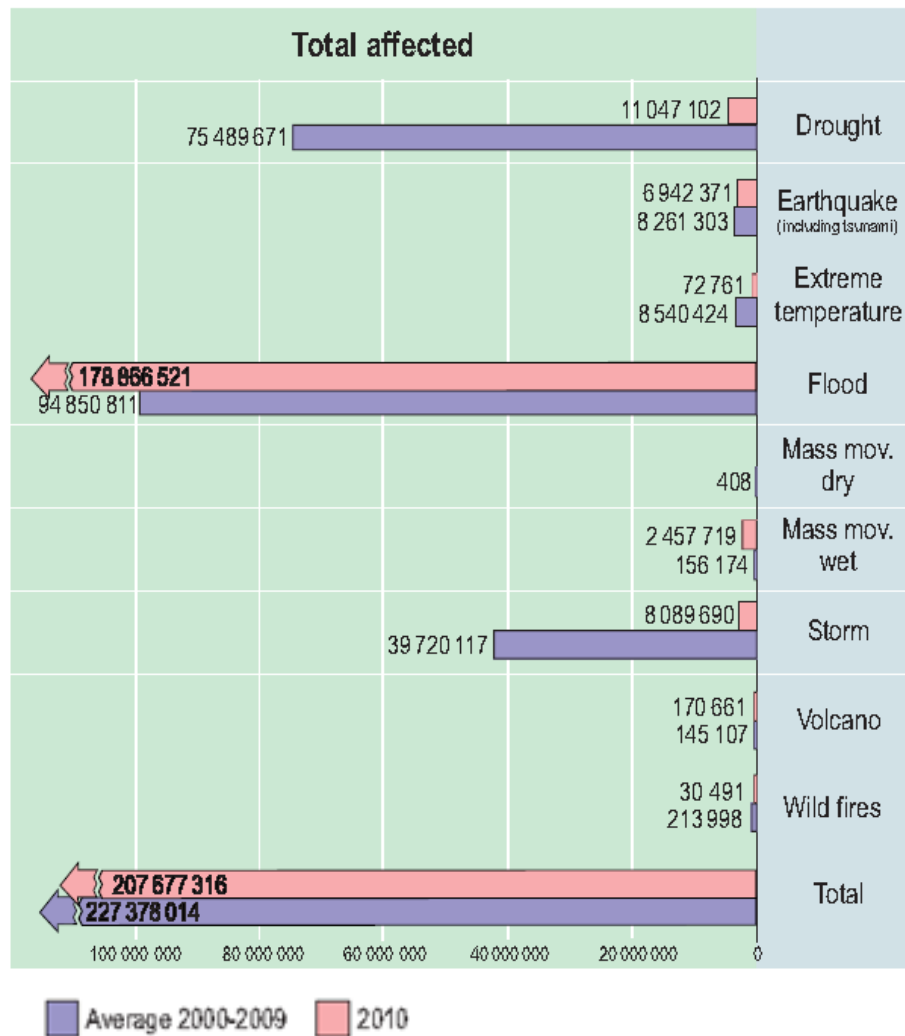


Figure 2.1: 2010 Human impact by disaster types compared to decade average (adapted from: CRED, 2011).

2.3 Earth Observation for Flood Disaster Management Cycle

The rapid development of remote sensing over the last decade has allowed remote sensing to become an important tool for mapping and monitoring of natural hazards and disasters (Gillespie et al., 2007; Joyce et al., 2009; Tralli et al., 2005; Voigt et al., 2007). An effective operational spaceborne system for disaster management should have two components (Sarti et al., 2001): an appropriate satellite revisit time, along with an appropriate required time for product generation; and appropriate sensor-types, resolution and image coverage. Therefore, the use of a particular type of remote sensing sensor will vary according to the nature and situation of a hazard and disaster. Table 2.1 gives examples of applications of different wavebands for disaster management.

Table 2.1: Applications of different wavebands for disaster management (adapted with modification from Lewis, 2009).

Wavelength	Waveband	Example applications	Example sensors
Visible	0.4-0.7mm	Vegetation mapping	SPOT; Landsat TM
		Building stock assessment	AVHRR; MODIS; IKONOS
		Population density	IKONOS; MODIS
		Digital elevation model	ASTER; PRISM
Near infrared	0.7-1.0mm	Vegetation mapping	SPOT; Landsat TM; AVHRR; MODIS
		Flood mapping	MODIS
Shortwave infrared	0.7-3.0mm	Water vapour	AIRS
Thermal infrared	3.0-14mm	Active fire detection	MODIS
		Burn scar mapping	MODIS
		Hotspots	MODIS; AVHRR
		Volcanic activity	Hyperion
Microwave (radar)	0.1-100cm	Earth deformation and ground movement	Radarsat-2; TerraSAR-X; TanDEM-X; COSMO-SkyMed; PALSAR
		Rainfall	Meteosat; Microwave Imager (aboard TRMM)
		River discharge and volume	Radarsat-2; TerraSAR-X; COSMO-SkyMed; PALSAR; AMSR-E
		Flood mapping and forecasting	Radarsat-2; TerraSAR-X; COSMO-SkyMed; PALSAR; AMSR-E
		Surface winds	QuikScat radar
		3D storm structure	Precipitation radar (aboard TRMM)

Optical and microwave remote sensing instruments have been used for mapping and monitoring hazards and disasters such as floods, earthquakes, volcanoes, wildfires, landslides and the urban heat island. Each of these different types of hazards requires different remote sensing and data analysis techniques. Table 2.2 lists some current satellite sensors with a summary of their characteristics which may be used in mapping hazards and disasters.

Table 2.2: Characteristics of some current satellite sensors used in mapping and monitoring hazards and disasters (Joyce et al., 2009).

Satellite	Sensor	Swath (km)	Nadir spatial resolution (m)	Revisit capability
Worldview	Panchromatic	16.4	0.46	1.1 days
	Multispectral	16.4	1.85	
QuickBird	Panchromatic	16.5	0.6	1.5–3 days
	Multispectral	16.5	2.4	
Ikonos	Panchromatic	11	1	1.5–3 days
	Multispectral	11	4	
RapidEye	Multispectral	77 x 1500	6.5	1 day
EO-1	ALI	60	30	Every 16 days
	Hyperion	7.5	30	
Terra	ASTER	60	15,30,90	4-16 days
Terra / Aqua	MODIS	2300	250,500,1000	At least twice daily for each satellite
ALOS	PRISM	35	4	Several times per year as per JAXA acquisition plan
	AVNIR	70	10	
	PALSAR (Fine)	40-70	10	
	PALSAR (ScanSAR)	250-350	100	
SPOT-4	Panchromatic	60-80	10	11 times every 26 days
	Multispectral	60-80	20	
SPOT-5	Panchromatic	60-80	10	
Komsat	Panchromatic	15	1	2–3 days
	Multispectral	15	1	
Landsat-5	TM Multispectral	185	30	Every 16 days
	TM Thermal	185	120	
Landsat-7	ETM+ Panchromatic	185	15	Every 16 days
	ETM+ Multispectral	185	30	
	ETM+ Thermal	185	60	
NOAA	AVHRR	2399	1100	Several times per day
Envisat	MERIS	575	300	2–3 days
Radarsat-2	Ultrafine	20	3	Every few days
Radarsat-1/-2	Fine	50	8	
Radarsat-2	Quad-pol fine	25	8	
Radarsat-1/-2	Standard	100	25	
Radarsat-2	Quad-pol standard	25	25	
Radarsat-1	Wide	150	30	
Radarsat-1/-2	ScanSAR narrow	300	50	
Radarsat-1/-2	ScanSAR wide	500	100	
Radarsat-1/-2	Extended high	75	25	
Radarsat-1	Extended low	170	35	
ERS-2		100	30	35-day repeat cycle
Envisat	ASAR standard	100	30	36-day repeat cycle
	ASAR ScanSAR	405	1000	
TerraSAR-X	Spotlight	10	1	11-day repeat cycle
	Stripmap	30	3	2.5-day revisit cycle
	ScanSAR	100	18	
Cosmo-SkyMed	Spotlight	10	<1	~37 hours
	Stripmap	40	3-15	
	ScanSAR	100-200	30-100	

The use of Earth observing systems for flood disaster management involves using an integrated cycle of phases that include: pre-flood mitigation and preparedness; response to flooding; and post-flood recovery (Samuels, 1999; European Commission, 2004) – where one phase cannot be effective in isolation from the others (Petak, 1985; Quarantelli, 1997; Norman, 2004; Ronan & Johnston, 2005; Gregg & Houghton, 2006; GDRC, 2008). The disaster management cycle is shown in Figure 2.2.

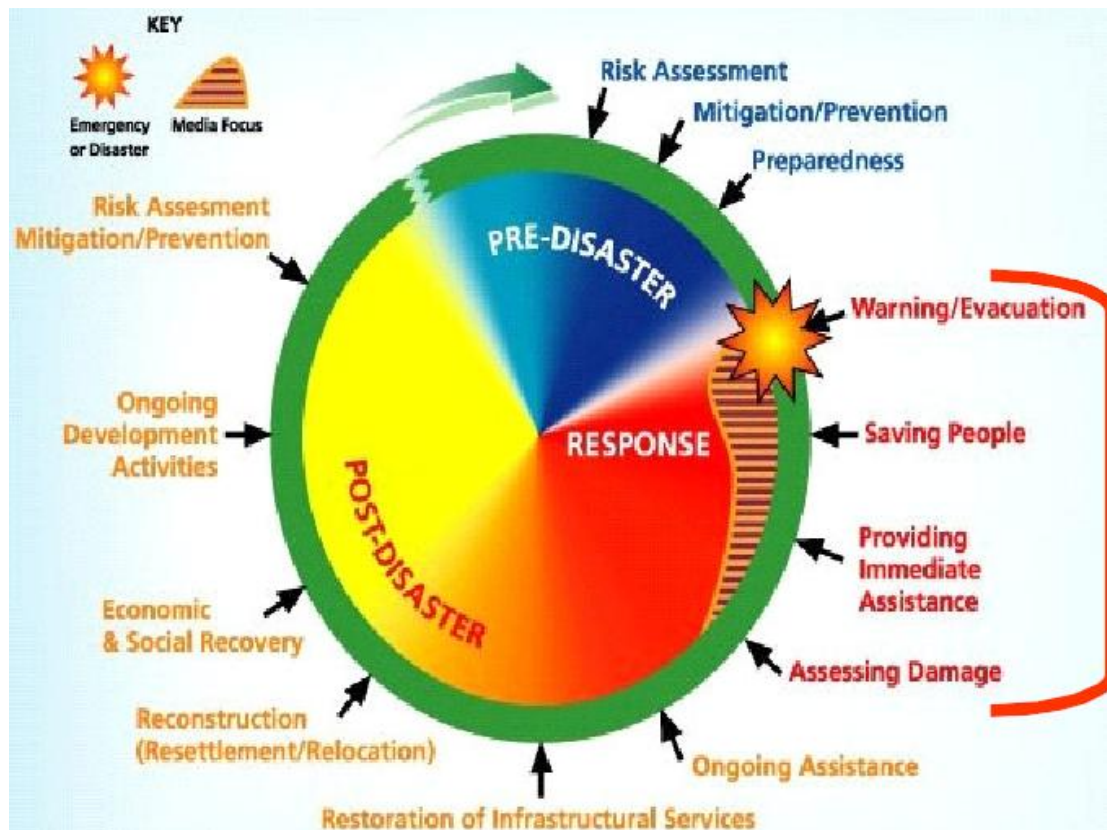


Figure 2.2: Disaster management cycle (Platzeck, 2009).

The use of remotely sensed data for the pre-disaster phase of a flood event involves the systematic mapping of vulnerable land and resources in flood-prone areas. It is essential to have available detailed maps of flood plains that quantify existing water bodies, productive land, settlements and other land use types to assess the potential risk of flooding.

The response phase entails the implementation of action plans. These actions will involve as soon as possible during or soon after floods occur by exploiting remotely sensed data. Data from remote sensing for response activities can involve actions designed to assess the impact of the event as it happens and may involve multi-data

image capture to map and monitor flooded areas; implement flood damage assessment for evacuation and sheltering displaced disaster victims; and to deploy immediate emergency relief efforts to flood-affected communities.

The goal of the recovery phase is to direct efforts after a flood disaster in terms of restoration and rehabilitation in the short term and long term until the community returns to normal. Examples of the use of remotely sensed imagery for this phase include the identification of appropriate locations and areas for establishing temporary housing, the assessment of flood damage for rebuilding infrastructures, and the restoration of business and community activities (Norman, 2004).

2.4 Initiatives for Using Remote Sensing for Disaster Management

Remotely sensed data can greatly assist operational activities in the aftermath of disasters during the response phase (Section 2.3). Although there have been many successful applications of remote sensing in supporting disaster management efforts, limitation of access to EO data within many less developed countries means that new solutions must be found. Several initiatives have therefore emerged for collaboration between international organizations and space agencies for data acquisition and delivery for countries affected by disasters.

A number of international and regional initiatives in recent years have contributed to making it easier to access space-based information in order to support disaster management. Examples of international initiatives include the International Charter on Space and Major Disasters (Bessis et al., 2004) and the UN Platform for Space-based Information for Disaster Management and Emergency Response (UN-SPIDER) (UNOOSA, 2007). Regional initiatives include the Sentinel Asia (2011) initiative, led by the Asia-Pacific Regional Space Agency Forum, and the Services and Application for Emergency Response (SAFER, 2011) project of the Global Monitoring for Environment and Security (GMES) programme by the European Union. The membership of such initiatives is made up of governmental and non-governmental organizations and agencies. A brief review of the Disaster Charter and the UN-SPIDER as examples of the international initiatives is presented in the following sections.

2.4.1 The International Charter on Space and Major Disasters

The International Charter on Space and Major Disasters, or the Disaster Charter, is a good example of the use of remote sensing in disaster management with activations that are global in scope. The Disaster Charter is an international agreement among space agencies to provide EO data to countries affected by disasters (Bessis et al., 2004). When a disaster occurs, a participating space agency activates the Disaster Charter to produce information ready for disaster-relief operations (Mahmood et al., 2002; Ito, 2005). For example, the Disaster Charter was activated 152 times for flood disasters between November 2000 and February 2011 (Disaster Charter, 2011) to support relief operations with thematic maps on flood extent.

The Disaster Charter, which started on 1st November 2000, was the first international mechanism to universally share remotely sensed data and knowledge for disaster management. By calling a single number, an authorized user can request the mobilization of space resources and associated ground resources of member agencies to obtain data and information on a disaster occurrence (Mahmood et al., 2002). Table 2.3 lists the current members and space resources of the Disaster Charter.

Table 2.3: Members of the Disaster Charter and available satellite resources (source: Disaster Charter, 2011).

Members	Acronym	Country	Space Resources
European Space Agency	ESA	EU	ERS, ENVISAT
Centre National d'Etudes Spatiales	CNES	France	
- Spot Image			SPOT
- National Space Organization	NPSO	Taiwan	Formosat
Canadian Space Agency	CSA	Canada	Radarsat
Indian Space Research Organization	ISRO	India	IRS
National Oceanic and Atmospheric Administration	NOAA	USA	POES, GOES
Comisión Nacional de Actividades Espaciales	CONAE	Argentina	SAC-C
Japan Aerospace Exploration Agency	JAXA	Japan	ALOS
United States Geological Survey	USGS	USA	Landsat
- Digital Globe			Quickbird
- GeoEye			GeoEye-1
DMC International Imaging	DMC		
- Centre National des Techniques Spatiales	CNTS	Algeria	ALSAT-1
- National Space Research and Development	NASRDA	Nigeria	NigeriaSat
- Tübitak-BILTEN/Space Technologies Research Institute	UZAY	Turkey	BILSAT-1
- British National Space Centre/Surrey Satellite Technology Limited	BNSC	UK	UK-DMC
- British National Space Centre/Qinetiq		UK	TopSat
China National Space Administration	CNSA	China	FY, SJ, ZY satellite series
German Aerospace Centre	DLR	German	TerraSAR-X, TanDEM-X

Although there is widespread confidence in the usefulness of the remote-sensing information obtained through the Disaster Charter for supporting disaster response efforts, there is a need to understand the effectiveness of such information in meeting user needs. For example, some end users stated in the *9th Annual Report* (Disaster Charter, 2010) that they could not fully exploit the Disaster Charter products because of a lack of appropriate equipment or because of problems dealing with the data formats, particularly of SAR products. Other end users have required technical training for data processing and interpretation (Disaster Charter, 2010). A significant attempt has therefore been made to overcome these difficulties in accessing and using space-based

information by establishing the UN-SPIDER, which the following section briefly reviews.

2.4.2 UN-SPIDER

The UN Platform for Space-based Information for Disaster Management and Emergency Response (UN-SPIDER) was established by the UN General Assembly in resolution 61/110 on 14 December 2006 to help all countries and organizations to gain access to and use of space-based information to support disaster management activities (UNOOSA, 2007). The UN-SPIDER programme is intended as a gateway to information obtained from space technologies for all phases of the disaster management cycle. Its activities are therefore aimed to ensure that countries and organizations are aware of the importance of such information and to develop its capacity to use the information effectively to reduce losses in disasters (Selg, 2009; Epler & Leitgab, 2011). The UN-SPIDER has agreements and cooperates with various mechanisms and initiatives for accessing the services of space-based solutions and facilitating coordination between users and existing initiatives. Examples of these on the international and regional level include the Disaster Charter, Sentinel Asia and the SAFER project of the GMES initiative (UNOOSA, 2010).

2.4.2.1 UN-SPIDER Global Network and Activities

The UN-SPIDER works on a global network through regional support offices and national focal points. Its regional offices aim to work closely with relevant regional and national centres of expertise in the use of space-based information for disaster management (UNOOSA, 2007). The regional offices help implement the UN-SPIDER work plan by providing expert technical advisory support, capacity-building and outreach (UNOOSA, 2010). Ten regional support offices have been created to date (Epler & Leitgab, 2011), and additional offices are currently being established. UN-SPIDER National Focal Points (NFPs) are governmental institutions dealing with disaster management and/or space technologies. The NFPs are nominated by national governments to collaborate with the UN-SPIDER to access and use space-based information for emergency management and to support their countries in incorporating

space-based technologies for disaster management into their national policies and activities.

UN-SPIDER support activities concentrate mainly on technical advisory support and on making it easier to access satellite data through its SpaceAid Framework. Its technical advisory support aims to provide technical advice to help national institutions to conduct assessments of their capacity with regard to access to and use of space-based solutions and to identify obstacles facing the use of space technology for managing disasters. This support is provided in a variety of forms such as meetings and remote computer desktop sharing, or technical advisory missions are carried out by experts from space and disaster management agencies in response to an official request from the respective member state (Epler & Leitgab, 2011). Another supportive activity of the UN-SPIDER is the SpaceAid Framework, which helps international and regional organizations to benefit from existing mechanisms and initiatives (i.e. Disaster Charter) during disasters by accessing space-based information to support the efforts of emergency response and recovery. Activation of the SpaceAid Framework can be triggered by the UN-SPIDER NFPs, UN-SPIDER regional support offices, UN organizations and authorized government agencies. A SpaceAid request includes all types of information provided by EO satellites, communication satellites and global navigation satellite systems. This can be implemented through a hotline on a 24 hours a day, seven days a week basis (Stumpf, 2010; UNOOSA, 2010).

2.4.2.2 UN-SPIDER Knowledge Portal

Since knowledge management is one of the main goals of the UN-SPIDER, it has established a web-based platform to provide people involved in disaster risk management with information, communication and shared experience in capacity-building on the use of space-based information. The knowledge portal consists of various resources and guides on space technologies that provide an overview of the different satellite missions and guides on the procedures of disaster management and the use of satellite technology for healthcare support (Epler & Leitgab, 2011). The portal also allows users access to available space-based products and services.

Users of the knowledge portal can find guidance on applications of space technologies to disaster risk management by using the Space Application Matrix (Figure 2.3). The Matrix is an attempt to guide users interactively to employ space technology appropriate to the disaster type and phase of the disaster management cycle. It consists of three categories – space technology, cycle phase and disaster type – and is also supported by case studies authored by experts and practitioners on applications of space technology to various phases of the disaster management cycle (Stumpf, 2011).

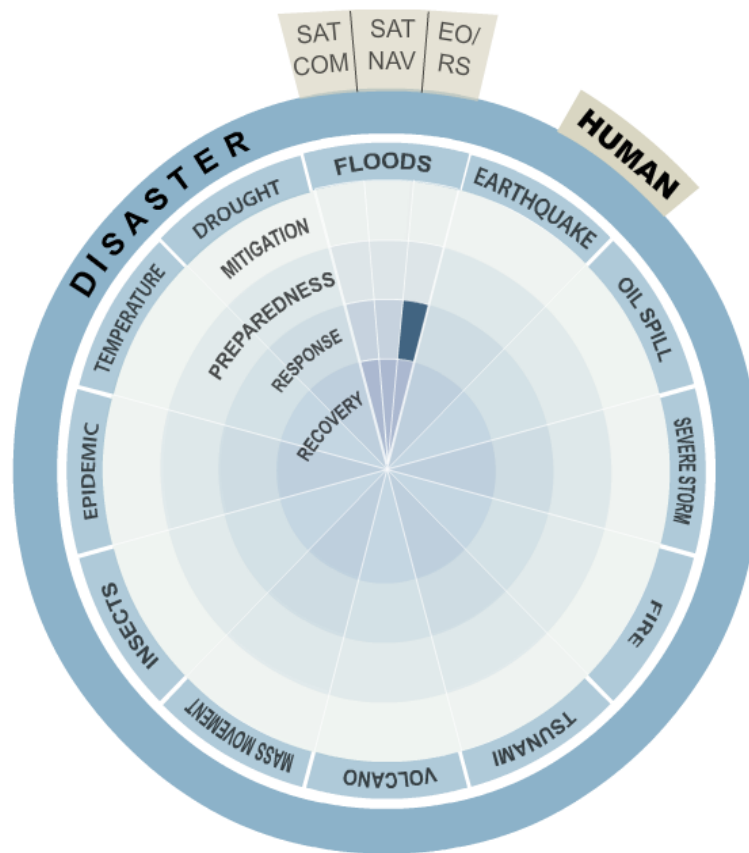


Figure 2.3: UN-SPIDER Space Application Matrix (adapted from: UN-SPIDER Portal, 2011).

2.5 The need for detailed flood area mapping

In the event of a major flood, local and national authorities, including rescue and other emergency services, require timely and accurate information regarding the geographic extent of flood affected areas (Allenbach et al., 2005). It is widely acknowledged that remote sensing can provide invaluable information for monitoring and mapping flood events, and particularly for damage assessment (Sanyal & Lu, 2004). The need for

detailed damage assessment of the flooded areas is very important for identification evacuation routes, safe deployment of search and rescue services, and delivering aid and other support. For example, during the 2010 Pakistan flood detailed maps were needed to help identify damaged roads and bridges for accessing flood-affected communities and for providing immediate relief (e.g. see Figures 2.4 and 2.5). Therefore, there is a clear need for high resolution imagery that can provide reliable maps during the event, and thereafter as the flood wave develops and moves through down the drainage basin, impacting communities. Radar remote sensing is potentially the most important technology for large area mapping of floods when cloud cover obscures the ground from optical sensors. However, it is not until now that synthetic aperture radar sensors (e.g. Radarsat-2 and TerraSAR-X) have been able to offer the high resolution data that could be used for detailed impact assessment. Because these data are new there is an urgent need to assess their capability for providing the detail needed for all phases of the disaster cycle: pre-flood, response and post-disaster.

Although one would wish to evaluate SAR data during an actual flood, the dynamic nature of such an event make this almost impossible to combine with the systematic evaluation of water (flood) area detection. Therefore, this study focused on mapping static water features in a flood-prone landscape to investigate the relative accuracy of Radarsat-2 and TerraSAR-X sensors for detecting and mapping water compared to other land cover types, and to evaluate the accuracy of using SAR for quantifying water area extent. For that reason, Chapters 5, 6, and 7 discuss the technical assessment of SAR products for water body detection. It is anticipated that the methods developed could be suitably adapted and applied to operational flood disaster management. Chapter 8 discusses the potential applications of the methods for mapping flood area in order to support flood disaster management.



Figure 2.4: an example of a damaged bridge - Pakistan flood-2010 (adapted from EPACHA, 2010).



Figure 2.5: An example of houses surrounded by floods - Pakistan flood, 2010. (Adapted from: [www. stamfordadvocate.com](http://www.stamfordadvocate.com)).

2.6 Summary

In view of the fact that floods are considered to be one of the worst types of disasters in terms of their impact on people worldwide, it is surprising that the potential of new high resolution radar remote sensing data for flood mapping has not been systematically studied in a quantitative way until now. Although attempts and efforts have been implemented for accessing and delivering earth observation data to the areas affected by flood disasters by regional and international initiatives, there is still a need to provide applications of radar remote sensing information that are well integrated into the different phases of the flood disaster management cycle (i.e. pre-flood mitigation and preparedness, response to flooding, and post-flood recovery). These data contribute valuable information in more than just the response phase.

There is a need to understand the full potential of the new SAR remote sensing data and to identify what processing methods are suitable for producing SAR products for flood disaster management applications. The following chapters outline a methodology that seeks to provide direct empirical assessment of two of the new generation of SAR systems (Radarsat-2 and TerraSAR-X) and uses high quality ground data on static water bodies in a major floodplain that is frequently flooded to investigate and quantify the potential of SAR for delivering high-quality reliable flood area mapping that can be applied to all phases flood disaster management.

Chapter Three:**PRINCIPLES OF MAPPING USING SYNTHETIC APERTURE RADAR****3.1 Background**

Remote sensing (RS) is the science, art and technology of obtaining information about physical objects or phenomena through the analysis and interpretation of imagery acquired by non-contact sensor systems (ISPRS, 2008; Lillesand et al., 2004). Remote sensing based disaster mapping has increasingly become an important data source for rapid response in terms of human relief and recovery (see chapter seven). It is an invaluable source of information for the detection, monitoring and analysis of several different types of natural hazards and disasters such as floods, earthquakes, wildfires, volcanic activity and landslides (Joyce et al. 2009). Satellite sensors consist of two main types: passive and active. Passive sensors record the emitted or reflected radiation from objects on the earth's surface. In most cases the source of radiation is the sun. These types of sensors capture or scan visible, near infrared, short wave infrared and thermal-infrared wavelengths (Figure 3.1). Examples of passive sensors include Landsat TM, ETM+ Ikonos, NOAA AVHRR and SPOT HRV satellites. Active sensors, on the other hand, transmit and receive their own energy, such as laser light (i.e. LIDAR), or radio waves RADAR (Radio Detection and Ranging). The main focus of this study is RADAR. The basic concept of radar is that microwaves are emitted from an antenna that reflect off a distant surface, allowing strength and roundtrip time of the signals to be measured by a receiving antenna (JPL, 2008; Rees, 2001; Short, 2008; Szekiolda, 1988). Radar systems normally transmit and receive signals in the wavelength range of 1 cm to 1 m, equivalent to a frequency of between 300 MHz and 30 GHz (Campbell, 2002; Freeman, 1996; Globe SAR) (Figure 3.1).

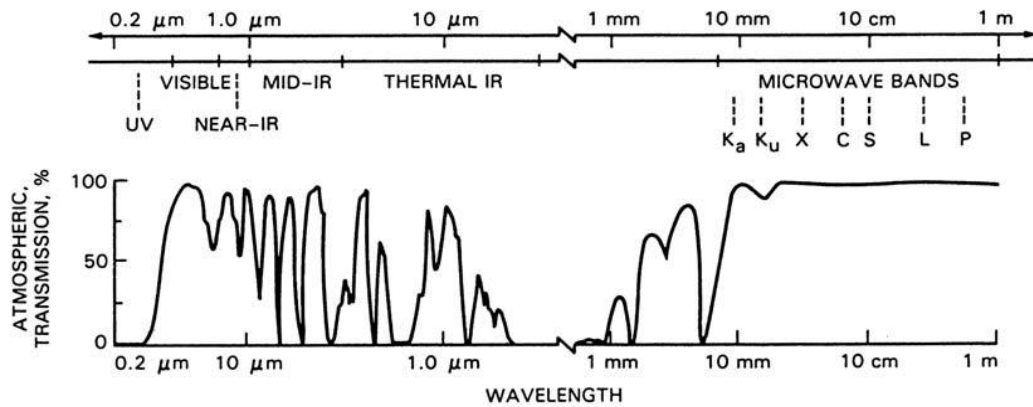


Figure 3.1: The electromagnetic spectrum showing the Visible, Near IR, Middle IR, Thermal IR, and Microwave regions and the efficiency of atmospheric transmission (Lewis and Henderson, 1998).

Whilst the development of radar systems was initially based on real-aperture side-looking airborne radar (SLAR), improvements in azimuth resolution using Doppler shifts of the return signals favour the development of synthetic-aperture radar (SAR). Table 3.1 highlights of SAR history.

SAR is an advanced technique used to reproduce the effect of long antennae by combining the returned signals received by the radar during its along-track movement, while the aperture of SLAR is the opening of the physical antenna used to collect the returned signals (Freeman, 1996). Until SAR was developed, the ground resolution of radar systems was dependent upon the physical size of the receiving antenna. This made achieving high-resolution images almost impossible. Advances in SAR technology enable very high levels of ground range resolution to be obtained from space-borne instruments. Optical sensors are able to detect water bodies and flood extent through high-resolution imagery. However, clouds and other weather conditions limit their abilities. Radar systems provide the possibility to deliver data 24 hours per day and provide all-weather coverage because the radar pulse is capable of penetrating cloud cover.

Table 3.1: Highlights of SAR history – from radar to SAR technology (DLR, 2011; Jackson and Apel 2004; JPL, 2011; Lusch, 1999; UGS COSMO-SkyMed, 2011).

1886	Heinrich Hertz discovers radio waves and finds that reflections can be received from objects.
1903	Christian Hulsmeyer obtains the first patent for using radar to detect ships.
1920	A.H. Taylor (US Naval Research Laboratory) develops a ground-based pulsed radar system.
1930	The US Naval Research Laboratory team uses a ground-based radar system to detect and track ships and aircraft.
1937	Sir Watson-Watt (UK) develops the first practical radar system for aircraft detection.
1938	First airborne radar images show the reflections from ships at sea to a range of 10 miles.
1940s	Independent and secret development in various countries of radar systems during WWII.
1950s	Real-aperture side-looking airborne radar (SLAR) developed.
1952	The first operational SAR system developed.
1953	The first airborne SAR image acquired.
Late 1950s	Goodyear Corporation and Ohio State University conduct research into measurements of terrain backscattering from static and airborne radars.
1960s	SLAR systems become commercially available.
1970s	Multichannel, airborne SAR systems are developed at the Environmental Research Institute Of Michigan, the NASA JPL and the Canadian Centre for Remote Sensing.
1972	The first space-borne SAR system, the Apollo Lunar Sounder Experiment radar, flown around the Moon on Apollo 17.
1978	SEASAT satellite, the first civilian SAR satellite with L-band SAR sensor, NASA (USA).
1981	Spaceborne Imaging Radar series starts – SIR-A
1984	SIR-B
1991	ERS-1, C-band, European Space Agency (ESA)
1992	JERS-1, L-band, Japan Aerospace Exploration Agency
1994	SIR-C
April 1995	ERS-2 - C-band, European Space Agency (ESA)
November 1995	Radarsat-1, C-band, Canadian Centre for Remote Sensing
2000	SRTM- C,X-bands. Shuttle Radar Topography Mission. NASA/DLR.
March 2002	ENVISAT (ASAR), C-band, European Space Agency (ESA)
January 2006	ALOS (PALSAR), L-band, National Space Development Agency of Japan
June 2007	TerraSAR-X, German Aerospace Centre
June 2007	COSMO-SkyMed X-band constellation (composed of four satellites), the first satellite of the constellation has been launched by the Italian Space Agency (ASI)
December 2007	Radarsat-2, C-band, Canadian Centre for Remote Sensing
June 2010	TanDEM-X, the first bistatic SAR Interferometry mission (TerraSAR-X Add-on), the two satellites flying in a closely controlled formation with distances between 250 and 500 m . German Aerospace Centre

Various studies have evaluated the potential of SAR data and verified its effectiveness in mapping flood extent. However, small flooded areas require further investigation: for example, Henderson (1995) found that the minimum water-body area that can be identified from 1:100.000 scale mapping is 8 ha.

In recent years, researchers working on the application of RS for flood mapping have been increasingly interested in SAR (see Table 3.2 for examples of current and near future SAR instruments). Huda (2004) evaluated optical imagery in mapping water bodies in Southeast Asia but encountered problems with cloud cover and poor seasonal coverage, and the detection of small water bodies was consequently limited. He also found that data from ERS-1 and NASA's SIR-C displayed difficulties in detecting a water body with a spatial size of less than 1000 m².

Table 3.2: Current and near future commercial earth observation SAR sensors.

Agency	Satellite and Instrument	Date of Launch	Band
European Space Agency (ESA)	Earth Remote Sensing Satellite 2 ERS-2	April 1995	C
Canadian Centre for Remote Sensing (CCRS)	Radarsat-1	November 1995	C
ESA	ENVISAT Advanced Synthetic-Aperture Radar (ASAR)	March 2002	C
National Space Development Agency of Japan	ALOS Phased Array Synthetic-Aperture Radar (PALSAR)	January 2006	L
German Aerospace Centre (DLR)	TerraSAR-X	June 2007	X
Italian Space Agency (ASI)	Cosmo-SkyMed (Constellation-4)	June 2007	X
CCRS	Radarsat-2	December 2007	C
DLR	TanDEM-X	June 2010	X
HISDESAT-Spain	PAZ	Due 2012	X
ESA, GMES	Sentinal-1	Due 2013	C
(CCRS)	Radarsat constellation	Due 2014	C

Although significant benefits have been achieved from applications of optical sensors, the SAR sensor has several advantages over optical satellite data:

- It has its own illumination source in the form of micro waves, while optical Sensors rely upon the sun's illumination or thermal radiation.
- SAR microwave energy can penetrate clouds and can be used at night and in all weather conditions. It may also, depending on polarization and frequency, penetrate, to some extent, vegetation, dry sand and snow.
- It has all-weather synoptic views and is thus able to map large areas systematically.
- Radar wavelengths are sensitive to the surface roughness and dielectric constant.
- SAR images can be produced from different polarizations and may be operated at various frequencies.

3.2 SAR System Parameters

Although SAR imagery formed by microwave backscattering depends upon environmental variations (i.e. soil, vegetation, manmade features), it is also significantly influenced by SAR system parameters. These parameters, discussed in the following sections, include wavelength, polarization, spatial resolution, incidence angle, look direction, backscattering and speckle.

3.2.1 SAR Frequency

SAR instruments considered in this study are Radarsat-2, which uses C-band microwave (centre frequency 5.405 GHz), and TerraSAR-X, which uses X-band (frequency 9.65 GHz). The C-band and X-band are useful for imaging open water and flooding areas, while the L-band (e.g. PALSAR 1.27 GHz) has a lower frequency and is more able to penetrate forest and vegetation canopies (Liew, 1997) (Figure 3.2). Table 3.3 shows the characteristics of current SAR satellite bands.

The sensors investigated in this study use different wavelengths (C-band 5.6 cm, and X-band 3.11 cm). Surface roughness in SAR imaging depends on the wavelength of the microwave. A land surface can appear smooth to a long-wavelength radar, while the same surface appears rough at a short wavelength. If a SAR, with an L-band (15 to 30

cm wavelength) illuminates a surface with a roughness of the order of 5 cm, the surface will appear dark because of low backscatter. In contrast, in an X-band (2.4 to 3.8 cm wavelength), the same surface will appear bright because of high backscatter (Liew, 1997).

Table 3.3: Characteristics of some current SAR satellite bands.

SAR Band	Frequency (GHz)	Wavelength (cm)
X (TerraSAR-X)	9.65	3.11
C (Radarsat-2)	5.405	5.6
L (PALSAR)	1.27	23.6

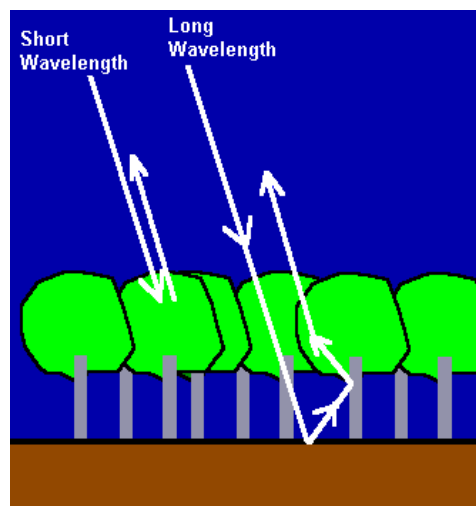


Figure 3.2: Short and long wavelengths reflected from a surface. Note that the long wavelength appears to be reaching through the canopy (adapted from Liew, 1997).

3.2.2 Polarization and Spatial Resolution

Polarization refers to the orientation of the electric field vector of the transmitted beam with respect to the horizontal direction (Yamazaki, 2007). If the beam is horizontally polarized, the vector oscillates along a direction parallel to the horizontal direction. On the other hand, if the oscillation of the electric field vector is along a direction perpendicular to the horizontal direction, the beam is vertically polarized (Liew, 1997).

When different polarizations are used, backscatter will also differ. Transmitting pulses from a SAR satellite can be polarized horizontally (H) or vertically (V) and can also be received in either H or V, or with a combination of HH, VV, HV or VH. The phase of the received pulses (HH and VV signals) in some SAR satellites can be measured. The correlation coefficient for the HH and VV can also be measured by determining the similarity of the HH and VV scatterers (Freeman, 1996). Multiple polarizations help to distinguish the physical structure of the scattering surface. Depolarization occurs because of the physical and electrical properties of ground features, such as roughness and volume scattering from non inhomogeneous media such as surface vegetation (Campbell, 2002).

The spatial resolution of a SAR sensor has two dimensions: range and azimuth. The range resolution depends upon the length of the microwave pulse. The shorter the pulse length, the finer the range resolution. In each cell of the radar image the signal is averaged and recorded. If a target is smaller than the cell, it is not possible to distinguish it (Trevett, 1986). The range (cross-track) resolution is dependent on the length of the pulse. If the separation between two targets is greater than half the pulse length, it is possible for it to be determined in the range dimension. Moreover, the ground range resolution depends on the incidence angle (Yamazaki, 2007).

3.2.3 Incidence Angle and Look Direction

The incidence angle is the angle between the incidence radar signal and the direction perpendicular to the ground surface that the signal strikes (Campbell, 2002; Liew, 1997). The incidence angle may be affected by topography (Figure 3.3). The SAR backscatter for a smooth surface is much less at a high incidence angle than that at low ones (Srivastava et al., 2009). Therefore, the smooth surface has higher differences between low and high backscatter while the rough surface has lower differences. When incidence angle is increasing, the contrast between water and land in SAR imagery is also increased, therefore, water detection is most successful with a high incidence angle (Solbo et al., 2003).

Look direction is the direction in which the radar antenna is pointing when transmitting signals and receiving backscatter from the ground surface. Radar shadow tends to be

maximized when look directions are perpendicular to topographic position (Campbell, 2002). Radar shadow extent depends on relief and the orientations of features relative to the flight path. Features positioned in the near range will have smaller shadows than those at the far-range edge of the image (Campbell, 2002; Globe SAR, 2008). To take account of this problem, the test site in the present research project was chosen for its very low relief.

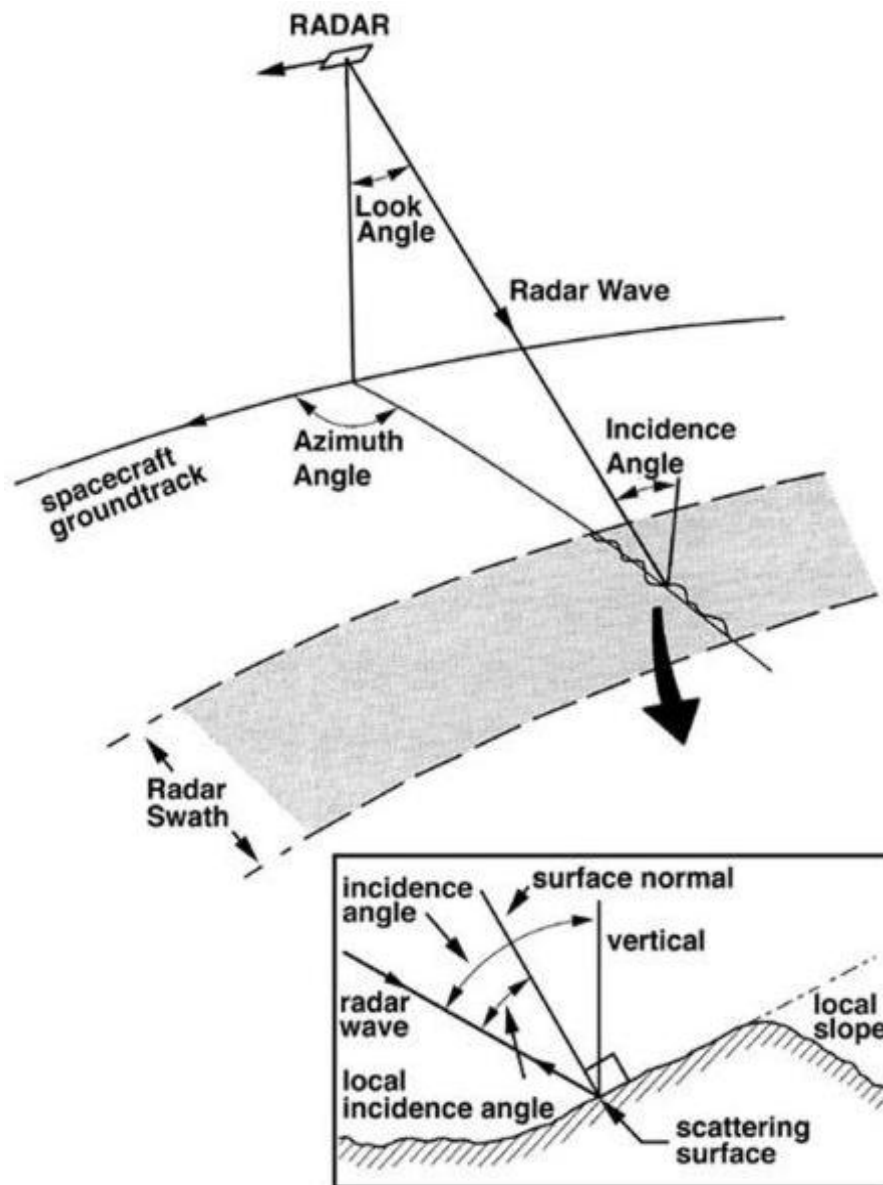


Figure 3.3: Schematic diagrams of geometry of radar image acquisition system and incidence angles. The incidence angle may be affected by planetary curvature. Local incidence angle may be affected by local topography (Henderson and Lewis, 1998).

3.2.4 Backscatter

A SAR image is usually presented as a grey scale, with the intensity of each pixel representing the amount of energy returned from that area on the ground (Liew, 1997). Darker areas in the image indicate low backscatter or little energy was returned to the radar, while brighter features represent high backscatter or a high portion of returned energy (Freeman, 1996). In general, the higher the backscatter intensity, the rougher the surface being imaged (Liew, 1997). A rough surface scatters the radar pulse in all directions while part of the radar energy is scattered back to the radar sensor.

The nature of backscattering from an area depends upon the SAR system and the environmental conditions. System parameters include the frequency and polarization of the radar pulses, the incidence angle of the radar beam and the look direction. Environmental variations comprise the types, sizes and shapes of features, the types of land cover (i.e. soil, vegetation or manmade features), the moisture content and geometric factors (i.e. roughness and slopes) (Freeman, 1997). Thus, when different frequencies are used, backscatter will also differ. The interaction between radar signals and the ground surface depends on the incidence angle of the radar pulse on the surface (Lillesand et al., 2004). Backscatter variations may result from the interaction of various roughnesses and incidence angles, as shown in Figure 3.4.

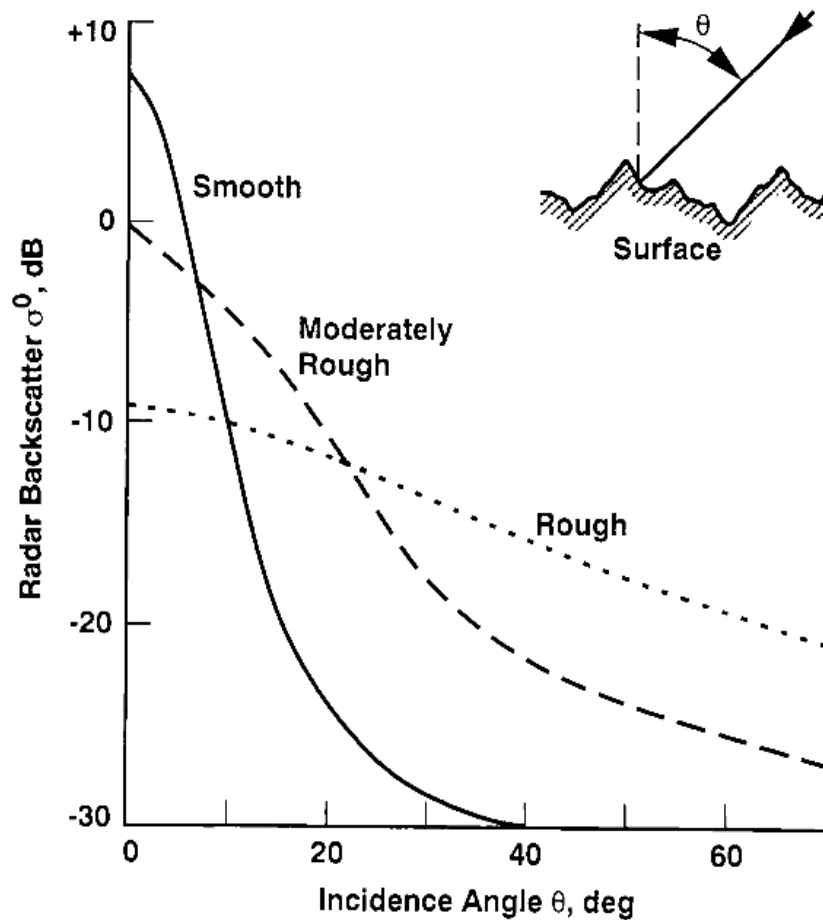


Figure 3.4: Typical radar backscatter curves for smooth, moderate and rough surfaces and different incidence angles (NASA, 1989, cited in Henderson and Lewis, 1998).

The pixel intensity values and the backscattering coefficient are measured in decibel (dB) units ranging from +5 dB for very bright objects to -40 dB for very dark surfaces (Freeman, 1996). Backscatter is sensitive to the dielectric constant, which is a measure of the electrical properties of surface materials (Lillesand et al., 2004), meaning that radar sensors are sensitive to the state and amount of water. Dielectric properties are a measure of the rotation of polar molecules of water (Waring et al., 1995). Lower dielectric constant indicates increased amounts of incidence energy absorption, such that the object will appear to be dark on the image (CCRS, 2008).

SAR can also assess variations in the state of water on land surfaces and within plants and soil. The smooth surface of water reflects all or most of the SAR signals away from the sensor. On the other hand, a water surface under a canopy of vegetation generates high backscatter because of interaction between the surface water and the trees, which enables flood mapping (Hess et al., 1990).

Vegetation can be a complicating factor as radar interaction depends strongly on the frequency and polarization of the microwave energy as well as the structure of the canopy (Figure 3.5). When water is smooth and calm it acts as a specular reflector to the radar signals (Figure 3.6). The returned signal will be at an angle equal to the incidence angle according to the law of specular reflection, which states that most of the energy is directed in a single direction. Thus the radar antenna receives low backscatter and the water appears dark in the radar imagery. Conversely, a rough water surface appears brighter in the SAR imagery. This aspect must be taken into account when monitoring flooded areas. When the radar pulse interacts with a target and is then returned to the sensor it may appear very bright in the image because of the corner-reflector effect or double-bounce effect (when a beam bounces twice off the surfaces back to the sensor). Figure 3.7 illustrates different types of surface and how they appear in a radar image (Campbell, 2002; Liew, 2001). These aspects of SAR backscatter intensity have been exploited in the detection of flooding (Dellepiane et al., 2000).

Within the land use of Bangladesh's floodplain, backscatter characteristics can be outlined through four major trends (Hasan et al., 1998): settlement areas and forested terrain are likely to give high backscatter; water bodies and open flooding tend to give low backscatter and after inundation the amount of backscatter is reduced; backscatter then rises again with the recession of floodwater (Leeuwen et al., 1997).

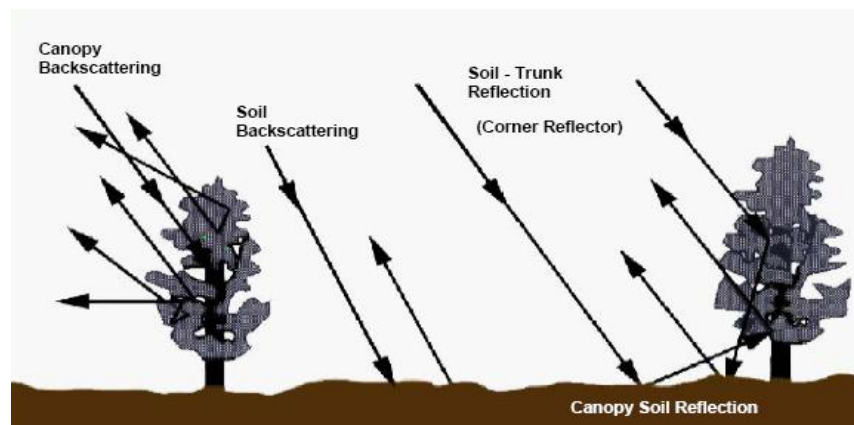


Figure 3.5: Radar energy scattering from different surfaces. Note that trunks of trees may cause the corner reflector effect (adapted from Globe SAR, 2008).

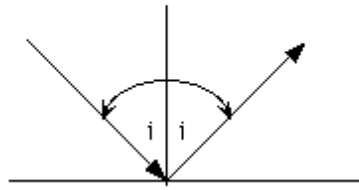


Figure 3.6: Backscatter from smooth surfaces (specular reflection) the angle of reflection is equal to the angle of incidence (adapted from Liew, 1997).

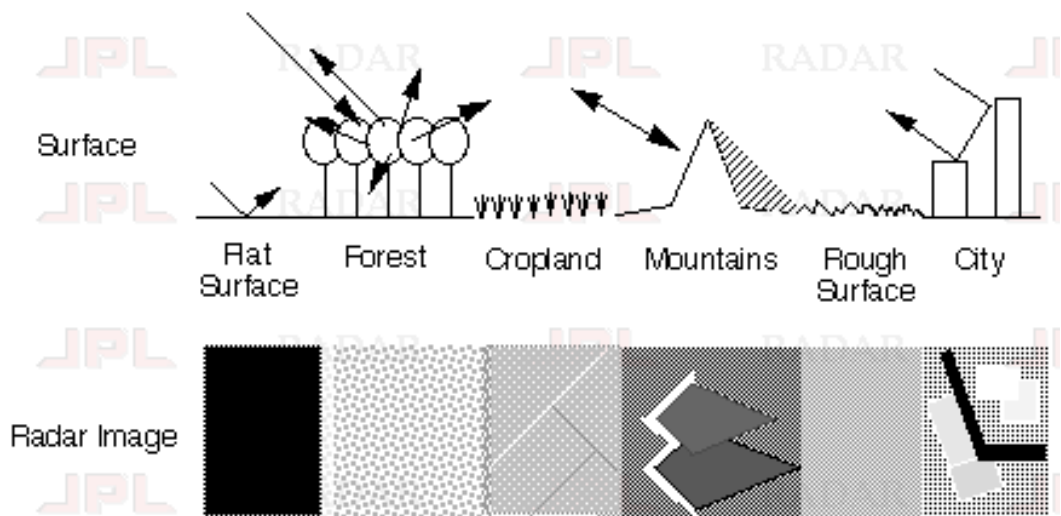


Figure 3.7: Imaging different types of surface with radar. Note how surfaces appear in a radar image (adapted from JPL-Freeman, 1996).

3.2.5 Speckle Filtering

Speckle is the coherent interference of waves (which is manifest as a grainy salt-and-pepper pattern in radar imagery) scattered from ground-surface elements (McCandless and Jackson, 2004). This causes random constructive and destructive interference in each resolution cell, resulting in random bright and dark areas in the radar images. Reducing speckle will enhance radiometric resolution, but at the cost of spatial resolution. Speckle noise in a digital image can be suppressed by the application of a speckle removal filter, which is necessary to improve classification and enhancement before image analysis (Liew, 1997; Lillesand et al., 2004). Speckle filtering will improve discrimination of scene targets and leads to easier automatic image segmentation with the use of non-adaptive and adaptive filters. Non-adaptive filters (i.e.

fast Fourier transform filters) consider the parameters of the whole image signal but not the local properties of the terrain backscatter or the nature of the sensor. Adaptive filters, such as the frost, lee, map gamma, local mean and local median filters, accommodate changes in local properties of the terrain backscatter. They should be used in preference to non-adaptive filters (Gagnon and Jouan, 1997; Globe SAR, 2008). If images are processed with a small number of ‘looks’, distribution intensities will have inconsistencies due to speckle noise. Therefore, in this case multi-look processing is usually applied (Lillesand et al., 2004; SARMAP, 2007).

3.3 Development in SAR Technology

The development of radar satellite instruments is advancing rapidly. The advanced technology and capabilities incorporated into the SAR satellites range from higher resolution and variety of beam modes to fully polarimetric products, higher resolution SAR-interferometry and higher accuracy DEMs. Examples of new civilian SAR satellites include Radarsat-2, TerraSAR-X and COSMO SkyMed. Section 3.8 proposes brief details about the Radarsat-2 and TerraSAR-X SAR sensors as examples of the advanced remote sensing systems and highlights the advanced technical design of SAR sensors and its implication on application and operational flexibility.

Enhancements in radar satellite imaging led to the production of higher spatial resolution (from three metre to up to 1 a metre) images of surfaces when allows more land cover details to be identified and improves object detection. Improved object detection enabled various applications include mapping at scale of 1:20,000 (Staples, 2005). The range of new imaging beam modes with various resolution swaths and incidence angles provide the opportunity for broad applications and strengthen the operational aspects. Examples of new beam modes incorporated into the recent SAR satellites include spotlight (1 m resolution) ultrafine and stripmap (3 m resolution) and Polarimetric-Fine Quad Polarization (8 m resolution) (for more details see section 3.8). Fully polaremetric (HH+VV+HV+VH) products enable more information to be extracted, better discrimination of various surface types and improved land cover classification (Staples, 2005). In addition to the SAR enhancements mentioned above, the higher resolution of SAR-Interferometry (InSAR) (Adam et al., 2008). The very high resolution SAR products enabled high accuracy deformation monitoring when

applying Persistent Scatterer Interferometry (PSI) technique (Gernhardt and Bamler, 2010). Moreover, development of SAR products extended to produce high accuracy operational global DEM products with (absolute: <10m, 90%; relative: <2m, 90%) by TanDEM-X (TerraSAR-X Add-on for Digital Elevation Measurements). The TanDEM-X DEMs are generated by using the bistatic InSAR stripmap mode which uses one satellite as a transmitter and the scattered signals are then received by both satellites simultaneously (Schulze et al., 2009).

3.4 Mapping Floods and Water Bodies

SAR imagery has shown essential benefits for various hydrologic applications, such as detecting and mapping lakes, water bodies, coastal wetlands, water levels and the extent of flooding. Because of the low backscatter associated with smooth water surfaces, and the high response from rough surfaces, most water bodies are visible on SAR imagery (Henderson and Lewis, 1998). However, monitoring and detecting the extent and timing of flooding is also vital for flood risk management. Applications of mapping water by SAR sensors focus on monitoring and detecting water bodies for resource management and monitoring the extent of flooding.

The mapping and monitoring of flooded terrain are often difficult using remote sensing with visible or near-infrared imagery, for three main reasons (Bakimchandra, 2006): a) the difficulty in delineating the land/water interface in visible bands, b) water bodies are often covered by clouds and may also occur under cover of darkness, and c) the vegetation canopy can obscure the flood boundary. The ability of radar to operate during darkness and to penetrate clouds makes it the optimal sensor for flood monitoring and mapping (Henderson and Lewis, 1998). The significant contrast between backscatter helps to delineate flooded areas. The application of satellite data to floods can quickly and precisely provide an overview of flooded areas. This is helpful as a first step in formulating a flood response strategy, by identifying the areas most vulnerable to flooding. Hence, radar is potentially a key tool in providing synoptic coverage over a wide area and for flood monitoring which has been used operationally in many areas (Brisco et al., 2008, Sanyal and Lu, 2004).

Mapping the extent of flooded areas using SAR data can be undertaken using a range of approaches. One approach applies segmentation techniques to imagery acquired after the flood. Another compares two SAR images taken before and after the flood, through visual interpretation of change. A third approach uses coherence information inferred from a pair of SAR images (Nico et al., 2000). Fourthly, thresholding is one of the most frequently used techniques to delineate flooded from non-flooded areas in a radar image (Brivio et al., 2002; Sanyal and Lu, 2003). The radar backscatter value of threshold is set and a binary algorithm is used to determine whether or not a raster cell is flooded (Sanyal and Lu, 2003). However, the most common problem in identifying flood extents from SAR imagery is that accuracy may be affected by the relationship between the radar wavelength and the terrain roughness and water the body (Yang et al., 1999).

There are several key studies of the application of radar for the detection of flooded areas. Brivio et al. (2002) used two ERS-1 images, one acquired one month before the studied flood, which occurred in the Piemonte region of Italy in November 1994, and the second one obtained three days after the event. They also used ancillary information to detect flooded areas such as digital topographic, aerial photographs to define ground truth areas, and maps of the actual inundated areas acquired from ground surveys for accuracy evaluation. The authors carried out a visual interpretation at the first stage and then applied two thresholding techniques. However, because of the time delay between the flood peak and the satellite overpass, they could detect only 20% of the flooded land during the satellite overpass. In order to overcome the limitation of this time delay, they developed a new procedure by integrating the flooded area from SAR imagery with digital topographic data from a GIS technique to estimate the flooded area at the peak time. The method they applied indicated inundated areas covering 96.7% of the peak flood area as determined from local government maps.

Nico et al. (2000) carried out a comparison of SAR amplitude and coherence flood detection methods for flood delineation by adopting change detection techniques for a flood event at Bezier in southern France, 1996. Three approaches were adopted: a) a comparison between two SAR images of the same area, one taken before the flood and the other after; b) the use of interferometric coherence by isolating low-coherence regions; and c) a combination of these two approaches. The first approach was undertaken by comparing several images for the same area taken before and after the

flood. This technique is based on using the radar backscatter coefficient to determine temporal variations in the scatter behaviour of the surface. Thus, flooded zones appeared darker on the flooded image than on the unflooded image. The technique they used was multi-temporal image subtraction of one image value from the other on a pixel-by-pixel basis in order to isolate zones of low backscatter. The second approach, interferometric coherence change detection, involves the normalized cross-correlation coefficient between two images. The image taken after flooding shows a lower coherence than non-flooded areas because of changes in the dielectric constant and the surface roughness. Results show that the third approach which combines the two pieces of information into a single map is better and effectively able to isolate most of the flooded area in a homogeneous contour line and without the spurious patches.

A comparison study was carried out by Komwong and Simking (2006) using Radarsat-1 and ALOS PALSAR data to detect flood boundaries in Sukhothai in Thailand. The ALOS PALSAR image was acquired on 25 May 2006, while the Radarsat-1 image was acquired two days later. The comparison between the two SAR data was in terms of return signals as illustrated in Figure 3.8 and shows that the pattern graph appeared similar even though the reflectance value of both imagery were different (Komwong and Simking, 2006). Their study found that both images could map flash flooding accurately.

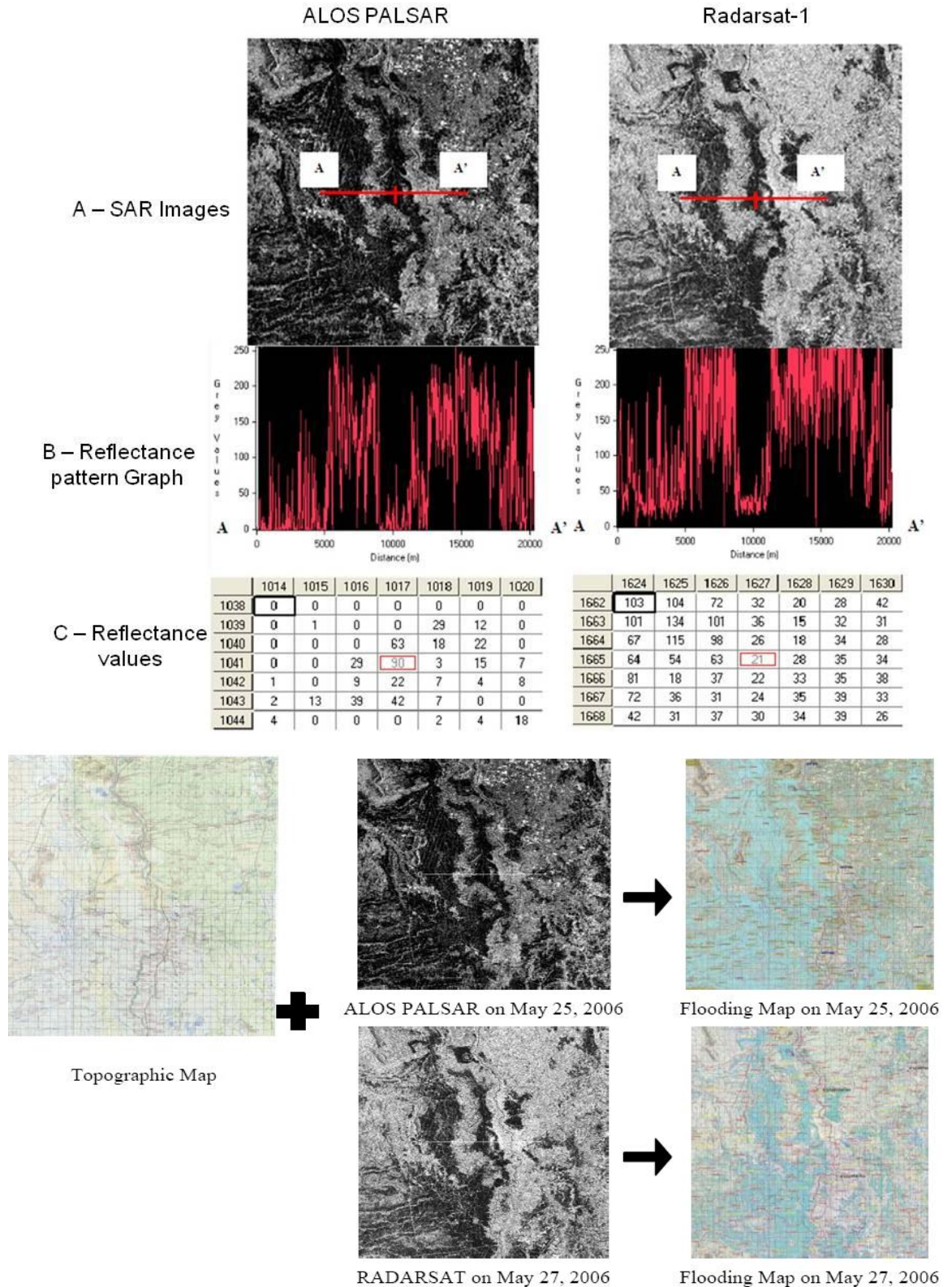


Figure 3.8: Reflectance significance comparison and flooding map using ALOS PALSAR and Radarsat-1 merged with a topographic map (A- SAR images, B-reflectance pattern graph, and C-reflectance values) (adapted from Komwong and Simking, 2006).

A study using combined Radarsat-1 and ERS SAR images in flood detection was carried out by Chen et al. (1999) to monitor flooding using multi-temporal and multi-platform data. In this study, eight Radarsat-1 and five SPOT5 multispectral optical images were used for the Mekong delta in Vietnam between June and December 1997. The SAR images were filtered, co-registered and calibrated, and the inundated areas were then extracted from the SAR images by applying thresholding methods. A comparison with SPOT multispectral images was applied as a ground truth. The results verified the effectiveness of using SAR data for flood monitoring by using multitemporal and multiplatform SAR data by applying thresholding methods. However, the problem is that ERS has a repeat (revisit) cycle of 35 days and, although this can be reduced to 17 days when taking into account both ascending and descending modes, it still has a limited temporal coverage compared to, for example, TerraSAR-X (which has a repeat cycle of 11 days). Therefore, another finding from this study was that the combined use of ERS and Radarsat-1 data would provide a high temporal frequency revisit capability, for applications such as flood monitoring.

Another comparison study between Radarsat-1 and ERS data for mapping and monitoring floods was carried out by Hasan et al. (1998) in Bangladesh. The method they used consisted of two phases: first, pre-processing and second, information extraction. In the pre-processing stage, they made co-registration of image to image by shifting the image in the X and Y directions. They also evaluated a number of filters (mean, median, lee, lee sigma, gamma map, forest and local region) and found that the mean filter produced the best results. After that, they collected ground control points using an IRS-1D Panchromatic image and a Landsat-5 Thematic Mapper image as references. The SAR images were projected into the Bangladesh Transverse Mercator (BTM) projection system, and they found geo-referencing errors within ± 10 and ± 30 metres for the SAR data. Information extraction included classification of the images into land-use and land-cover classes, which allowed identification of settlements, water bodies and seasonal variations in the vegetation features. They identified six major land-use classes for the monsoon landscape in the study area (permanent water, seasonal water, rice, jute, sugarcane and settlements). The multi-temporal images were classified into 140 classes by adopting an unsupervised iterative self-organizing data analysis (ISODATA) clustering technique. They prepared two files: one for the 140-class image, and the second for the signature that contained mean digital number values of the 140

classes. Hasan et al. (1998) established a relationship between the ground data and signatures, and the signatures were then grouped according to land-use/land-cover types. Of the ground data, 70% was used to identify and label these types in the classified image, while the remaining 30% was used to assess the accuracy of SAR image classification.

Various studies have attempted to find the best SAR imagery specifications for flood detection. For example, McMillan et al. (2006) investigated the optimal SAR imagery specifications for urban flood monitoring using Radarsat images taken over the study area in New Orleans, USA. They used a simple change detection technique by creating a preliminary RGB false-colour composite for each beam for the 'before', 'during' and 'after' images. These facilitate identification of flooded areas. Low-pass and median filters were used to reduce speckle and to create coherent flood polygons. McMillan et al. (2006) found that the low-pass filter showed a more coherent flood extent and boundary. To validate SAR-derived flood extent against the flood estimation derived from optical imagery, two approaches were adopted: 1) a manually derived flood boundary-based approach, and 2) an area-based flood-detection approach. Regarding the boundary-based validation, manual flood vector delineation was implemented for the beam unfiltered difference images. The same delineation method was applied to the optical images. McMillan et al. (2006) compared the radar delineated flood boundaries with the optically derived boundaries by calculating:

- the flood boundary lengths;
- the lengths of the flood lines within each boundary (lines corresponding to the edge of the image extent were ignored);
- the percentage of each flood boundary within a certain zone.

Within the area-based flood detection approach, McMillan et al. (2006) created binary flood (1) and no-flood (0) classes. They masked out other land-cover types such as wetland and forest in order to display flood changes. The optically derived datasets were also passed through this mask to create a similar dataset. Saturated areas were then removed using a saturation threshold. The validation data was also rasterized and converted to class 1 or 0 for flood and no flood, respectively. The optical and radar layers were added to create four classes of contingency matrix image, showing areas of flood agreement and disagreement, false positives and negatives. The accuracy of the

area-based method was tested using user and producer accuracies and Kappa coefficients. The authors found that the most accurate results were obtained using descending mode of high incidence angle of the fine beam mode 5 Radarsat imagery.

Very little literature is available on the automatic detection of water bodies from SAR imagery. Ahtonen and Hallikainen (2005) attempted the automatic detection of water bodies from SAR images by using a method divided into two stages: pre-processing and delineation. In pre-processing, the SAR images were calibrated and geo-coded before being de-speckled with a gamma-map filter using a 7×7 window. The SAR scene was thresholded to land and water classes. The active contour statistical snake technique was applied for flood delineation. The open water detection system was tested qualitatively with six ERS-2 SAR scenes (C-band, VV polarization). For quantitative accuracy validation, a high-resolution (2 m) image used from airborne imaging spectrometer for applications (AISA) and Radarsat-1 scene (25 m) were acquired. The thresholding error was below 12 AISA pixels and within 1 Radarsat-1 pixel.

To validate SAR-derived flood extent against the flood estimation derived from optical imagery, two approaches may be adopted: 1) a manually derived flood boundary-based approach, and 2) an area-based flood-detection approach. These techniques can then be compared for flood boundaries by calculating boundary lengths, flood line lengths within each boundary and the percentage of each flood boundary within a certain zone.

Multi-temporal TerraSAR-X data was adopted by Lu et al. (2009) for flood mapping. The study area was chosen to be in Iowa, USA, during the flood season in 2008. The authors applied mean shift filtering for image segmentation and k-means clustering for region merging. A comparison between the proposed method and manual interpretation by ARCGIS and retrieval by texture on sub-blocks was performed to assess the accuracy of the proposed method. They found that the proposed procedure has better results and good edge for water body extraction compared with the method of retrieval by texture on sub-blocks with 5% improvement.

Herrera-Cruz and Koudogbo, (2009) worked for an automated procedure for mapping flood extent using TerraSAR-X data based on two case studies: the flooding in the Mississippi River, USA, 2008 and the Gulf Country region in north Queensland,

Australia, 2009. Data used include TerraSAR-X stripmap for the Mississippi event while a ScanSAR scene was acquired for the Gulf Country. The authors used Definiens Developer for the development of the flood mapping procedure. Object-based classification was performed in three steps including segmentation, water mask extraction, and flood extraction and refinements. Results showed that the developed procedure is five times faster than that of the manual work and provides more details when compared to the manual digitization.

From the above discussion, SAR flood monitoring appears to have limitations due to the time delay between flood peak and satellite overpass. Moreover, many studies have been widely based on non-high-resolution satellite SAR data for water and flood mapping. There are limited studies which tackle the very high spatial resolution for flood detection (i.e. Herrera-Cruz and Koudogbo, 2009; Lu et al., 2009; Martinis et al., 2009; Mason et al., 2010) due to the recent launch of the advanced SAR spacebornes, but still there is a gap for assessing the capability of those new SAR sensors' products for mapping floods. Therefore, the present research project is an attempt to bridge this gap by evaluating the capability of the new high-resolution SAR data products in the detection of flooding and water bodies.

3.5 SAR Data Interpretation

SAR image interpretation is dependent upon understanding the interaction between the radar waves and surface. Both sets of parameters of the system (polarization, incidence angle and frequency) and of the land surface (surface roughness, terrain geometry and surface and volume scattering) affect the appearance of the image (see Figures 3.3, 3.4, 3.5, 3.6, and 3.7). Image interpretation factors such as tone, texture, shape, size, pattern and shadow can be used to analyse SAR imagery (Henderson and Lewis, 1998). Differences in the grey tones on an image occur because of changes in the radar backscatter from the terrain and are affected by a range of factors (such as moisture, surface roughness and slope). The rougher the surface being imaged, the higher is the backscatter intensity (Liew, 2001).

Texture is related to the surface roughness (i.e. degree and homogeneity) and can be described as smooth or rough, salt-and-pepper, grainy and speckled. The contrast of the

component elements of texture on an image is affected by system and environmental parameters. Identification of the shape and size of individual features along with their texture and tone improves SAR image interpretation. Another approach in interpreting SAR imagery is contextual analysis, which can be conducted by examining a pixel or a group of pixels in the context of surrounding pixels or pixels in the whole scene (Henderson and Lewis, 1998).

3.6 Limitations of Using SAR data to detect flooded areas

Although SAR sensors have the ability to delineate water areas, there are limitations that might constrain its usefulness in some cases. These include for example potential difficulties in differentiating between water, smooth surfaces, wet land (shallow water) and radar shadows. Hasan et al. (1999) found limitations in the analysis of the SAR image signature for floodplain land cover in Bangladesh, particularly smooth roads, which have a signature similar to that of permanent water. A study carried out by Oberstadler et al. (1997) examined the applicability of ERS-1 data for mapping flooded areas under operational conditions. An automatic classification based on evidence-based interpretation of satellite images (EBIS) was used, and it was found that: a) the actual timeframe of ERS-1 could not ensure the recording of flood events, and so operational use is rarely possible; b) where data are available mapping of the flood extent on arable land is possible with high accuracy, while in settlements and forests there was no definite outcome of the delineation. As a result, visual interpretation was found to be more accurate than the classification. Misclassification occurred in forested areas and wet arable land, which had similar signatures to inundated surfaces. High-resolution TerraSAR-X stripmap imagery for flooded urban areas detection was investigated by Mason et al. (2010) using HH polarization. The study area was located in Tewkesbury, U.K., during the flood of July 2007. They used aerial photography for validation and LiDAR data to estimate regions of shadow and layover caused by buildings and taller vegetation. A statistical active contour model (or snake) was modified to be conditioned on both SAR and LiDAR data to reduce error of flood delineation. The accuracy of detecting rural flooding was estimated to be 80% while a 76% success rate was achieved for urban flooding areas excluding the shadow and layover regions. The flood detection accuracy including regions of shadow and layover was estimated to be 58%.

3.7 Evaluation of SAR Frequency and Polarization

Most SAR systems transmit and receive pulses as different polarizations, which increases the information in SAR datasets. Polarization, as described in Section 3.2.2, can be helpful in distinguishing land surfaces. The choice of frequency (wavelength) is also important for assessing land features. Radar backscatter from terrain depends on frequency because of differences in the dielectric constant of water. Studies suggest that lower-frequency sensors are better suited to soil moisture estimation; Ulaby and Batlivala (1976) recommended a frequency of 4 GHz (C-band) for effective mapping of soil moisture. HH polarization in SAR C-band was found better than VV polarization for mapping wetlands (Baghdadi et al., 2001).

Dobson et al. (1998) compared the expected accuracy of orbital SAR systems for land-cover classification. They simulated various system configurations from SIR-C/X-SAR data and compared simulation data and results obtained from actual ERS-1/2 and the Japanese JERS-1 data of the same region. The evaluation was undertaken in terms of frequency and polarization for classifying land cover and estimating forest properties. SIR-C/X-SAR L-, C- and X-band data with VV polarization were acquired at various incidence angles. The best results were obtained when using multi-frequency data rather than multi-polarized data.

Karszenbaum et al. (2004) evaluated HH and VV polarizations of ENVISAT ASAR data to understand the differences in radar backscatter in identifying the extent of standing water and related land-cover features in the delta of the Paraná River, Argentina. The data was modelled as a set of vertical cylinders (shoots), defined by radius, height, density and gravimetric moisture, on a normal flooded surface, and simulations were computed using a scattering model developed at Tor Vergata University, Italy. The data supported previous observations acquired through ERS2 and Radarsat-1 data in HH-VV polarizations with the same environmental conditions provided about the delta and showed considerable differences between HH and VV and the effects of the environmental parameters on radar backscatter. The results also indicated that C-band multi-polarized SAR is able to detect and distinguish between marsh species.

Baghdadi et al. (2008) examined the sensitivity of TerraSAR-X radar signals to surface soil parameters reflected by the roughest and the smoothest areas over agricultural fields, using HH polarization and various incidence angles (26°, 28°, 50°, 52°). Two study area sites were used: the first is in Villamblain, South of Paris and the second site is located at the Orgeval watershed, located to the East of Paris. Seven TerraSAR-X images were acquired in the spotlight mode with a spatial resolution of 1m during January and February 2008. Baghdadi et al. (2008) also analysed the potential of L-band of ALOS PALSAR images acquired in February 2008 with HH polarization at a 38° incidence angle and 6.25 m spatial resolution. A single ASAR image was also acquired in February 2008 with both HH and VV polarizations in the 1S2 mode (image swath) with 23° incidence and 12.5 m resolution. Ground truth measurements of soil moisture content, bulk density, and surface roughness were performed by collecting gravimetric soil moisture samples at depths in the range 0–5cm. They calculated the volumetric soil moisture by multiplying the gravimetric soil moisture by the dry soil bulk density. Each training field estimated the backscattering coefficient σ° by averaging the linear value of σ° for all pixels related to a given field followed by converting results into decibels (dB). The study arrived at the following conclusions: 1) TerraSAR-X radar signal is to some extent more sensitive at high incidence angles to surface roughness, 2) sensitivity increases in the L-band (low frequency) with PALSAR/ALOS data, 3) the dynamics of radar signals for frozen or very wet soils is reduced based on the roughness parameter (rms), 4) under very wet soil conditions radar signals decrease at high or low incidence angles, and 5) soils with high water content appear darker in TerraSAR-X imagery.

Multi-polarized ENVISAT ASAR data was evaluated for flood-mapping capabilities by Henry et al. (2006). The study used Image mode and Alternating Polarizations mode along with ERS-2 data acquired quasi-simultaneously, and an optical Landsat-7 ETM+ image as a reference. They extracted flood extents from each image and compared each result. The analysis indicated that HH polarization is more suitable for discriminating flooded areas than HV or VV. Moreover, HV improved the existing HH data, and VV polarized data was highly influenced by surface conditions. The study concluded that an Alternating Polarizations Precision image with like- and cross-polarization presents a better image for flood mapping than a mono-polarized image.

SAR frequencies and polarizations evaluation by different studies led to important results. The different SAR frequencies have various sensitivities to surface roughness in which sensitivity increases when using SAR data with low frequency (Baghdadi et al., 2008). The use of SAR Multi-frequency data performed better results for land cover classification (Dobson et al., 1998). Evaluation of polarization types indicated that there are differences between HH and VV on radar backscatter (Karszenbaum et al., 2004). HH polarization was found to be better in SAR C-band mapping wetlands than VV polarization (Henry et al., 2006; Baghdadi et al., 2001). Although some studies evaluated different SAR frequencies and polarizations they are very few, and most importantly there is a gap in the currently existing studies concerning evaluation of the capability of the new SAR satellite sensors (C- and X-bands) in particular.

3.8 Radarsat-2 and TerraSAR-X SAR Remote Sensing Systems

The development of SAR satellite systems in the last couple of years has achieved very high spatial resolution imagery from 3 metres down to one metre there have been built and launched by different international agencies. In this study, the assessment of SAR products and evaluation of their applicability for monitoring and detection of floods is based on the Radarsat-2 (Canadian Space Agency) and on the TerraSAR-X (German Aerospace Centre) SAR sensors. A brief description of these two SAR systems is in the following sections.

3.8.1 Radarsat-2

Radarsat-2, was jointly funded by the Canadian Space Agency and MacDonald, Dettwiler and Associates (MDA) and was built by the MDA. It was launched in December 2007. Radarsat-2 is the C-band imaging radar follow-on mission to Radarsat-1, which was launched in November 1995. Radarsat-2 has advanced technology over Radarsat-1 which includes: three metre high resolution; fully-polarimetric modes; enhanced ground system; routine left and right looking capability; increased geometric accuracy; and on-board solid state recorders (Staples, 2005). Radarsat-2 left- and right-looking modes provide more revisits and up-to-date data which reduce planning lead times for data acquisition (CSA, 2007). The various advances in Radarsat-2 technology allow for many earth observation applications such as disaster management, agriculture,

cartography, forestry, geology, hydrology, marine surveillance, ice studies and coastal monitoring (CSA, 2007). Data from Radarsat-2 has been used in disaster responses such as floods, earthquakes, tsunamis, landslides, and forest fires. Table 3.4 lists some features of the Radarsat-2 system and their benefits.

Table 3.4: Some features of Radarsat-2 and their benefits (CSA, 2007).

Features	Benefits
Spatial Resolution: 3 to 100 meters	- Suite of spatial resolution options accommodates a wide range of applications. -Ultrafine beam improves object detection and classification
Polarization: HH, HV, VV and VH	Better discrimination of various surface types and improved object detection and recognition
Look Direction: Left- and right-looking imaging	Decreases revisit time for greater monitoring efficiencies
Onboard Recording Device: Solid-state recorders	-Guarantees image acquisition anywhere in the world for subsequent downlinking -High capacity (300 GB) random access storage -Simultaneous reading and writing
Onboard Location Accuracy Device:GPS receivers onboard	-± 60-meter real-time position information -GPS-derived geometric accuracy, provides greater positional control for fast delivery products (no ground control)
Attitude Control: Yaw steering	Control of yaw steering for zero Doppler shift at beam centre facilitates accurate image processing

3.8.1.1 Radarsat-2 Instrument System

The spacecraft of Radarsat-2 is mainly composed of the Bus and the payload module along with the extendible support structure between the Bus and antenna structure (Figure 3.9) (CSA, 2007). Table 3.5 summarizes the spacecraft and Antenna general characteristics. The Bus provides the general support functions such as attitude measurement and control, telemetry and command, data storage and retrieval, power generation and storage, and thermal control. The synthetic aperture radar (SAR) payload consists of two major components, the sensor electronics subsystem and the SAR antenna, and support equipments such as timing and control of the payload, signal distribution, signal detection, thermal control, data storage, and X band downlink (Livingstone et al., 2005; Morena et al., 2004).

The radar transmitter and receiver operate through an electrically steerable antenna (MDA, 2009). The transmitted pulses generated by the antenna are of constant amplitude and phase modulated waveforms for each range resolution and up-converted to 5.405 MHz are sent to the Antenna subsystem for transmission (Livingstone et al., 2005). The antenna has more than 10,000 radiating elements fed by 640 Transmit/Receive modules. Polarization can be controlled by correcting timing of the signal from or to each radiating element pair to achieve H or V polarization on transmit and receive paths (GLOBSAR, 2008; Riendeau and Grenier, 2007). The subsystem diagram of the Radarsat-2 sensor electronics and the antenna are shown in Appendix 3.1.

Table 3.5: Radarsat-2 spacecraft and Antenna general characteristics (adapted from CSA, 2007).

General characteristics	
Total mass at launch	2,200 kg
Mission life	7 years
SAR antenna dimensions	15 m x 1.5 m
Solar arrays (each)	3.73 m x 1.8 m
Bus	3.7 m x 1.36 m
Antenna Characteristics	
Active Antenna	C-Band T/R modules
Centre Frequency	5.405 GHz
Bandwidth	100 MHz
Polarization	HH, VV, HV, VH
Polarization Isolation	> 25 dB
Aperture Length	15 m
Aperture width	1.37 m
Mass	750 kg

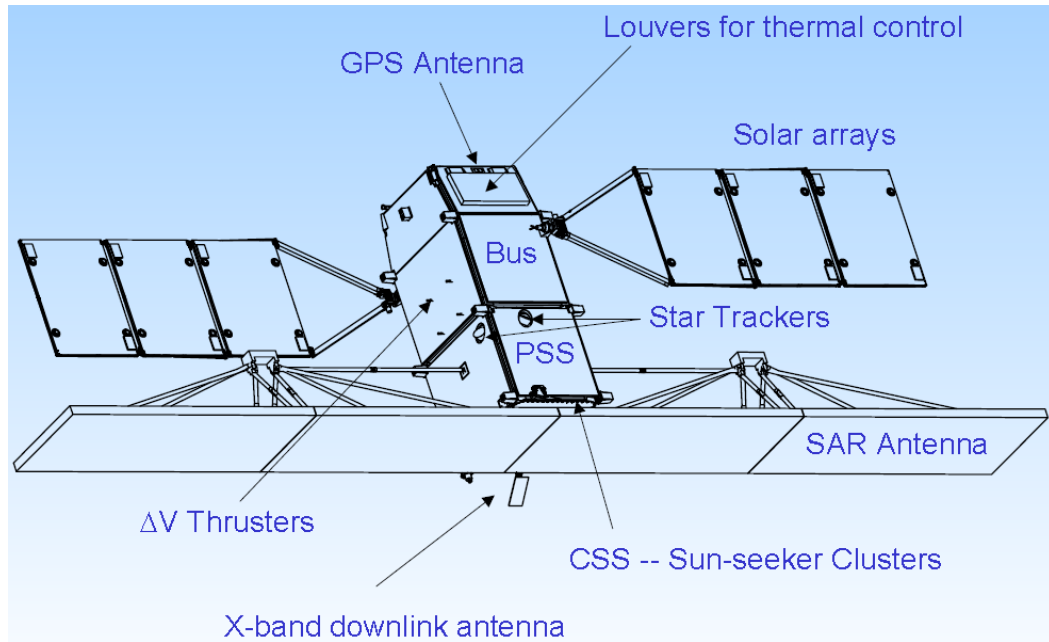


Figure 3.9: Radarsat-2 configuration (Adapted from GLOBSAR, 2008).

3.8.1.2 Satellite Orbit

Radarsat-2 has a sun-synchronous orbit (a dawn-dusk orbit) with the ascending mode at 18:00 hours ± 15 min local mean time and completes 14 orbits per day with a repeat cycle of 24 days. The average altitude of the orbit is 798 km with an inclination of 98.6° (CSA, 2007; Morena et al., 2004). Table 3.6 shows the orbit characteristics of Radarsat-2.

Table 3.6: Radarsat-2 orbit characteristics (NRCAN, 2007).

Parameter	Value
Altitude (average)	798 km
Inclination	98.6°
Period	100.7 minutes
Ascending Node	18:00 hrs
Sun-synchronous	14 orbits per day
Repeat Cycle	24 days

3.8.1.3 Beam Modes and Polarizations

Radarsat-2 has all of the Radarsat-1 imaging modes plus the addition of new modes such as ultrafine, multi-look fine, fine quad-polarization and standard quad-polarization (Morena et al., 2004). Figure 3.10 illustrates the Radarsat-2 SAR beam modes of operation. The Radarsat-2 antenna directs the emitted signals in a narrow beam to the earth's surface where the elevation angle and the elevation profile of the beam can be adjusted to obtain the desired range of incidence angles (MDA, 2009). Each beam mode is characterized by a specific incidence angle and width, as shown in Figure 3.10. Additional details about imaging modes in terms of resolution, scene size, incidence angle, number of looks and polarization are shown in Table 3.7.

The Radarsat-2 SAR sensor obtains data in three polarization configurations: single, dual, and quad polarization (see Table 3.7). Single polarization products can be obtained by operating the radar sensor with the choice of co-polarized HH or VV, or Cross-polarized HV or VH. Dual-polarization products are obtained by the choice of HH and HV, or VV and VH. Quad-polarization means that four amplitude channels and the phase of information can be acquired including HH, HV, VH, and VV.

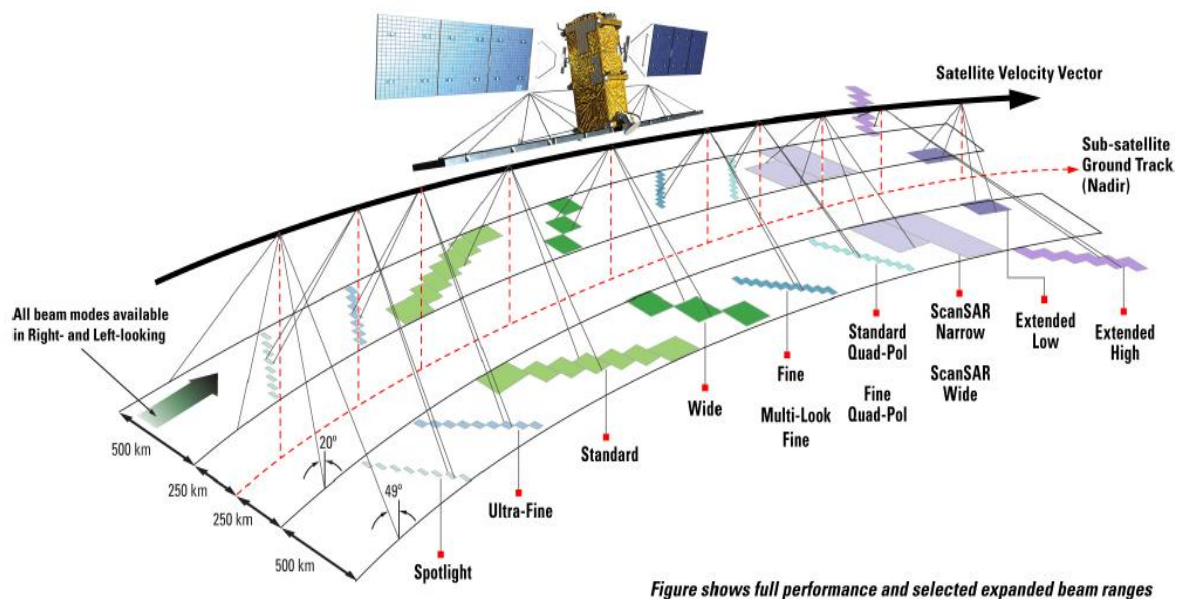


Figure 3.10: Radarsat-2 SAR beam modes of operation (Adapted from MDA, 2007).

Table 3.7: Radarsat-2 beam modes and products (MDA, 2009).

Beam Mode	Resolution (m)	Scene size (kmxkm)	Incidence Angle (°)	Number of Looks	Polarization
Spotlight	1	18x8	20-49	1x1	SSP
Ultrafine	3	20x20	20-49	1	SSP
Multi-look fine	8	50x50	30-50	2x2	SSP
Fine	8	50x50	30-50	1x1	SSP or SDP
Standard	25	100x100	20-49	1x4	SSP or SDP
Wide	30	150x150	20-45	1x4	SSP or SDP
Scan SAR Narrow	50	300x300	20-46	2x2	SSP or SDP
Scan SAR wide	100	500x500	20-49	4x2	SSP or SDP
Extended high	25	75x75	49-60	1x4	SP
Extended low	25	170x170	10x23	1x4	SP
Fine quad-pol.	8	25x25	18-49	1x1	QP
Standard quad-pol.	25	25x25	18-49	1x4	QP

Note:

1. SP: Single polarisation - HH.
2. SSP: Selective single polarisation - HH or HV or VV or VH.
3. SDP: Selective dual polarisation - HH+HV or VV+VH.
4. QP: Quad polarisation - HH+HV+VV+VH acquired (full polarimetric).

The ultrafine beam mode products were selected for this study due to its high spatial resolution of three metres. In this mode the radar operates its highest sampling rate with a limited ground swath coverage to keep the data rate within the recorder limits (MDA, 2009).

3.8.2 TerraSAR-X

The TerraSAR-X satellite was launched in June 2007 as a joint project between the German Aerospace Centre (DLR) and the German industry (ASTRIUM) and was equipped with active phased array antenna technology in X-Band (DLR, 2010). The TerraSAR-X system can provide a geometric resolution down to one metre in 2-D earth surface imaging and also a 3-D imaging with its partner the TanDEM-X (launched in June 2010) (Pitz and Miller, 2010). The advanced technology of the TerraSAR-X

system allows it to have several advantages; high radiometric accuracy, resolution up to 1m; imaging 5 to 100 km swath width and up to 1500 km length; revisit time up to 2.5 days and a repeat cycle of 11 days. The different SAR imaging modes of TerraSAR-X along with its high resolution and high operational flexibility allow it to support several applications. Examples of these applications include monitoring of urban environments, agriculture, forestry and environment; monitoring the sea ice and the volume of icebergs, monitoring of the oceans and coastal regions; and mapping and cadastre (DLR, 2009). TerraSAR-X products have been used for mapping hazard and damage assessment for different events such as floods, earthquake, tsunami, landslides, and wildfire.

3.8.2.1 TerraSAR-X Instrument System

TerraSAR-X is a side-looking X-band synthetic aperture radar (SAR) based on active phased array antenna technology. The active antenna allows not only the conventional stripmap imaging mode but additionally spotlight and ScanSAR mode (DLR, 2008). The system parameters of the platform and the SAR instrument are shown in Table 3.8. The satellite bus with a hexagonal cross-section has a length of 5 metres and a width of 2.4 metres and is fitted with the electronic boxes of the SAR instrument. The radar antenna is fitted on one of the six sides of the bus and the solar generator, 5.25 square metres in size are fitted on other side. A downlink antenna for data recording has a 3.3 meters long mast for avoiding interferences which may be caused by the radar antenna. Figure 3.11 illustrates the TerraSAR-X system components. The TerraSAR-X SAR antenna (4.80 metres long and 80 centimetres wide) can operate in two polarizations, H (horizontal) and V (vertical) and consists of 12 antenna panels, each equipped with 32 slotted waveguide subarrays. Each subarray is fitted with a TRM, so that the whole antenna consists in total of 384 TRMs. The TerraSAR-X instrument functional block diagram and radar antenna panel are shown in Appendix 3.2 (DLR, 2009).

Table 3.8: TerraSAR-X system parameters (DLR, 2008).

Parameter	Value
Satellite size	5 meters height by 2.4 meters diameter
Satellite mass	approx. 1,230 kilogram
Radar carrier frequency	9.65 GHz
Radiated RF Peak Power	2 kW
Incidence angle range for stripmap / ScanSAR	20°– 45° full performance (15°-60° accessible)
Polarizations	HH, VH, HV, VV
Antenna length	4.8 m
Nominal look direction	Right
Antenna width	0.7 m
Number of stripmap / ScanSAR elevation beams	12 (full performance range) 27 (access range)
Number of spotlight elevation beams	91 (full performance range) 122 (access range)
Number spotlight azimuth beams	229
Incidence angle range for spotlight modes	20°– 55° full performance (15°-60° accessible)
Pulse Repetition Frequency (PRF)	2.0 kHz – 6.5 kHz
Range Bandwidth	max. 150 MHz (300 MHz experimental)
Operational life	at least 5 years

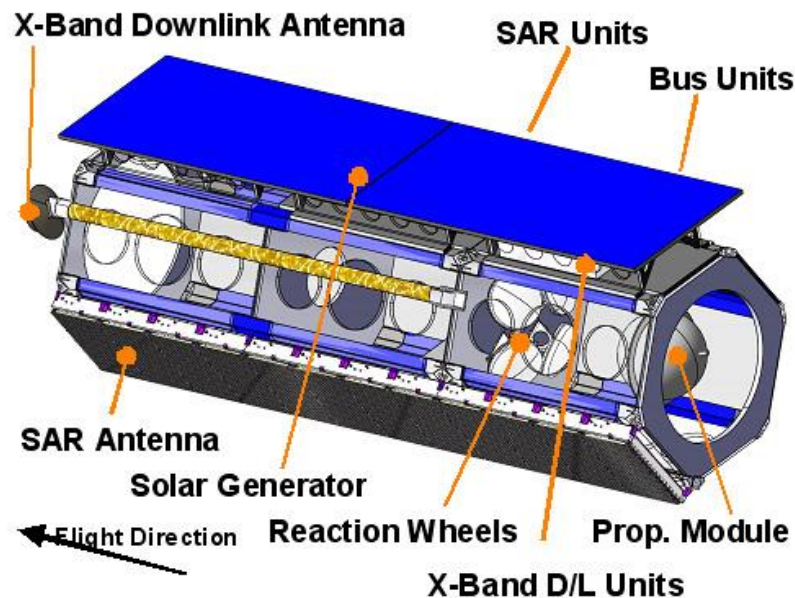


Figure 3.11: TerraSAR-X system components (DLR, 2011b).

3.8.2.2 Satellite Orbit

The TerraSAR-X satellite is orbiting in altitude of around 514 kilometres, near-polar orbit. It flies in a sun-synchronous, dusk dawn orbit with an orbit repeat cycle of eleven days (see Table 3.9).

Table 3.9: TerraSAR-X orbit and attitude parameters (DLR, 2008).

Parameter	Value
Orbit type	Sun-synchronous
Nominal altitude at equator	514 km
Orbits per day	15 2/11
Orbit repeat cycle	11 days /167
Inclination	97.44°
Ascending mode equatorial crossing time	18:00 ± 0.25 h (local time)

3.8.2.3 Beam Modes and Polarizations

The TerraSAR-X operational modes include high resolution spotlight, spotlight, stripmap and ScanSAR. TerraSAR-X sensor modes of operation are given in Figure 3.12. The high resolution spotlight mode has a resolution up to one metre and a scene size of 5 km by 10 km. The spotlight can image up to two metre resolution with a scene size of 10 km by 10 km. The stripmap mode can produce up to a 3m resolution product with a scene size of 20 km 30 km and can be extended to 1.500 km. The ScanSAR mode resolution is around 18 metres and can produce a scene size of 100 km by 150 km with the capability to extend the scene length to 1.650 km (Table 3.10) (Infoterra, 2011).

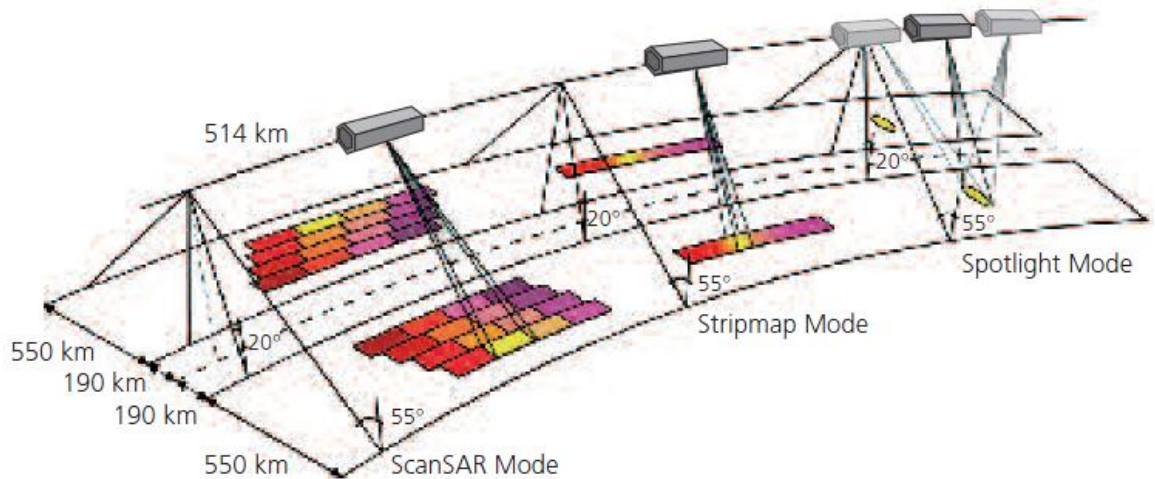


Figure 3.12: TerraSAR-X SAR modes of operation (source: DLR, 2009).

Table 3.10: TerraSAR-X beam modes and products specifications (DLR, 2010).

Beam mode	Resolution (m)	Scene size (km)	Incidence Angle (°)	Polarization
High resolution Spotlight	1.1 (SP) 2.2 (DP)	5 x 10	20 - 50	SP or DP
Spotlight	1.7 (SP) 3.4 (DP)	10 x 10	20 - 55	SP or DP
Stripmap	3.3 (SP) 6.6 (DP)	30 x 50 15 x 50	20 - 45	SP or DP
ScanSAR	18.5	100 x 150	20 - 45	SP

Note:

1. SP: Single polarization - HH or VV
2. DP: Dual polarization - HH/VV

In this study, stripmap mode products were used from the TerraSAR-X sensor. This type of mode allows the ground swath to be illuminated with a continuous sequence of pulses while the antenna beam is pointed to a fixed angle in elevation and azimuth results which has constant image quality in azimuth (DLR, 2008). The acquisition's maximum length is limited by several factors such as battery power, memory and thermal conditions in the sensor. The characteristic parameters of stripmap mode are listed in Table 3.11.

Table 3.11: Characteristic parameters of stripmap mode (DLR, 2008).

Parameter	Value
Swath width (ground range)	30 km single pol., 15 km dual pol.
Nom. L1b product length	50 km
Full performance incidence angle range	20° - 45°
Data access incidence angle range	15° - 60°
Number of elevation beams	27 (12 full perf.)
Azimuth resolution	3.3 m (6.6 m dual pol.)
Ground range resolution	1.70 m-3.49 m (@ 45°.. 20° incidence angle)
Polarizations	HH or VV (single) HH/VV, HH/HV, VV/VH (dual)

3.9 SAR Data Accuracy Assessment

‘No land cover classification project would be complete without an accuracy assessment’ (Cihlar 2000). Accuracy assessment of remotely sensed data is a relatively new procedure for testing map accuracy. The accuracy of spatial data may be defined as “the closeness of results of observations, computations, or estimates to the true values or the values accepted as being true” (USGS, 1990). Accuracy assessment is an important factor in analysing SAR images (Banko, 1998). It is the identification and measurement of map error by comparing sites on a map against accurate reference data (Congalton and Green 2009). In other words, accuracy assessment is adopted to assess map errors in order to identify the quality of remotely sensed information. Figure 3.13 shows possible sources of error in remotely sensed data. Remotely sensed data is measured by positional accuracy and thematic accuracy. The first involves the accuracy of the location features on a map compared with land position. While the thematic accuracy measures whether the attributes of features on the map are different from those on the Earth’s surface (Congalton and Green 2009).

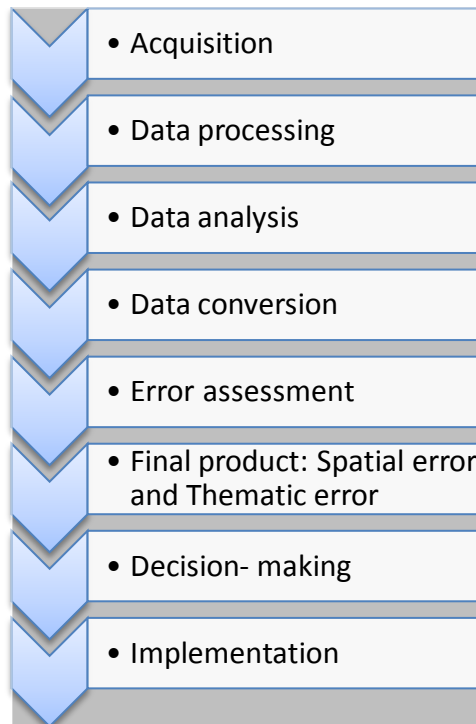


Figure 3.13: Possible sources of error in remotely sensed data (adapted with modification from Congalton and Green 2009).

The development of validation methods in remote sensing image classification have led to the move from using qualitative confidence-building assessment to the use of statistical measurements (Grenier et al., 2008). The accuracy of image classification methods can be measured statistically through two approaches: model-based inference and design-based inference (Hansen et al., 1983; Stehman, 2009). Model-based inference estimates the error of the classification process (or model) that generated the map, rather than estimating the accuracy of the thematic map. Design-based inference is an estimation of the accuracy of the thematic map based on statistical principles. A frequently used method is the error matrix (section 3.9.2) which compares reference information to samples of information on a map. This leads to a descriptive evaluation using statistical measurements of overall, producer's and user's accuracy (Congalton and Green 1998).

Accuracy assessment has three basic components: 1) the sampling design used to select the reference sample; 2) the response design used to obtain the reference land-cover classification for each sampling unit; and 3) the estimation and analysis procedures (Stehman and Czaplewski, 1998; Strahler et al., 2006).

3.9.1 Sampling Design

The sampling design (Stehman and Czaplewski, 1998) is the protocol that can be followed to select the reference sample units. Sampling design planning depends on the accuracy objectives and the sampling design criteria. Several design criteria should be taking into account when selecting a sampling design for accuracy assessment such as the following (Stehman, 2009):

- The sampling design must correctly be implemented and analysed.
- The sampling design must be cost effective.
- The sample is spatially well distributed.
- The variability of the sampling accuracy estimates should be small.
- Ability to change the sample size during the implementation of the design.

Depicting samples from a population can be implemented by a number of methods. The most common are simple random, stratified random, cluster, and systematic sampling (Stehman and Czaplewski, 1998). The selection of a sampling technique depends upon various issues such as the size of the study area, the type and distribution of land cover features, and the costs of acquiring verification data (Banko, 1998). There are several types of sampling units that the accuracy assessment process is dependent upon, which are individual pixels, clusters of pixels, or polygons.

3.9.2 Accuracy Assessment Methods

A common method used to assess classification accuracy is the error matrix or confusion matrix (Congalton, 1991). The error matrix, also known as a confusion matrix, is a method of calculating the accuracy of classified classes with respect to the reference data (Congalton and Green 2009). The matrix is presented as rows and columns of a square array of numbers that represent the number of sample units assigned to a specific category in a particular classification in relation to another classification that also consists of a number of sample units assigned to a specific category (Congalton and Green 2009). The error matrix is illustrated in Figure 3.14.

In Figure 3.14, the diagonal of the matrix (e.g., $X_{1,1}$, $X_{2,2}$) summarizes those pixels or polygons that were assigned to the correct class. Errors in the classified images relative to the ground reference information is summarized in the off-diagonal cells of the matrix (e.g., $X_{1,2}$, $X_{2,1}$, $X_{2,3}$). The column and row totals around the margin of the matrix are used to compute errors of inclusion (commission errors) and errors of exclusion (omission errors). The outer row and column totals are used to compute producer's and user's accuracy.

		Ground Reference Test information					Row total
		Class	1	2	3	k	
Remote Sensing Classification	1	$X_{1,1}$	$X_{1,2}$	$X_{1,3}$	$X_{1,k}$	X_{1+}	
	2	$X_{2,1}$	$X_{2,2}$	$X_{2,3}$	$X_{2,k}$	X_{2+}	
	3	$X_{3,1}$	$X_{3,2}$	$X_{3,3}$	$X_{3,k}$	X_{3+}	
	k	$X_{k,1}$	$X_{k,2}$	$X_{k,3}$	$X_{k,k}$	X_{k+}	
	Column total	X_{+1}	X_{+2}	X_{+3}	X_{+k}	N	

Figure 3.14: The Error Matrix (adapted from Ongsomwang, 2006).

The reference data derived from collected data usually uses the columns in the matrix, while the rows usually display the classified data derived from remotely sensed data. The error matrix can compute errors present from an included area in an incorrect category (a commission error) and can also calculate the occurrence of error when an area is excluded from the category (an omission error). Moreover, from the error matrix it is possible to measure overall accuracy, producer accuracy and user accuracy. Overall accuracy is the sum of correctly classified sample units (major diagonal) divided by the total number of sample units in the entire error matrix, while producer accuracy (row category) and user accuracy (column category) are performed to compute individual category accuracies (Congalton and Green 2009). The user's accuracy represents the commission error, which is the percentage of pixels labelled in an incorrect class, while the producer's accuracy represents the omission error, which is the percentage of pixels

excluded from the class. In other words, the producer's accuracy is a measure of how well the situation on the ground can be mapped, while the user's accuracy measures how reliable the map is when comparing it with the real world. The general concept of producer's and user's accuracy is shown in Figure 3.15.

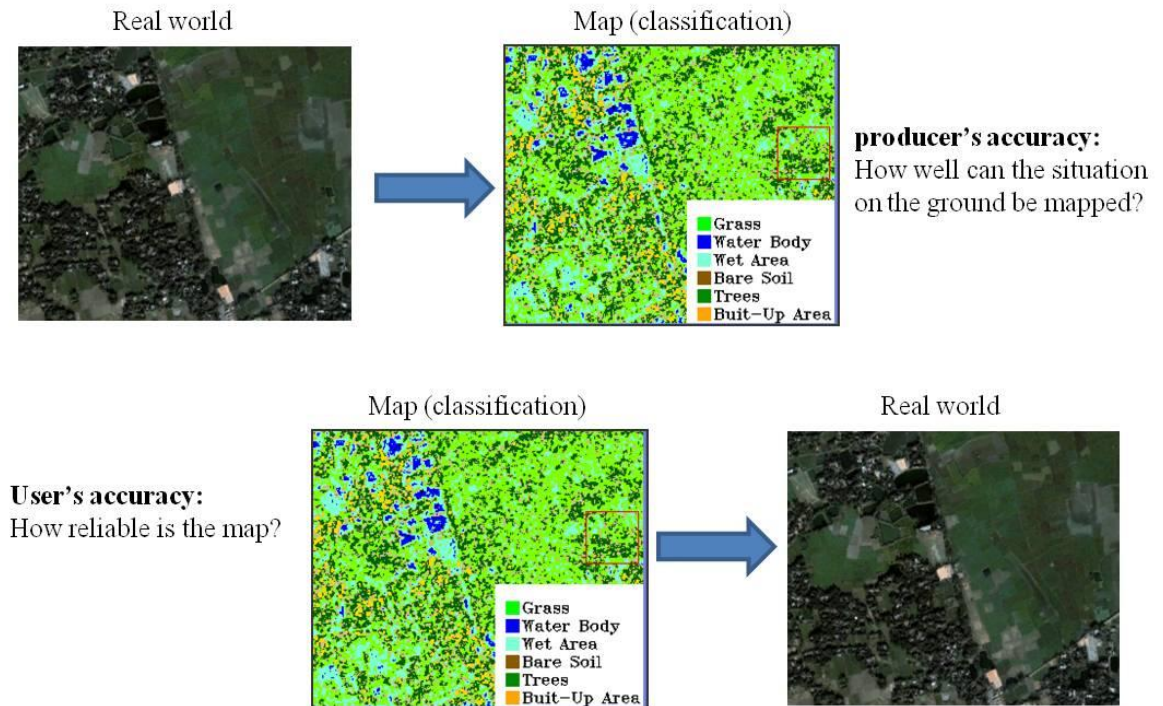


Figure 3.15: The general concept of producer's and user's accuracy (based on Banko, 1998).

Another measure of map accuracy derived from the coefficient matrix is the Kappa Coefficient which is to accommodate for the effects of chance agreement (Foody, 2002). It is a measure of overall agreement or accuracy based on the difference between the actual agreement in the error matrix and the chance agreement (Banko, 1998; Congalton and Green 2009). The Kappa coefficient reflects the agreement percentage between the classified image and the reference data, while the overall accuracy is an indication of the probability of the correctness of the classified image.

3.9.3 Accuracy Assessment Applications in SAR Remote Sensing

Numerous papers on the classification accuracy assessment of SAR data are available. McMillan et al. (2006) investigated the optimal imagery specifications of Radarsat-1 fine beam mode and standard beam mode images for urban flood detection in New Orleans, USA. An area-based validation method was applied by comparing radar-derived flood classes with SPOT optical validation layers. Accuracy assessment showed producer accuracy of 74% and 85% and user accuracy of 64% and 90% for flooded and non-flooded classes, respectively, while the Kappa coefficient showed moderate agreement of 0.56. The study found that the most-accurate results were achieved using descending mode, high incidence angle and fine beam mode imagery, which were recommended for use in future detailed analyses of flooding.

The effect of the incidence angle on classification accuracy was evaluated by Li et al. (2007). They examined the influence of Radarsat-1 incidence angle on the discrimination of wetlands in the Mer Bleue bog area in Ontario, Canada. They classified Landsat-7 with Radarsat-1 S1 and S5 images separately using a maximum-likelihood classifier. Classification accuracy assessments were performed by randomly generating 200 validation samples and using aerial images as reference data. Results from classification confusion matrices with Kappa statistics showed that the classification accuracies of wetland classes were improved. The results indicated that the lower incidence angle Radarsat-1 is the optimal beam mode when used in combination with Landsat images for discrimination and classification of wetlands.

Another study investigated the classification accuracy of class separability and per-pixel classification using a maximum-likelihood classifier (Mroz and Mleczko, 2008). They evaluated the potential of TerraSAR-X stripmap data in mapping agricultural crops in single- and dual-polarization mode. A confusion matrix and Kappa index of agreement were calculated for the classified data. Results of the Kappa index agreement were in the range 0.61–0.80 and the overall accuracy in the range 0.81–1.0.

Martinez and Toan (2007) assessed the classification accuracy of a time series of JERS L-band images to map flooding compared with an individual image. The research methods were based on mean backscatter for land-cover classes and total change was

assessed by the absolute change estimator used for estimating landscape change. The accuracy assessment showed good results, with a Kappa value of about 0.8, with improved results over smooth surfaces compared with the accuracy of classification realized with an individual image. The study indicated a lower accuracy in discrimination between open water surfaces, bare soils and low vegetated areas, because of the lower sensitivity of L-band data to smooth surfaces.

Accuracy has also been assessed in texture evaluation. Arzandeh and Wang (2002) investigated Radarsat-1 imagery for wetland mapping. They evaluated the use of texture analysis by classifying wetland and other land cover over a single-date Radarsat-1 image in Walpole Island, Canada. For texture measurement, they used a grey-level co-occurrence matrix, and for classification they employed a maximum-likelihood supervised classifier. Various combinations of texture feature were examined during the evaluation procedure, and classification results were compared for the Kappa coefficient and overall accuracy. The accuracies of the classification results were compared and analysed to select the preferred input parameters such as window size, inter-pixel distance and inter-pixel angle. A Z-pairwise statistical test was also performed to assess the differences between two classifications.

A comparison of classification accuracies between fully polarimetric, dual-polarization and single-polarization SAR data was evaluated by Lee et al. (2001, cited in Lee and Pottier, 2009) for P-band, L-band and C-band using the JPL AIRSAR (airborne SAR) dataset of Flevoland, in the Netherlands, for crop classification. They performed a quantitative comparison to assess the classification capabilities of all combinations of polarizations for three frequencies. As a reference class map, training sets were used to evaluate classification accuracy. The study involved the following basic classification procedure: 1) select training sets from a ground truth map; 2) filter polarimetric SAR data; 3) apply maximum-likelihood classifiers to each individual polarization, to combinations of dual polarization, to combined sensors and to each individual sensor; and 4) identify the correct classification compared with the reference class map. The quantitative analysis showed that complex HH and VV polarizations is the preferred combination, and L-band polarimetric SAR data is more accurate for crop classification. The study also revealed that L-band complex HH and VV modes can attain classification rates that are almost as good as those for full polarimetric SAR data.

Gebhardt et al. (2008) evaluated two simple image-processing approaches for flood classification: a histogram-based method (a segmentation of an image histogram using a threshold) and a texture-based technique (separating homogenous from heterogeneous areas by thresholding the resulting image). Two TerraSAR-X stripmap images analysed for deriving inundation surface areas were acquired over the plain of reeds in the Mekong delta during the dry season in 2007 and the rainy season in 2008. For accuracy assessment, the study derived reference data from TerraSAR-X images because of a lack of field reference data. However, the water masks derived within five defined test areas were evaluated against the reference data. The overall accuracy for the whole classified images for the threshold and the texture-based approach during the dry season was found to be 96.8% and 91.6%, respectively. For the buffer zones, on the other hand, both approaches showed lower accuracies (80.8% and 70.6%, respectively).

3.10 Conclusion

considerable development at both levels, the SAR system technology and the SAR products application techniques has allows the significance of SAR remote sensing as a tool for mapping and monitoring of natural hazards and disasters to take a step forward. The emergence of new high spatial resolution SAR satellite sensors (i.e. Radarsat-2 and TerraSAR-X) will allow mapping of flood hazards in more details which will improve efforts of disaster relief at a local scale. Therefore, assessment of their ability and also identification of the optimum sensor system for flood detection are essential for maximum exploitation of their advantages.

The principles of synthetic aperture radar (i.e. wavelength, polarization, spatial resolution, incidence angle, look direction, backscattering and speckle) as such briefly reviewed in this chapter along with the literature has discussed its applications particularly in mapping floods, are used as a theoretical basis to achieve the objectives of this thesis. The high incidence angle is appropriate for flood mapping (i.e. Baghdadi et al., 2008; McMillan et al., 2006; Srivastava et al., 2009). The HH polarization is better than VV polarization for mapping wetlands (i.e. Baghdadi et al., 2001; Henry et al., 2006). Understanding of new development specifications of the new SAR sensors as

reviewed in section 3.8 would allow appropriate selection of type products, processing, and image interpretation.

Evaluation of SAR products for discrimination of surface water from other land cover would be incomplete without accuracy assessment. Therefore, reviewing procedures of the accuracy assessment of remotely sensed data for flood maps accuracy in terms of accuracy assessment methods, and sampling design along with the applications of the classification accuracy assessment of SAR data constitute the appropriate accuracy assessment procedures for this thesis.

It is worth noting that although there are various studies which assessed different SAR sensors and products in a range of SAR system parameters, there are very few and this is considered as a gap in the assessment of the new advanced SAR satellite sensors (C- and X-bands) in particular. Therefore, the most important limitation and lack of studies are:

- Lack of assessing high resolution SAR products and system parameters (i.e. polarization) for flood and water detection at a local scale which is certainly needed in order to support efforts of disaster management in terms of flood damage assessment and human relief on the one hand and water resource management on the other. Therefore, bridging this gap will assist in this domain.
- Lack of evaluation of the image processing methods for the high resolution SAR products for flood detection and mapping small water bodies at local scale will inhibit better utilization of SAR data.
- Lack of a comparison assessment between new SAR instruments working with different frequencies such as C-band (i.e. Radarsat-2) and X-band (i.e. TerraSAR-X) with regard to mapping flood extent and small water bodies might limit the maximum exploitation of their capabilities.

For these reasons, an evaluation approach of the new high resolution Radarsat-2 and TerraSAR-X products for water body mapping will be discussed in the following chapters of this thesis. The approach will be based on appropriate methodologies to the nature of this research project concerning SAR data acquisition parameters, field data specifications, data processing, and accuracy assessment. The high resolution SAR

products available for this thesis will be obtained from the Radarsat-2 and TerraSAR-X instruments. Appropriateness of acquisition mode selection was based on better coverage and higher resolution. Thus, the most suitable SAR products for this study would be the stripmap (TerraSAR-X) and the ultrafine (Radarsat-2), using high incidence angles to decrease backscatter and thus increase the contrast between water and land surfaces. It is essential to select a topographically flat area to avoid radar layover and foreshortening effects that may occur with hilly areas.

Since assessment of the mapping capabilities of SAR data for water body mapping is one of the objectives of this study, therefore it is important to define the polarization applicability with regard to the operational use for flood mapping. Therefore, a number of SAR images may be acquired in HH and VV polarization covering the study area where there should be contained many permanent water bodies with different sizes and shapes in order to ensure their availability during radar imaging. Verification and assessment of the results of radar interpretation are required by performing a field survey for mapping water bodies by using GPS equipment simultaneously with the SAR data acquisitions.

Data processing methods in light of the previous studies can be based on textural analysis using a grey-level co-occurrence (i.e. Arzandeh and Wang, 2002; Gebhardt et al., 2008) and using a maximum-likelihood classifier for image classification (i.e. Li et al., 2007; Mroz and Mleczko, 2008). Beside the textural image classification it is important to strengthen the image interpretation procedure by taking into account other factors such as shape, size and pattern (Henderson and Lewis, 1998) and therefore, the object-based classification will be appropriate to exploit the contextual information of the SAR objects (i.e. water bodies) (see for example, Herrera-Cruz and Koudogbo, 2009). The accuracy assessment of the flood maps compared with the dGPS ground truth data can be based on the error matrix method using statistical measurements include overall, producer's, and user's accuracy (i.e. McMillan et al., 2006; Mroz and Mleczko, 2008). Moreover, an accuracy comparison should be implemented between classified images of both Radarsat-2 and TerraSAR-X sensors in order to identify any differences in mapping floods.

Chapter Four:

DESCRIPTION OF THE STUDY AREA

4.1 Introduction

The aim of this chapter is to describe the study area in terms of geographical location, climate, land cover and land use. In this project, the study area has been analysed in two phases. The first is the acquisition of the SAR satellite products over the study area, while the second is the fieldwork campaign. The fieldwork project provided essential information to support the research objectives in interpreting the SAR imagery and, most importantly, in ground truthing.

The challenge was to select the most appropriate study area that can be used to achieve the research objectives and within the available time and resources. Several criteria were taken into account when selecting the area of study, an area at risk from freshwater flooding, the availability of a large number of water bodies during non flood periods, ease of access, requirements for logistics and fieldwork risk assessment and availability of suitable SAR imagery. The following section discusses the study area justification further.

4.2 Justification of the Study Area

Bangladesh is an alluvial deltaic plain divided into three main regions: hills, terraces and flood plains. It has an approximate total area of 147,570 km². A large part of Bangladesh is densely populated, with a total population of about 140 million (Bangladesh Bureau of Statistics [BBS], 2006). Most of the land is located within the floodplains of the three rivers of the Ganges, the Brahmaputra and the Meghna and their regional rivers and channels (Cityriskpedia, 2001). The country is flood prone because of its low-lying deltaic plain location (Figure 4.1). Flooding is a normal occurrence in Bangladesh particularly the during monsoon season. However, the most severe floods have impacted large areas of the country and caused widespread disruption and loss of life and livelihood. Figure 4.2 gives an indication of the areas impacted during large events.

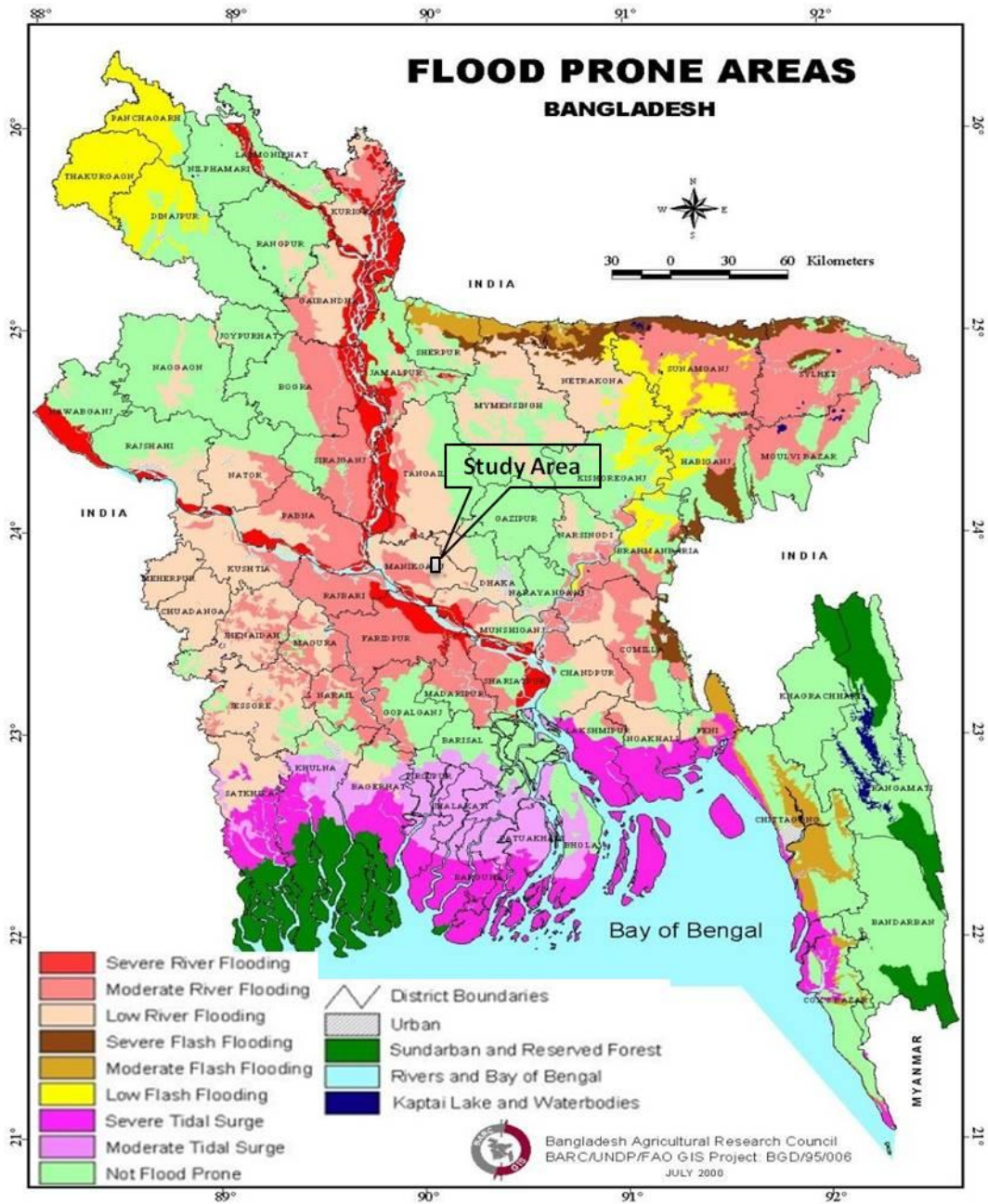


Figure 4.1: Flood prone areas of Bangladesh (Source: FAO, 2000).

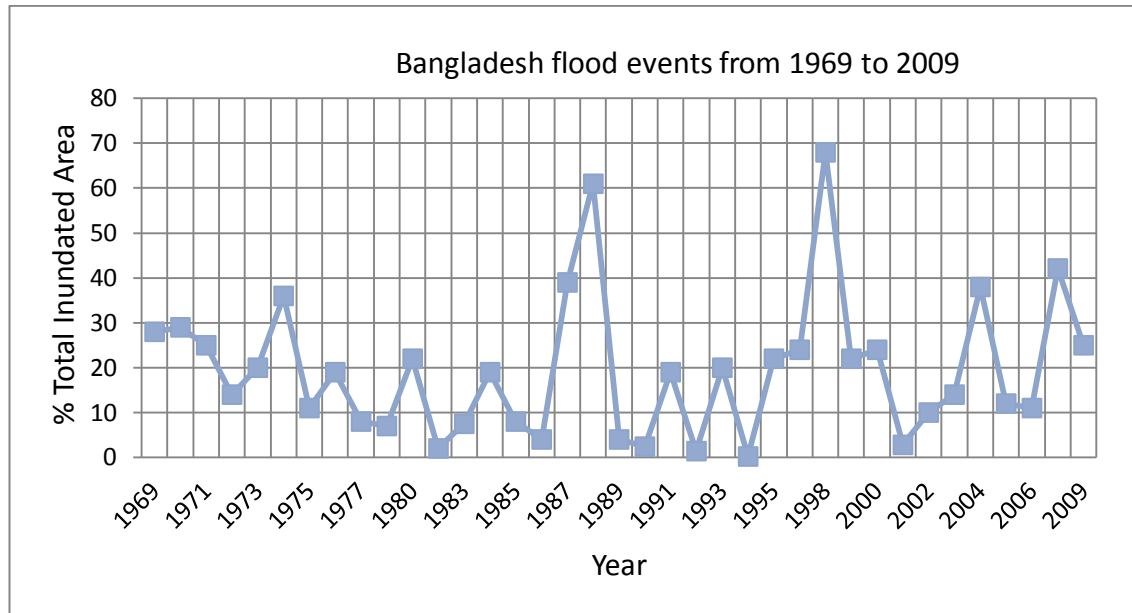


Figure 4.2: Maximum flooded area in Bangladesh 1969–2009 (based on data from MoEF, 2009).

Topographically, the study area is flat land. Low topography is useful for radar studies because it eliminates the need to deal with the topographic effects on backscattering. The study area was selected to include a range of land cover types including settlements, vegetation, crops and a large numbers of water bodies that persist outside the annual seasonal monsoon. The study area is large enough to assess the capability of high-resolution SAR data in delineating the sizes and shapes of a good range of water bodies. In summary, the study area was chosen for the following reasons:

- A large number of water bodies are available with a range of sizes and shapes.
- It is a region typical of the floodplains of Bangladesh.
- It has low topography, which is useful for radar studies because it eliminates the effect of topographic features on backscattering.
- It has a broad diversity of land use and land cover (for example, settlements, water bodies, vegetation, crops during dry and monsoon seasons).
- There is ease of access for detailed ground-based mapping using dGPS.
- Uniform alluvial soils.

Besides the reasons listed above, several specific requirements were taken into account when selecting the test sites within the study area:

- A sufficient number of water bodies distributed within a small area in order to allow visits within a reasonable time.
- Availability of water bodies located within varied land-cover and land-use surroundings.
- Availability of water bodies of various sizes and shapes within a specific site.
- Easy of access and within a reasonable distance from a city.
- Ability to identify the water bodies in aerial imagery such as that available in Google Earth.

4.3 Geographical Location of the Study Area

The study area lies in the region of the eastern basin of the main rivers of Jamuna and Padma and their tributaries. It is located on the east and west banks of the regional Bangshi River and within three Upazilas (subdistricts), namely, Savar, Dhamrai and Singair. The three Upazilas are in the Dhaka district in the division of Dhaka (Banglapedia, 2011). The eastern part of the study area (eastern bank of the Bangshi) is within the administrative region of Savar Upazila. The western part of the study area (western bank) is located within two Upazilas: the north-western area is part of the Dhamrai Upazila, while the south-western area is part of the Singair Upazila (Figure 4.3).

In terms of administrative areas, the surveyed water bodies are located in various local regions within the study area: Choto-Ashulia, Demran, Tetulia, Panch Ghugudia, Genda and Bandi Mara. The study area covers approximately 204 km² (17×12 km) and is located within the coordinates: NE corner 23°57'20"N – 90°17'45"E, NW corner 23°57'12"N – 90°10'48"E, SE corner 23°47'57"N – 90°17'56"E and SW corner 23°47'49"N – 90°11'0"E.

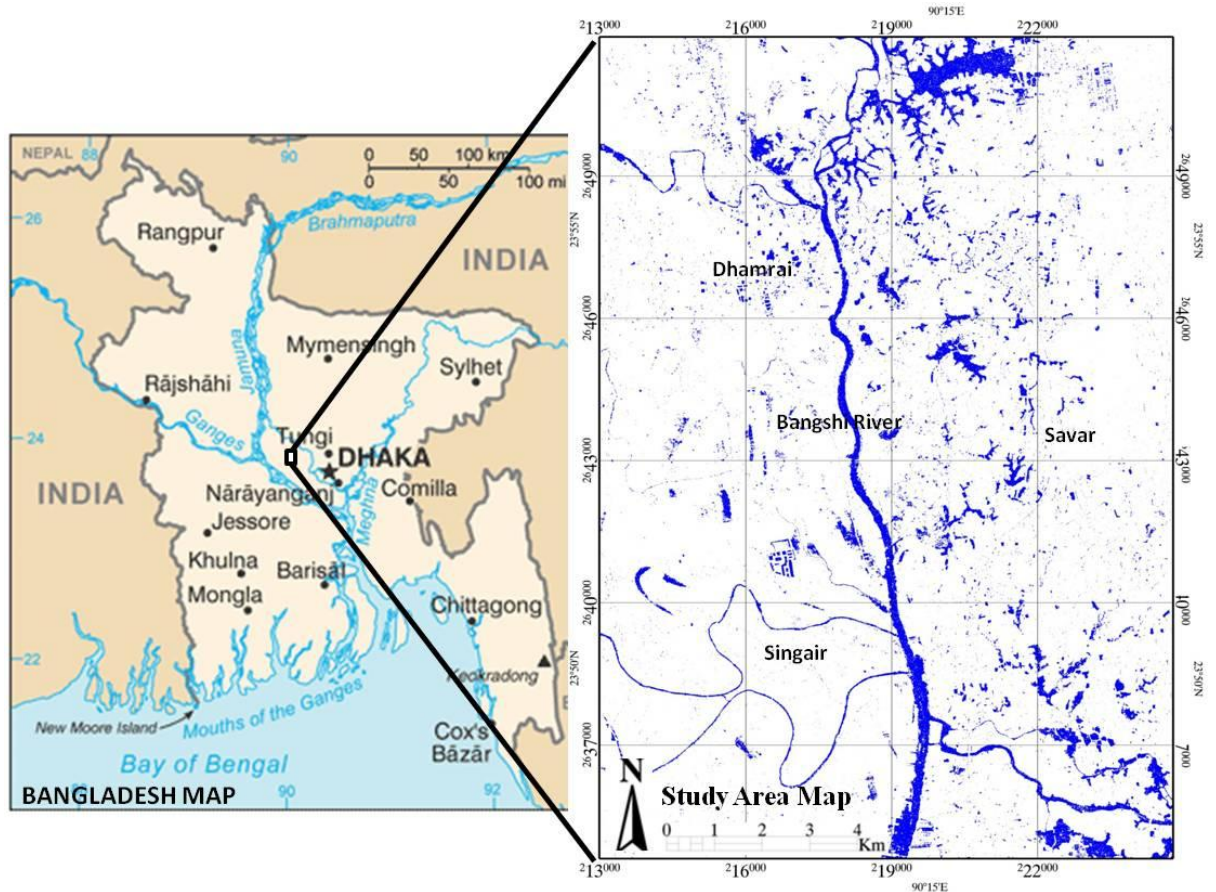


Figure 4.3: Location of the study area within Bangladesh. Note that it is located within Savar, Dhamrai and Singair Upazilas and lies in the Eastern and Western banks of Bangshai River. The water bodies in blue colour extracted from Radarsat-2 HH image density-sliced. Map of Bangladesh adapted from CIA, 2011.

4.4 Climate

Bangladesh has a tropical monsoon climate. Three distinct seasons may be recognized: a cool dry season (Winter), a pre-monsoon hot season (Summer) and a rainy monsoon season (Monsoon). The winter season is from November to February where the average temperatures vary from a minimum of 7–17°C in the north-eastern and north-western areas to 20–21°C in the coastal regions. The pre-monsoon hot season runs from March to May and has a temperature range from 27°C in the north-east to 30°C in the west central part of the country and may reach a maximum temperature of 40°C in some areas. Finally, the monsoon season is from June to October and has very high humidity with a temperature that ranges from 27°C in the south-eastern to 29°C in the north-

western regions (see the climate map of Bangladesh in Figure 4.4) (Barry et al., 1998; BBS, 2006).

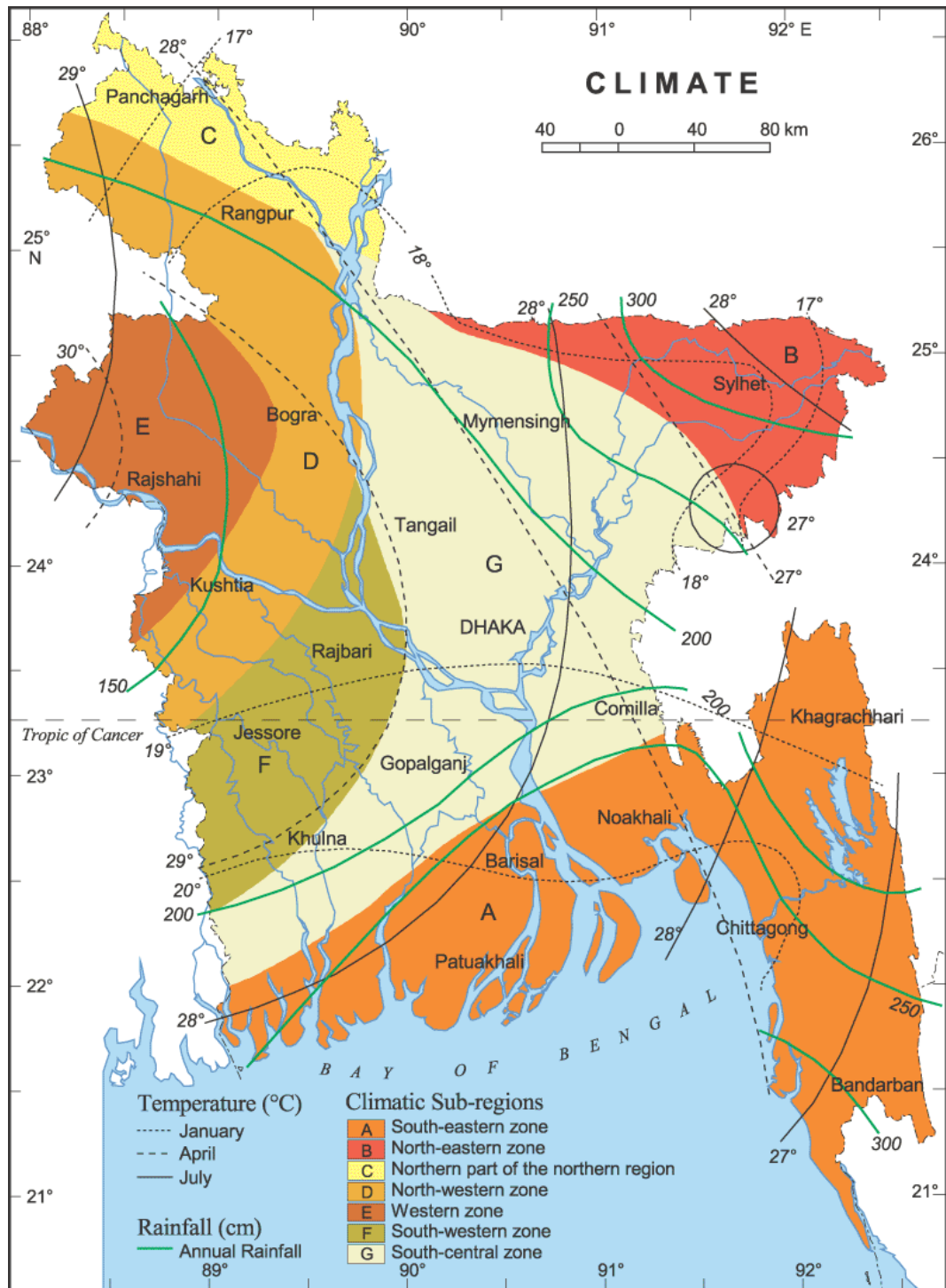


Figure 4.4: Climate map of Bangladesh (Source: Rashid, 1991).

In the winter, the total rainfall comprises 2% to 4% of the total annual precipitation. During the pre-monsoon, when the hot season starts, the rainfall gradually increases and accounts for 10–25% of the total annual rainfall. During the rainy season the total annual rainfall increases by up to 70% in the eastern region of Bangladesh. In the south-west it accounts for 80% and is over 85% in the north-west. In the west-central region there is an average of 60 rainy days. In contrast, this varies from 95 days in the south-east to over 100 days in the north-east of the country. According to geographic distribution, the west-central region of Bangladesh accounts for 150 cm of the country's annual rainfall, while the north-east and the south-east account for more than 400 cm. The average monsoon annual rainfall of Bangladesh between June and September varies from 1429 to 4338 mm, which accounts for 80% of the total annual rainfall (Islam et al., 2008).

The climate of the study area is generally typical for north-central of Bangladesh. The fieldwork campaign and the acquisition of SAR products were undertaken during the dry season in January 2009 in order to identify and map each water body detected during interpretation and assessment of the SAR imagery. The dry season begins in mid-December in this part of Bangladesh and then advances towards the east and south. The dry winter season (November to February) has a temperature range from 5°C to a 30°C. The temperature in the hottest season (April and May), as shown in Figure 4.5, exceeds 40°C.

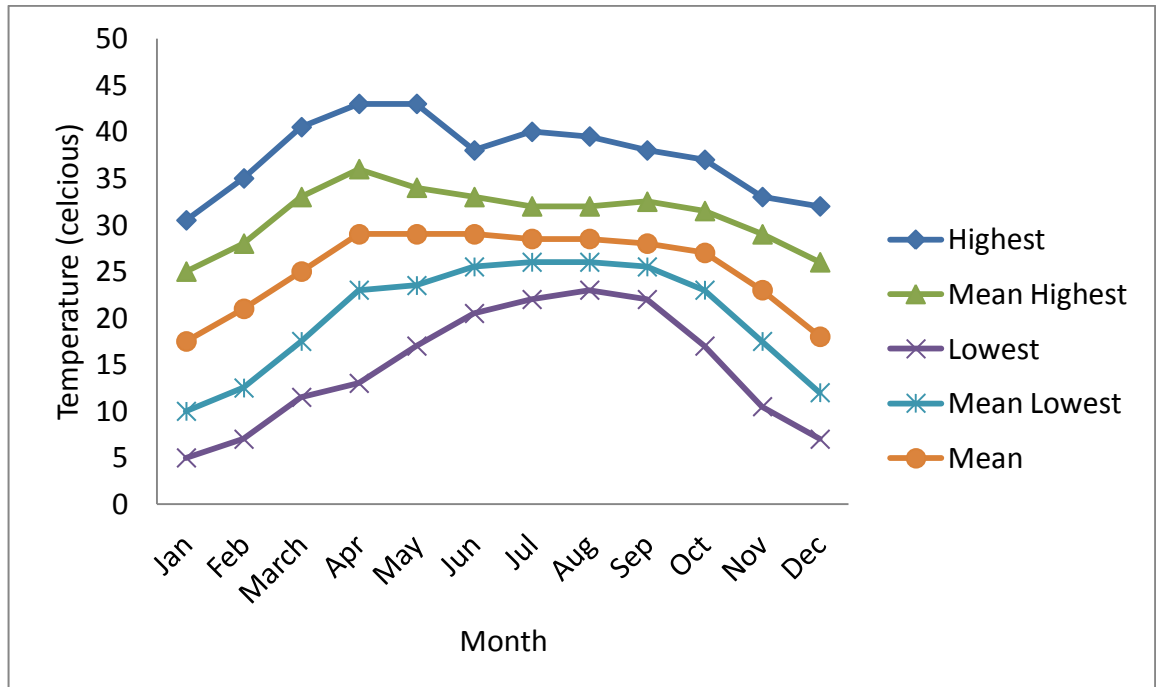


Figure 4.5: Average temperature of the study area (SRDI, 1997, in Huda, 2004).

The average rainfall of the study area varies during the year. It starts from less than 5 mm during the dry season in December and January to reach more than 350 mm in July, then decreases until it is again less than 5 mm in December (Figure 4.6).

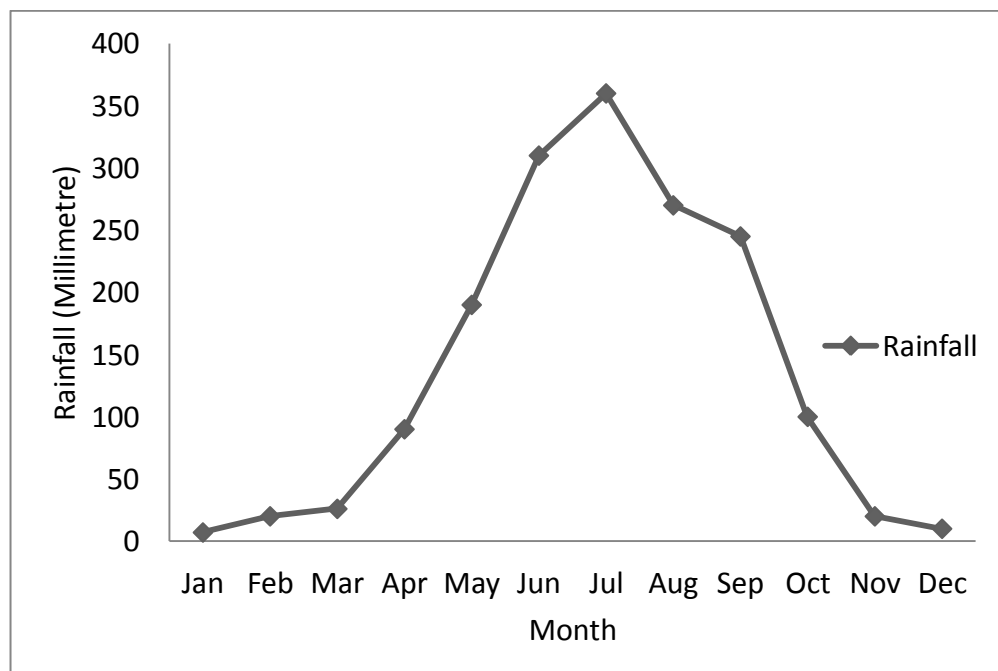


Figure 4.6: Average mean monthly rainfall in millimetre of the study area (modified from SRDI, 1997, in Huda, 2004).

Wind may induce surface roughness on water bodies (CCRS, 2011). The wind speed in Bangladesh is generally lower in the dry winter season and higher in the hot season. The average wind speed in the north-central region where the study area is located is approximately 4 - 5 m/s (Khan et al., 2004) (Figure 4.7). Wind generally peaks in the daytime and tends to be at a lower speed in the evening. The SAR products studied were acquired during the winter season and in the evening when the wind speed is at its minimum.

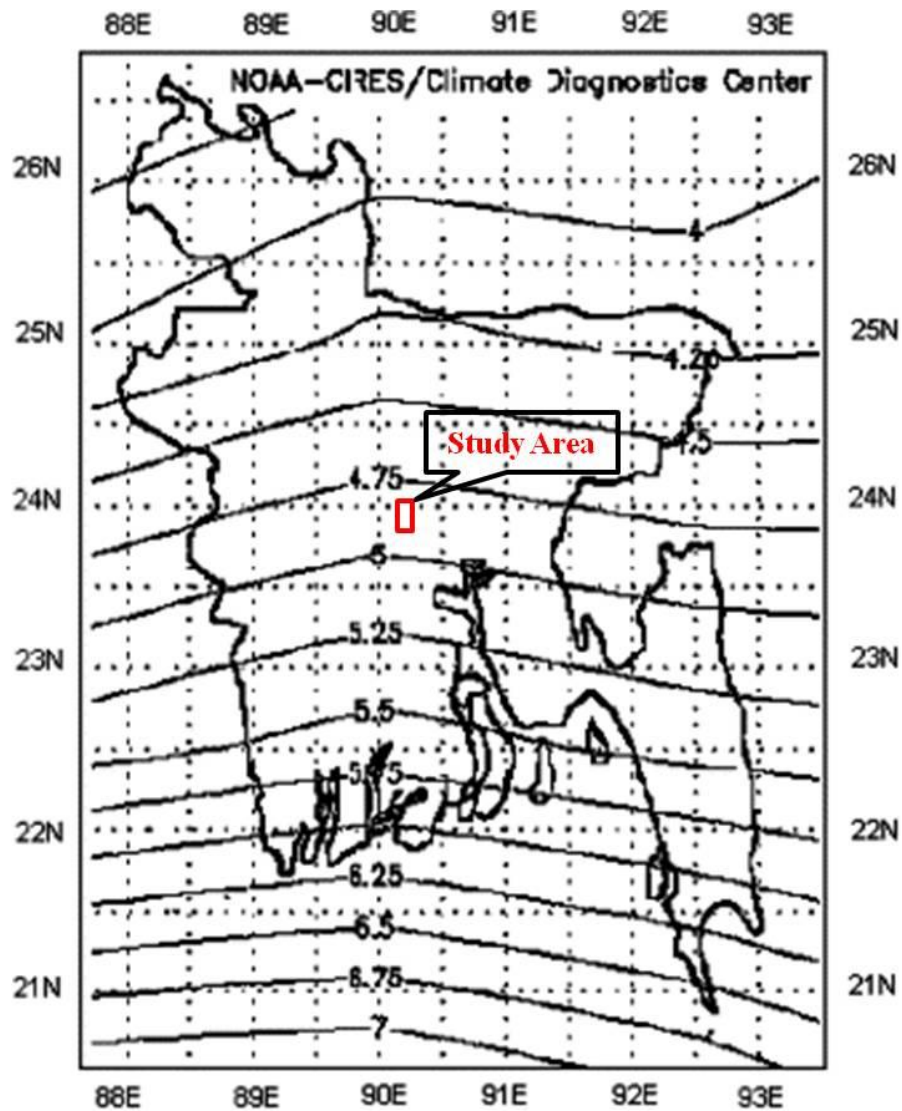


Figure 4.7: Average wind speed (m/s) in Bangladesh at surface level from January to December (adapted from Khan et al., 2004).

4.5 Floodplain and Drainage Network

Floodplains in Bangladesh occupy 80 per cent of the land area (MoEF, 2009). The country, has a network of 230 rivers with a total length of about 24140 kilometres dominated by the Ganges, the Brahmaputra, the Meghna, the Padma, the Teesta, the Surma and the Karnaphuli (BBS, 2009; Garg et al., 2007). Run-off from higher levels forms natural drainage systems in most regions of the country (Huq, 2000). The drainage system of Bangladesh consists of four major networks: the Brahmaputra–Jamuna river system, the Ganges–Padma river system, the Surma–Meghna river system and the Chittagong region river system (Figure 4.8). The drainage basins of the major rivers regularly experience high-magnitude floods (Islam & Sado, 2000). The annual discharge of the combined systems reaches 1,174 billion m³ (Khan, 1990; Rashid, 1991).

The elevation of the study area surface ranges between 2 and 4 m above sea level (Khan et al., 2004). The study area lies within the basin of the Brahmaputra–Jamuna and Padma rivers (see Section 4.3). Several regional rivers are distributed within this low-lying area, such as the Bangshi, Dhaleshwari, and Buriganga (see Table 4.1 and Figure 4.8).

Table 4.1: Regional Rivers and their lengths across areas of Bangladesh included Dhaka Division (the highlighted rivers are crossing the study area) (BBS, 1999).

River	Length (km)	Area covered (km)
Arial Khan	160	Faridpur (102) Barisal (58)
Bangshi	238	Mymensingh (198) Dhaka (40)
Betna-Kholpotua	191	Jessore (103) Khulna (88)
Bhadra	193	Jessore (58) Khulna (135)
Bhairab	250	Jessore, Khulna
Bhogai-Kangsa	225	Mymensingh (225)
Brahmaputra-Jamuna (Jamuna 207)	276	Rangpur (140) Pabna (136)
Buriganga	27	Dhaka (27)
Chitra	170	Kushtia (19) Jessore (151)
Dakatia	207	Comilla (180) Noakhali (27)
Dhaleshwari	160	Mymensingh, Dhaka
Dhanu-Baulai-Ghoraotra	235	Mymensingh (126) Sylhet (109)
Donai-Charalkata-Jamuneshwari-Karatoya	450	Rangpur (193), Bogra (157), Pabna (100)
Ganges-Padma (Ganges 258, Padma 378)	378	Rajshahi (145), Pabna (98), Dhaka and Faridpur (135)
Gorai-Madhumati-Baleshwar	371	Kushtia (37), Faridpur (71), Jessore (92), Khulna (104), Barisal (67)
Ghaghat	236	Rangpur (236)
Karatoya-Atrai-Gur-Gumani-Hurasagar	597	Dinajpur (259), Rajshahi (258), Pabna (80)
Karnafuli	180	Chittagong HT, Chittagong
Kobadak	260	Jessore (80) Khulna (180)
Kumar	162	Jessore, Faridpur
Kushiyara	228	Sylhet (228)
Little Feni-Dakatia	195	Noakhali (95) Comilla (100)
Lower Meghna	160	from Chandpur to the Bay of Bengal
Matamuhuri	287	Chittagong HT and Chittagong
Mathabhanga	156	Rajshahi (16), Kushtia (140)
Nabaganga	230	Kushtia (26) Jessore (204)
Old Brahmaputra	276	Mymensingh (276)
Punarbhaba	160	Dinajpur (80) Rajshahi (80)
Rupsa-Pasur	141	Khulna (141)
Sangu	173	Chittagong (80), Chittagong Hill Tracts (93)
Surma-Meghna	670	Sylhet (290), Comilla (235), Barisal (145)
Tista	115	Rangpur (115)

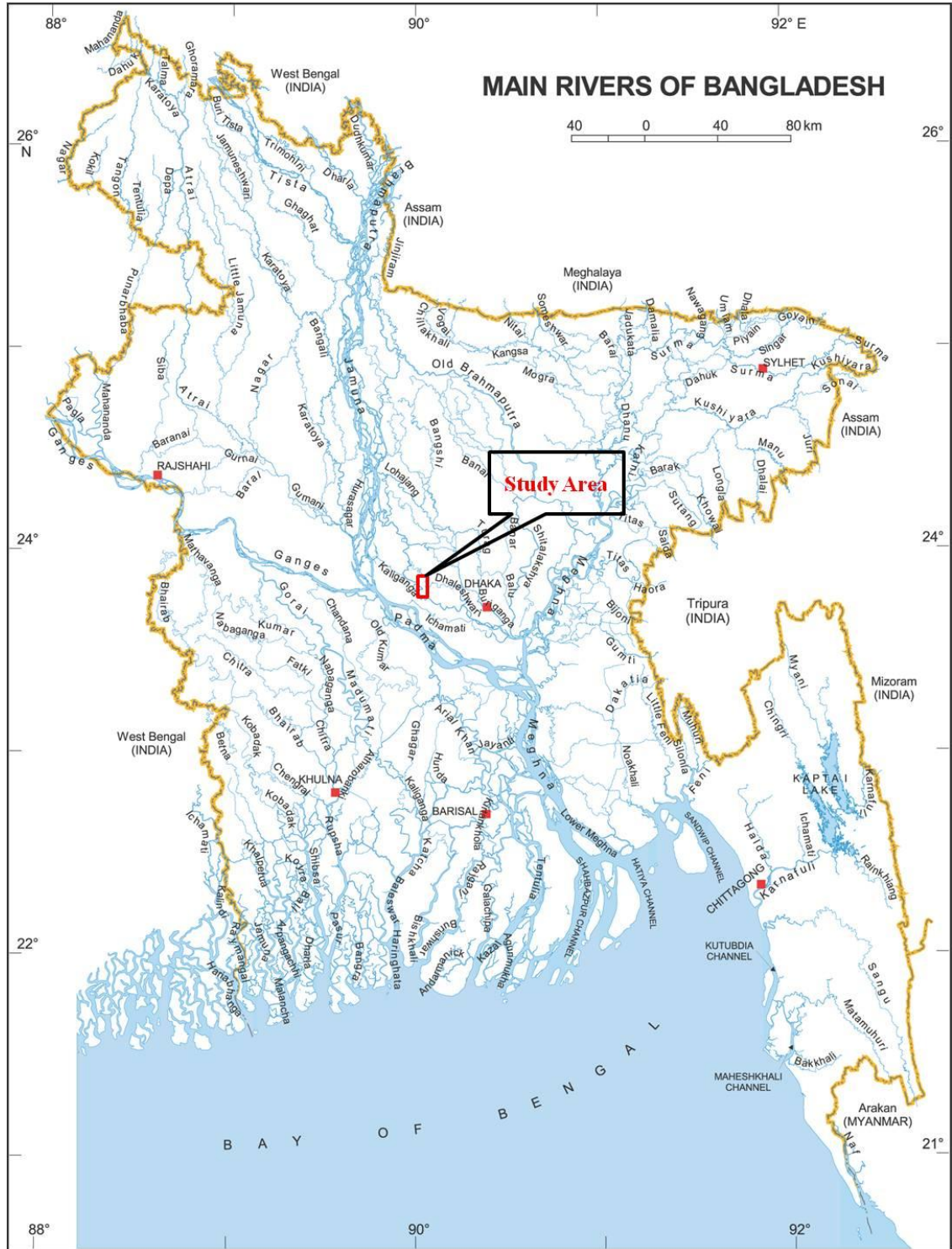


Figure 4.8: Main and regional rivers’ map showing the location of the study area within a basin of rivers’ network (Rashid, 1991; Wazed, 1991).

4.6 Soil

The alternating seasonal wet and dry conditions are a key to soil formation. The soils of the study area are located in a low-lying floodplain consisting of alluvium deposited by the Brahmaputra–Jamuna river system. The topsoil is Non-calcareous Grey Floodplain Soils (Dewan et al., 2007; MoEF, 2009) (Figure 4.9). On this type of floodplain, the soil formation process is dominated by sediment deposition. Unlike the hill and uplifted terrace areas, the composition of the floodplain of the study area is 79% loam, 15% clay and 6% sand (FAO, 2011).

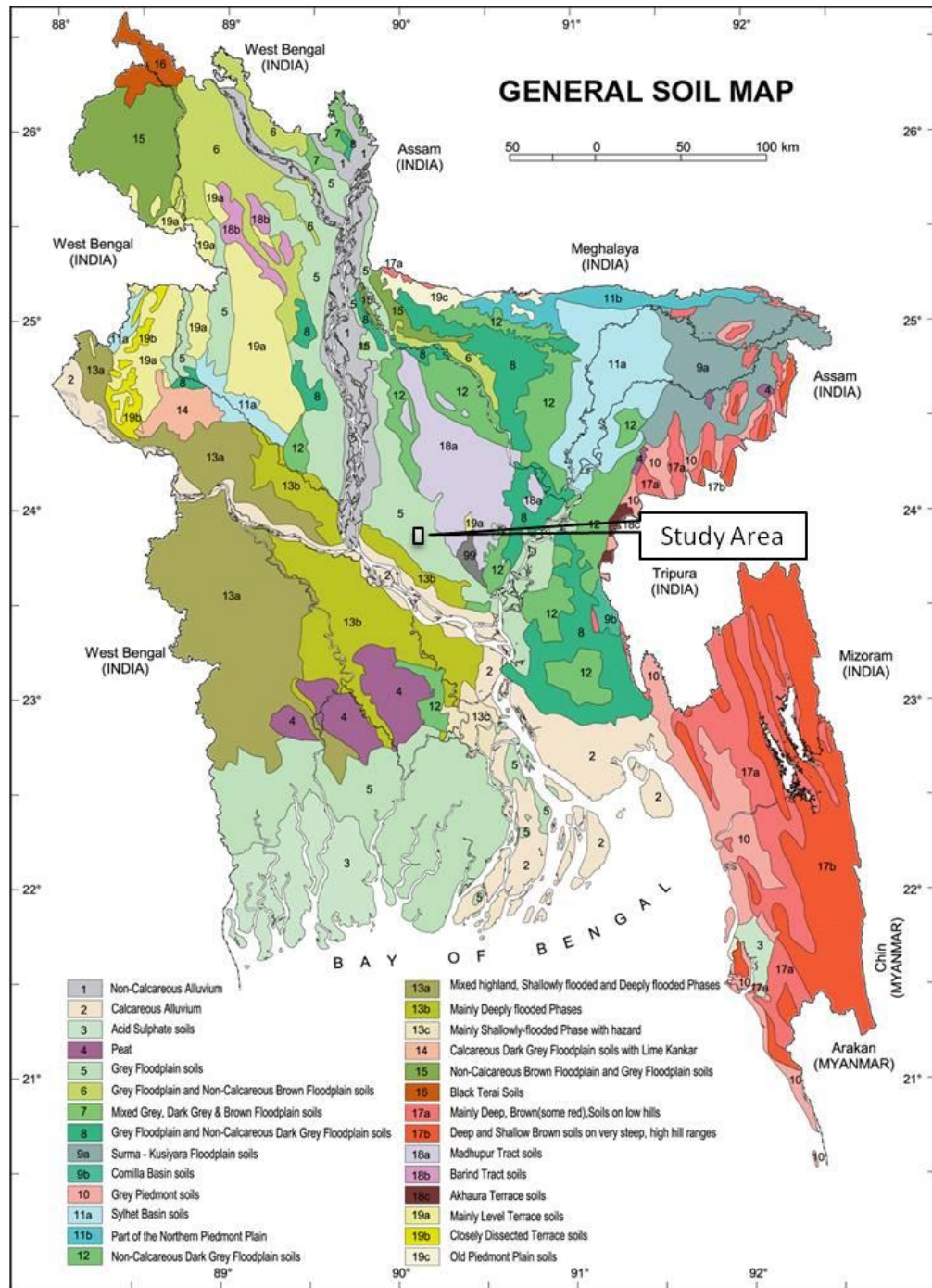


Figure 4.9: General soil map of Bangladesh (note the study area located within grey floodplain soils) (FAO/UNDP, 1986).

4.7 Hydrology and Water Resources

Bangladesh has eight distinct hydrological regions: north-east, north-central, north-west, south-east, south-central, south-west, eastern hills, and river and estuaries (Hossain, 2003) (Figure 4.10). The study area is located within the north-central region. The main

sources of water in Bangladesh can be divided into two main categories: surface water and groundwater.

Surface water in Bangladesh has different forms – transboundary flow of rivers, canals, streams and water bodies. During the monsoon (July–October) many floodplain areas become inundated from both local rainfall excess and huge transboundary flow of rivers. In addition to rivers, water is retained in natural or artificial reservoirs known as *beels* for use in the dry season. The average total volume of such standing water bodies is about 0.61 billion m³ (Ahmed & Roy, 2007).

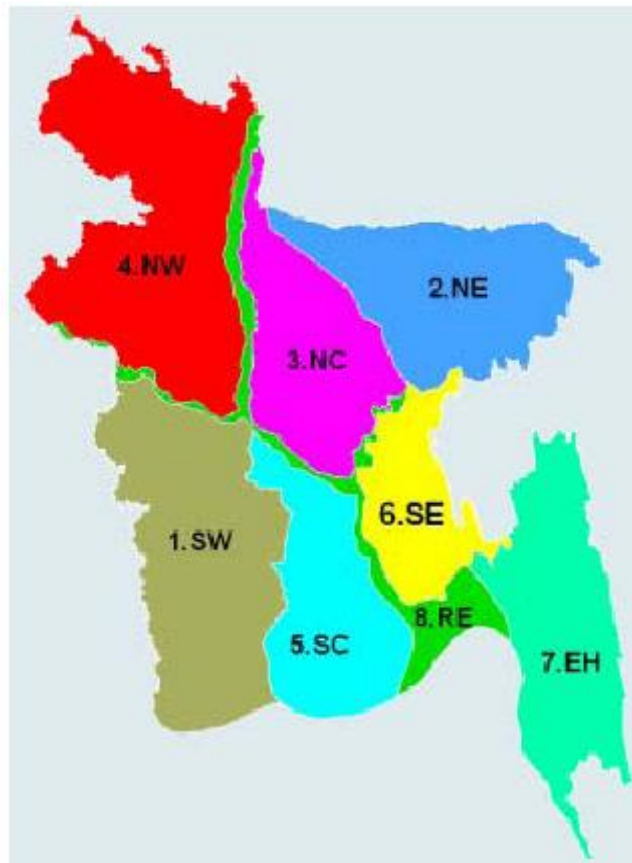


Figure 4.10: Hydrological regions of Bangladesh. Note that the location of the study area is within the NC region (Adapted from Hossain, 2003).

4.7.1 Groundwater

Groundwater storage reservoirs recharge from surface-water sources such as river-flow water, monsoon rainfall and floods, and standing water bodies (Huq, 2000). The unconfined aquifers found in most of Bangladesh have been formed from the

sedimentary alluvial and deltaic deposits of the three major rivers are mostly at depths varying from 0 to 20 m below the ground surface (Ahmed & Roy, 2003).

During the dry season the consumption of groundwater increases for cultivation and rice production, which is irrigated artificially (Uchida & Ando, 2007; WFP, 2011). Irrigation from groundwater is conducted by mechanisms such as deep and shallow tubewells and by traditional groundwater devices such as hand tubewells, treadle pumps and dug wells (WFP, 2011).

4.7.2 Floods in Bangladesh

Floods in Bangladesh are of four types: rainfall flood, flash flood, river flood and flood due to cyclonic storm surges. In north-central Bangladesh, where the study area lies, rainfall floods are the dominant type. Many parts of the floodplain are inundated after heavy local rainfall. When water flows over the riverbanks, low-lying areas it may become a connected sheet of water (CEGIS, 2003). The population of Bangladeshis take simple and traditional measures to live with flood. Examples of these measures are building houses and other constructions on high mounds above the average flood level and building roads on embankments (Brammer, 1994, 1995).

Floods in Bangladesh have an impact on people, crops and infrastructure and have several causes. These include a low floodplain, intense monsoon precipitation in the upstream country or in the mainland, drainage congestion and cyclonic storm surges snow glacier melt, El Nino Southern Oscillation (ENSO). (Tingsanchali & Karim, 2005; Mirza, 2003) (Figure 4.11).

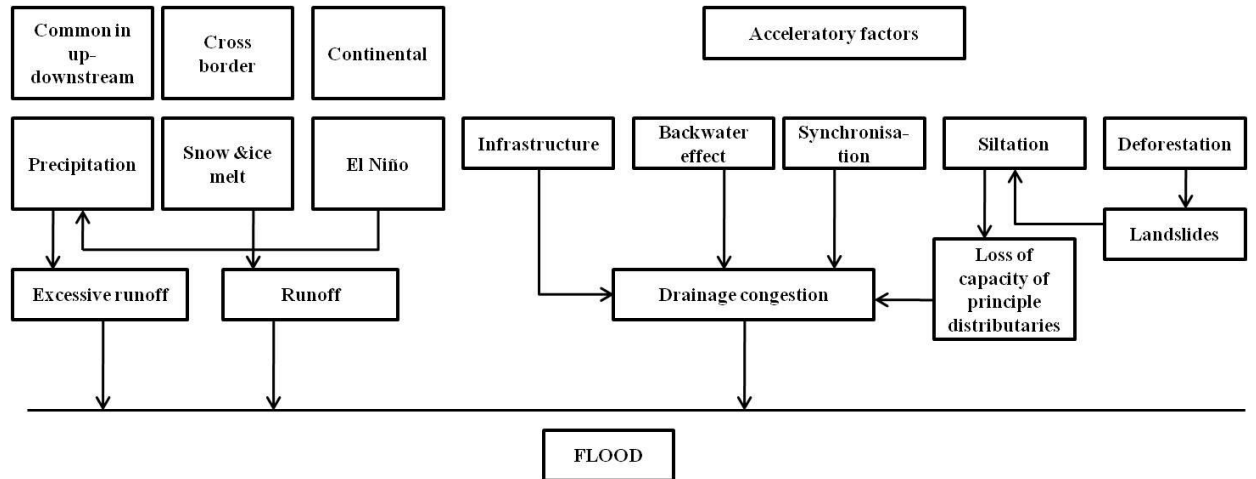


Figure 4.11: Causes of floods in Bangladesh (Modified from Mirza, 2003).

Therefore, Bangladesh is one of the countries most prone to extreme floods. It is the most vulnerable country in the world to tropical cyclones and the sixth most vulnerable country to floods (UNDP, 2004; MoEF, 2009). Two-thirds of Bangladesh area is less than 5 meters above sea level. A quarter of the country is inundated in an average year. On average, Bangladesh has experienced at least one severe flood every couple of years that may affect more than 60 percent of the country and resulting in significant losses) people, crops, houses, and infrastructures (Dasgupta et al., 2011). Records shown that Bangladesh was affected by extreme floods in the last three decades (1980-2010) include floods of 1984, 1987, 1988, 1998, 2004, 2007 and 2009 where human loss and economic damage were enormous (MoEF, 2009). Table 4.2 shown impacts of the severe floods affected Bangladesh in the recent decades.

Table 4.2: Bangladesh severe floods in the last three decades (MoEF, 2009).

Year	Impact
1984	Inundated over 50,000 sq. km, estimated damage US\$ 378 million
1987	Inundated over 50,000 sq. km, estimated damage US\$ 1 billion, 2,055 deaths
1988	Inundated 61% of the country, estimated damage US\$ 1.2 billion, more than 45 million homeless, between 2,000-6,5000 deaths
1998	Inundated nearly 1,000,000 sq.km, rendered 30 million people homeless, damaged 5000,000 homes, heavy loss of infrastructure, estimated damage US\$ 2.8 billion, 1,100 deaths
2004	Inundated 38%, estimated damage US\$ 6.6 billion, affected nearly 3.8 million people, deaths 700
2007	Inundated 32,000 sq.km, over 85,000 houses destroyed and almost 1 million damaged, approximately 1.2 million acres of crops destroyed, estimated damage over US\$ billion, 649 deaths
2009	180 total deaths, 7153 people injured, 860200 family affected, 4825954 people affected, 609592 houses damaged, 318140 crops damaged.

4.7.3 Water Bodies

Bangladesh has a large number of water bodies with a range of sizes and shapes, either artificial or natural. The number of small water bodies in Bangladesh in 1989 was estimated by the BBS (1994) to total 1.95 million. The natural standing water bodies such as *beels* (lakes) are generally connected to rivers during the monsoon season (Huq, 2000). Most of the small water bodies are manmade on the floodplains and result from the excavation of earth for building houses at elevations higher than the expected flood level (Huda et al., 2010).

For every eight people in Bangladesh there is approximately one acre of water (Khan, 2000). Water bodies range in size from 25–400 m² (*doba*: ditch), 150–1000 m² (*pukur*: perennial water source), >750 m² (*dighi*: reservoir) and >1000 m² (*beel*: saucer-shaped or an ox-bow lake) (Table 4.3). These small water bodies form an integral part of the rural economy in Bangladesh because they are used for a variety of functions, including

drinking water, bathing, washing, fisheries, aquaculture, irrigation, and cattle feeding (Khan, 2000).

Table 4.3: Characteristics of various sizes of small water bodies (adapted from Huda, 2004).

Name	Size (sq. metres)	Characteristics
Doba/Pagar (ditch)	25–400	Manmade, retains water mainly in wet season.
Pukur (pond)	150–1000	Manmade or natural, retains water throughout the year.
Dighi (reservoir)	>750	Manmade/natural retains water throughout the year.
Beel	>1000	Natural, open inland water, saucer-shaped depression, generally retains water throughout the year.

Water bodies occur extensively in the study area, are of various sizes and shapes, and lie within a variety of land-cover/land-use locations (Figure 4.12). Generally, water bodies are located in an open area, surrounded by trees and adjacent to built-up areas. The depth of the surveyed water bodies ranges from 0.5 to 4 m. Water weeds often float on the water surface which may create a rough layer, that can diffuse the radar energy.



Doba



Pukur



Dighi



Beel

Figure 4.12: Examples of typical water-body types of various sizes in rural Bangladesh.

Water bodies are important in everyday life in Bangladesh in a number of ways. They are used in fisheries, for irrigation, and in households (Figure 4.13).



Figure 4.13: Importance of small bodies of water in everyday life in Bangladesh. A-Fish culture; B-Crop; C-Homestead purposes.

4.8 Agriculture

There are three growing periods for four main crops, where each type of crop needs particular seasonal and hydrological conditions. These periods differentiate the agricultural activities of Bangladesh: *Kharif-1* (March–July), *Kharif-2* (July–October) and *Rabi* (October–March) (Garg et al., 2007). The major crop during the monsoon season is deepwater rice, or floating rice (*aman* rice). During the *Rabi* (dry winter) growing period, specific types of crops are grown on land that has enough moist soil but drains quickly. Crops of the *Rabi* agricultural season are grown during the period between the end of the monsoon season in November and the end of March. The most

common *Rabi* (winter season) crops are rice, wheat, jute, mustard, maize, groundnut, sesame, potato, sugarcane and grass pea.

Rice is the most widespread crop across cultivated areas in Bangladesh (Table 4.4). It is categorized into three types according to the season in which they are harvested. *Aman* is a class of rice harvested in December–January, *boro* is harvested during March–May and *aush* is harvested in July–August. Wheat is the second most important crop in Bangladesh after rice and is cultivated as a winter crop. Jute is the third most cultivated crop and is grown mainly in the low-lying areas of the Brahmaputra–Jamuna and Padma floodplains. The fourth important crop is mustard, which is also grown in the low-lying areas of Brahmaputra–Jamuna floodplains. Mustard crops and non-cereal crops are also cultivated in the *Rabi* season (FAO, 2011).

The point that should be raised here is that the acquisition of SAR scenes were conducted in January during the dry season when many crops such as rice, wheat, jute, mustard and other winter crops are at a level of sufficient growth. Therefore, this type of land cover may appear to have a rough texture, as shown in the example in Figure 4.14. It should also be noted that many regions in the study area were undergoing irrigation at the time of the fieldwork campaign (Figure 4.15), such as rice field ploughing and new transplantation of rice fields and this may appear wet in the SAR imagery. This type of land-cover wetland should be taken into account during the SAR image interpretation.



Figure 4.14: Crop fields during the fieldwork in January 2009.



Figure 4.15: Examples of two types of wetlands: (A) irrigated newly transplanted fields; (B) rice field ploughing.

Table 4.4: Percentage of land area planted by crop in 2004–5 in Bangladesh (FAO/WFP, 2008).

Crop	Land area percentage
Rice	79.4
Vegetables	>4.14
Wheat	4.09
Jute	>2.86
Pulses	>2.80
Potato	>2.39
Oilseeds	>2.37
Spices and condiments	>2.21
Fruits	>1.36
Sugarcane	>1.15
Tea	>0.39

Various types of trees are grown in the study area, often surrounding the water bodies (Figure 4.16). Examples include mango, bamboo, palm, guava, blackberry, mahogany, karai, eucalyptus and coconut. The average height of the trees varies from 10 to 20 m. Tall trees surrounding small water bodies may cause two types of confusion: first a high volume of backscattering due to canopy and trunk double-bounce reflection, which result in water appearing bright rather than dark in radar images; and second radar shadow, which appears dark, similar to water texture.



Figure 4.16: Some types of trees adjacent to water bodies.

Aquatic weeds grow on the surfaces of a variety of water bodies. One of the most dominant aquatic weeds is water hyacinth (Figure 4.17). This type of weed is a free-floating plant with its leaves above the water surface and its roots in the water. Hyacinth weeds are useful as food for fish and cattle and to give shelter to wildlife. The height of the plant and the length of its roots vary according to its type. Some types of hyacinth may grow to 45 cm with a root length of up to 90 cm (Reza, 2000). Water bodies covered partially with water weeds may need to be taken into account during SAR image analysis and interpretation in terms of backscattering and confusion between water weeds and dry land vegetation.



Figure 4.17: Water hyacinth floating on a water body.

4.9 Built-up Areas

The land use of the study area has geographically different categories. The eastern and south-eastern parts of the study area, especially Savar city, are extensively urbanized and highly populated. In contrast, the northern and eastern parts have low residential density and lesser built-up areas.

The highly built-up areas include various urban built-up units, including settlements, industrial and commercial developments and road networks. Most buildings in this area are made of concrete, and some of their roofs are made of tin. In some parts of this area the urban built-up units are combined with water bodies. Rural villages are distributed over north-eastern and western parts of the study area, in which people carry out farming. The housing units are mixed: some are made of wood, while others are built of concrete with roofs made of wood or tin. Most houses in the rural areas are surrounded by trees.

The road network of high-density built-up areas comprises main roads and minor roads, where most are made of asphalt. The rural roads connecting villages are narrow and made of asphalt, while roads connecting farms and village are mostly mud. Most of the roads have planted trees on both sides (Figure 4.18). Bridges are made of concrete and metal.



Figure 4.18: Typical rural road made of asphalt, showing planted trees on both sides.

Since radar energy interacts with the built-up areas differently from other land-cover types, special care has to be taken when interpreting SAR images. Built-up areas

according to radar remote-sensing principles usually appear bright in SAR imagery, because of corner reflections. Moreover, roofs made of tin may cause high backscatter when they are in a position facing the radar waves. Flat surfaces such as roads made of asphalt normally appear as dark areas in SAR imagery, since most of the incident radar energy reflects away from the SAR antenna.

4.10 Synthesis

This description of the study area emphasizes the importance of the chosen area for supporting the research objectives. It highlights the rationale for selection of the study area in terms of the fieldwork campaign and the acquisition of SAR satellite scenes. Understanding the climate characteristics of all seasons can help in making the right decision on when to carry out the fieldwork and the SAR image acquisition. In this way, the dry season was selected in order to identify standing water bodies.

Land-cover and land-use types are significant parameters for SAR image analysis and interpretation. Most of the area is made up of cultivated fields and grassland, with sections of trees among built-up areas and along the sides of many roads. Wetlands mainly arise from the irrigation of newly transplanted fields. Settlements and built-up areas are concentrated in Savar city within the study area, while other parts have less built-up areas. A large number of small water bodies are distributed over the study area with varying shapes and sizes and can be found in open areas, surrounded by trees or near to buildings. The study area is typical of low lying alluvial floodplains in south Asia that had similar topography, soils, and land cover.

Gathering information from the study area involved two main methods. First, the fieldwork campaign, which was based on two distinct approaches: gathering information about land cover/land use and identification of water bodies by using GPS equipment alongside understanding the water-body surrounding area. The second method involved programming the acquisition of the SAR imagery to coincide with the fieldwork.

Chapter Five:**METHODOLOGY****5.1 Introduction**

SAR data acquisition parameters and field data specifications require a number of decisions. Assessment of the high resolution SAR images for flood detection requires selecting a suitable study area (chapter three) which consists of different shapes and sizes of water bodies where should be permanent or at least exist long enough to allow ground survey and imaging of them by the SAR sensors.

Appropriateness of acquisition mode selection was based on better coverage and higher resolution. However, dual and polarimetric acquisition modes were avoided due to their reduced resolution which are not suitable for this study. Thus, stripmap (TerraSAR-X) and ultrafine (Radarsat-2) were chosen to cover the study area. A shallow incidence angle for SAR products acquisition was selected for mapping the water bodies as steep incidence angles which lead to stronger backscatter for open water thus reduce the contrast to land surfaces.

The type of SAR data has a major influence on the selection of the processing methods. Since SAR imagery has a single band which is based on intensity of grey level formed from radar backscatter, texture is the main source of information used to study land cover and land use (Dekker, 2003) particularly water cover. However, texture is not the only source of image information: shape, size and relationship of image objects can also be obtained through the object-based analysis. Therefore, it has been decided to conduct both methods of texture and contextual analysis to achieve both benefits.

Consequently, the research methods used in this study have been developed taking into account the availability and type of SAR products collected, suitability of the test sites and the remote sensing software available. A variety of approaches have been taken to achieve the aim and the research objectives listed in Chapter One.

5.1.1 Data collection methodology

A data collection methodology was established for SAR image acquisition and field data collection. The major activities of data collection were the acquisition of SAR products using the Radarsat-2 and TerraSAR-X instruments. A number of SAR images were acquired during the dry and rainy seasons of the study area in HH and VV polarization.

The gathering of ground data during the field campaign was performed using differential GPS (dGPS) equipment. The main aim of the survey was to map water bodies which are suitable for assessment and validation. Both SAR products and field data were obtained concurrently.

5.1.2 Data Processing

Data collected from SAR sensors and fieldwork were processed according to a data processing framework as shown in Figure 4.1. The pre-processing phase involved reprojecting SAR products along with geometric correction using GCPs extracted from the dGPS data and then subset all images according to the size of the study area. The dGPS vector data were also reprojected and prepared for SAR geocorrection and randomly divided into training data and test data for classification processing.

The textural analysis included density slice analysis for SAR images and evaluation texture measures. Following the identification of the appropriate texture measures, a supervised classification approach was then performed for flood map production. The contextual analysis was performed using object segmentation followed by contextual classification for the water bodies.

5.1.3 Data Evaluation

The data evaluation approach, focussed on assessing the accuracy of the SAR images compared with dGPS ground truth data and comparing the SAR products of the two SAR sensors (see Figure 5.1). The post classification analysis of each SAR image was performed using field test data for accuracy assessment of the produced maps of both sensors. An accuracy comparison between classified images of both polarizations (HH

and VV) was implemented for water delineation. The analysis of results of both Radarsat-2 and TerraSAR-X sensors were subjected to a comparison procedure in order to identify any differences in detecting the extent of flooding.

Each phase of data input analysis involved a specific framework for data processing which will be explained and justified in the following sections.

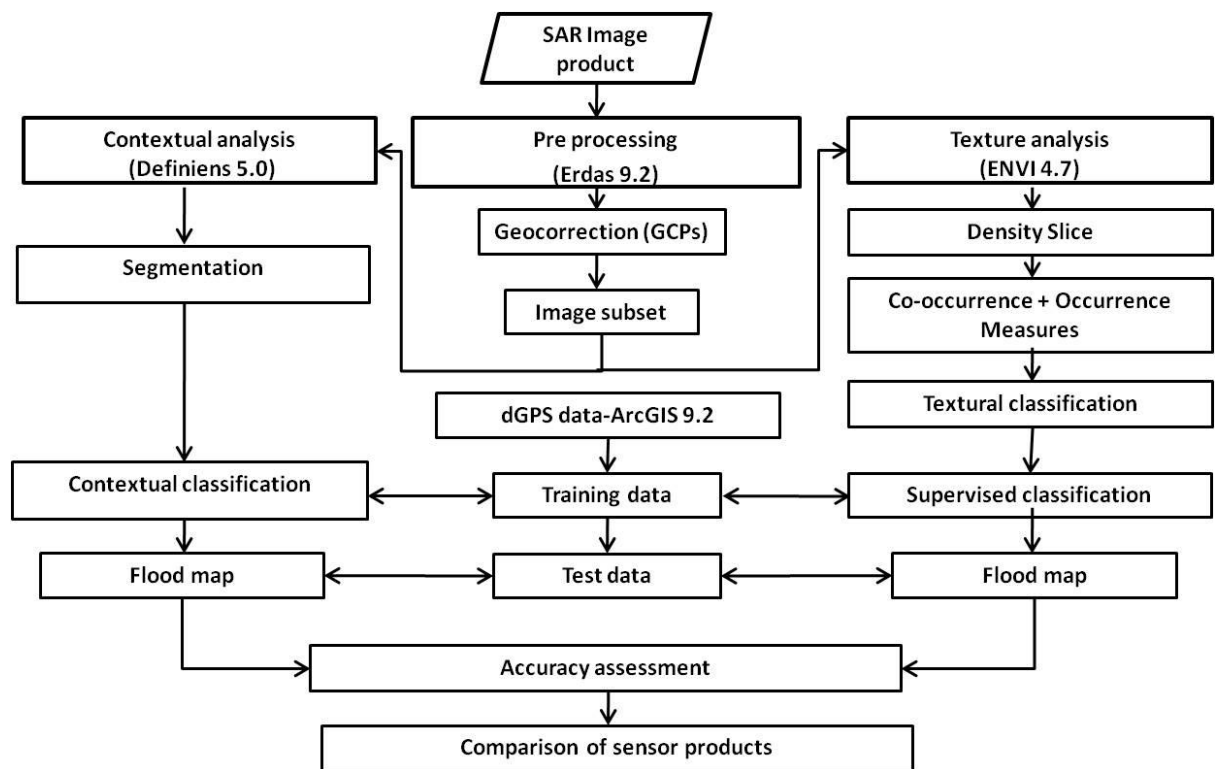


Figure 5.1: An overall workflow of the data processing methodology.

5.2 Data Description

Data for this study can be categorized under two headings: the SAR data and the dGPS data collected during the fieldwork along with methods of collecting field data. SAR images are the primary source of information in this study, whilst the dGPS data, which based on water body identification, is used as a benchmark for SAR product evaluation. In order to perform geometric correction, ground control points (GCPs) were extracted from the dGPS data.

5.2.1 SAR Data Description

At the time this research began, Radarsat-2 and TerraSAR-X were the only commercially available high-resolution SAR products. Attempts were made to acquire a number of products of this type. However, the acquisition of multiple high-resolution SAR products is an expensive process. One SAR image may cost around £2700, and obtaining the required images was beyond the scope of the available research budget. Therefore, research proposals were prepared to obtain access to Canadian Space Agency Radarsat-2 and German Aerospace Centre (DLR) TerraSAR-X data. Upon approval for research purposes, a number of products from each of the sensors were then provided (Table 4.1). Two SAR products were acquired in different polarizations from each SAR sensor during the dry season in order to ensure that water bodies were not in a flooded condition, to achieve better detection rates, while the other two products were acquired during periods of flooding in order to identify flood extent. The parameters for the SAR products obtained are given in Table 5.1.

Table 5.1: Parameters of SAR product acquisitions

SAR Sensor	Band	Beam Mode	Pol.	Res. (m)	Inc. Angle	Scene Size (km)	Look dir.	No. of Scenes	Date of acquisition	Scene coordinate
Radarsat-2	C-band	Ultra-fine	HH	3	41.01	20×20	Right	2	30/01/2009 21/10/2009	23° 46'N-23° 59'N 90° 08'E-90° 21'E
		Ultra-fine	VV	3	41.01	20×20		1	01/02/2009	
TerraSAR-X	X-band	Strip-map	HH	3	39.91–42.14	30×50	Right	2	20/01/2009 11/10/2009	23° 65'N-24° 20'N 90° 02'E-90° 42'E
		Strip-map	VV	3	39.91–42.14	30×50		1	28/08/2009	
		Spot-light	HH	1.5	39.91–42.14	10×5		1	07/04/2009	23° 88'N-23° 95'N 90° 17'E-90° 29'E

5.2.2 Radarsat-2 Data

Two Radarsat-2 products were obtained during the dry season in ultra-Fine beam mode. The products of a single polarization Horizontal-transmitted, Horizontal-received (HH) and Vertical-transmitted, Vertical-received (VV) were obtained on 6th and 8th January 2009 respectively, with a ground range resolution of 3.4 m. Another ultrafine HH image was obtained on 21st October 2009 (Table 5.1). The images were distributed by MacDonald, Dettwiler and Associates (MDA) via File Transfer Protocol (FileZilla software). An example of the Radarsat-2 product with HH polarization acquired for the study area is shown in Figure 5.2.

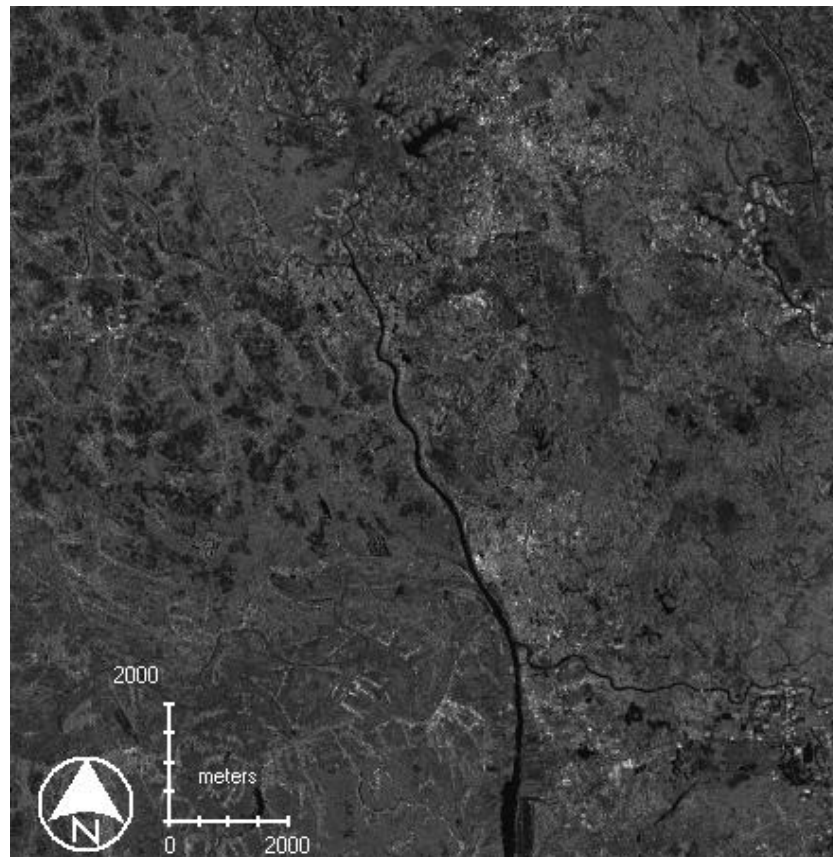


Figure 5.2: Radarsat-2 product acquired with HH polarization for the study area before Geocorrection.

The ultrafine resolution products cover a limited ground swath with nominal coverage of 20x20 km within the incidence angle range of 20° to 49°. Images were delivered in Geographic Tagged Image File Format (GeoTIFF), with the path image of the SAR Georeferenced Fine (SGF) with a standard pixel spacing, where the processing aligns

the scene parallel to the satellite track. The SGF images generated by MDA have standard ground coordinate pixel dimensions and a descending orbit (MDA, 2009).

5.2.3 TerraSAR-X Data

Images from TerraSAR-X were acquired with two stripmap HH polarization on 20th January and 11th October 2009 with a 3.3 m ground resolution. A further product of each stripmap VV and spotlight HH polarization was acquired (see Table 5.1). The stripmap products have a ground swath of 30 km (width) by 50 km (length) within the full performance incidence angle range of 20° to 45°. The spotlight HH product was acquired on 7th April 2009 with 1.5 m ground range resolution. TerraSAR-X products were generated by the DLR as Multi-look Ground-range Detected (MGD) products with Spatially Enhanced (SE) processing. The SAR products were ordered and obtained using the EOWB software on the DLR website.

5.2.4 Field Data Description and Organization

The aim of the fieldwork was to delineate a sufficient number of suitable water bodies to allow assessment of the accuracy of the SAR products. The field methodology was developed in the context of the research objectives and focused on mapping an appropriate number and sizes of water bodies. Secondary goals of the fieldwork were to determine the nature of land cover in the study area and to enable discussions with local people about the water bodies and flood impacts.

In this study, field data was collected at the same time as the SAR images were acquired. In order to delineate suitable water bodies in the study area covered by the SAR satellite sensors, the entire area was inspected either by driving or walking. Most water bodies within the study area are owned by local people who request clarification about the aims of the visit in order for them to allow the survey. This task proved difficult, requiring the assistance of an interpreter.

Surveying was undertaken using a dGPS in Real-Time Kinematic mode, which require a clear sky and may not work properly when surveying among dense trees. However, to overcome this problem and to avoid access limitation when walking along the edges of

some water bodies, a small local boat was used to carry the dGPS-Rover equipment in some cases (Figure 5.3).



Figure 5.3: Using a small local boat carrying dGPS-Rover equipment to avoid access limitation and steep areas.

5.2.4.1 GPS Equipment and Data Collection

The main equipment used during the fieldwork was a dGPS Magellan ProMark3-RTK. Ancillary equipments were clinometers for measuring the heights of trees and buildings surrounding the water body, and a measuring tape for measuring the size of the water body. In order to obtain sufficient information about each water body, a digital camera was used to capture photos of each water body and its surrounding area. Data sheets were used to collect the information.

The Magellan ProMark3-RTK positioning system has the capability to perform real-time survey with centimetre accuracy. One of the receivers was used as base station and the other as a rover (Figure 5.4). The ProMark3-RTK, using a GPS+SBAS RTK algorithm, ensures quick initialization with single frequency receivers and takes full advantage of maximum satellite coverage from the dual constellation. RTK implementation in ProMark3-RTK relies on the use of a base/rover system with its licence-free radio data link. The base station broadcasts corrections through a radio data link. Magellan FAST Survey software was used to perform the survey.



Figure 5.4: ProMark3-RTK dGPS equipment - Base station (A) and Rover (B).

5.2.4.2 ProMark3-RTK Base/Rover Configuration

The ProMark3 equipment required setting up and configuring as follows. First, the base was set up with the radio at a site that offers the best possible GPS reception conditions (i.e. where the antenna has a clear view of the sky in all directions) (Figure 5.5). The survey processing was then started by launching the “FAST Survey” software, included in the ProMark3 equipment. Each water body was acquired by creating a new job in “FAST Survey”.



Figure 5.5: Setting up the ProMark3 equipment (base and rover) during fieldwork in Bangladesh.

5.2.4.3 Water Body Information and Field Visits

Ground data was used both for geometric correction and for accuracy assessment of the classified images. The ground data was collected during a field visit to the study area within Bangladesh which is located between latitude $23^{\circ}57'20''$ and $23^{\circ}47'57''$ N and longitude $90^{\circ}11'00''$ and $90^{\circ}17'56''$ E (see Figure 5.6).

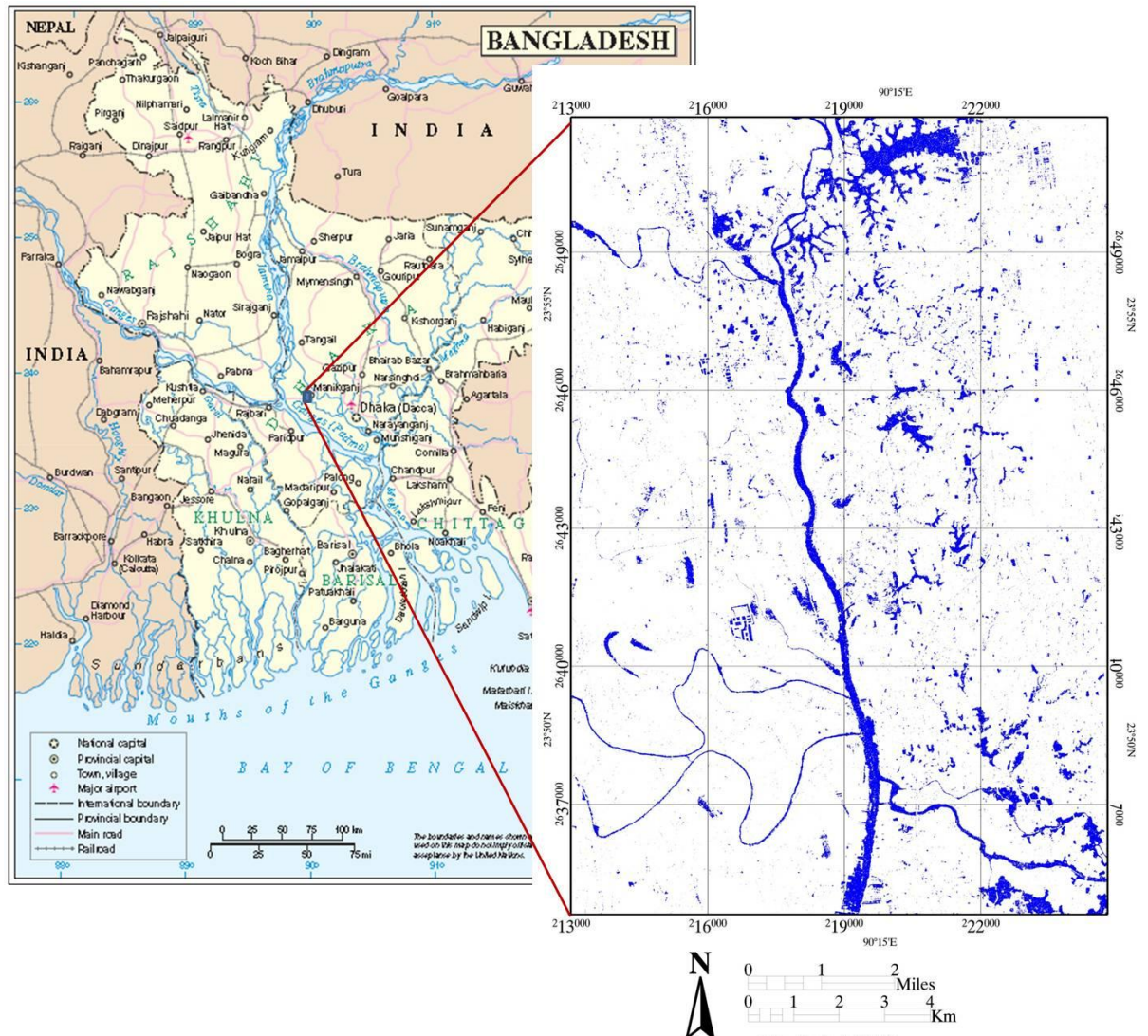


Figure 5.6: Study area extracted from Radarsat-2 HH image showing water bodies extracted from density slice analysis (Bangladesh map adapted from UNHCR, 2004).

A fieldwork campaign was carried out from 12th January to 4th February 2009 in the study area. The fieldwork timetable is shown in Table 5.2. Within the study area, a number of water bodies occur in different sizes and shapes. During field visit period 69 water bodies were delineated using dGPS equipment. Types and numbers of water bodies surveyed are shown in Table 5.3. Sampling methodology and field data preparation are outlined in section 6.2.1.

Table 5.2: Fieldwork timetable (from 13 January to 4 February 2009).

Test site	Number of WBs	Date	Duration/days	Comments
-	-	12 Jan	1	Arrival in Bangladesh
All test sites	-	13–15 Jan	3	Setup dGPS + sites visit
All test sites	69	16–29 Jan	14	Survey WBs
selective	All	30 Jan – 3	5	Revisit test sites +corrections +
-	-	4 Feb	1	Departure from Bangladesh
Total	69	-	24	-

Table 5.3: Overview of water body (WB) numbers and sizes surveyed during fieldwork in Bangladesh.

Type	Size	Number of WBs
Doba (ditch)	very small	14
Pukur (pond)	small	45
Dighi (reservoir)	medium	8
Beel (small lake)	large	2
Total		69

The focus of the fieldwork methodology was on:

- delineating the boundary of each water body by kinematic dGPS equipment, and
- collecting data about each water body in terms of the following aspects:
 - Photos from different angles by digital camera,
 - Size and shape by measuring tape,
 - The area percentage covered by water weeds, and
 - Surrounding features (i.e. trees, constructions and buildings) by measuring their distance from the boundary of the water body and their heights by using a clinometer.

A follow-up water body data sheet prepared for the fieldwork campaign can be seen in Appendix 5.1. An example of a water body captured by digital camera during fieldwork is shown in Figure 5.7.



Figure 5.7: A water body (scale: 14mx24m) photographed during fieldwork.

Fieldwork is essential to verify satellite data and to validate the ground truth. A predesigned field survey methodology for mapping water bodies was prepared before conducting the field visit. The collected field data of the water bodies from the test site ranged in size between 48 m² to 12,540 m². The focus of the fieldwork methodology was on the different shapes and sizes of water body selected, the percentage covered by water weeds and the surrounding features of each water body.

5.2.4.4 Surveying Water Bodies

The kinematic GPS was used to delineate the boundaries of each water body selected as samples for this study. To achieve this, the procedure involved walking along the boundary of each water body with the Rover to record the boundary of the water body at one metre intervals. For checking purposes, some data collected by ProMark3-RTK was converted to KML format and viewed in Google Earth in order to match its location.

5.3 Remote Sensing and GIS Software Used

Various software were used for data processing. Fieldwork data collected by GPS was processed in ArcGIS 9.2 software, whilst the SAR images were processed in three remote sensing packages (ERDAS Imagine 9.3, ENVI 4.7 and Definiens Professional 5.0).

5.3.1 ArcGIS

ArcGIS 9 is a set of tools for geographic analysis, data editing, data management, visualization and geoprocessing. ArcGIS 9 has three applications: ArcMap for map production and analysis, ArcCatalog for managing data and ArcToolbox for data conversion and analysis. In this study, mapping, visualization and editing tasks were conducted on the fieldwork data using ArcMap 9.2, while data management was performed through ArcCatalog 9.2. All GPS data was downloaded from the ProMark3-RTK equipment to ArcGIS 9.2 in shapefile format and then transformed from polyline to polygons.

5.3.2 ERDAS Imagine

Earth Resource Data Analysis System (ERDAS) Imagine software has tools for image mapping, visualization, enhancement, geocorrection and reprojection, including remote sensing analysis and spatial modelling. Imagine 9.3 has two types of data format access – direct access and import and export – for many raster data formats, including Radarsat-2 and TerraSAR-X products used in this study. For this study, pre-processing SAR data was conducted in Imagine 9.3 with basic image manipulation tools, reprojection and geocorrection processing.

5.3.3 ENVI

Another software used in processing the data was the Environment for Visualization Images (ENVI) software. This is an Interactive Data Language (IDL)-based image processing package that enables users to access and work with images in multiple formats and sources. ENVI 4.7 was used for texture analysis with texture filters of occurrence and co-occurrence along with unsupervised and supervised classifiers.

5.3.4 Definiens Professional (eCognition software)

The image classification approach in Definiens involves the use of an object-oriented technique through a segmentation step rather than the classification of single pixels. In

this study, the contextual classification phase was performed using Definiens 5.0 software (see section 5.5.3).

5.4 Data Preparation

The methodology of data preparation involved both SAR products and field data. SAR data pre-processing was performed using Erdas and Envi software while field dGPS data was processed within ArcGIS environment. A general flow chart of the data preparation methodology can be seen in Figure 5.8.

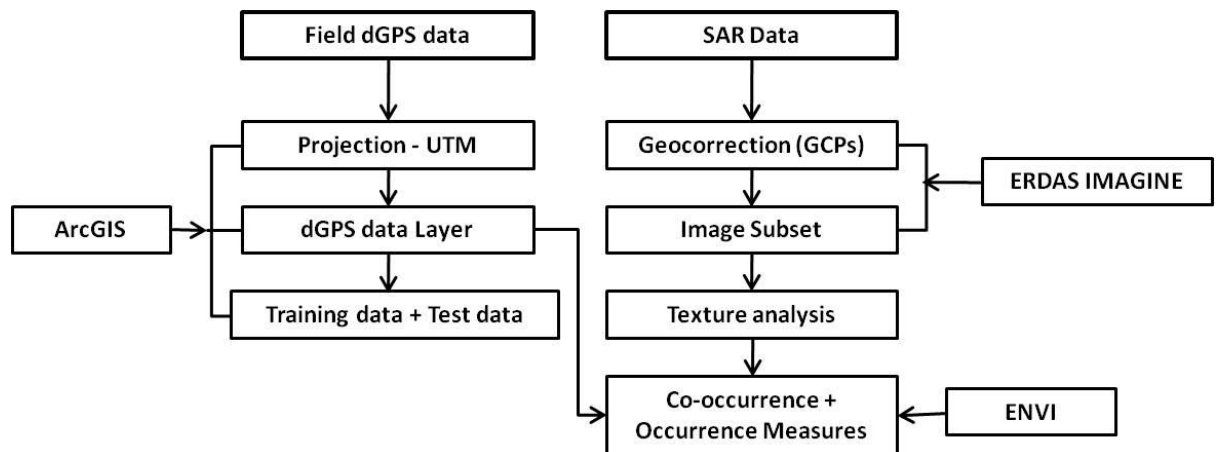


Figure 5.8: Methodology workflow of data preparation.

5.4.1 Data Pre-Processing

Data preparation was undertaken on the field data and SAR products acquired for the study area. The dGPS data was processed using ArcGIS software. The main pre-processing procedure for the SAR data included georeferencing, resampling, and geometric correction by extracting GCPs from the fieldwork data of dGPS. Several filters have been proposed in the literature to reduce speckle noise in SAR images (i.e. Mean, Median, Lee, Lee Sigma, Gamma-map, Forest, Local region). Speckle in RADAR imagery decreases the capability of identifying fine details within the image (Matgen et al., 2007). A number of the above filters were tested on SAR images to evaluate effectiveness in improving visual appearance. Analysis of the results reveals that the original images are richer in detail regarding water bodies and more useful for

visual interpretation. Accordingly, no speckle removal filters were applied during the pre-processing data phase.

Pre-processing techniques were applied to the raw data to generate a reliable image database. Geometric correction required the preparation of a map reference and the transformation of images to a specific map projection system. Satellite data may have different distortions and geometric errors. Thus, an understanding of the sensor geometric distortions of all satellite data in this study was required (Sandholt et al., 2001).

5.4.1.1 Georeferencing and Resampling

Image rectification and georeference transformation were applied to process the SAR products within ERDAS Imagine software. Images from the Radarsat-2 sensor were two ultrafine images in HH polarization and two ultrafine images in VV polarization. The TerraSAR-X images were two stripmap images in HH polarization, two stripmap images in VV polarization and one spotlight image in HH polarization.

SAR data were loaded into ERDAS Imagine 9.3 for data preparation and reprojection to Universal Transverse Mercator (UTM). The UTM was selected because of its simple x,y coordinates to image line, sample conversion (Logan et al., 1996). After setting the reprojection parameters within the ERDAS software, transformation was performed for resampling the SAR images.

5.4.1.2 Geocorrection by dGPS Ground Control Points

SAR products have some distortions due to satellite instability and the earth's rotation. This distortion requires geometric correction in order to increase the accuracy of the thematic maps generated from SAR images. A first-order polynomial transformation was therefore used to correct this SAR image distortion. A polynomial model is a traditional method for rectification particularly for flat terrain (Huang et al., 2004; Mather, 2004). Due to the lack of a reference map, GCPs were extracted from fieldwork dGPS data to be used as reference data for geocorrection processing. ERDAS Imagine 9.3 was chosen for rectification of all SAR products. Geometric correction included the

use of a polynomial model before establishing a set of GCPs by extracting the geographic position of each GCP from the fieldwork dGPS data. When a satisfactory number of GCPs have been chosen, total root mean square (RMS) errors were calculated, and resampling then had to be performed. An example of a GCP extracted from dGPS data on a water body as reference and from SAR-input data is shown in Figure 5.9.

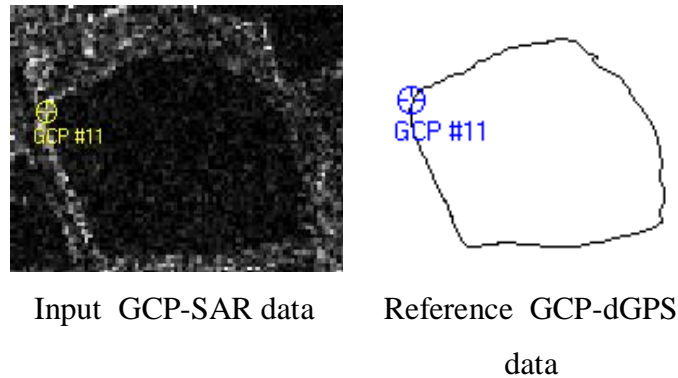


Figure 5.9: An example of a GCP extracted from a water body for both dGPS-reference and SAR-input data.

5.4.1.3 Geocorrection via Google Earth

The SAR data used for water body mapping was geocorrected based on the dGPS data. Google Earth imagery was used to identify and evaluate the apparent accuracy of the dGPS data for SAR image geocorrection by overlaying the imagery with the data derived in the field using the dGPS. A number of GCPs were extracted from Google Earth by selecting a specific geographic position that is visually recognizable in both Google Earth and the SAR image (i.e. a corner of a building). The first is treated as input data and the second as reference data within the ERDAS 9.3-GCP tool. The Google Earth geocorrection procedure and results are discussed in section 6.2.5.

5.4.2 Textural Analysis

Texture refers to the spatial distribution and variation of grey value in an image. Textural analysis is based on statistical methods, for which there are two approaches. One is structure analysis, which is based on texture distribution; the other is statistical analysis, which is the analysis of texture according to statistical features. In this study, statistical analysis has been applied (Li and Shenghui, 2003). The ability of texture analysis to distinguish water from other types of feature had to be examined, and so each texture measure was studied to determine to what extent water can be identified clearly. In other words, all texture measures were calculated to observe which works best. One method is Grey-level Co-occurrence Matrices (GLCM), which is a second-order texture measure because it considers the calculation of any two pixels with an interval in any direction (Li and Shenghui, 2003).

Several texture filters can be computed from the GLCM (Haralick et al., 1973) based on occurrence measures or co-occurrence measures, which can be implemented in ENVI. Eight texture filters based on co-occurrence measures have here been applied: mean, variance, homogeneity, contrast, dissimilarity, entropy, second moment and correlation. Occurrence has five measures: data range, mean, variance, entropy and skewness. Texture calculations for occurrence measures use the number of occurrences of each grey value within a specific processing window. Various window sizes were examined for this study in order to determine the best window size for distinguishing flood extent from other land features.

The co-occurrence measures calculate texture values by using a grey-tone spatial dependence matrix. The co-occurrence matrix shows the number of occurrences of the relationship between two specific neighbouring pixels. Co-occurrence is defined in four directions, 0° , 45° , 90° and 135° , for directional invariance in the calculation of the texture measure. The principle of shifting windows is used to create the co-occurrence matrix. The following example of matrices with a 3×3 window size and shift values of $X=1$, $Y=0$ (directions) shows how the co-occurrence texture filters measure the co-occurrence value. It demonstrates how the pixels in the 3×3 base window and the pixels in a 3×3 window shifted by one pixel are used to create the co-occurrence matrix (Figure 5.10).

4	5	3
3	5	6
6	4	3
Base Window		

3	5	6
5	6	3
4	6	3
Shift Window		

Gray Level

	3	4	5	6
3	0	0	2	1
4	2	0	0	0
5	2	0	0	2
6	1	1	0	0
	Co-occurrence Filters Matrices			

Figure 5.10: Co-occurrence matrix (Haralick et al., 1973).

In this study, the selection of appropriate texture measures is based on the investigation of all texture measures available in ENVI 4.7. First, each texture measure was statistically examined using reflectance profile measurements and a density slice technique, and then visually compared with the original image. According to the results of the analysis, the best texture measures were then selected.

5.4.2.1 Density Slicing

Density slicing is a digital interpretation method that can be used for individual brightness bands in a SAR image. Density slicing is carried out by dividing the range of digital numbers (DN) of the grey levels in a SAR image into intervals, then assigning each interval to a specific colour (Campbell, 2002). The ENVI software offers functions for density slice analysis. The density slice technique was applied here for water classification in the SAR images. The process involves assigning a colour to the water class data range and masking the remaining data range with another colour. Thus, results of the threshold of the water bodies are shown in one colour in order to improve analysis.

5.5 Water body mapping

Image classification is a process of classifying each individual pixel based on all existing information using the grey values and spatial information of an image. In this study, two common methods were used for classification: unsupervised and supervised (Lillesand et al., 2004). The unsupervised classification technique is an automatic process based on the numerical quantities of the input data and requires little user input apart from selection of an appropriate algorithm. It separates data into groups with clustering then classifies data into categories (classes). The user then has to make decisions on assigning a name to each class of data. During supervised classification, on the other hand, the user trains the image processing software by using training samples of known identity extracted from specified locations in the image to classify pixels of unknown identity. Figure 5.11 illustrates the general methodology flowchart for mapping flood.

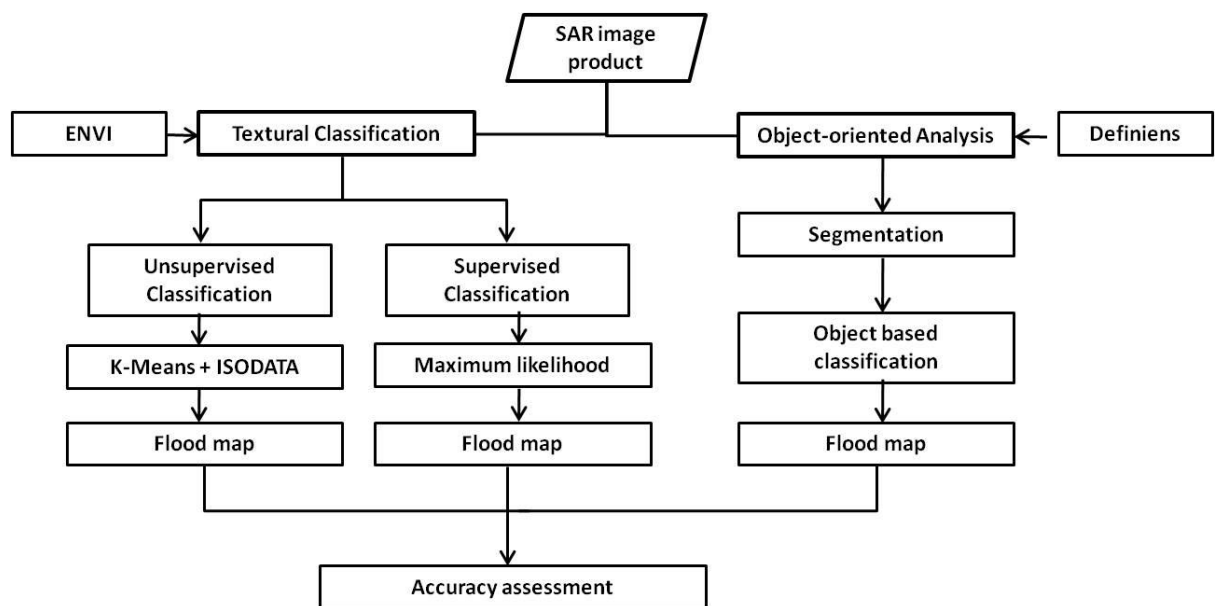


Figure 5.11: General methodology flowchart for mapping flood.

5.5.1 Unsupervised classification

The unsupervised classification methods were applied and tested in terms of their applicability for mapping water bodies (see section 7.3.1). In this type of classification no extensive prior knowledge of the area is required. The unsupervised classifiers examine the unknown pixels in an image and aggregate pixels with the same or similar values into a number of classes. Unsupervised classification involves two common techniques: K-Means and the Interactive Self Organization Data Analysis Technique (ISODATA). The K-Means unsupervised classifier is a process of analysis and relocates clusters in the data, by an iterative process until a sufficient level of spectral separability is achieved. The objective of the ISODATA is to calculate class means equally distributed within the data then cluster the remaining pixels in an iterative procedure using a minimum distance technique. In ISODATA, an image is segmented into unknown classes then the interpreter labels those classes, resulting in a classified image. Thus, the output of the unsupervised classification process is the identification of separable spectral classes. In order to associate output classes with land cover types, knowledge of the area along with the ground truth data is required.

5.5.2 Supervised classification

In order to perform supervised classification, samples of a known identity were selected to classify pixels of unknown identity, where samples of known identity lie on training sites. Then, statistical evaluation of the training samples was achieved using error matrix. A set of training data collected from fieldwork on water bodies was used to train the computer for the water class. The training data for the water body class were converted from shapefile to region of interest (ROI) in ENVI, while training samples for other classes were extracted from the texture images as ROI samples. Four mean classes were identified: water body, wet area, vegetation and built-up area/trees.

The process of supervised classification involves three main steps: training the system for land cover classes, undertaking classification and obtaining the output of the classified image. The process of training the system involves selecting areas as closed polygons in image that represent each unique class. To perform supervised classification on the SAR images, samples of known regions were selected to classify

pixels of unknown identity to be used as representative training data for each land cover class. Factors affecting classification performance include the use of a sufficient number of training samples and how well distributed these are in relation to the target class distribution. The second step in supervised classification involves undertaking the classification. The third stage comprises presenting the results of classification for images from both sensors, discussed in the following sections. The main purpose of image classification in this study is to distinguish water class from other land cover types rather than to classify different types of land cover features.

5.5.2.1 Maximum likelihood

The supervised classification algorithm used in this thesis is the maximum likelihood (ML) classifier, one of the most popular methods of classification (Bailly et al., 2007; Jensen, 2005; Lillesand et al., 2004; Richard, 1999; Weng, 2002). The ML classifier assigns each pixel to the class with the highest probability. This classification process involves calculating the discriminant functions for each pixel in the image (Figure 5.12) (Richards, 1999).

$$g_i(x) = \ln p(\omega_i) - \frac{1}{2} \left| \sum_i \right| - \frac{1}{2} (x - m_i)^t \sum_i^{-1} (x - m_i)$$

Figure 5.12: Discriminant functions calculated for each pixel

where:

i = class

x = n -dimensional data (where n is the number of bands)

$p(\omega_i)$ = probability that class ω_i occurs in the image and is assumed the same for all classes

$\left| \sum_i \right|$ = determinant of the covariance matrix of the data in class ω_i

\sum_i^{-1} = inverse matrix

m_i = mean vector.

5.5.3 Object-Oriented Image Processing

Object-based image processing has two approaches: segmentation and classification. Object-based image classification is not only based on spectral statistics but also on shape information and relationships to neighbouring objects. The classification of image objects is performed after segmentation. Definiens Professional 5.0 has tools that involve object-based processing. Classification within this software depends on a classification hierarchy file. The class hierarchy includes rules of classification for the image.

The contextual classification does not classify single pixels (i.e. supervised classification), but rather image objects or segments. The supervised classification depends on the spectral reflectance of pixels, while the contextual classification with its knowledge base includes other attributes (i.e. shape, texture, relation to neighbouring objects) additional to the spectral information provided in an image. The contextual classification approach first involves image data segmentation, which segments the image into a network of homogeneous image objects. The second stage of contextual classification is object-oriented, whereby land cover classes are related to the segmented image objects.

Contextual classification offers some advantages over traditional classification (*eCognition User Guide*, 2004):

- Image objects contain additional information for classification, such as shape, texture and the relational network of information.

- The segmentation process can separate adjacent objects that are textured or have noise.

- Segmentation can make classification work significantly faster, because it reduces the total number of elements needed to be handled for classification.

- Extracting homogeneous regions (segmentation) and then classifying them reduces salt-and-pepper noise in the classification results.

Definiens Professional software was used for contextual classification of the water bodies and other land cover types within the study area. The schematic diagram in Figure 5.13 shows the methodology flow chart of the contextual classification.

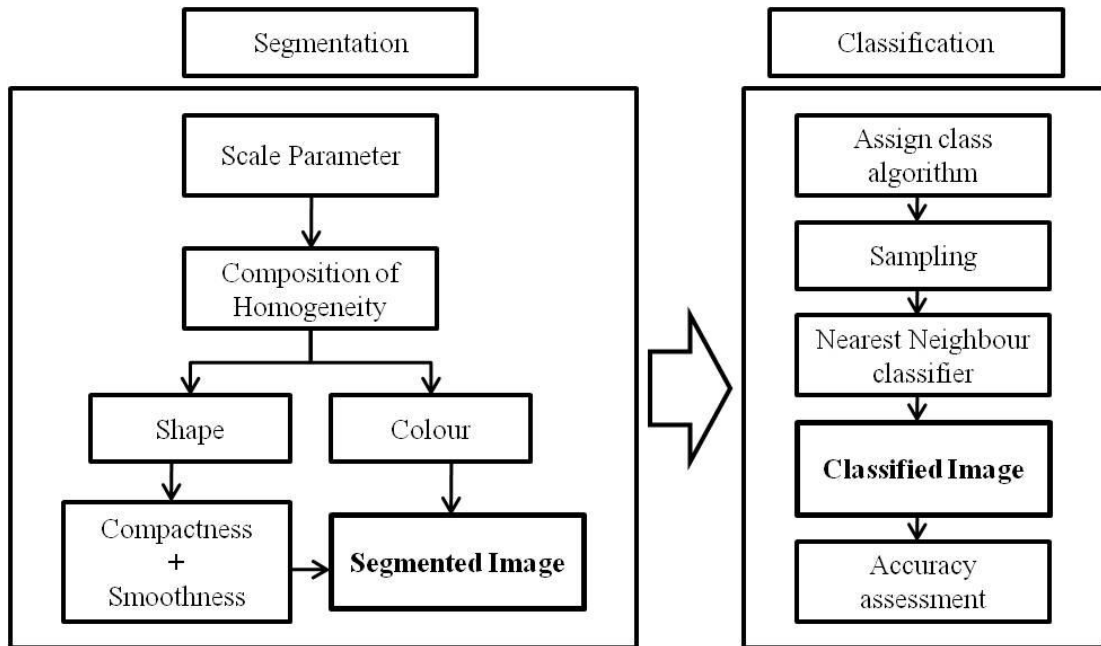


Figure 5.13: Methodology flow chart of the contextual classification used for segmentation and object-oriented classification.

5.6 Remote Sensing Data Accuracy Assessment

Accuracy assessment is an important factor in analysing SAR images (Banko, 1998). It is the identification and measurement of map error by comparing sites on a map against accurate reference data (Congalton, 2009). In other words, accuracy assessment is performed to assess map errors in order to identify the quality of remotely sensed information. Possible sources of error are shown in Figure 3.13.

5.6.1 Sampling Design for Mapping Accuracy Assessment

The thematic accuracy verification procedure of the classified maps produced in this study will be as follows:

- Identify the data to be verified and select the thematic criteria;
- Identify the number of sample regions to be evaluated;
- Use suitable sampling protocol and select samples;
- Conduct sampling procedure.

The design criteria (Stehman, 2009) taken into account when selecting the sampling design of this study includes using spatially well distributed samples, performing and analysing sampling design correctly, obtaining different size samples, and determining variability of sampling accuracy estimate to be small.

The (methodology) approach performed for accuracy assessment consists of three main components: response design, sample design, and analysis design (Stehman and Czaplewski, 1998).

5.6.1.1 Response Design

Response design deals with the protocols used to identify the reference data and to determine the agreement when comparing the map labels to reference labels (GOF-GOLD, 2010). In other words, it identifies the required rules for assigning each sample unit to a single land-cover class (Powell et al., 2004). The response design outlines the criteria used to validate the classified images obtained from Radarsat-2 and TerraSAR-X SAR sensors based on the land cover classes established, (see Figure 7.11) namely water, wetland, grassland, and builtup area/trees. A class description for reference data evaluation protocol is shown in Table 5.4. The total land area is approximately 204 km² is illustrated in Figure 4.3. The most important aspect in response design is to use reference data to allow accuracy assessment focusing on water bodies classification since this is one of the study objectives. The other land classes' precision is also important since the water bodies are distributed among them and therefore distinct discrimination between each class is needed.

Source of error can be reduced using appropriate protocols for validation and based on more precise data (Radoux et al., 2006). This protocol outlines two types of reference data used: 1) reference samples represent water class obtained from the dGPS; and 2) reference samples represent other classes mentioned above extracted from SAR imagery.

The reference data used for verifying the SAR image derived water class were obtained from field data collected using dGPS equipment. The number of water bodies or

(polygons) delineated and used as reference data was 25 in a total of 2950 pixels (see section 6.2.1). The dGPS equipment used is the Magellan ProMark3-RTK which has the ability to survey with centimetre accuracy (see section 5.2.4.1). The ground field visits also provided excellent knowledge regarding the nature of the study area (section 5.2.4) by collecting data by other methods such as photographing water bodies and the surrounding areas and gathering land cover type/land use information by using data sheets.

The validation samples of the land cover classes mentioned above were derived from the SAR imagery based largely on the several sources of information:

- Familiarity with the study area gained from the fieldwork campaign and communication with local people;
- The visual interpretation of the high resolution SAR images acquired from Radarsat-2 and TerraSAR-X;
- The visual interpretation of the very high resolution (1 m) TerraSAR-X spotlight image acquired where it covered most of the study area and contains details about land cover and land use;
- The visual interpretation of the high resolution (0.61 m) QuickBird-Google Earth imagery captured on January 2009 during the same month of SAR data acquisition.

The procedure used to collect reference data is based on the delineation of a block of pixels or polygons where all pixels in the polygon are used for the verification. All polygon samples related to each category or land cover type were grouped into a single layer (shapefile) and labelled. Each reference label is paired with the classified image class concerned in order to be used for the error matrix processing.

In order to ensure that samples extracted have sufficient separation since boundaries between classes are ambiguous (Powell et al., 2004), they were evaluated using Jeffries–Matusita separability measure to find out how significant the classes are spectrally separated. Values greater than 1.9 indicate that the ROI pairs have good separation, while values of less than 1 indicate very low separability (for more details see section 7.3.2.1).

Table 5.4: Class description for reference data evaluation protocol

Class	Criteria
Water	Open water surfaces such as ponds, lakes, and rivers
Wetland	very shallow water (i.e. irrigated fields)
Grassland	Short vegetation (i.e. grass and crop fields)
Builtup area/Trees	Settlements, industrial areas, and tall trees

5.6.1.2 Sample Design

The sampling design refers to the protocol followed to select the reference sample units (see section 3.9.1). The procedure focused on the selection of the best sample size for each land category. The study area is relatively small (17km×12 km) with various land cover/land use types distributed over the study area in different shapes and sizes. Therefore, the appropriate sampling strategy for this study area is random sampling. Verification polygon samples were selected randomly from each land cover type. Polygons are used where reference information is difficult to obtain (Radoux et al., 2006).

The classification of water class was validated by using the water-body dGPS dataset. The dGPS dataset was divided randomly into two layers independently, one was used for validation while the other was assigned for training. The validation data was used for assessing the maps produced from both the pixel-based and object-based classifications.

For consistency, the selection of the polygon samples was based on several rules in order to reduce bias that may be caused during sample extraction from each land cover type in SAR imagery:

- An in-depth visual interpretation is performed for the locations obtained from the SAR imagery using both the familiarity of the landscapes of the study area and the knowledge of the different types of the SAR backscatter;
- Cross-checking is implemented with the information acquired from the field visit;
- Cross-checking for the same locations is performed in QuickBird imagery;

- Select sample areas related to a land type that are most observable and distinguishable;
- Avoid ambiguous areas such as boundaries between different land classes.

The random sampling strategy adopted uses sufficient sample size for each land class that will allow for the assessment of the map accuracy. Table 5.5 listed the number of polygons and size of pixels used for each class.

Table 5.5: Specifications of validation data used

Class name	Number of polygons	Size in pixels
Water	25	2950
Wetland	20	1526
Grassland	20	3750
Builtup/Trees	20	2354

5.6.1.3 Analysis Design

The analysis procedure for assessing map accuracy was implemented automatically using post classification evaluation in the ENVI software package. Results were presented in an error matrix showing user accuracy, producer accuracy, overall accuracy, and Kappa coefficient of the classified maps (for more details about the error matrix see section 3.9.2).

Precision of estimates for the SAR classified imagery is an essential issue. Therefore efforts should be focused on minimizing any bias that may occur in any phase of the sampling design strategy (i.e. sampling, or size and distribution of reference data). This can be done by repeating the sampling procedure with different sample sizes and locations and also performing qualitative assessment and manual verification using information discussed in section 7.3.2.1.

The methodology (approach) used to develop sampling design for mapping accuracy assessment was implemented using field- and image-based validation methods. The verification quality of the produced maps is based largely on the dGPS water bodies

data obtained from the field visits and also on the interpretation of very high resolution SAR imagery (3m and 1m resolution) and QuickBird-Google Earth imagery. Moreover, the study area field visits strengthen the knowledge of the land cover/land use types and nature. All these factors support the methodology of the accuracy assessment and consequently lead to high quality validation data.

5.7 Conclusion

Data processing and evaluation comprised four steps. The first step focused on data preparation and pre-processing for all SAR products and dGPS fieldwork data. The second step involved data processing, which included texture analysis. The third step dealt with contextual analysis, while in the fourth step the accuracy of each classified image was assessed and SAR sensor images are compared.

The results of data pre-processing and data processing along with data evaluation are discussed in the following chapters.

Chapter Six:

DATA PREPARATION

6.1 Introduction

This chapter discusses the preparation of data used in this study, since the objective at this stage is to process SAR data and field data in order to prepare them for water body mapping and consequently validate the optimum image processing and spatial analysis methods for separating water bodies from other ground features. A number of techniques were used for the preparation of data from SAR products and dGPS data from the field. All data was reprojected, and SAR products were processed for geometric correction. A methodology for delineating flooded from non-flooded areas was developed based on radar backscatter texture analysis. Several texture filters were based on co-occurrence, and occurrence measures were compared and evaluated for image texture analysis of water body scenes in order to improve image classification accuracy. A number of software packages were used for the data processing. Field data was processed within ArcGIS software, while SAR data was processed in ERDAS Imagine and ENVI software. A comparison of geocorrection and texture analysis results was performed between images from the two sensors. The methodology of the data preparation is illustrated in Figure 6.1. A follow-up table prepared for SAR data processing is shown in Appendix 6.1.

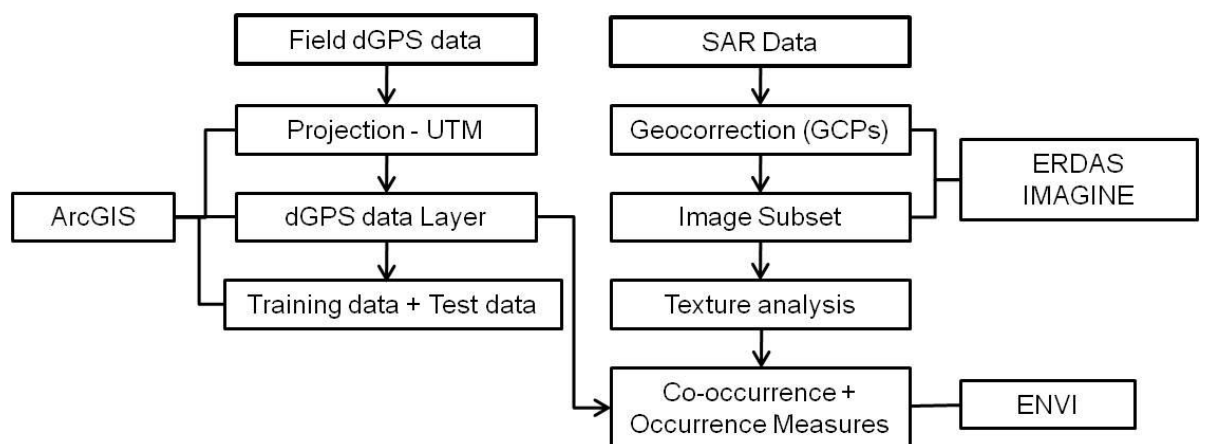


Figure 6.1: Methodology flow chart of data preparation.

6.2 Data Pre-Processing

6.2.1 Fieldwork Data

The general aim of the fieldwork survey was to delineate a sufficient number of suitable water bodies with dGPS to establish ground truth, and to assess the accuracy of the SAR images. In Chapter Five, the methodology of the fieldwork campaign was discussed, including the methods used for gathering the data on each water body such as delineating each water body's boundaries, measuring its size, taking photographs of it and identifying its surrounding features.

The data collected during fieldwork with dGPS-ProMark3-RTK for the study area was downloaded to a laptop, and a copy was saved in external data storage as a backup. Table 6.1 lists the number of water bodies collected during fieldwork according to type. In brackets in the table are local names in Bangladesh that often indicate each body type's size and how it is used. For example, dopa: human-made pit or ditch (approx. 25–400 m²), and most are located close to homesteads. Pukur: larger than dopa, at 150–1000 m². Dighi: a small tank or reservoir, of over 750 m². Beel: a saucer-shape depression, often an ox-bow lake, and vary in size from 1000 m² to several km² (Huda et al., 2010).

Table 6.1: Number of water bodies surveyed by dGPS during fieldwork according to water body type.

Ditch (Dopa)	Pond (Pukur)	Reservoir (Dighi)	Ox-bow lake (Beel)	Total
14	45	8	2	69

During delineation of the water bodies the ProMark3 polylines drew on points collected. The data collected was then converted to shapefile format within the ProMark3-RTK equipment. Back at the office in Durham University, fieldwork data was downloaded to ArcGIS 9.2 software for preparation and processing. All data was projected to a UTM-WGS84-Zone 46N coordinate system. Since dGPS data was in the form of polylines, as mentioned above, the data needed to be converted to polygons. The problem was that some polyline shapes had minor inconsistencies such as dangling nodes or unclosed

polylines. It is important to clean a polyline layer before converting polylines to polygons (more details on how to clean polylines can be found in *ArcGIS Desktop Help*). Subsequently, dGPS data was merged into one layer. In order to obtain training and test data for SAR image processing and evaluation, the dGPS data was divided randomly into two datasets and each merged into two separate layers (Table 6.2). One layer was chosen to be used as training data for the classification process, while the second was selected for test data for validation purposes, as shown in Figure 6.2.

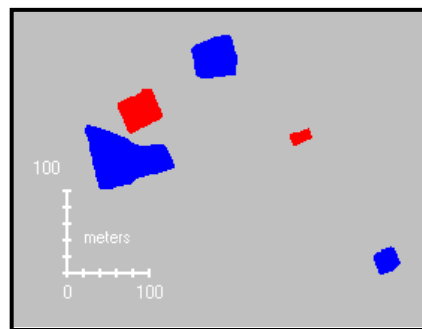


Figure 6.2: An example of training data (blue) and test data (red) extracted from dGPS data layers.

Table 6.2: Number and size of training and test data.

Data type	Number of water bodies	Size in pixels
Training	27	4,814
Test	25	2,950

When it was found that the dGPS data of delineated water bodies contained to some extent parts of the surrounding areas, a buffering step was then selected. This arose during the GPS surveys when attempting to avoid obstructions such as steep edges or a copse of trees adjacent to a water body. Each polygon of water body was buffered from inside 3 m from the edge, and the buffered areas were removed to ensure that each water body polygon included only areas of water, as demonstrated in Figure 6.3.

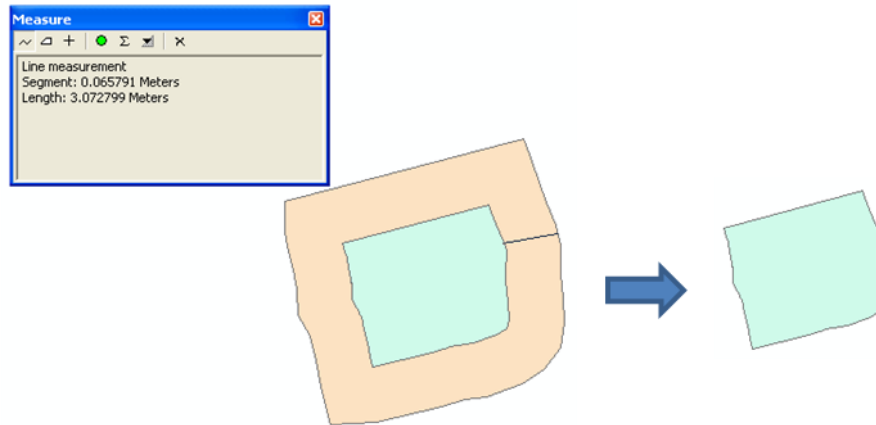


Figure 6.3: An example of the buffering process.

6.2.2 Rectification of SAR Data

Radarsat-2 products were generated by MacDonald, Dettwiler and Associates (MDA) in a format of SAR Georeferenced Fine (SGF) process with standard ground coordinate pixel dimensions (MDA, 2008). SGF georeferences are aligned with the satellite track but not on a map projection (more information about Radarsat-2 product specifications can be found in *Radarsat-2 Product Format Definition*, MDA, 14 March 2008). TerraSAR-X products were generated by the German Aerospace Centre (DLR) as Multi-look Ground-range Detected (MGD) products with Spatially Enhanced (SE) processing. MGD has reduced speckle and approximately square resolution cells on the ground. The image coordinates are oriented along the flight direction and the ground range. Geometric projection is in azimuth-ground range without terrain correction (more information about TerraSAR-X product specifications can be found in *TerraSAR-X Basic Product Specification Document*, DLR, 18 March 2009).

The ERDAS Imagine package version 9.3 was used in this study for Radarsat-2 and TerraSAR-X products for rectification, geometric correction and obtaining data subsets. All SAR images (see Chapter Four) were georeferenced to the same coordinate system to achieve compatibility when using them in different software packages and with the dGPS vector data. Rectification transforms a SAR image from its sensor coordinate grids into a map projection. All SAR products were geometrically rectified to a Universal Transverse Mercator (UTM) projection using the Data Preparation Tool

within the ERDAS Imagine software. The projection was carried out by loading the SAR data in a Tiff file to ERDAS Imagine 9.3 and reprojecting them to UTM - WGS 84 and to the UTM Zone of the study area – Bangladesh, which is North (46). Figure 6.4 shows the study area before and after projection for Radarsat-2 and TerraSAR-X SAR images in HH polarization, along with their histograms.

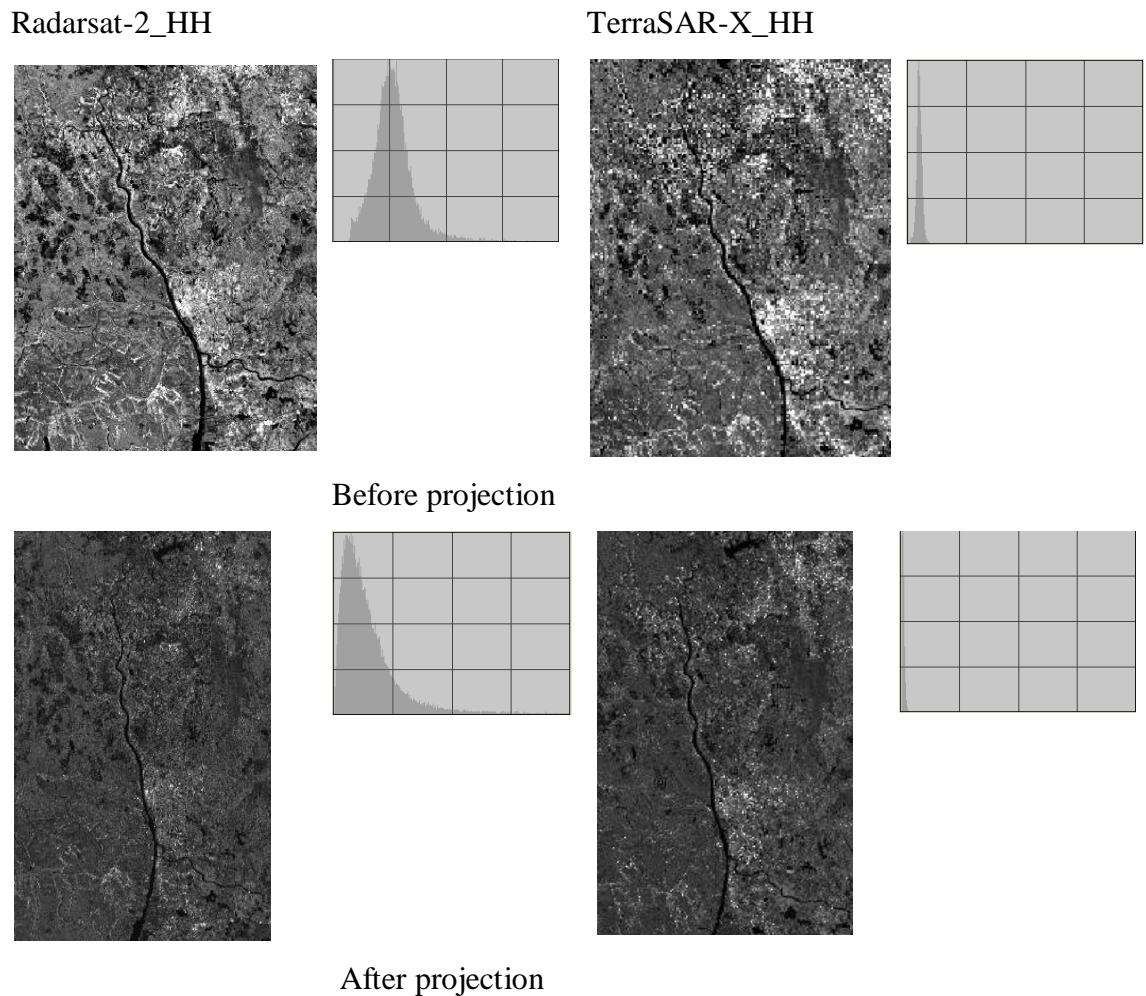


Figure 6.4: Radarsat-2 and TerraSAR-X in HH polarization with their histograms before and after projection.

6.2.3 Geometric Correction

The geocorrection process consists of two steps: rectification and resampling. Before SAR data processing such as texture analysis and classification, all SAR products have to be geometrically corrected. Geometric correction requires geographical features of known locations that are recognizable on images. Because of the lack of geocorrected images or registered maps for the study area, SAR images were rectified to a dGPS

vector file collected during the fieldwork. Ground control points (GCPs) can be used as a traditional method of resampling the pixel positions to the appropriate map projection.

When geocoding a SAR image, fewer GCPs are required than an optical image, particularly in flat terrain as in this study area.

6.2.4 Geocorrection by dGPS GCPs

All SAR images were processed for geometric correction by applying a polynomial model and extracting GCPs as reference points from the dGPS data. The polynomial geometric model uses polynomial coefficients to map between image spaces and is applicable to flat regions (Mather, 2004) as with the area under study. Within ERDAS Imagine software the polynomial geometric model was selected from the Set Geometric Model dialog box in order to undertake polynomial calculations. The first-order polynomial was selected because it is suitable for edge detection such as a water body's boundaries (Lira-Chavez, 1995). ERDAS Imagine software allows GCPs to be matched on the dGPS vector shape file to the SAR image that needs geocorrecting. Locating the GCPs extracted from dGPS polygons on the SAR images can be challenging since the process aims to match the dGPS polygon point to the same location of the point on a water body on the SAR image. The ground points were mainly corners or borders of the water bodies extracted from the dGPS shapefile data.

Reference points were collected via the GCP Tool dialog box, which allows the user to specify the source from which to collect the points. In all, 13 GCPs were extracted from the dGPS data and evenly distributed over the study area. These were then saved in a separate file in .gcc format to be loaded as reference points for the remaining SAR images. Figure 6.5 shows the locations of the GCPs and dGPS data distributed over the study area.

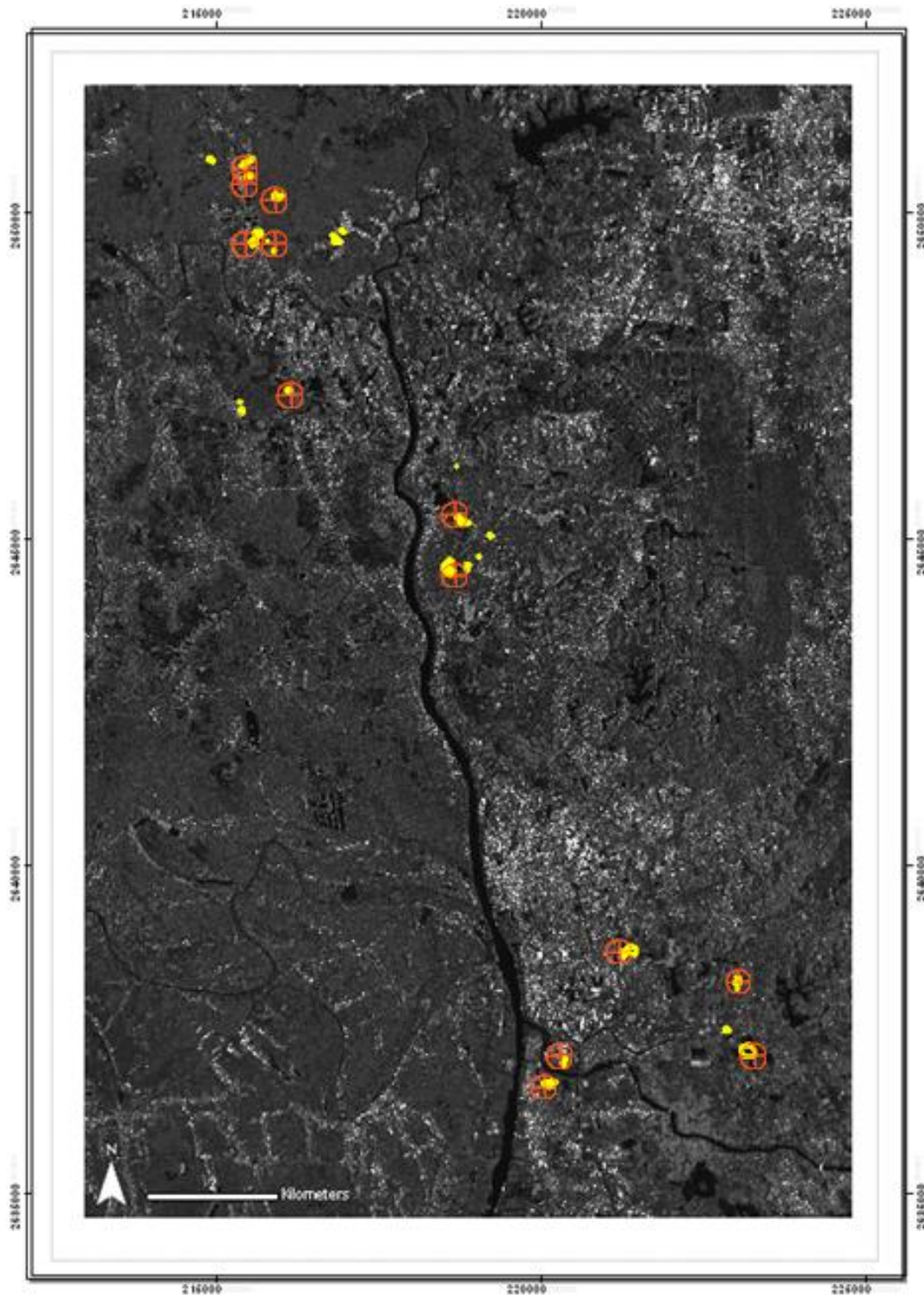


Figure 6.5: GCPs and dGPS data distributed over the study area.

The input points for each SAR image were selected by matching the locations of features (water body) on the SAR image viewer with those on the dGPS shapefile viewer. After selecting all locations over a SAR image that matched those on the dGPS shapefile viewer, the total root mean square (RMS) error was calculated. A comparison

between the data of the two sensors was performed during data pre-processing and geocorrection by control point error (Table 6.3).

Table 6.3: Comparison of control point error for Radarsat-2 and TerraSAR-X products based on dGPS data.

Images	X	Y	Total RMS error
Rsat2_HH	1.53	1.86	2.41
Rsat2_VV	1.71	1.60	2.34
TSX_HH	1.42	1.68	2.21
TSX_VV	1.55	1.31	2.03
TSX_spotlight_HH	1.51	1.69	2.27

The next step in the geocorrection process is to begin resampling using the nearest-neighbour method to create a rectified image. Since the grid of pixels in the SAR image does not match the grid for the dGPS data, the pixels are resampled so that the new data file values for the output file can be calculated. In the nearest-neighbour method the value of the closest pixel is assigned to the output pixel. In other words, the pixel in the new grid has the value of the closest pixel in the old grid. This is the most suitable method because it is appropriate for thematic files, can be applied before classification and it transfers original data values (*ERDAS Field Guide*, 2009).

Before geocorrecting the Radarsat-2 HH and TerraSAR-X HH products with GCPs, there was an approximate average of 46 m slight distortion to the west with the Radarsat-2 HH products. The TerraSAR-X HH products, however, were shifted only around 8 m on average, as shown in Figure 6.6, which illustrates this with an example of the shift extracted from the products of both sensors.

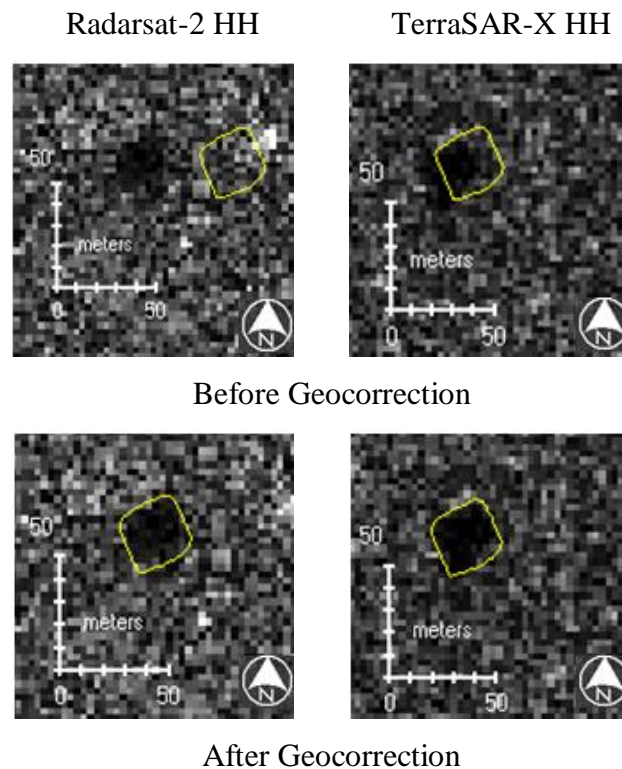


Figure 6.6: Radarsat-2 HH and TerraSAR-X HH products extracted before and after geocorrection (the dark area is a water body, while the yellow polygon is the dGPS data). Note Radarsat-2 has 46 m slight distortion while TerraSAR-X has only 8 m and both distortions are to the west.

6.2.5 Geocorrection via Google Earth

Google Earth satellite images, which are high resolution and regularly updated from satellites such as QuickBird, can be used for geocorrection by extracting GCPs directly from them for mapping process. In order to evaluate this in terms of geocorrection, 12 GCPs were extracted from Google Earth within the study area and used as reference data for the SAR image (Figure 6.7). Although only 12 GCPs have been used, a visual assessment shows that these are of good quality. This might be due to the advanced onboard navigation and positional technology of the new SAR systems, which has improved geometric accuracy and provided greater positional control (CSA, 2007, DLR, 2011b). Moreover, the study area is topographically flat and also relatively small in spatial size (17 km x 12 km). Therefore, the new generation of SAR imagery (i.e. Radarsat-2) can be geocorrected with several accurate GCPs or even without GCPs when using geometric models e.g. hybrid Toutin's model (Cheng and Toutin, 2010).

An example of results of the control point error is shown in Table 6.4. A visual comparison was performed to determine the accuracy of the Google Earth imagery available for the study area (Figure 6.8). It was found that there is only a small shift (approximately 3 m) in comparison with the dGPS data over the study area. The visual assessment (Figure 6.8) and the results of the total RMS error (Table 6.4) indicate good accuracy, and so the imagery may be used as reference data if up-to-date high-resolution imagery is available for the target area.

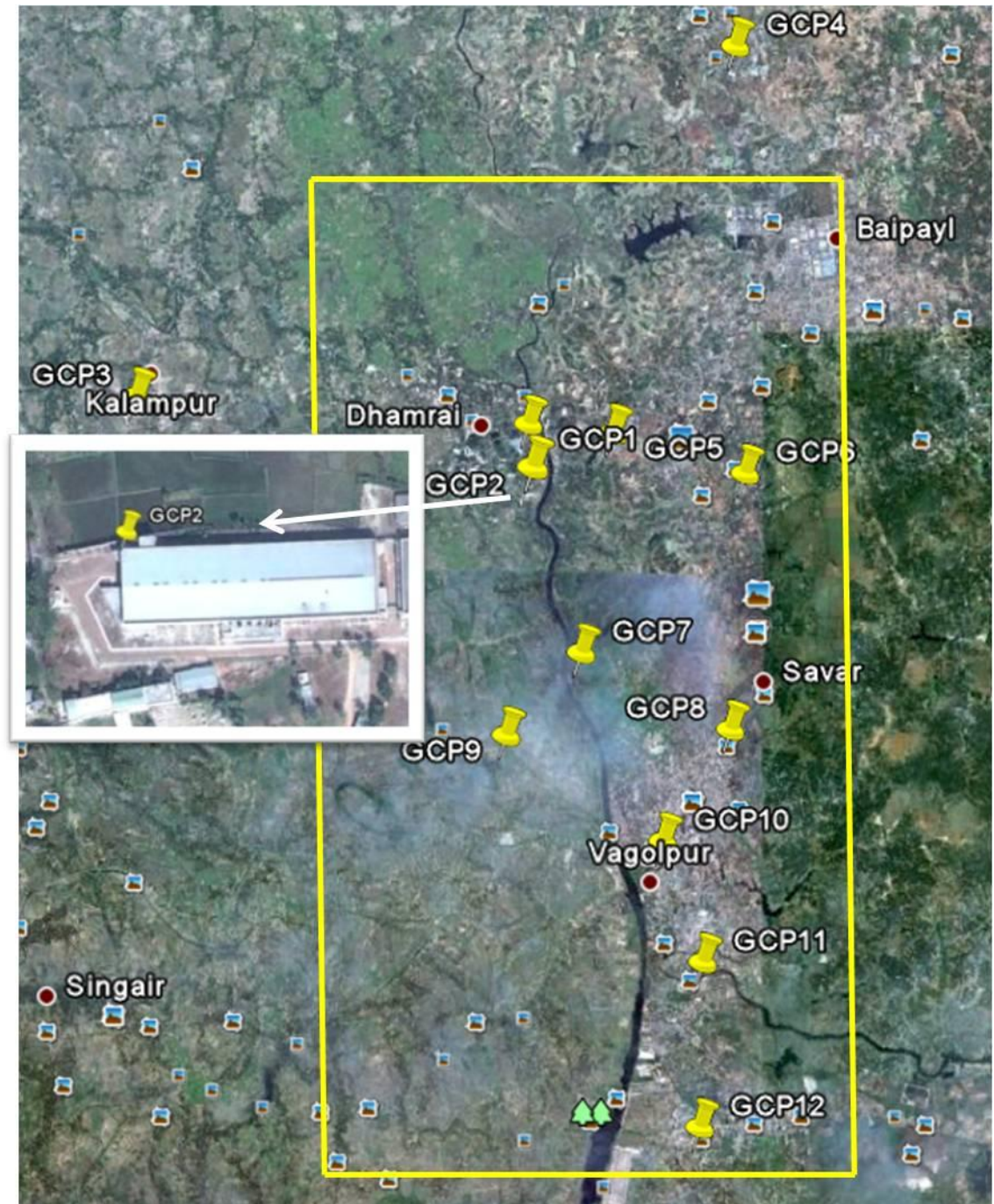


Figure 6.7: The spatial distribution of the GCPs over the study area (yellow rectangle) extracted from the Google Earth, 2010. An example of a GCP (inset in the white rectangle) shows its position in the corner of a building.

Table 6.4: An example of the total RMS error for Google Earth imagery.

Data	X	Y	Total RMS error
Google Earth	1.90	1.17	2.23

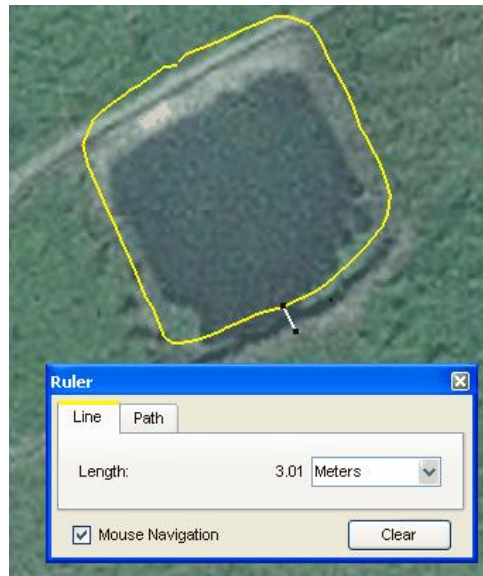


Figure 6.8: Distance of distortion of a water body extracted from Google Earth, 2010, overlaid with dGPS data. Note the distortion measured approximately 3 metres.

6.2.6 Spatial Subset for SAR Images

All SAR images were subjected to subsetting according to the size of the study area. This process was carried out within ERDAS Imagine software and using the Data Preparation Tool. Four corners of the study area (Figure 6.9) were specified for the output image.



Figure 6.9: Image subset corners.

6.3 SAR Image Texture Analysis

The principles of photo-interpretation can be used for radar imagery interpretation. In optical sensors, measurements for target detection are related to colour, chemical composition and temperature (ESA, 2008). However, the interpretation of radar images with respect to land surface parameters is based mainly on shape (the object's outline), tone (the average intensity of the grey level), object size and structure (the spatial arrangement of features throughout a region). Texture is a significant aspect in radar image interpretation; it consists of texture primitives (or elements) and can be described as fine, coarse, grained or smooth. Tone is based on pixel intensity properties in the elements, while structure represents the spatial relationship between elements.

Radar image texture can be considered at various levels. (1) Micro-texture (i.e. speckle) occurs from the radar system and not from the scene; it arises from the interference of random scatterers within each resolution cell, and this speckle noise appears as grains or is noise-like and should be avoided (CCRS, accessed 2010). (2) Meso-texture or scene texture is spatially organized average grey tone on the scale of several resolution cells. (3) Macro-texture or structure corresponds to variations in radar backscatter levels within boundaries of relative homogeneity over many resolution cells; an example of this level of image texture is a smooth texture of water body and an adjacent grass area with a rough texture. Smooth or specular surfaces such as calm water appear as dark tones, and diffuse surfaces such as vegetation appear as intermediate tones. In contrast, metallic surfaces and corner or double-bounce reflectances appear as very bright tones. Various types of land surface imaging with RADAR sensor and corresponding features captured by digital camera during the fieldwork are shown in Figure 6.10.

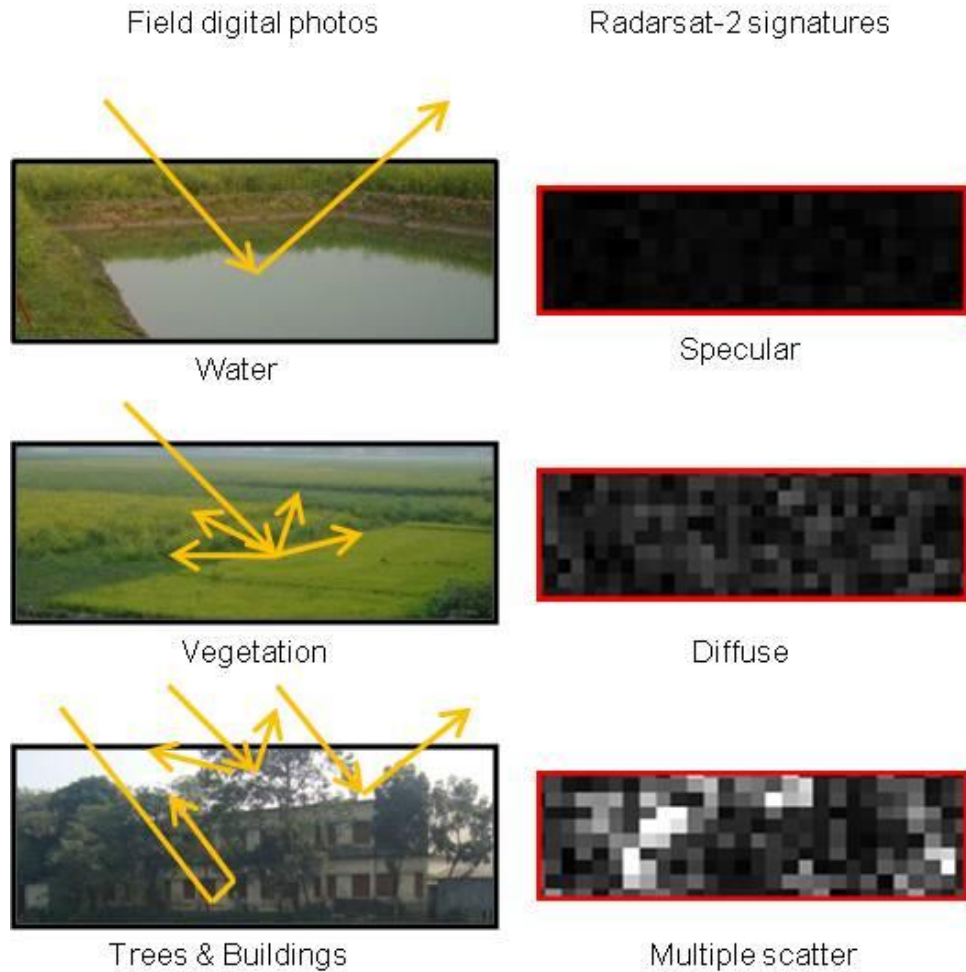


Figure 6.10: Imaging SAR sensor-HH polarization for various types of land cover compared to the field digital photos.

Texture analysis has been widely used for classification in remote sensing and can be assisted through the use of computer software such as texture features computed from grey-level co-occurrence matrices (GLCM). In other words, SAR image texture analysis computes texture features from the GLCM. The main aim of the texture analysis approach used in this study is to support the evaluation of SAR images in terms of their ability to discriminate water class from other features, and to improve the accuracy of image classification. Statistical analysis has been applied in this empirical study in order to analyse the texture features of SAR images on the basis of their statistical features. More details about the texture analysis approach can be found in Section 6.4.1.

There are two types of texture measures: first-order (occurrence) and second-order (co-occurrence). Texture filters based on co-occurrence and occurrence measures were

examined and analysed first individually and then with a combination of texture filters. In occurrence measures, texture calculations employ the number of occurrences of each level of grey tone within the processing window. Occurrence has five measures: *data range*, *mean*, *variance*, *entropy* and *skewness*. In co-occurrence measures, texture values are calculated using a grey-tone spatial dependence matrix. Eight texture filters based on co-occurrence measures were also examined: *mean*, *variance*, *homogeneity*, *contrast*, *dissimilarity*, *entropy*, *second moment* and *correlation*. A water body was selected for use as a test scene, shown in Figure 6.11, for texture analysis and for density slicing for the water and texture filters of the occurrence and co-occurrence measures.



Figure 6.11: A water body used as test scene showing surrounding features captured by digital camera during the fieldwork.

6.3.1 Speckle Noise Reduction

Analysis of the results of testing speckle removal filters such as Mean, Median, Lee, Lee Sigma, Gamma-map, Forest and Local region reveals that original SAR images show more detail concerning water bodies when no speckle filters are used. Therefore, no speckle removal filters were applied during this stage of the process. However, an enhancement filter consisting of convolution median filter from the ENVI software with a kernel size of 3 by 3 was applied to the texture filter images, but not to the raw SAR data. The median filter maintains edges larger than the kernel size when smoothing an image.

SAR images used in this study are not extensively contaminated with speckle, because of advanced technology developed for the latest SAR systems and advanced processing software. However, many small black noise spots remained over the images that may be misinterpreted, particularly when interpreting regions with very small water bodies. In the ENVI software, enhancing filters can be used for smoothing SAR images. After testing all the filters, the median filter was found to work the best, particularly with 3×3 windows.

Applying a 3×3 window size smooths land features without a loss of information on very small objects (i.e. very small water bodies). In contrast, a window size of 5×5 or above smooths the backscatter signal too much to enable very small water bodies to be distinguished from the background. Figure 6.12 illustrates that the 3×3 window size is more suitable for this study than the window size of 5×5. The occurrence measure of the *mean* texture filter showed that very small water bodies ($< 300 \text{ m}^2$) are better distinguished by the use of an enhanced median filter with a 3 by 3 window size.

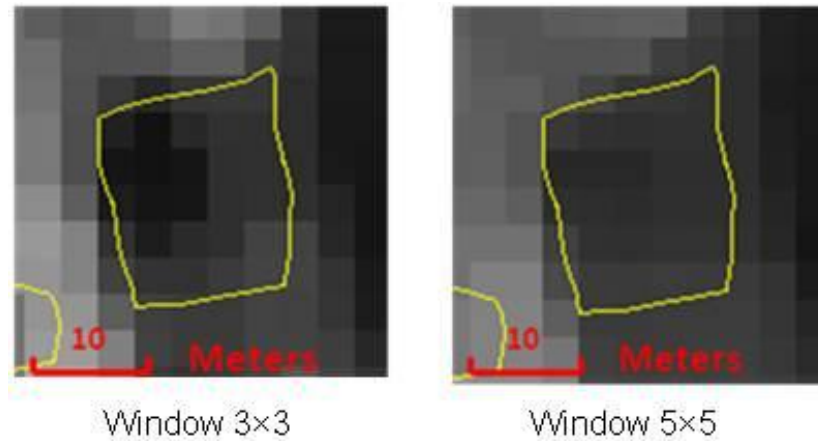


Figure 6.12: A comparison between 3×3 and 5×5 window sizes of enhanced median filter with an area of 238m² – note that the 5×5 window size shows less intensity.

6.3.2 Analysis of Texture Measures

Based on Haralick's texture measures principle, the ENVI occurrence and co-occurrence texture filters were exploited to create an image for each texture filter. Examining the various texture filters of occurrence and co-occurrence variables led to the selection of the most suitable texture measures for water identification. Each texture filter for the occurrence and co-occurrence measures was examined to decide which texture filter is better at discriminating water bodies from other land features.

The method of assessing the texture filters was based on three approaches. The first involved visual analysis based on the fact that the area of water for each water body is mostly represented as a solid colour. Visual analysis was performed to identify the ability of each texture filter to differentiate water bodies from other land features. This process involved overlaying the dGPS data over the output image for comparison purposes. The second approach was to examine each texture filter within the ENVI software and to determine its signature by using reflectance profile measurements. This was carried out to identify the most appropriate texture filter for SAR image classification. Each raw SAR image was associated with each texture filter when processing the reflectance measurements to create spectral profiles. In the third approach, a density slice technique was applied to the water class for each texture filter. In other words, to improve analysis of the texture filters, each image created from a

texture filter was compared to the reflectance profile and to the density slice of the water class for the same texture image.

Various pixel window sizes for occurrence and co-occurrence measures analysis were examined in order to select the appropriate window size for discriminating water bodies from other land features. From the results, it appears that processing pixel window size has a significant effect on separability between water and other land cover features. The 3×3 pixel windows used to drive the texture values for water regions were found to be the most suitable window size to determine particular water bodies with very small spatial size.

A pixel location within the texture of a water body was identified in a horizontal profile and then extracted from the products of both sensors in order to generate the reflectance profiles. The sample pixel was selected on the basis of the minimum reflectance and was then applied for all texture measures. Figure 6.13 shows the reflectance profiles of the original SAR images, which have zero values. For the Radarsat-2 image, the pixel's sample located at 215568.5 E, 2649542.5 N and is in sample 860 and line 799. The TerraSAR-X image sample pixel was extracted from sample 864 and line 807, located at 215580.5 E, 2649518.5 N.

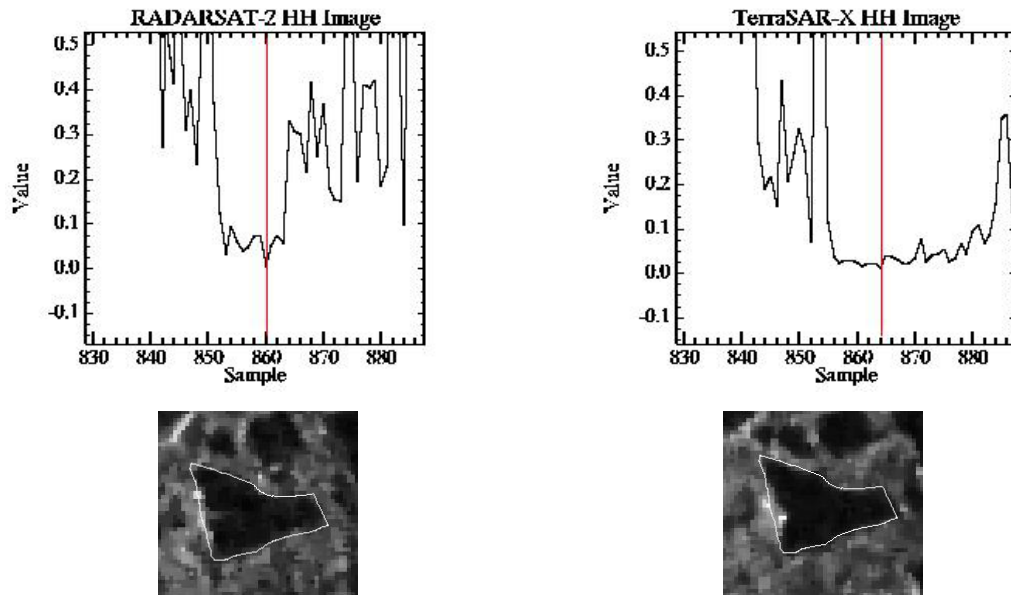


Figure 6.13: Reflectance profiles of specific sample pixel for the original SAR images with no texture filter, along with extracted texture scenes smoothed by median 3×3 window.

6.3.2.1 Occurrence Measures

Occurrence measures use the number of occurrences of each grey level within the processing window for the texture calculations. Radarsat-2 and TerraSAR-X products were analysed with occurrence measures. Assessment of occurrence measures was performed by testing each texture filter with Radarsat-2 HH and TerraSAR-X HH images, as shown in Figures 6.13, 6.14, 6.15, 6.16 and 6.17.

a. Data Range

Occurrence *data range* texture filter analysis is demonstrated in Figure 6.14 for the Radarsat-2 HH and TerraSAR-X images. The green spectrum represents the reflectance profile HH of the texture filter, while the white spectrum relates to the raw SAR image. This is because the *data range* texture feature characterizes the difference in values of pixels. Therefore, the results of the reflectance profiles in both SAR images suggest that the signatures are similar to those in the raw images. The water body in the texture scene has clear edge areas and can therefore be visually discriminated from surrounding features. The density slice water class of the *data range* filter for the Radarsat-2 image has texture values in the range 0.0–7000 in blue and 7000–65000 in yellow. With TerraSAR-X the values are in the range of 0.0–70 in blue and 70–15000 in yellow. The results of density slicing analysis for both SAR images indicate that the spatial size of the water body can also easily be identified. Consequently, the overall results of analysis show that the *data range* texture filter has the ability to distinguish the water feature and can therefore be used for image classification for both sensors.

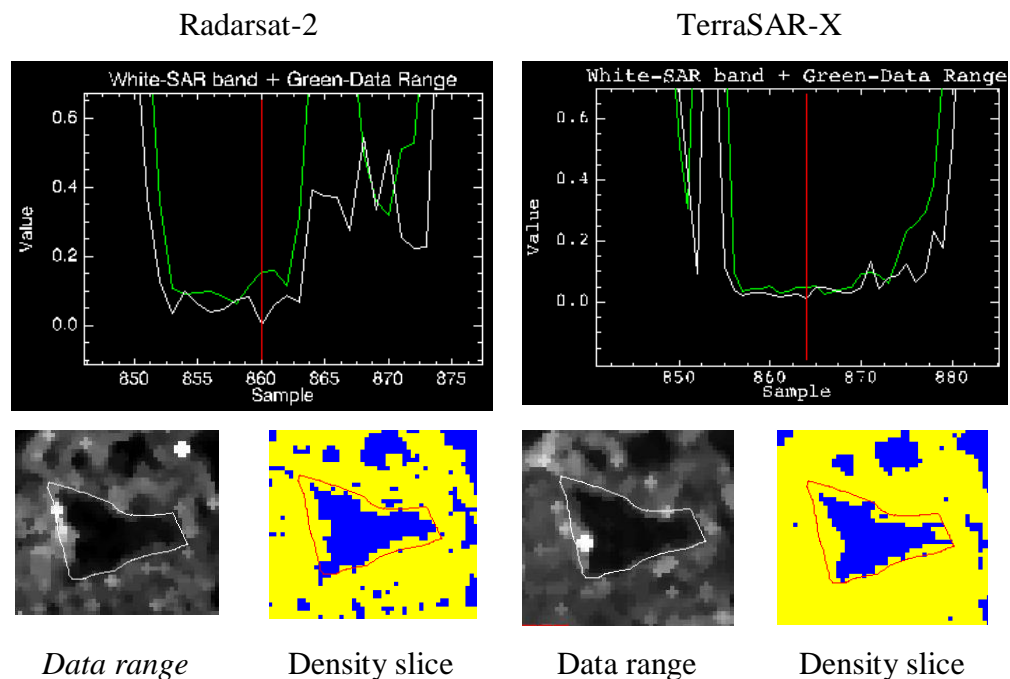


Figure 6.14: Reflectance profiles of occurrence *data range* texture measure with extracted texture scenes smoothed by median 3×3 window, along with density sliced scenes for Radarsat-2 and TerraSAR-X HH images.

b. Mean

The *mean* texture filter, with its high contrast between water regions and other features, clearly distinguishes the water body, as shown in Figure 6.15. When looking at the reflectance plot of the occurrence *mean* texture filter in the figure for the images from both sensors, we find that the spectra are very similar to the raw SAR spectra. This is because the *mean* texture image appears much like the raw SAR image demonstrated in Figure 6.13. When visually comparing the spatial sizes of the water body within the density slice image and the dGPS polygon, a great deal of similarity can be observed. Values of the density slice of the Radarsat-2 *mean*-filter image range from 0.0 to 5000 in blue and 5000 to 60000 in yellow, while the TerraSAR-X *mean*-filter image values range from 0.0 to 80 in blue and 80 to 4300 in yellow. This is because the water body in Figure 6.15 has a high level of spatial recognition alongside the spectra similarity. The occurrence *mean*-filter measure is therefore suitable for our image classification analysis.

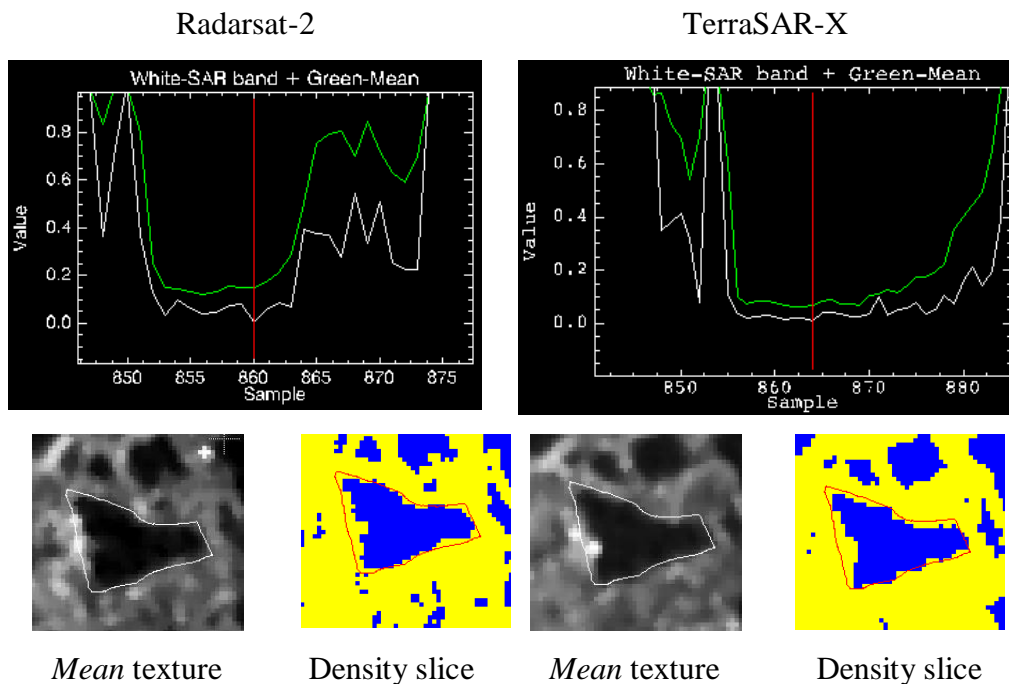


Figure 6.15: Reflectance profiles of occurrence *mean* texture measure for Radarsat-2 and TerraSAR-X HH images with extracted texture scenes smoothed by median 3×3 window, along with density slice scenes.

c. Variance

The occurrence *variance* texture filter was tested with images from both sensors and was found to work with the images from Radarsat-2 but not with those from TerraSAR-X, as illustrated in Figure 6.16. This is because there are no output texture signatures from the *variance* image of TerraSAR-X except for a solid black colour. Therefore, the spectrum appears similar to that of the raw image since the pixel's sample reflectance profile matches that of the raw image. Hence, the *variance* filter was excluded from the image classification process because of the absence of water texture signatures. The textural signatures of the *variance* filter for Radarsat-2 image are somewhat similar to the raw SAR image, as shown on the left of Figure 6.16. This can be observed in the reflectance plot and the density slice image, which has values ranging from 0.0 to 5000000 in blue and 5000000 to 850000000 in yellow. As a result, the *variance* texture filter was used only for Radarsat-2 image classification.

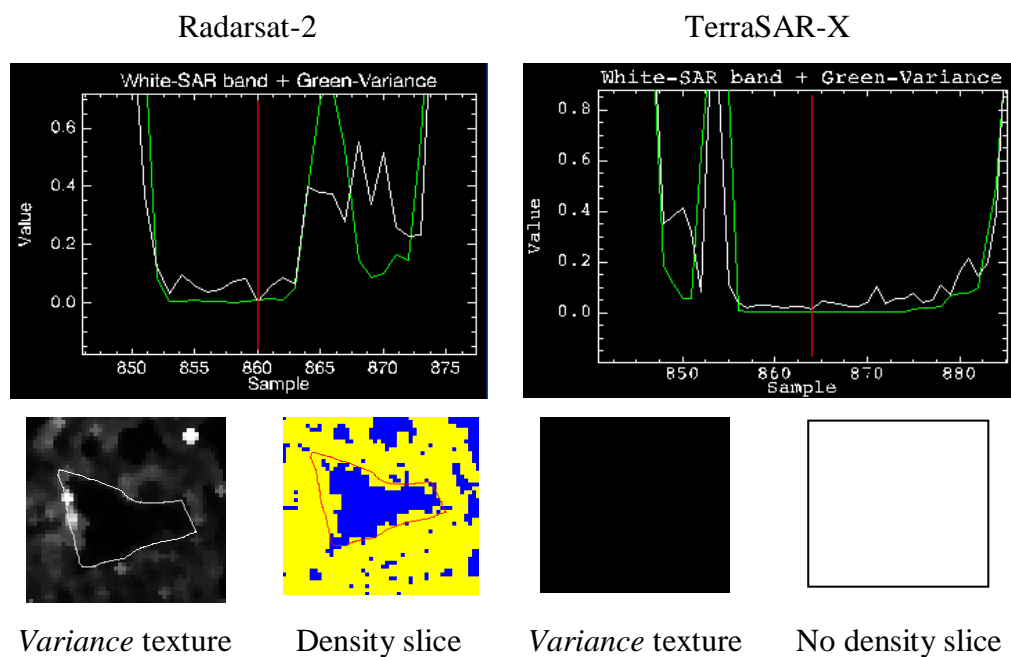


Figure 6.16: Reflectance profiles of occurrence *variance* texture measure with extracted texture scene for Radarsat-2 HH and TerraSAR-X images (note that there is no output texture signature for the TerraSAR-X image and accordingly no density slice).

d. Entropy

The occurrence *entropy* filter has no output of water signatures other than a solid white colour, and as a result there is no density slice for water class. This appears in images from both SAR sensors, but with some black spots in the TerraSAR-X image, as shown in Figure 6.17. This explains why the spectrum in the Radarsat-2 plot appears as a horizontal straight line with a high brightness value of 1.0 on the y axis, since the raw SAR image has a value of zero. The reflectance profile of the TerraSAR-X plot generally appears as a horizontal straight line but with very small differences in values of between 0.8 and 1.0, represented as black spots in the texture image. This is because the *entropy*-filter grey-tone values of water texture are almost 1.0 on the y axis. Therefore, water texture is shown by the very bright region, similar to the high-backscatter features. In this case *entropy* texture is not able to distinguish water from other features.

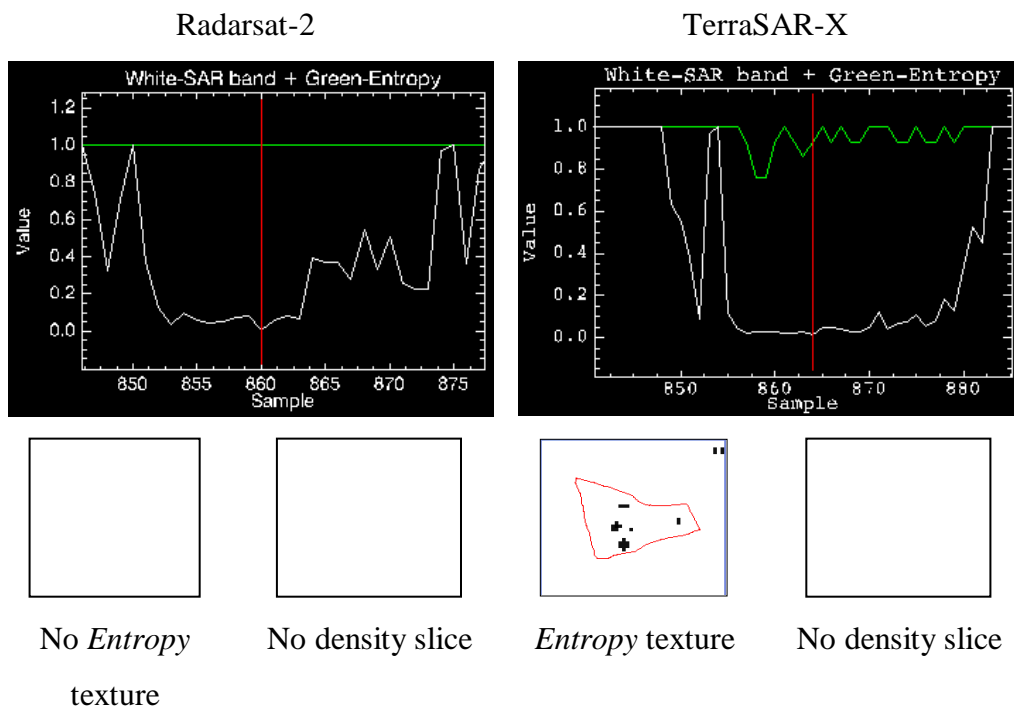


Figure 6.17: Reflectance profiles of occurrence *entropy* texture measure for Radarsat-2 HH and TerraSAR-X HH images (note that there is no output texture signature other than a solid white colour, and as a result there is no density slice).

e. Skewness

The *skewness* texture images for images from both sensors represent water texture in bright tones, unlike the other texture measures, as demonstrated in Figure 6.18. This is despite the texture of the water body having a less-homogeneous area. The reflectance profiles illustrate this unique texture, where values across the y axis range from -0.5 to 1.0 with the Radarsat-2 image, while they range from -0.1 to 1.0 with the TerraSAR-X image. It is difficult to identify the density slice value range for the *skewness* texture of the SAR images in this study. It was found that the density slice values with the Radarsat-2 texture image range from -0.0 to 0.0 , from which a density slice for water class could not be obtained. In *contrast*, density slice values of the TerraSAR-X texture image range from -0.0096 to 0.0001 in yellow and 0.0001 to 0.011 in blue. This is because the image of a water body with the *skewness*-filter has less *homogeneity* and *contrast* and is therefore not useful in discriminating water bodies from other land features.

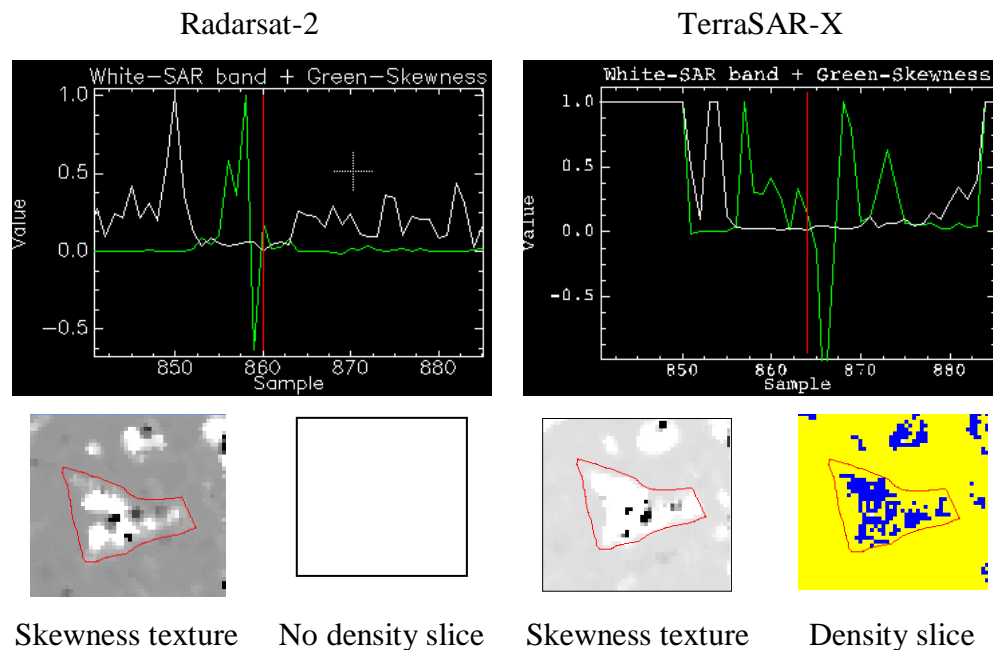


Figure 6.18: Reflectance profiles of occurrence *skewness* texture measure with extracted texture scenes for Radarsat-2 HH and TerraSAR-X images (note that there is no density slice range for the Radarsat-2 HH texture image since the value range is -0.00 to 0.00).

After analysing occurrence texture filters it was found that water class could best be distinguished by *data range*, *mean* and *variance* texture filters with the Radarsat-2

products. The best-performing texture measures for the TerraSAR-X products were *data range* and *mean*. These texture filters were selected because they correlated with one another.

6.3.2.2 Co-Occurrence Measures

The second-order grey-level co-occurrence matrix computes the relationship between pairs of pixels that consist of the reference and the neighbouring pixel. The eight co-occurrence measures available with the ENVI software were all used to determine which showed the best results. This type of texture filter requires the value of X and Y directions of the matrix calculation to be specified. In this study, various values of X and Y were examined for the SAR products, and it was found that altering these values has no effect on the results. Therefore, the default values of X=1 and Y=1 were used with the ENVI software.

No output results were produced when co-occurrence measures were applied to the products of the TerraSAR-X single polarization 16-bit unsigned data type used in this study. This might be due to the 16 bit restrictions. An attempt was made to examine co-occurrence measures with 8-bit unsigned compressed SAR products, although the texture filters worked with 8-bit or less pixel depth, but it was decided not to use the 8-bit image. However, the 16-bit data type has more pixel depth than the 8-bit data and provides sufficient dynamic range with greater ability to conserve the rich textural information of the SAR product, and so is suitable for this study. Therefore, the co-occurrence measures were applied to the Radarsat-2 products only.

a. Mean

The *mean* filter measures the average of the area values for each GLCM. Figure 6.19 shows that the co-occurrence *mean* texture filter provides results similar to those of the occurrence *mean* texture filter. This is because the co-occurrence *mean* filter averages the grey level in the local window. This principle can be observed in the intensity and the homogeneous area of the sample's water body shown at the bottom of the figure along with the density slice image. The ability of the co-occurrence *mean* filter to separate water regions from other land features means that it is among the best co-occurrence texture filters for classifying water bodies.

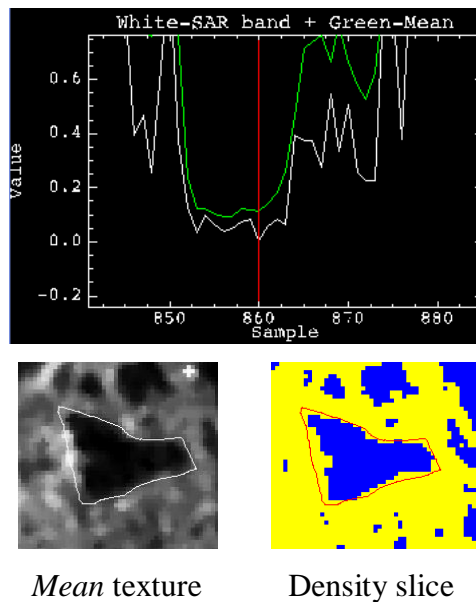


Figure 6.19: Reflectance profile of co-occurrence *mean* texture measure for the Radarsat-2 HH image with extracted texture scene, and density slice in the ranges 0.0–4 (blue) and 4.0–60 (yellow).

b. Variance

The co-occurrence *variance* texture filter calculates the dispersion of the difference between the pixels next to each other in the GLCM. Results of the co-occurrence variance-filter analysis are similar to those of the occurrence *variance* filter. The reflectance profile of the *variance* texture image shown in Figure 6.20 shows good similarity to the raw image reflectance. Moreover, the dGPS polygon spatial size of the water body when compared with both the texture image and the density slice image demonstrates that the *variance* filter is able to distinguish to a good level the water class from surrounding features.

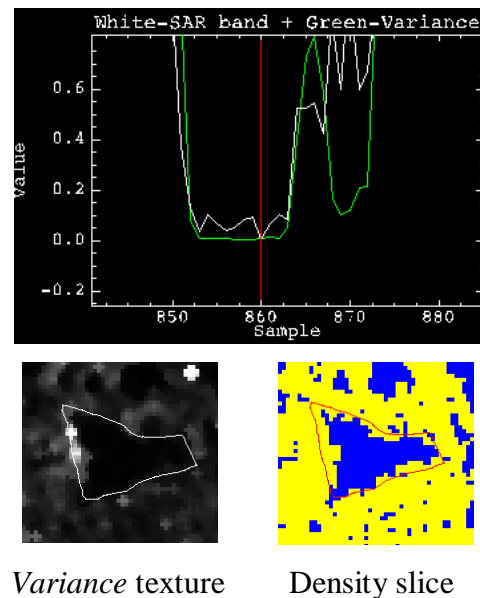


Figure 6.20: Reflectance profile of co-occurrence *variance* texture measure for the Radarsat-2 HH image with extracted texture scene, and density slice in the ranges 0.0–5 (blue) and 5–800 (yellow).

c. Homogeneity

The *homogeneity* texture filter measures the smoothness of an image and assigns high values to uniform areas. This is why water texture within the water body in Figure 6.21 is shown as grey levels of varying brightness. The *homogeneity* filter presents the specular surfaces in a bright tone, unlike the raw SAR image in which they are shown in dark tones. The difference in the brightness of the grey level is related to the difference in intensity between the pixels. Visually, the *homogeneity* texture filter appears to be suitable to some extent for water classification. However, the reflectance profile and the density slice results demonstrate that it performs less well than the *mean* and *variance* filters.

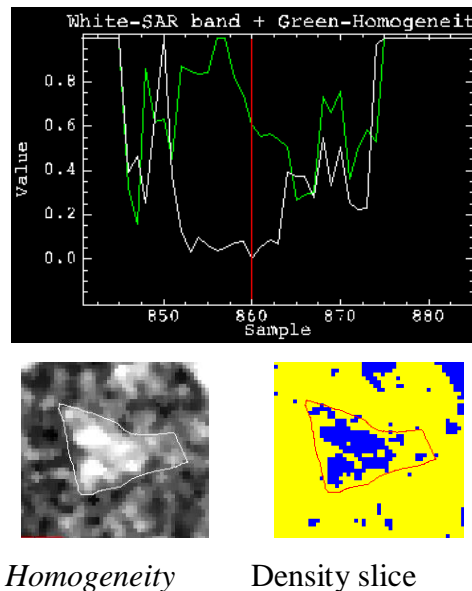


Figure 6.21: Reflectance profile of co-occurrence *homogeneity* texture measure for the Radarsat-2 HH image with extracted texture scene, and density slice in the ranges 0.0–0.4 (yellow) and 0.4–0.8 (blue).

d. Contrast

The *contrast* texture filter as illustrated in Figure 6.22 is the opposite of the *homogeneity* filter, where the *contrast* filter computes the amount of local variation in an image (Haralick et al., 1973). It resembles the *variance* texture filter but with small differences. This similarity can visually be identified when comparing the extent of the water body boundaries between *variance* and *contrast*. Therefore, the *contrast* variable appears to work well for water identification.

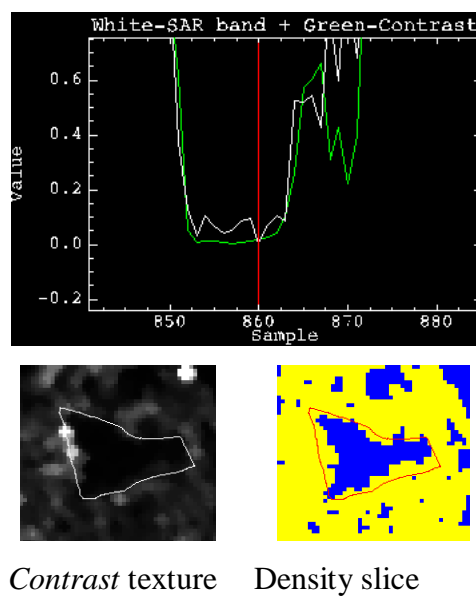


Figure 6.22: Reflectance profile of co-occurrence *contrast* texture measure for the Radarsat-2 HH image with extracted texture scene, and density slice in the ranges 0.0–10 (blue) and 10–1800 (yellow).

e. Dissimilarity

The *dissimilarity* texture filter calculates the difference between pixels of the co-occurrence matrix and thus will assign high values to local regions with greater contrast. The *dissimilarity* filter is comparable to the *contrast* filter but shows greater contrast between water and other land cover, as shown in Figure 6.23. The high contrast of the *dissimilarity* filter results in better discrimination of water bodies but it displays less-homogeneous intensities within the water body. Further analysis will be carried out during texture image classification (see Chapter Seven) in order to decide which of these two filters performs better.

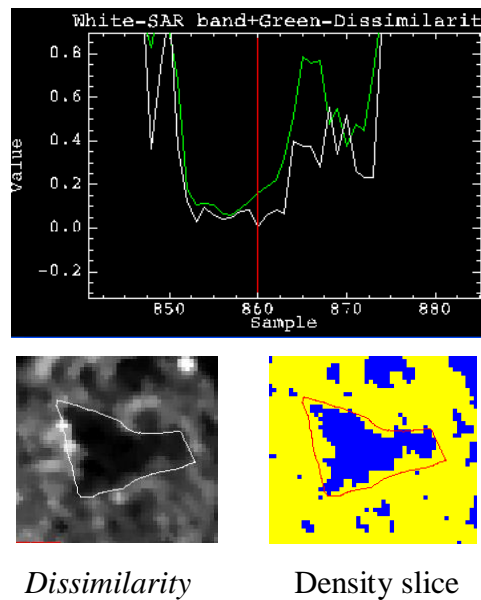


Figure 6.23: Reflectance profile of co-occurrence *dissimilarity* texture measure filter for the Radarsat-2 HH image with extracted texture scene, and density slice in the ranges 0.0–2.5 (blue) and 2.5–39 (yellow).

f. Entropy

The co-occurrence *entropy* texture filter measures the disorder of an image and assigns high values when the values of the pixels of the GLCM are high. In Figure 6.24 it can be seen that the reflectance profile of the *entropy* filter (in green) is very different from that of the raw SAR image, which is high and close to 1.0. Most of the texture image therefore appears as a high level of brightness. In this case, the *entropy* filter is not useful in this study for image classification.

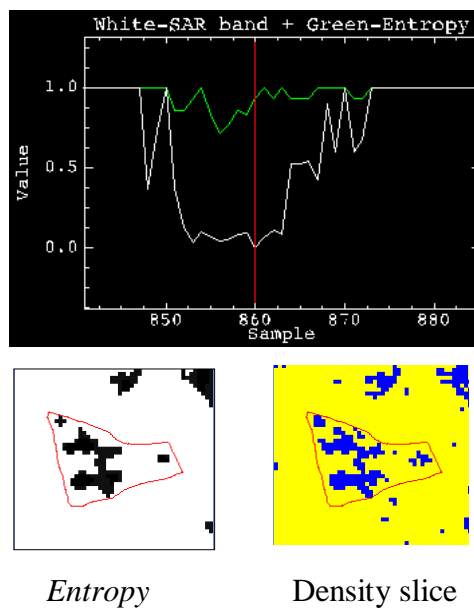


Figure 6.24: Reflectance profile of co-occurrence *entropy* texture measure for the Radarsat-2 HH image with extracted texture scene, and density slice in the ranges 0.0–2 (blue) and 2–2.2 (yellow).

g. Second moment

The second moment filter measures the local *homogeneity* of the image and assigns it high values (Haralick et al., 1973). The texture image of the water body in Figure 6.25 represents some parts of the water body but in a bright white tone. The reflectance profile and the density slice image indicate that the second-moment filter is not suitable for distinguishing small water bodies.

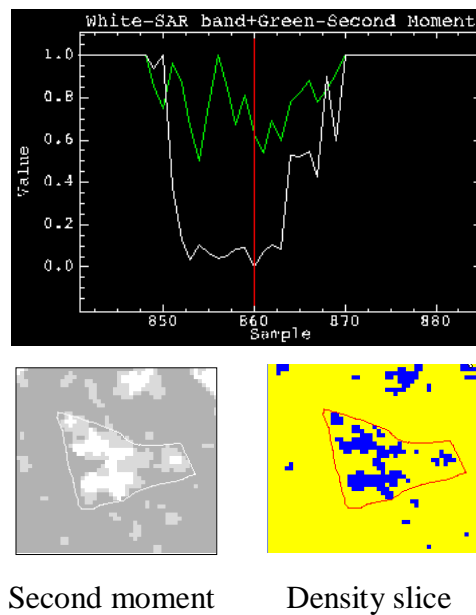


Figure 6.25: Reflectance profile of co-occurrence second-moment texture measure filter for the Radarsat-2 HH image with extracted texture scene, and density slice in the ranges 0.0– 0.14 (yellow) and 0.14–0.4 (blue).

h. Correlation

The *correlation* filter measures the linear dependency of the grey level and assigns high values to their areas (Haralick et al., 1973). The spectral profile of the *correlation* filter assigns to the sample pixel very high values of around 35.0, as illustrated in Figure 6.26. The density slice image and the texture image of the *correlation* filter cannot provide specific statistical information for the water signatures.

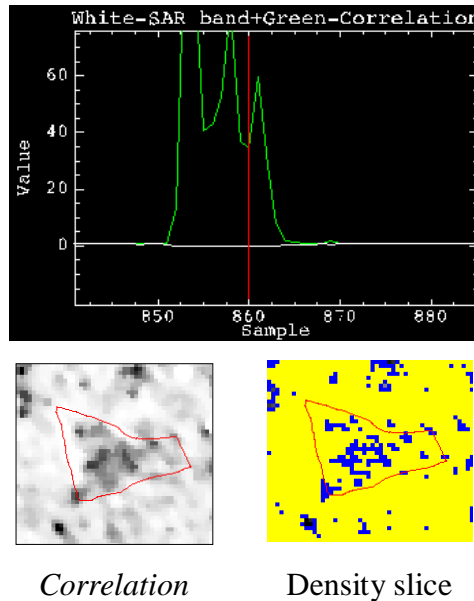


Figure 6.26: Reflectance profile of co-occurrence *correlation* texture measure for the Radarsat-2 HH image with extracted texture scene, and density slice in the ranges -25 to -7 (blue) and -7 to 4 (yellow).

6.3.3 Texture Analysis with a Combination of Texture Measures

The next step in the texture assessment was to compute a combination of texture measures selected from the recommended texture filters. The process of combining texture filters was important for applying it to image classification and for identifying and evaluating its advantages in water detection. Three texture filters of occurrence measures of *data range*, *mean* and *variance* were applied to the Radarsat-2 images, while the two texture measures of *data range* and *mean* were used for the TerraSAR-X images. Occurrence texture analysis was undertaken for both single polarizations HH and VV for both sensors, as shown in Figure 6.27. A dGPS polygon was overlaid over the test water body for comparison of the spatial size of the water body. A combination

of co-occurrence measures of *mean*, *variance* and *contrast* was also used. Figure 6.28 shows the results of texture analysis with the combined three co-occurrence measures for Radarsat-2 HH and VV polarizations.

A visual comparison was performed first between HH and VV single polarizations for each SAR sensor. The results show that there is little difference between HH and VV polarizations in detecting small water bodies. A second comparison was implemented between the two sensors for HH and VV polarizations (Figure 6.27). Products of both SAR sensors show similarity when comparing images to the dGPS polygon. A third comparison was undertaken between occurrence and co-occurrence. Co-occurrence selected measures were tested and results compared to the occurrence measures to identify the advantages of each. The results of this evaluation show that there are almost no differences between occurrence and co-occurrence measures with regard to the detection of water bodies (Figure 6.29). Analysis of density slicing was also carried out, with the same results (Figure 6.30).

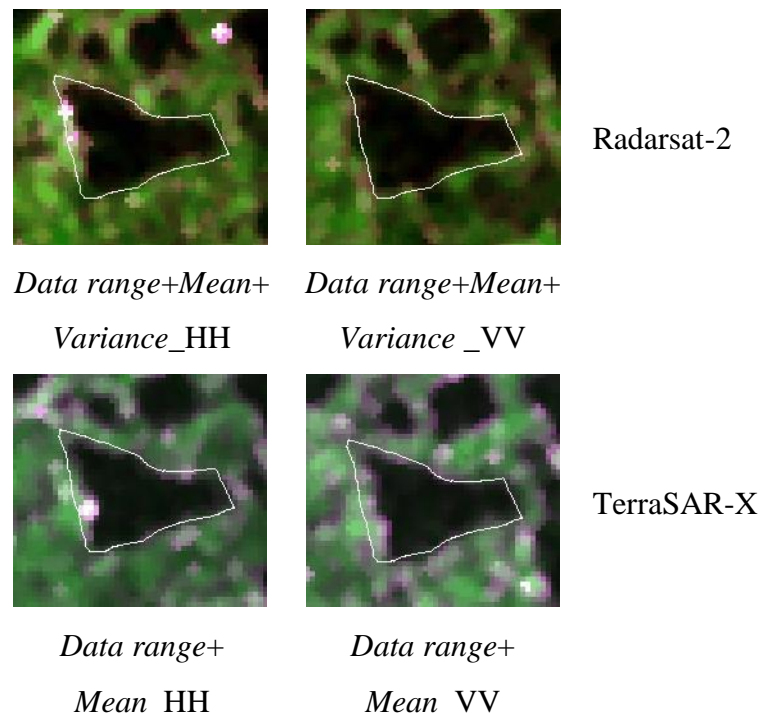


Figure 6.27: Texture analysis for products of both sensors with HH and VV polarizations with a combination of occurrence measures.

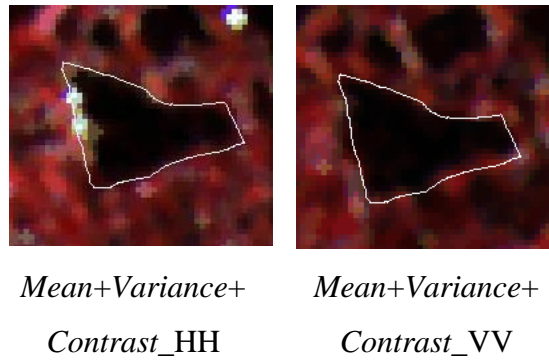


Figure 6.28: Texture analysis for products of Radarsat-2 HH and VV polarizations with a combination of co-occurrence measures.

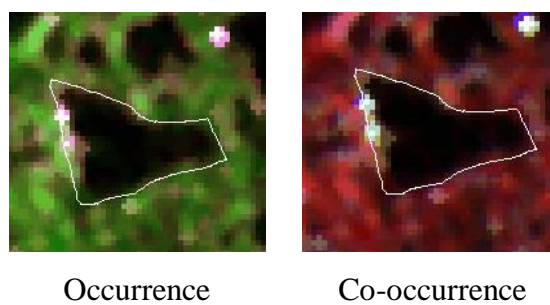


Figure 6.29: Comparison between occurrence and co-occurrence combined texture measures with Radarsat-2 HH.

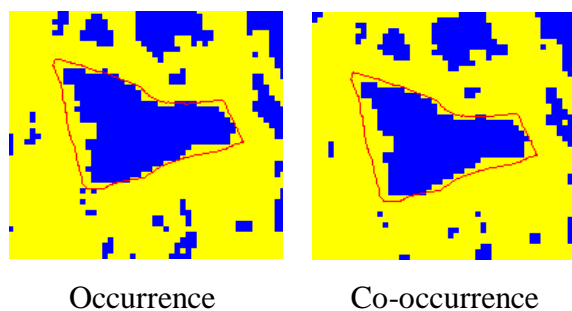


Figure 6.30: Comparison between occurrence and co-occurrence *mean* texture measure using density slice technique with Radarsat-2 HH.

6.4 Conclusion

This chapter has described the preparation of data used in this study. The dGPS field data will be used as training and validation data for flood classification images. Pre-processing SAR images in terms of geometric correction and obtaining subset data is an essential stage for ensuring consistency when using the images for analysis and image classification. Analysis of occurrence and co-occurrence measures was performed to determine which texture filters perform well in water signature discrimination. The performance results for each texture filter varied. However, the best texture filters for Radarsat-2 products were *data range*, *mean* and *variance*, while for TerraSAR-2 products, only the *data range* and *mean* texture filters showed good performance.

The co-occurrence measures were applied only to Radarsat-2 products, because no output results were obtained when using them with TerraSAR-X products. Attempts were made to process it with an 8-bit image, and results showed that this worked better. Nevertheless, because of the low depth of the 8-bit image, this step was consequently omitted, as discussed in section 6.3.2.2. The co-occurrence texture measures of *mean*, *variance*, *dissimilarity* and *contrast* were found to show the best performance in calculating water texture regions for Radarsat-2.

Results of applying co-occurrence measures as discussed previously demonstrate that there is no significant difference when comparing them to the occurrence texture measures. Results of texture analysis and evaluation of occurrence and co-occurrence texture measures will support the analysis of SAR products along with generating and evaluating water body mapping in the following chapter. The texture variables that showed better identification of water bodies in this analysis and are therefore recommended are the following:

- I. Occurrence variables of *data range*, *mean* and *variance* for Radarsat-2 products, but only those of *data range* and *mean* for TerraSAR-X products.
- II. Co-occurrence variables of *mean*, *variance*, *dissimilarity* and *contrast* for Radarsat-2 products only.

Chapter Seven:

WATER BODY MAPPING

7.1 Introduction

This chapter provides an analysis of TerraSAR-X and Radarsat-2 SAR image products and image processing and spatial analysis techniques to discriminate between water bodies and other land cover features. Image processing of TerraSAR-X and Radarsat-2 images include a range of techniques ranging from simple density slicing of backscatter signal to use of backscatter texture variables, polarimetric information and contextual classification.

The image classification methodology used both per-pixel and object-oriented classification approaches in order to address the intrinsic difficulties of separating water bodies from other surfaces with similar backscatter properties. A workflow was developed to ensure that all SAR images were processed to a similar level to allow objective accuracy assessment with ground truth data and cross comparison among the available image products. Figure 7.1 illustrates the proposed methodology flow chart of water body mapping.

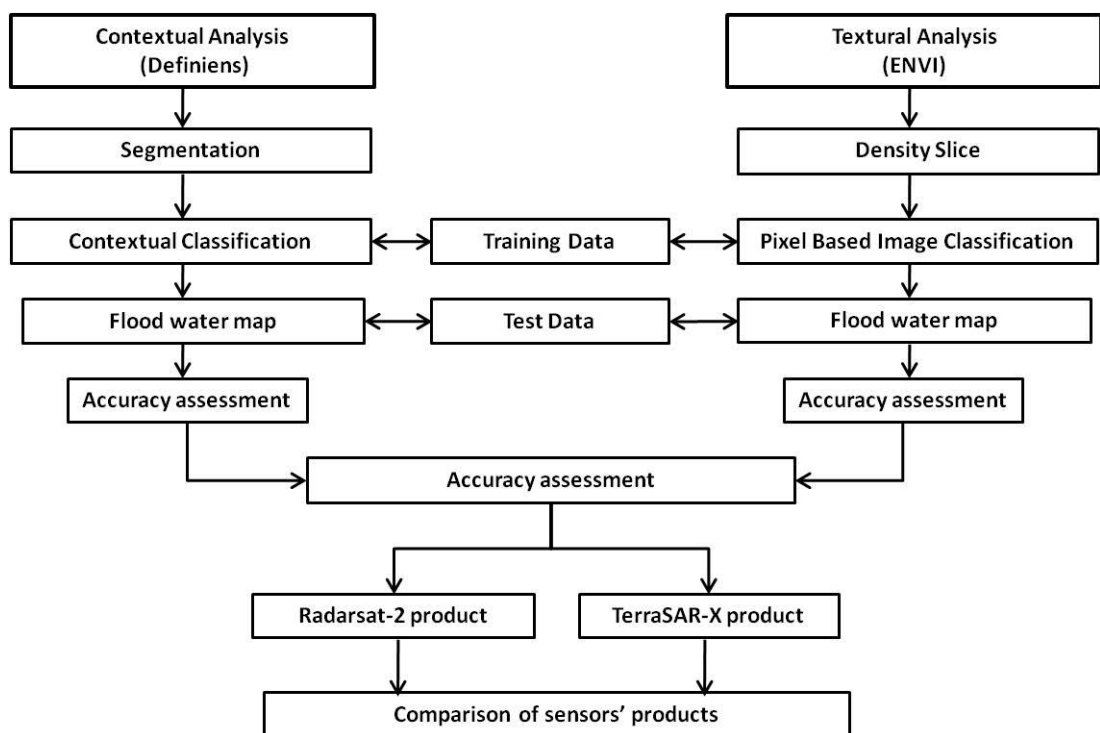


Figure 7.1: Methodology flow chart of water body mapping and accuracy assessment.

7.2 Water Body Mapping Using Backscatter Density Slicing

Density slicing is the process of converting the grey levels of an image into a series of discrete classes, each of which is equivalent to a data-range value. It provides a means of visually assigning classes to differences in radar backscatter or backscatter texture according to image brightness. Generally, a density slice is applied to a single variable by selecting data ranges and highlighting thematic classes or areas of interest by colour coding. The density slice technique was employed in this study to map water bodies by using single-band backscatter and texture of backscatter images using the algorithm in the ENVI software package.

In the case of mapping water and non-water surfaces, density slicing assumes a threshold for identification of water bodies, since it is based on levels of brightness (or radar backscatter differences) where relatively smooth surfaces such as calm water appear in the radar image as dark tones. The approach assumes that water bodies appear in SAR imagery as areas of low backscatter, but low returns may also include pixels of smooth non-water regions. Nevertheless, the density slice technique has been used in this study to evaluate the performance of the products of each SAR sensor for water identification.

In order to perform density slicing, a texture image with a single texture measure (variable) of occurrence or co-occurrence measures should be applied. The *occurrence mean* variable has been selected here for density slicing, according to the results of texture measures assessment discussed in Section 6.4.2.1. The *mean* texture variable is better able to provide a clear separation for the water bodies because of its high contrast between water regions and other land cover features. Availability of field data is essential in order to select the effective range of values of the *Water class* to be used for density sliced images. Therefore, a manual and interactive procedure was implemented to achieve the optimal data range by slicing the histogram according to the ground truth data. The density slice technique was applied to all SAR images to evaluate its performance in identifying water for the products of each SAR sensor. Density slice statistical results have been calculated using minimum, maximum, mean and standard deviation for each texture image.

7.2.1 Density Sliced Radarsat-2 Products

Data-range values when applying the *occurrence mean* variable for the *Water* class to Radarsat-2 images are 0.0–5000.00. For co-occurrence those for the *mean* variable are 0.0–4.00. Figures 7.2 and 7.3 illustrate the density slice ranges for *Water* class in the Radarsat-2 image in HH polarization with the *co-occurrence* and *occurrence mean* variable, along with an example of a water body extracted from the density sliced results.

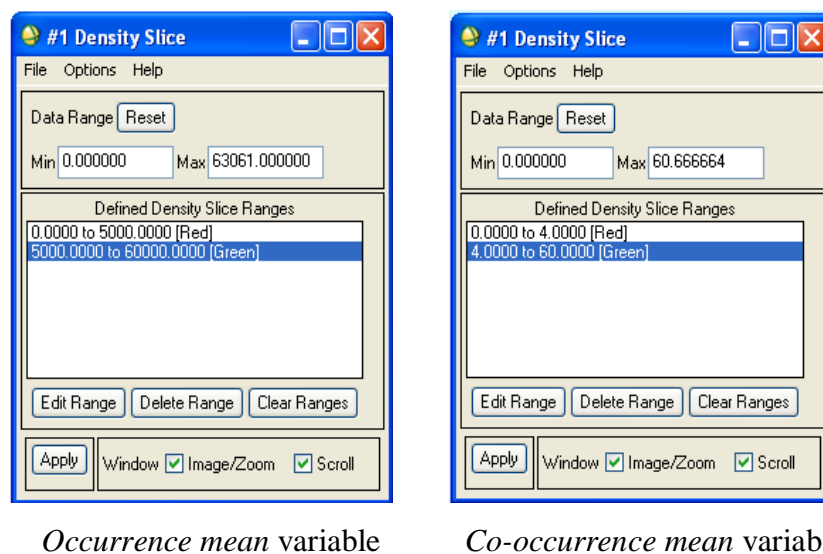


Figure 7.2: Defining density slice ranges for *Water* class using *co-occurrence* and *occurrence mean* variable - Radarsat-2-HH image.

Results from the density slice technique show that the spatial size estimation of the water body illustrated in Figure 7.3 was around 3,381 m² compared with 4,990 m² estimated from the ground truth data. This pond is used to illustrate results from different classification algorithms. Note that differences of water and non-water area in the middle left side of the water body between HH and VV occur because of the presence of trees (see left side of Google photo) facing the SAR antenna when HH descending orbit and caused strong backscatter and so the area appears dry, while in VV ascending orbit, the left side of the trees is facing the SAR antenna and result in radar shadowing where the right side appears dark similar to water. Statistical results show that mean and standard deviation of occurrence and co-occurrence Radarsat-2 HH gave very similar results (Figures 7.4 and 7.5). Percentages of water in the entire scene estimated with HH polarization for co-occurrence and occurrence are 15.66% and

20.16%, respectively. With VV polarization, these are 16.61% and 11.12% for co-occurrence and occurrence, respectively.

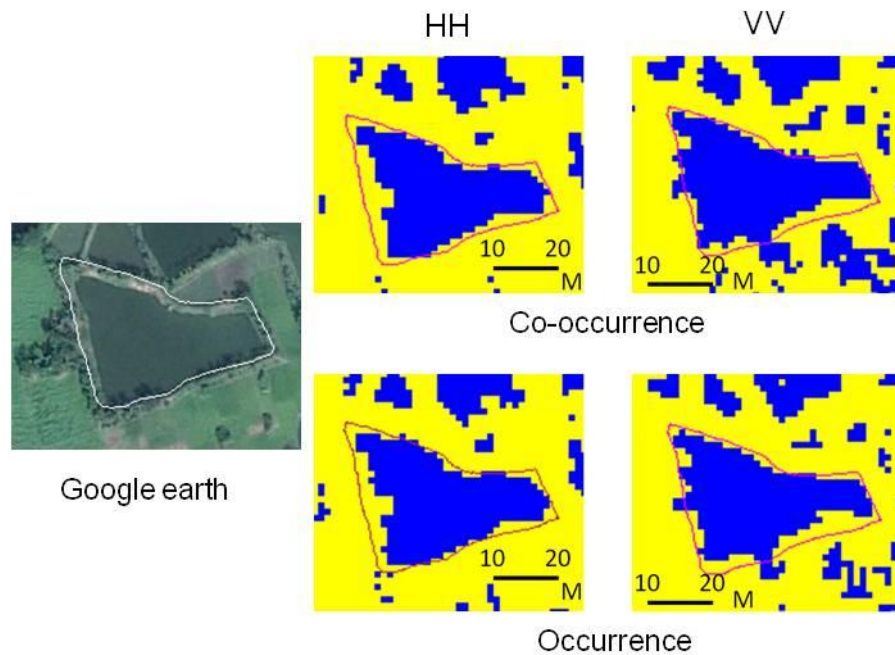


Figure 7.3: Example of density sliced results of *co-occurrence* and *occurrence mean* variable - Radarsat-2 HH and VV.

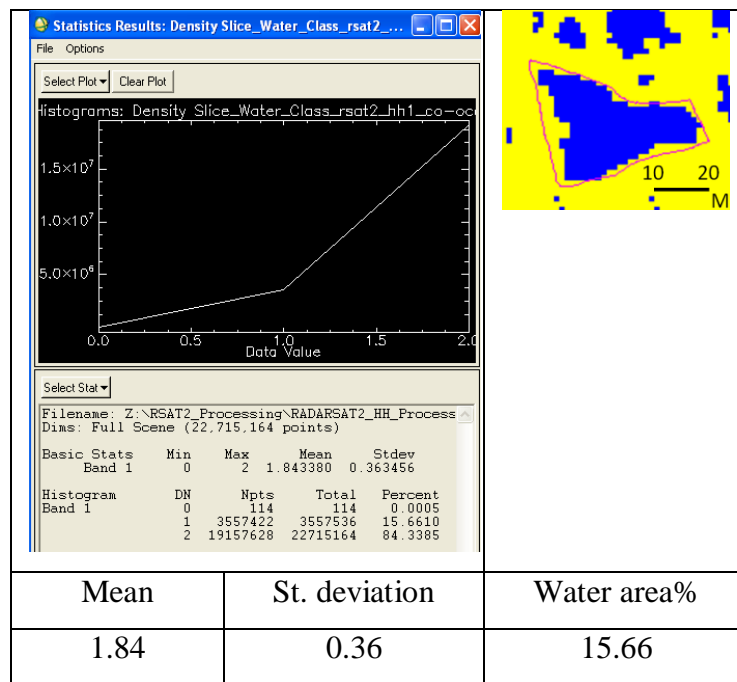


Figure 7.4: Statistical results of density slicing for *water* class with *co-occurrence mean* variable - Radarsat-2 HH.

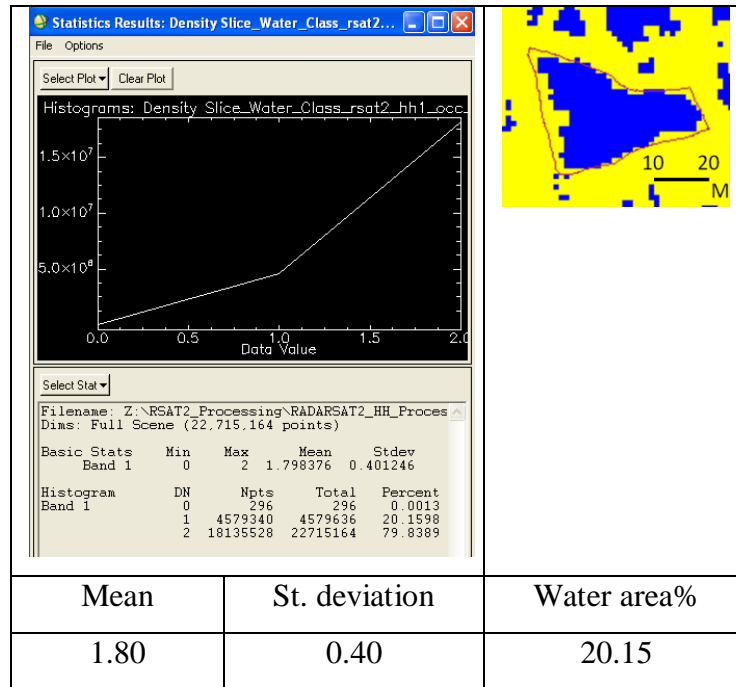
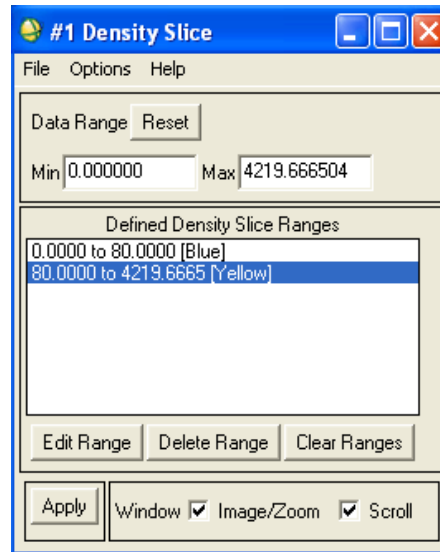


Figure 7.5: Statistical results of density slicing for water class with *occurrence mean* variable - Radarsat-2 HH.

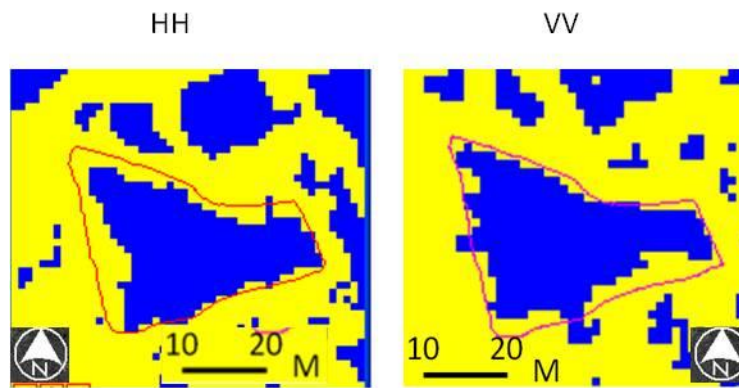
7.2.2 Density Sliced TerraSAR-X Products

The *data-range* values used to density slice *water* class in TerraSAR-X images HH and VV polarizations for the occurrence texture *mean* variable are 0.0–80.00 Density slice ranges along with extracted results are shown in Figures 7.6 and 7.7.



Occurrence mean variable

Figure 7.6: Defining density slice ranges for *water* class with *occurrence mean* variable - TerraSAR-X.



Occurrence

Figure 7.7: Example of density sliced results of TerraSAR-X HH and VV *occurrence mean* texture variable.

The area of water mapped from the test water body extracted from the density sliced image is 3,394 m² compared to 4,990 m² from the dGPS data. Statistical results demonstrate that the mean and standard deviation of density sliced TerraSAR-X HH images show close similarity to those of Radarsat-2 (Figure 7.8). The percentage of *Water* class for the entire scene for the TerraSAR-X HH *occurrence mean* texture measure was estimated to be 18.46%.

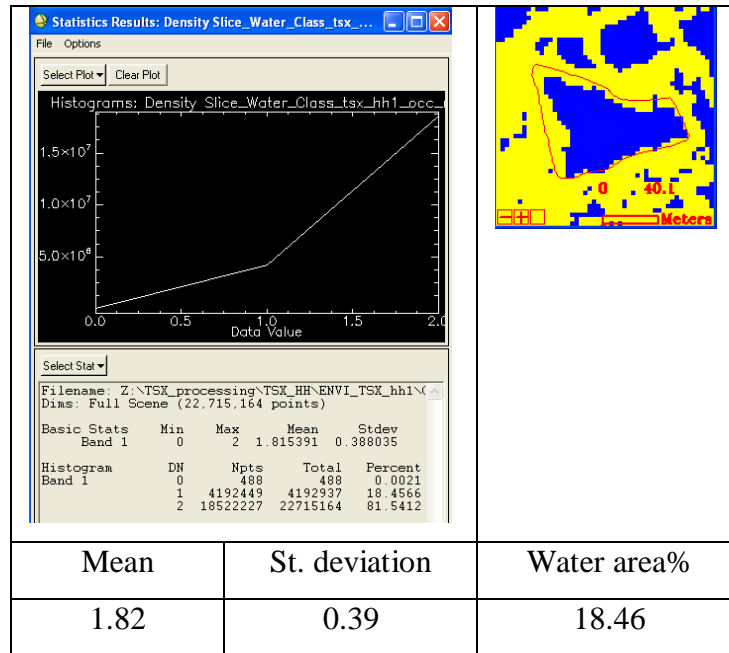


Figure 7.8: Statistical results of density slicing for *water* class of TerraSAR-X HH occurrence mean variable.

7.2.3. Comparison of Density Slice Assessment between the Two Sensors

Table 7.1 compares the sizes of four water bodies between the two sensors. The larger example water bodies have sizes close to the dGPS and the areas mapped by the two radar sensors are very similar. While the relative differences in greater for smaller water bodies, the TerraSAR-X here appears closer to the ground-based dGPS mapping. Range of density values is different between the two sensors. Table 7.2 compares the density values and water area estimation of HH and VV between Radarsat-2 and TerraSAR-X. The range values of C-band Radarsat-2 products are between 0.0-5000 while the X-band TerraSAR-X products are from 0.0-80. The absolute values are not directly comparable but it is possible that the sensors have different radiometric sensitivities that may in turn affect their ability to map low backscatter targets such as water bodies. However, the results show that water area estimation is almost similar between both sensors, with 20.16% and 18.46% of the study area mapped as water by HH polarization Radarsat-2 and TerraSAR-X respectively.

Table 7.1: A comparison of mapped area of four example water bodies extracted from Radarsat-2 HH and TerraSAR-X HH imagery compared with dGPS data.

WB example #	Radarsat-2_HH (m ²)	TerraSAR-X_HH (m ²)	dGPS data (m ²)
1	3381	3394	4990
2	3067	3075	4209
3	1244	1471	1838
4	332	415	739

Table 7.2: Comparison of Density values and water area estimation of HH and VV between Radarsat-2 and TerraSAR-X.

		Water area estimation%		
		Density values	HH	VV
Radarsat-2	Occurrence	0.0-5000	20.16	11.12
	Co-occurrence	0.0-4.00	15.66	16.61
TerraSAR-X	Occurrence	0.0-80	18.46	25.3 (beginning of wet season)
	Co-occurrence	No co-occurrence results (see section 6.3.2.2)		

7.2.4 Analysis of Polarization

A comparison of HH and VV polarizations of Radarsat-2 ultrafine images and TerraSAR-X Stripmap images was performed using density slicing occurrence texture filters. The results show that, when compared with dGPS data, both HH and VV with 3-m ground-resolution products can detect water bodies with a spatial size of 4000 m² to a high degree of accuracy (Figure 7.9).

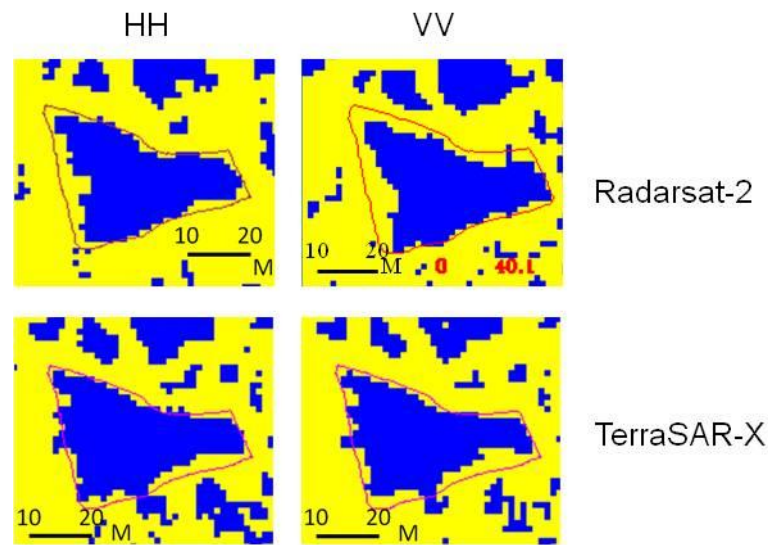


Figure 7.9: A visual comparison of SAR sensor polarizations between Radarsat-2 and TerraSAR-X.

7.3 Water Body Mapping Using Image Classification

7.3.1 Unsupervised Classification

The unsupervised classifiers, as described above, examine the unknown pixels in an image and aggregate pixels with the same or similar values into a number of classes. Unsupervised classification involves two common techniques: K-Means and the Interactive Self Organization Data Analysis Technique (ISODATA). The K-Means unsupervised classifier is a process of analysis and relocates clusters in the data, iteratively repositioning them until a sufficient level of spectral separability is achieved. The objective of the ISODATA is to calculate class means equally distributed within the data then cluster the remaining pixels in an iterative procedure using a minimum distance technique. In ISODATA, an image is segmented into unknown classes then the interpreter labels those classes, resulting in a classified image. Thus, the output of the unsupervised classification process is the identification of separable spectral classes. In order to associate output classes with land cover types, knowledge of the area along with the ground truth data is required.

In the present study, four classes have been specified with both classifiers of K-Means and ISODATA. Adjusting the parameters of unsupervised classification through a

number of trial runs in order to separate *Water* class from other classes, results of ISODATA and K-Means for the Radarsat-2 and TerraSAR-X products were obtained (Figure 7.10). The results of the ISODATA classifier in products of both sensors show, to some extent, better separability for *Water* class over the K-Means classifier. Nevertheless, the results of unsupervised classification indicate some confusion between water bodies and some land cover types, which is a common result since the process is automated. Therefore, unsupervised classification is not sufficiently suitable to be used in this study for identifying very small water bodies in SAR data.

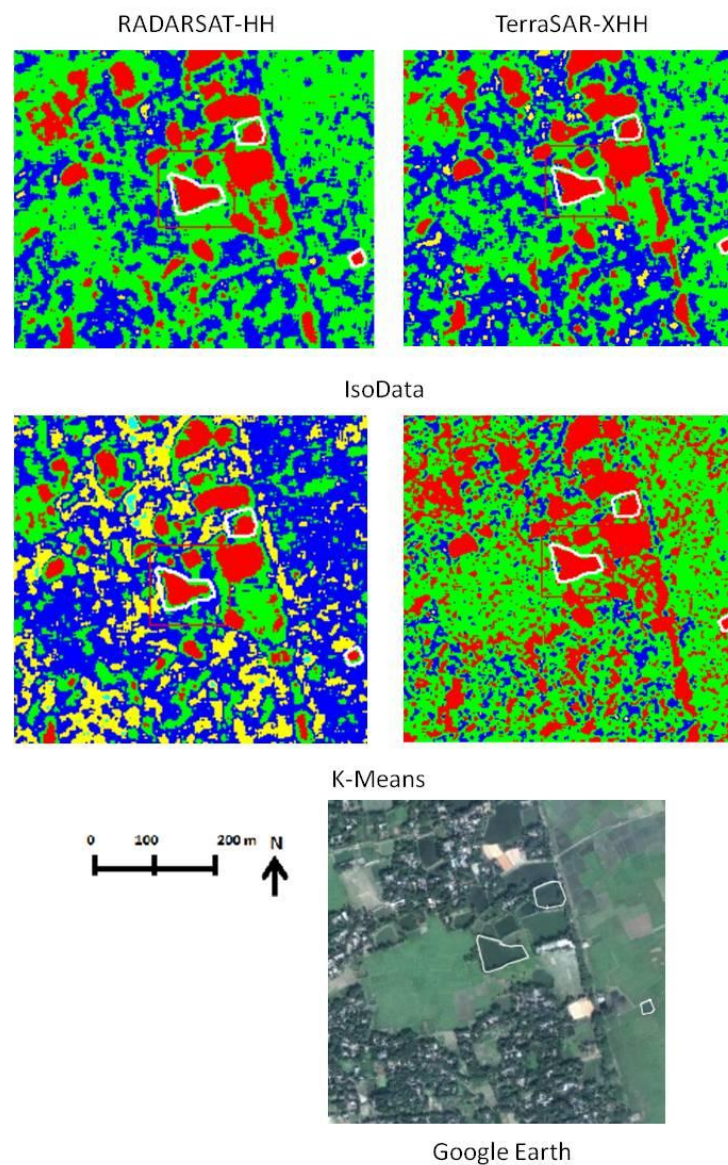


Figure 7.10: Unsupervised classification ISODATA and K-Means comparison between RADARSAT-2 and TerraSAR-X images (red indicates water); maps shown here cover a small portion of the study area.

7.3.2 Supervised Classification

This section first discusses the evaluation of training classes used, followed by the analysis and comparison of results from supervised classified images of the SAR sensors. ENVI software image processing was used for supervised classification. The process of supervised classification involves three main steps: training the system for land cover classes, undertaking classification and obtaining the output of the classified image. The process of training the system involves selecting areas as closed polygons in the target image that represent each unique class. To perform supervised classification on the SAR images, samples of known regions were selected to represent training data for each land cover class. Factors affecting classification performance include the use of a sufficient number of training samples and how well distributed these are in relation to the target class distribution.

The second step in supervised classification involves undertaking the classification. In this study, supervised classification has been performed with the maximum likelihood classifier (MLC), one of the most robust and widely used methods of classification (Bailey et al., 2007; Jensen, 2005; Lillesand et al., 2004; Weng, 2002). The MLC assigns a likelihood function to each pixel the class with the highest probability. The third stage comprises presenting the results of classification for images from both sensors, discussed in the following sections. The main purpose of image classification in this study is to distinguish *Water* class from other land cover types rather than to classify different types of land cover features.

7.3.2.1 Analysis of Training Data

Training and test datasets of *Water* class were extracted from the dGPS field data (Section 6.2.1). The water-body field data was divided randomly into two datasets: a training dataset (4841 pixels) to train the system, and a test dataset (2950 pixels) to validate the classifier. Both water training data and water test data were converted to Region-Of-Interest (ROI) in ENVI software and saved as two vector layers in order to use them for classification and post-classification. The remaining categories of training samples of land cover classes were derived from the SAR images. This step was performed by drawing ROIs using a polygon-based approach in the ENVI software.

From analysis of land cover types in the study area, four mean classes of information were established: *Water*, *Wetland*, *Grassland*, and *Builtup/Trees* (Figure 7.11).

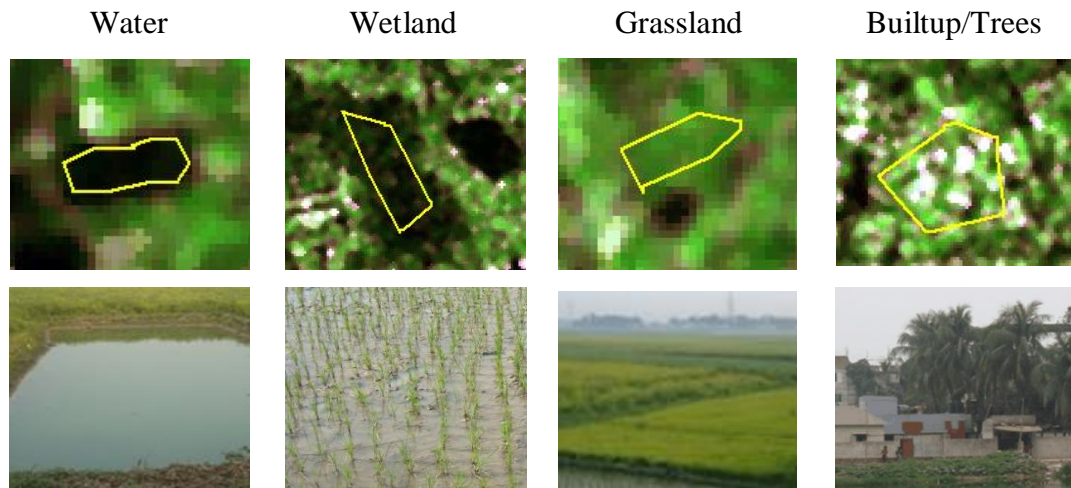


Figure 7.11: Land cover types with fieldwork photographs

In the output maps e.g. Figure 7.12, blue depicts water bodies, cyan identifies wetland, green represents grassland and red is assigned to builtup/trees. The training samples of each class were selected from SAR images on the basis of two sources: field mapping and general knowledge of the scene area and high-resolution QuickBird images from Google Earth. Google Earth images over the study area were taken in January 2009, at around the same time that SAR image acquisition and the fieldwork campaign took place. To improve the classification performance, sufficient and representative training data for each class must be collected.

Water



The water surface includes the water-body polygons extracted from the dGPS field data (Section 6.2.1). *Water* class represents all types of water bodies, such as ponds, lakes and rivers. Its signature appears as a very dark tone in the SAR backscatter imagery because of specular reflection. *Water* class is shown by the colour blue.

Wetland



Wetland is usually caused by irrigating cultivated fields or precipitation. It is very shallow water where water level may be raised just up to a few centimetres. This may cause less backscatter in SAR imagery and may be interpreted as a water body or flooding. This class was established to train the system to distinguish between water and wetland in order to avoid classifying wetland as water. *Wetland* class is shown by the colour cyan.

Grassland



As no details of field data on different types of vegetation were available, all types of grassland cover were aggregated into a single class. Therefore, the *Grassland* class in this study represents all types of short vegetation, such as grass and crops, but not tall trees. Grass has higher backscatter compared with water and thus provides a moderate bright signature. *Grassland* class is shown by the colour green.

Builtup areas/Trees



Builtup areas and trees are treated as one class because trees were found among settlements. The *Builtup/Trees* class includes settlements that are a mixture of homesteads and are associated with tall trees and industrial areas. This class has very high backscatter because of roof reflection and double bounce reflection from building corners and tree trunks. Thus, this class appears clearer and more easily identifiable because of its high backscatter. This class is shown by the colour red.

The spectral separability of the selected ROIs training samples was evaluated using Jeffries–Matusita distance to determine how statistically separate the selected classes are (Richards, 1993; Schmidt & Skidmore, 2003). The Jeffries–Matusita separability measure found values in the range of 0–2.0 (ENVI, 2005; Richards, 1999). Values greater than 1.9 indicate that the ROI pairs have good separability, while very low separability is signified when values are less than 1 (Richards, 1999; Ye, 2008).

Results of the spectral separability evaluation between training samples in Radarsat-2 HH, VV and TerraSAR-X HH, VV indicate that selected ROI training samples do separate (Table 7.3). In all HH images, values of *Water* and *Grassland* classes are greater than 1.9, indicating that these two classes have good separability. However, Water and Wetland have low separability of 0.55–1.27, which indicates that there is some confusion between these classes. The VV polarization data have low Jeffries–Matusita separability between water and wetland in both sensors compared to HH. Confusion with VV may be due to the relative proportion of radar echo signal backscattered away from the SAR sensor because wetland areas may act as specular reflectors, which could be confused with open water bodies.

Table 7.3: Jeffries–Matusita distance separability matrix of land cover training samples for pairs of classes of Radarsat-2 and TerraSAR-X data using *occurrence data-range* and *mean* and *co-occurrence mean*, *variance* and *contrast* texture variables.

sensor	Texture measures	<i>Water-wetland</i>	<i>Water-grassland</i>	<i>Water-builtup/trees</i>	Polarization
Radarsat-2	Occurrence	0.96	1.99	1.81	HH
		0.69	1.95	1.81	VV
	Co-occurrence	1.02	1.99	1.99	HH
TerraSAR-X	Occurrence	1.27	2.00	1.95	HH
		0.55	1.77	1.78	VV

7.3.3 Supervised Classification of Radarsat-2 Data

Maximum likelihood supervised classification for Radarsat-2 HH and VV products was performed using occurrence and co-occurrence texture variables for image classification. The selection of all texture variables was based on the results of the evaluation discussed in Section 6.3.2. The recommended occurrence texture variables for Radarsat-2 products (Section 6.3.2.1) were *data range*, *mean* and *variance*. However, because variance did not lead to any output signature in the TerraSAR-X texture images, the variance variable has been excluded from the image classification in order to obtain a reliable comparison between the classified images of the two sensors.

The co-occurrence variables suggested in Section 6.3.2.2 were *mean*, *variance*, *dissimilarity* and *contrast*. *Dissimilarity* and *contrast* variables are very similar in terms of water-body identification. Therefore, both of these will be evaluated by combining each with *mean* and *variance* in a separate texture image for image classification in order to identify which performs better.

The following sections present the results of occurrence and co-occurrence image classification for Radarsat-2 HH and VV polarizations.

7.3.3.1 Classified Occurrence Texture Images

7.3.3.1.1 HH Polarization

Results of supervised classification for Radarsat-2 HH texture images with *occurrence data-range* and *mean* variables (Figure 7.12) show good discrimination between water bodies and other land cover types. A visual comparison between the supervised classification map and the texture image indicates that land classes in the classified image are more homogeneous and more uniform than the unsupervised classified images (Figure 7.10), particularly for the *Water* class. This highlights the importance of image texture variables in providing image classification with quantitative information to improve the quality of classified images. Moreover, the results indicate that supervised classification shows better performance than unsupervised classification, described in Section 7.3.1, in identifying flooding and small water bodies.

The SAR images were classified twice, before and after employing an enhancement median filter 3×3 kernel size window in the ENVI software. The median 3×3 window is large enough to smooth anomalous signal while small enough to preserving the detail of very small water bodies (Section 6.3.1). The classification process was conducted with and without the median 3×3 window in order to examine the effect of the median 3×3 filter on improving the quality of classification, particularly the *Water* class.

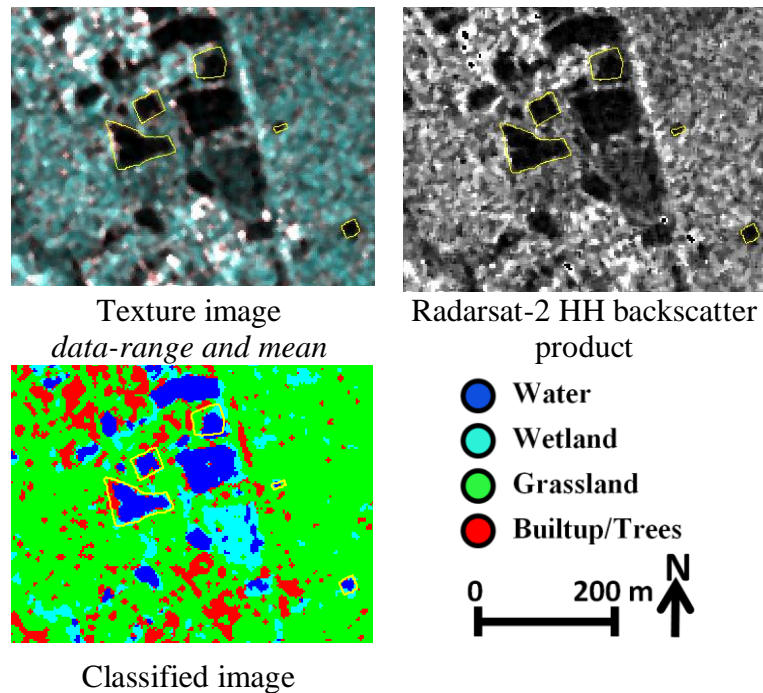


Figure 7.12: Supervised classification of *occurrence data-range and mean* texture image for Radarsat-2 HH overlaid with dGPS data compared to the original SAR product and the texture image; maps shown here and subsequent maps cover a small portion of the study area.

The quality of the supervised images was assessed for accuracy with the use of an error matrix method. The error matrix, also known as a confusion matrix, is a method of calculating the accuracy of classified classes with respect to the reference data (Congalton & Green, 2009) (Section 3.9.2). User accuracy, producer accuracy, overall accuracy and Kappa coefficient of the classified images were computed from the confusion matrix. The overall accuracy is an indication of the correctness of the classified image, where the Kappa coefficient reflects the agreement percentage between the classified image and the reference data. Producer accuracy is a measure of how well the classified image is produced and quantifies the omission errors of a class. User accuracy measures how well the pixels are assigned on the classified image and quantifies the commission errors on a class within the classified image.

Supervised classification was employed with images smoothed by the median 3×3 window to examine its effectiveness in improving the classification accuracy of land cover classes, particularly the *Water* class, and to verify the results of analysis discussed in Section 6.3.1. The error matrices of the classified images of Radarsat-2 HH texture

images with and without median 3×3 window are shown in Tables 7.4 and 7.5, respectively. The producer accuracy of the *Water* class that results from classifying texture image without a median 3×3 window is 88.31%, and the user accuracy is 92.84%. The classified image of the texture image that used the median 3×3 window has a producer accuracy of 88.61% and a user accuracy of 94.30%. These results indicate an improvement in the quality of the classified images when using enhanced images. This means that the data that has been pre-processed with a median 3×3 window provides better identification of water bodies.

There is confusion of 14% between *Water* and *Wetland* (Table 7.4), which decreased to 11.4% (Table 7.5) upon using the median 3×3 window. Many areas of wetland were found in the study area during the acquisition of SAR images and the fieldwork and most were caused by activities relating to irrigation of newly transplanted field. This confusion occurred because there was less backscatter due to the smoothness of the wetland surfaces (see Section 7.3.2.1 and Table 7.3).

The results highlight the efficiency of the selected texture variables of *data-range* and *mean backscatter*, which were evaluated for water identification in Section 6.3.2.1. Therefore, supervised classification of Radarsat-2 HH texture images with at least two texture variables provides homogeneous and separable land cover classes and a high level of accuracy for *Water* classification. The high user accuracy of 94.30% for the *Water* classification emphasises the capability of Radarsat-2 HH ultrafine data for mapping water bodies. Table 7.5 shows that the confusion between *Water* and other classes is only with the *Wetland* class, where the overlap is estimated at 11.4% which reduced the producer's accuracy to 88.61%.

Table 7.4: Confusion matrix (percentage) of classified image of Radarsat-2 HH occurrence data-range and mean variables without median 3×3 window applied.

	Reference Data					
Class Image	<i>Water</i>	<i>Wetland</i>	<i>Grassland</i>	<i>Builtup/ Trees</i>	Commission	User Acc.
<i>Water</i>	88.31	14	0.06	0.00	7.16	92.84
<i>Wetland</i>	7.22	79.48	7.53	0.08	40.49	59.51
<i>Grassland</i>	3.42	6.26	89.42	23.92	10.55	89.45
<i>Builtup/Trees</i>	1.05	0.07	2.99	76.00	12.05	87.95
Producer Acc.	88.31	79.48	89.42	76.00		
Omission	11.69	20.52	10.58	24.00		
Overall Accuracy: 85.90% ; Kappa Coefficient: 0.7838						

Table 7.5: Confusion matrix (percentage) of classified image of Radarsat-2 HH occurrence data-range and mean variables with median 3×3 window applied.

	Reference Data					
Class Image	<i>Water</i>	<i>Wetland</i>	<i>Grassland</i>	<i>Builtup/ Trees</i>	Commission	User Acc.
<i>Water</i>	88.61	11.38	0.00	0.00	5.70	94.30
<i>Wetland</i>	7.12	85.24	3.05	0.00	26.51	73.49
<i>Grassland</i>	2.20	3.38	94.49	16.65	6.97	93.03
<i>Builtup/Trees</i>	2.07	0.00	2.46	83.35	10.74	89.26
Producer Acc.	88.61	85.24	94.49	83.35		
Omission	11.39	14.76	5.51	16.65		
Overall Accuracy: 90.41% ; Kappa Coefficient: 0.8521						

7.3.3.1.2 VV Polarization

The classified image of VV polarization compared visually with the texture image (Figure 7.13) reveals to some extent a separable *Water* class, but less so than with HH polarization (Figure 7.12). The VV error matrix in Table 7.6 shows lower overall accuracy (79.46%) compared to the HH polarization (90.41%) shown in Table 7.5. Although the user accuracy of the *water* class is high, there is a level of omission which

is quantified as 27% compared to 11% in HH. This strongly suggests that HH polarization is better than VV in the detection of water.

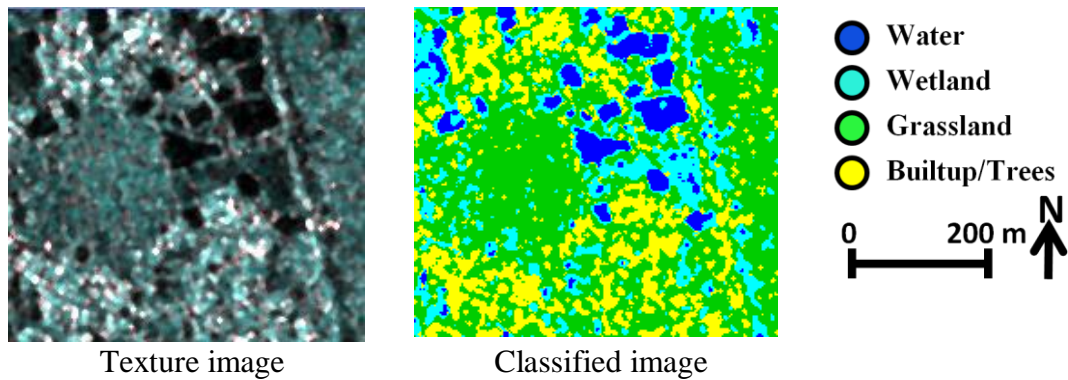


Figure 7.13: Supervised classification of *occurrence data-range and mean* texture image for Radarsat-2 VV compared to the texture image

Table 7.6: Confusion matrix (percentage) of classified image of Radarsat-2 VV *occurrence data-range and mean* with median 3×3 window applied.

Class Image	Reference Data					User Acc.
	<i>Water</i>	<i>Wetland</i>	<i>Grassland</i>	<i>Builtup/Trees</i>	Commission	
<i>Water</i>	72.47	14.51	0.00	0.00	7.29	92.71
<i>Wetland</i>	14.03	83.94	0.36	0.00	30.07	69.93
<i>Grassland</i>	10.95	1.12	94.84	22.15	35.76	64.24
<i>Builtup/Trees</i>	2.54	0.43	4.80	77.85	12.87	87.13
Producer Acc.	72.47	83.94	94.84	77.85		
Omission	27.53	16.06	5.16	22.15		
Overall Accuracy: 79.46%; Kappa Coefficient: 0.7144						

7.3.3.2 Classified Co-occurrence Texture Images

The recommended co-occurrence variables of *mean*, *variance*, *contrast* and *dissimilarity* in Section 6.3.2.2, which are better identifiers of water texture, were applied for supervised classification. The co-occurrence variables were divided into two combinations of texture images, and each texture image contained three variables for the image classification. The first classified image (A) was processed with *mean*, *variance* and *dissimilarity*, while the second one (B) was processed with *mean*, *variance* and *contrast* (Figure 7.14). This step was implemented to test which combination of variables shows more improvement for *Water* class classification.

Visual analysis of the co-occurrence image classification results (Figure 7.14) demonstrates that the *Water* class has good homogeneity and can easily be distinguished from surrounding land cover features. Results of accuracy assessment for co-occurrence image classification also show a high overall accuracy of greater than 90% and a high Kappa coefficient of 0.8514 as presented in the error matrices (Tables 7.7 and 7.8). The accuracy assessment of the *Water* class classification is high, with a producer accuracy of greater than 87% and a very high user accuracy of greater than 95%. The confusion between *Water* and other land classes is almost zero, except for the *Wetland* class, calculated at 7–8%. A possible reason for this *Water–Wetland* confusion is the similarity of surface smoothness between water bodies and wetland areas, as explained in Section 7.3.3.1.

Evaluation of the effectiveness of dissimilarity and contrast variables when used alongside the two variables of *mean* and *variance* (Figure 7.14 and Tables 7.7 and 7.8) revealed that dissimilarity and contrast worked well in identifying small water bodies. For co-occurrence with three variables, the image classification results of the overall accuracy and the Kappa coefficient, in particular user and producer accuracy of *Water* class, appear almost similar to those for occurrence with two variables, as shown in Table 7.9. This indicates that *Water* class can easily be delineated to a high level of identification either with selected occurrence or with co-occurrence variables.

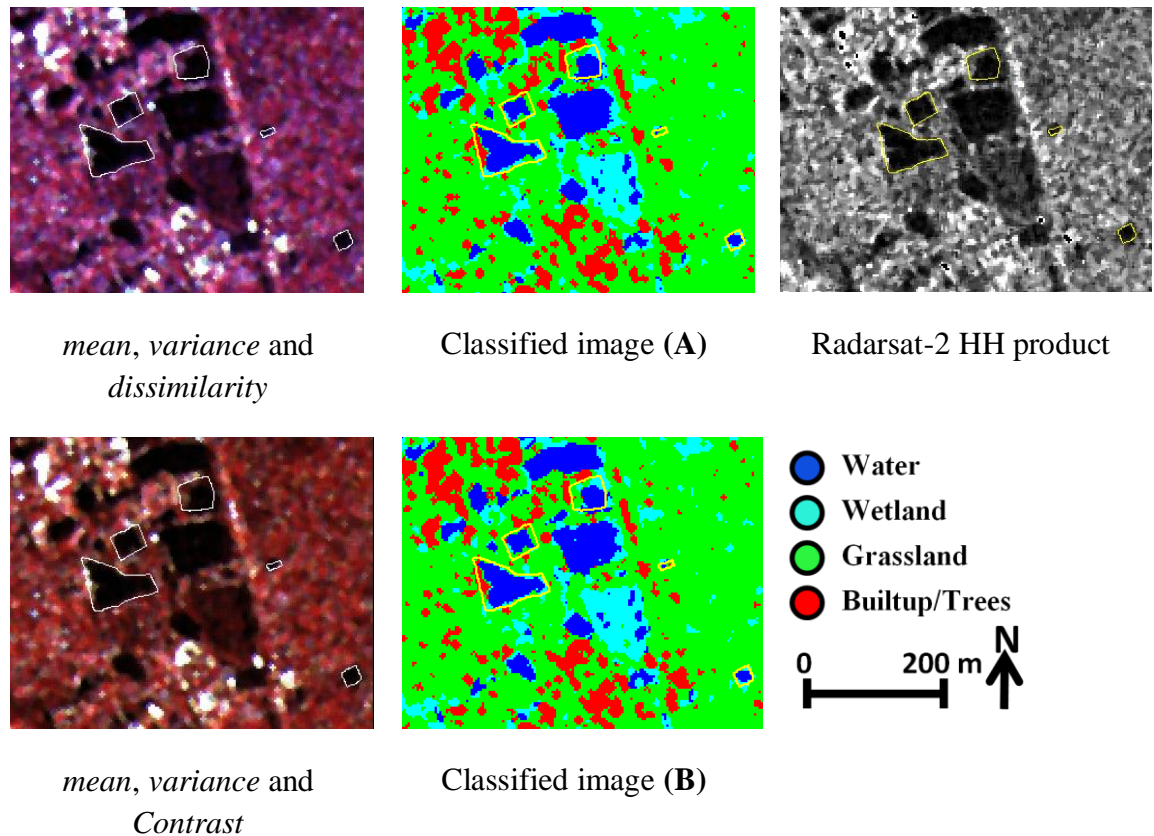


Figure 7.14: Supervised classification of Radarsat-2 HH produced after applying co-occurrence variables of (A) *mean, variance and dissimilarity*, and (B) *mean, variance and contrast* overlaid with dGPS data

Table 7.7: Confusion matrix (percentage) of classified image of Radarsat-2 HH with *co-occurrence mean, variance and dissimilarity* with median 3×3 window applied.

Class Image	Reference Data				commission	User Acc.
	<i>Water</i>	<i>Wetland</i>	<i>Grassland</i>	<i>Builtup/Trees</i>		
<i>Water</i>	87.19	8.86	0.03	0.00	4.63	95.37
<i>Wetland</i>	7.19	88.19	4.07	0.00	29.07	70.93
<i>Grassland</i>	4.85	2.95	94.23	16.06	7.73	92.27
<i>Builtup/Trees</i>	0.78	0.00	1.67	83.94	6.70	93.30
Producer Acc.	87.19	88.19	94.23	83.94		
Omission	12.81	11.81	5.77	16.06		
Overall Accuracy: 90.36% ; Kappa Coefficient: 0.8514						

Table 7.8: Confusion matrix (percentage) of classified image of Radarsat-2 HH with *co-occurrence mean, variance and contrast* with median 3×3 window applied.

Class Image	Reference Data					User Acc.
	<i>Water</i>	<i>Wetland</i>	<i>Grassland</i>	<i>Builtup/Trees</i>	Commission	
<i>Water</i>	87.19	7.13	0.00	0.00	3.71	96.29
<i>Wetland</i>	7.63	90.28	4.23	0.00	29.55	70.45
<i>Grassland</i>	4.44	2.59	94.13	15.00	7.80	92.20
<i>Builtup/Trees</i>	0.77	0.00	1.64	83.31	6.51	93.49
Producer Acc.	87.19	90.28	94.13	83.31		
Omission	12.81	9.72	5.87	16.69		
Overall Accuracy: 90.39% ; Kappa Coefficient: 0.8522						

Table 7.9: Comparison of accuracy assessment (percentage) between classified images using occurrence and co-occurrence variables for Radarsat-2

Classes		Occurrence – two variables (Table 7.5)		Co-occurrence – three variables (Table 7.8)	
		Prod. Acc.	User Acc.	Prod. Acc.	User Acc.
	Overall Accuracy	90.41		90.39	
	Kappa Coeff.	0.8521		0.8522	
<i>Water</i>		88.61	94.30	87.19	96.29
<i>Wetland</i>		85.24	73.49	90.28	70.45
<i>Grassland</i>		94.49	93.03	94.13	92.20
<i>Builtup/Trees</i>		83.35	89.26	83.31	93.79

7.3.4 Supervised Classification of TerraSAR-X Data

The image classification of TerraSAR-X HH Stripmap images was undertaken by applying the same occurrence variables of *data-range* and *mean* used for the classification of Radarsat-2 images. The TerraSAR-X images were classified before and after applying the enhancement median 3×3 window, in order to identify any differences, as also carried out for the Radarsat-2 texture images (see Section 7.3.3.1).

7.3.4.1 Classified Occurrence Images

7.3.4.1.1 HH Stripmap Polarization

Results of the image classification of HH polarization (Figure 7.15) showed a high level of separability for land cover features. The *Water* class was identified with a high level of homogeneity and considerable separability. In order to assess the classified images quantitatively, an error matrix method was used to calculate accuracy. The confusion matrices of the classified images with and without using the median 3×3 window for TerraSAR-X HH Stripmap are shown in Tables 7.10 and 7.11, respectively. The classified image obtained using the median 3×3 window has an overall accuracy of 91.52%, while the classified image without median 3×3 window has an overall accuracy of 87.25%. This indicates a considerable improvement in classification accuracy when using the median 3×3 window. Accuracy of water classification also improved from 97.13% to 98.78% for user accuracy, and improvement in producer accuracy from 92.98% to 93.12% was observed. This enhancement with the median 3×3 window in TerraSAR-X image classification and with the Radarsat-2 classified images (Section 7.3.3.1) highlights the reliability of the median 3×3 window effectiveness.

Regarding the classified image with the median 3×3 window, overall accuracy of the X-Band TerraSAR-X HH Stripmap classified images reaches over 91% and has a Kappa coefficient of 0.8828. The Kappa coefficient indicates a high level of agreement of 0.8828 between the classified image and the reference data. There is almost no confusion between *Water* and the other classes, except for *Wetland*, which was found to be very low, around 2.0%, which indicates a low level of bias and a very high user accuracy (98.78%). The water classification gave a producer accuracy of 93.12% and a

user accuracy of 98.78%. This is a very high level of user accuracy for the *Water* class and indicates that almost all the water pixels are correctly assigned. This result indicates that the X-Band TerraSAR-X 3-m resolution product has excellent potential to discriminate water from other land cover types and is very suitable for flood extent mapping.

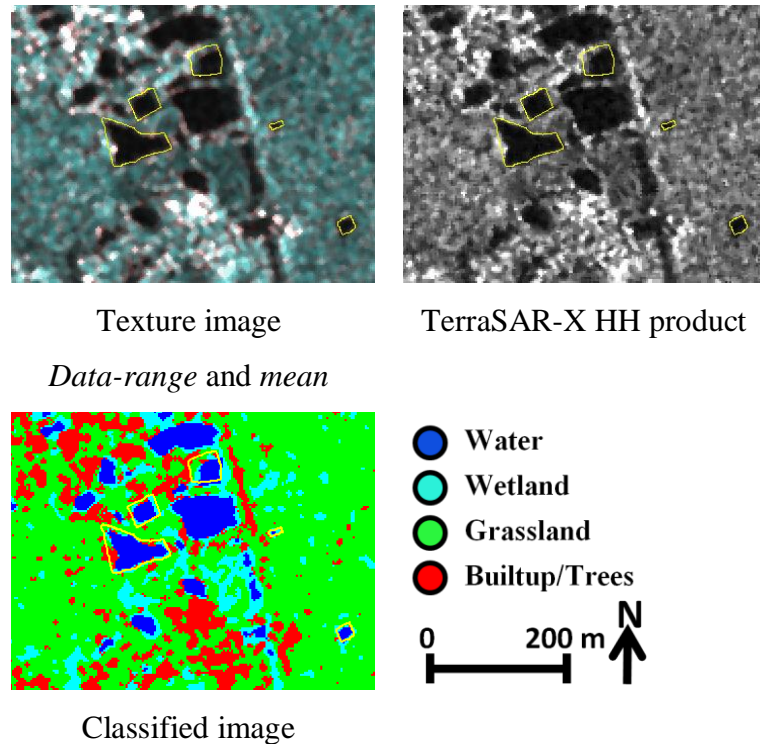


Figure 7.15: Supervised classification of *occurrence data-range* and *mean* texture image for TerraSAR-X HH Stripmap overlaid with dGPS data compared to the original SAR product and the texture image

Table 7.10: Confusion matrix (percentage) of classified image of TerraSAR-X HH occurrence data-range and mean with median 3×3 window applied.

Class Image	Reference Data					User Acc.
	<i>Water</i>	<i>Wetland</i>	<i>Grassland</i>	<i>Builtup/Trees</i>	Commission	
<i>Water</i>	93.12	2.23	0.00	0.00	1.22	98.78
<i>Wetland</i>	4.24	92.40	3.36	0.14	15.26	84.74
<i>Grassland</i>	0.20	5.37	93.63	14.93	10.30	89.70
<i>Builtup/Trees</i>	2.44	0.00	3.01	84.93	9.36	90.64
Producer Acc.	93.12	92.40	93.63	84.93		
Omission	6.88	7.60	6.37	15.07		
Overall Accuracy: 91.52% ; Kappa Coefficient: 0.8828						

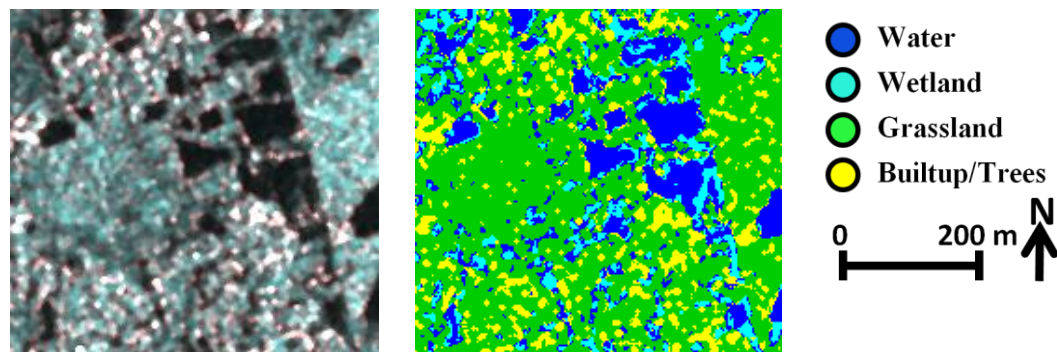
Table 7.11: Confusion matrix (percentage) of classified image of TerraSAR-X HH occurrence data-range and mean with no median 3×3 window applied.

Class Image	Reference Data					User Acc.
	<i>Water</i>	<i>Wetland</i>	<i>Grassland</i>	<i>Builtup/Trees</i>	Commission	
<i>Water</i>	92.98	5.31	0.00	0.00	2.87	97.13
<i>Wetland</i>	5.19	87.48	8.00	0.57	25.83	74.17
<i>Grassland</i>	0.61	7.21	88.91	23.32	15.68	84.32
<i>Builtup/Trees</i>	1.22	0.00	3.09	76.11	8.65	91.35
Producer Acc.	92.98	87.48	88.91	76.11		
Omission	7.02	12.52	11.09	23.89		
Overall Accuracy: 87.25% ; Kappa Coefficient: 0.8236						

7.3.4.1.2 VV Stripmap Polarization

Close inspection of the supervised classification results of TerraSAR-X VV Stripmap polarization, presented in Figure 7.16, shows that land cover features have less homogeneity than those seen in the HH polarization classified images (Figure 7.15). The confusion matrix of the VV classified images is shown in Tables 7.12. The overall

accuracy of the classified image is 82.50% and the Kappa coefficient is 0.7558. There is a confusion of 11.44% between *water* and *wetland* which is higher than the results obtained from the HH as well as with the omission of the *water* class (see Table 7.11). This indicates that the choice of HH for discriminating water bodies from wetland areas is recommended. Although the producer's and user's accuracies 88.27% and 93.10% respectively are high, they are noticeably lower than the equivalent HH accuracy data (see Table 7.12).



Texture image

Classified image

Data-range and mean

Figure 7.16: Supervised classification of *occurrence data-range* and *mean* texture image for TerraSAR-X VV compared to the texture image.

Table 7.12: Confusion matrix (percentage) of classified image of TerraSAR-X VV *occurrence data-range* and *mean* with median 3×3 window applied.

	Reference Data					
Class Image	<i>Water</i>	<i>Wetland</i>	<i>Grassland</i>	<i>Builtup/Trees</i>	Commission	User Acc.
<i>Water</i>	88.27	11.44	0.24	1.32	6.90	93.10
<i>Wetland</i>	1.97	87.10	0.00	0.78	4.91	95.09
<i>Grassland</i>	1.19	1.19	96.84	48.10	41.42	58.58
<i>Builtup/Trees</i>	2.03	0.26	2.92	49.81	13.59	86.41
Producer Acc.	88.27	87.10	96.84	49.81		
Omission	11.73	12.90	3.19	50.19		
Overall Accuracy: 82.50% ; Kappa Coefficient: 0.7558						

7.3.4.1.3 HH Spotlight Image

The texture image variables applied to the TerraSAR-X spotlight image product were *occurrence data-range* and *mean*. Five land classes were established for the high-resolution spotlight according to visual analysis of land cover features in the study area. The classes used were *Water*, *Wetland*, *TallGrass*, *ShortGrass* and *Builtup/Trees*. The *Grassland* class is divided into two classes – *ShortGrass* and *TallGrass* – because noticeable backscatter differences were found between short and tall grass. The *TallGrass* regions appear with higher backscatter than the *ShortGrass* areas in the SAR image (Figure 7.17).

Visual inspection of the classified image (Figure 7.17) shows that the spotlight image provides more detailed information regarding very small water bodies. The classified spotlight image appears to produce a more detailed map of water bodies but there are small patches of water appear within areas of *wetland* may be because of areas of standing water in rice paddy. Also areas of *wetland* within water bodies may be due to surface weed or wind induced surface roughness.

Comparing the accuracy of the results of classified images before and after using the median 3×3 window reveals observable improvements in the overall accuracy and in user and producer accuracy for the *Water* class (Tables 7.13 and 7.14). The improvement in accuracy in the spotlight image after using the median 3×3 window is more obvious than that in the Stripmap imagery. According to Table 7.13, *Water* class shows a user accuracy of 97.04%. However, 10.07% of pixels are still misclassification. Table 7.14 also shows a high overall accuracy of 87.94% and a Kappa coefficient of 0.8158.

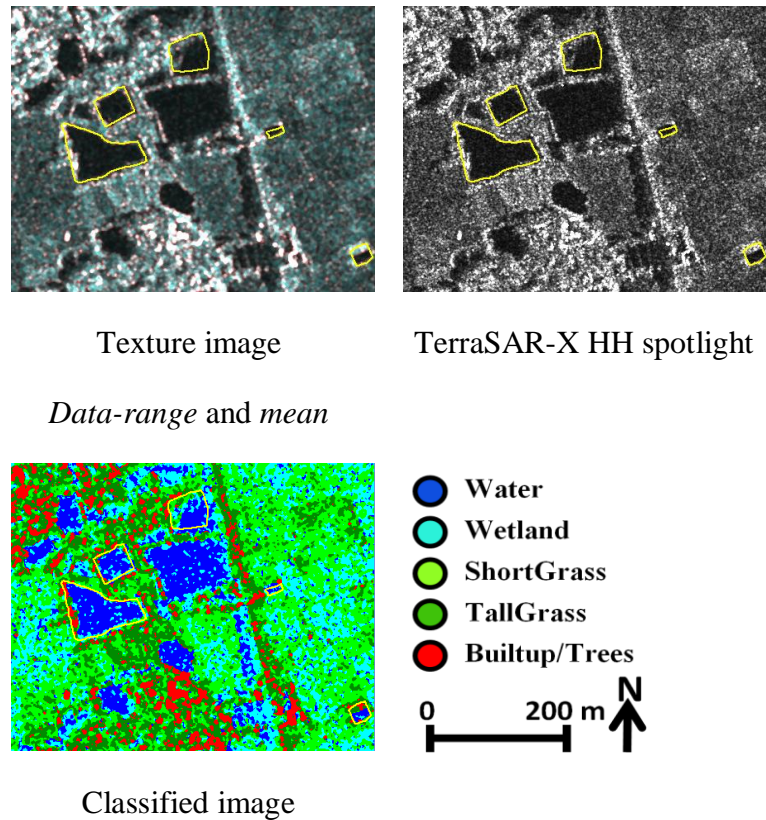


Figure 7.17: Supervised classification of *occurrence data-range and mean* texture image for TerraSAR-X HH spotlight overlaid with dGPS reference data in yellow compared to the original SAR product and the texture image

Table 7.13: Confusion matrix (percentage) of TerraSAR-X spotlight HH *occurrence data-range and mean* texture image without median 3×3 window applied.

Class Image	Reference Data						User Acc.
	<i>Water</i>	<i>Wetland</i>	<i>TallGrass</i>	<i>ShortGrass</i>	<i>Builtup/Trees</i>	Commission	
<i>Water</i>	86.01	14.23	0.00	0.20	0.19	2.96	95.62
<i>Wetland</i>	13.94	82.06	0.00	3.73	0.09	30.56	60.61
<i>TallGrass</i>	0.00	0.00	78.29	12.11	22.54	21.17	74.67
<i>ShortGrass</i>	0.05	3.71	19.65	83.96	0.47	20.31	70.93
<i>Builtup/Trees</i>	0.00	0.00	2.06	0.00	76.71	3.07	96.70
Producer Acc.	86.01	82.06	78.29	83.96	76.71		
Omission	10.14	12.71	12.82	15.67	17.40		
Overall Accuracy: 83.50% Kappa Coefficient: 0.7503							

Table 7.14: Confusion matrix (percentage) of TerraSAR-X spotlight HH *occurrence data-range* and *mean* texture image with median 3×3 window applied.

	Reference Data						
Class Image	<i>Water</i>	<i>Wetland</i>	<i>TallGrass</i>	<i>ShortGrass</i>	<i>Builtup/ Trees</i>	Commission	User Acc.
<i>Water</i>	89.86	10.07	0.00	0.00	0.00	2.96	97.04
<i>Wetland</i>	10.14	87.29	2.12	0.00	0.00	30.56	69.44
<i>TallGrass</i>	0.00	0.00	84.33	10.70	17.44	20.31	79.69
<i>ShortGrass</i>	0.00	2.64	13.61	87.18	0.00	21.17	78.83
<i>Builtup/Trees</i>	0.00	0.00	0.00	2.06	82.60	3.07	96.93
Producer Acc.	89.86	87.29	84.33	87.18	82.60		
Omission	10.14	12.71	15.67	12.82	17.40		
Overall Accuracy: 87.94% ; Kappa Coefficient: 0.8158							

7.4 Contextual Analysis

The contextual classification does not classify single pixels (i.e. supervised classification), but rather image objects or segments. The supervised classification depends on the spectral reflectance of pixels, while the contextual classification with its knowledge base includes other attributes (i.e. shape, texture, relation to neighbouring objects) additional to the spectral information provided in an image. The contextual classification approach first involves image data segmentation, which segments the image into a network of homogeneous image objects. The second stage of contextual classification is object-oriented, whereby land cover classes are related to the segmented image objects.

Contextual classification offers some advantages over traditional classification (*eCognition User Guide*, 2004):

1. Image objects contain additional information for classification, such as shape, texture and the relational network of information.
2. The segmentation process can separate adjacent objects that are textured or have noise.

3. Segmentation can make classification work significantly faster, because it reduces the total number of elements needed to be handled for classification.
4. Extracting homogeneous regions (segmentation) and then classifying them reduces salt-and-pepper noise in the classification results.

Definiens Professional software was used for contextual classification of the water bodies and other land cover types within the study area. The schematic diagram in Figure 7.18 illustrates the methodology and work flow of the contextual classification.

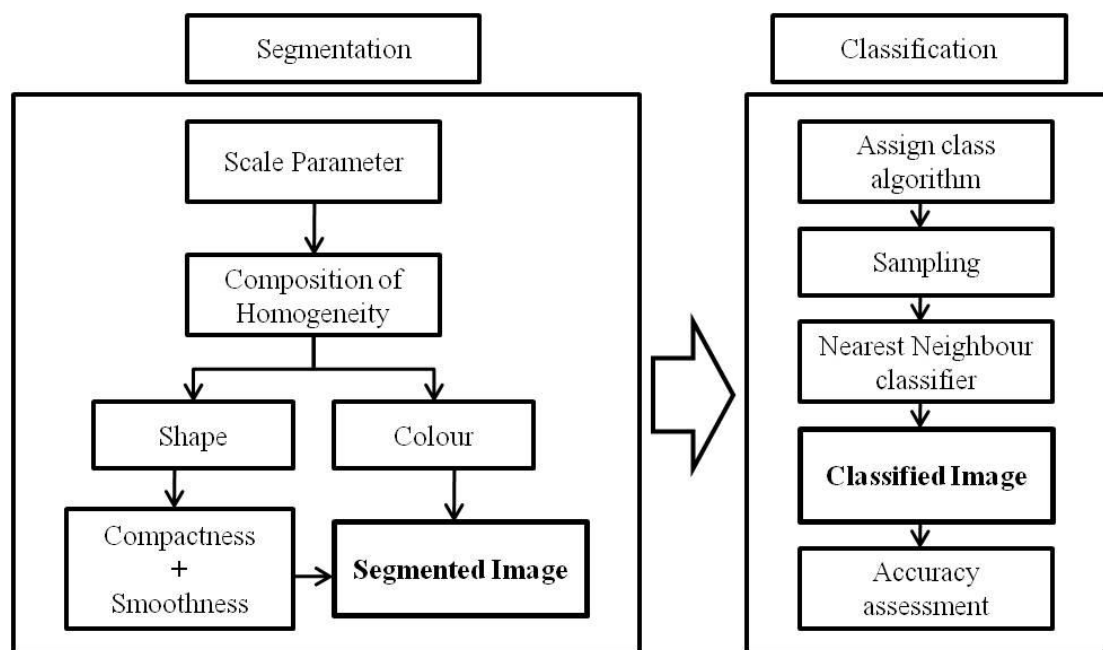


Figure 7.18: Methodology flow chart of the contextual classification used for segmentation and object-oriented classification.

7.4.1 Segmentation

Image segmentation is a technique of bottom-up region merging that starts with merging smaller image objects into larger ones. In this technique an image is segmented into unknown classes, which are then labelled as particular classes, resulting in a classified image. The image segmentation algorithm is not only influenced by the pixel values but also by three parameters: scale, colour/shape and compactness/smoothness (Definiens, 2006). The scale parameter is set by the user to define the resolution of the image object level to obtain maximum change in pixel heterogeneity when merging

image objects. Adjusting the scale parameter value enables the user to control the sizes of the created image objects. The colour parameter is related to the percentage of the spectral value contribution of the image objects to the homogeneity composition in contrast to the percentage of the shape homogeneity (Mitri & Gitas, 2004). In other words, the colour parameter balances the colour of object homogeneity with its shape homogeneity. Image data with similar spectral values but of very different shapes is optimized with the compactness parameter, while very heterogeneous data is optimized with smoothness. Smoothness and compactness are used to define homogeneity of shape. Image objects with smoother edges can be achieved by increasing the smoothness parameter, where a more compact form of image objects can be generated by increasing compactness. The segmentation parameter specifications were set within the Definiens software after running trials of multi-resolution segmentation, i.e., different segmentations with different parameters were performed until the results were satisfactory.

For this study a higher value was assigned to the shape parameter compared to the colour parameter in all SAR image segmentation, because it is more important to identify the different shapes of water bodies than the colour parameter. Values of the compactness parameter were set higher than smoothness to optimize the different shapes of water-body objects that have similar spectral values. Finally, the smoothness parameter was assigned lower values to reduce data heterogeneity. Because the segmentation scale in this study focuses on the water bodies, the process was conducted with level 1 segmentation. The segmentation and classification was conducted for two types of SAR images: images smoothed by median 3×3 window (see Section 6.3.1) but without using texture variables, and images with texture *occurrence data-range* and *mean*. This approach was performed to identify any improvements in the accuracy of the contextual classification results with or without the use of texture variables.

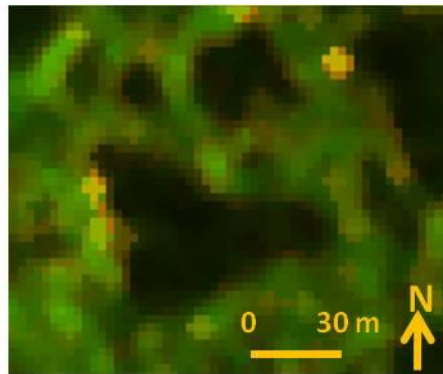
7.4.1.1 Radarsat-2 HH Image Segmentation

The scale parameter for the Radarsat-2 HH texture image occurrence *data-range* and *mean* is defined as 50 to set the size of image objects for the segmentation process. The criterion for defining the scale parameter is based on the identification of the spatial sizes of very small water bodies. The value of 0.8 was found to work better for the shape parameter, while the colour value was automatically set to 0.2. The compactness parameter value of 0.7 was found to be the most suitable for water-body identification (Table 7.15). The segmented texture image is presented in Figure 7.19. Visual analysis of the segmented image showed that the water bodies appear well segmented, including the very small ones. Differences in homogeneity within the water body in the segmented image (Figure 7.19) may relate to texture roughness differences arising from wind or surface water weeds such as hyacinth, which is common in Bangladesh.

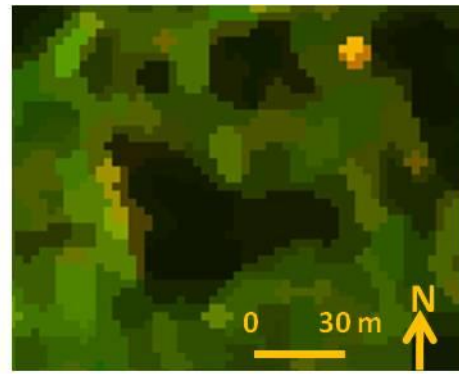
Segmentation was also performed for the Radarsat-2 HH images without texture variables. This step was carried out to examine any difference that may have occurred when using the original SAR image compared to the segmented texture image. The scale parameter of 100 and values of 0.7 for shape and compactness were found to be the most suitable for this type of image (Table 7.16). A small area extracted from the segmented image is shown in Figure 7.20. Visual analysis of water-body identification within the segmented image demonstrated that each water body was segmented as a homogeneous object, as shown in the extracted area in Figure 7.20. This is one of the advantages of using segmentation for identifying bodies of water.

Table 7.15: Segmentation parameters for Radarsat-2 HH occurrence *data-range* and *mean* texture image

Scale Level	Scale Parameters	Colour/Shape Factor	Compactness/Smoothness
1	50	0.2/0.8	0.7/0.3



Radarsat-2 HH Texture Image

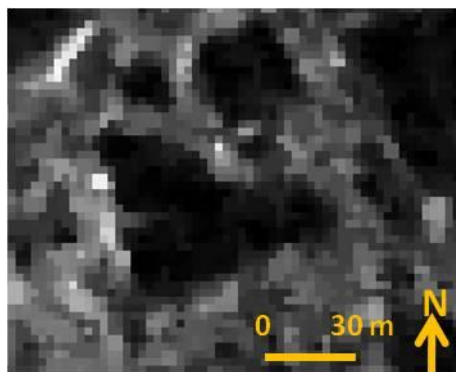


Segmented Image

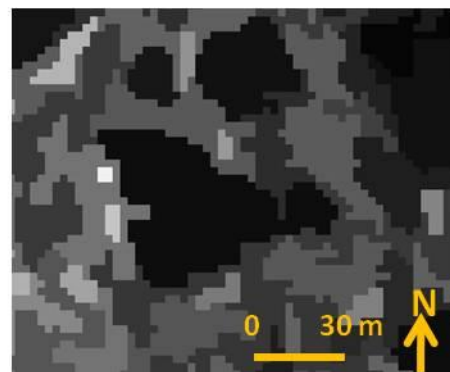
Figure 7.19: Radarsat-2 HH texture image (*data-range* and *mean*) before and after segmentation

Table 7.16: Segmentation parameters for Radarsat-2 HH non-texture image.

Scale Level	Scale Parameters	Colour/Shape Factor	Compactness/Smoothness
1	100	0.3/0.7	0.7/0.3



Radarsat-2 HH product



Segmented Image

Figure 7.20: Radarsat-2 HH original image (non-texture image) before and after segmentation

7.4.1.2 TerraSAR-X HH Image Segmentation

Segmentation of the TerraSAR-X HH texture image was based on a scale parameter of 10, which was found to be the most suitable scale for water-body object sizes. The shape value parameter was adjusted to 0.8 after running trials to obtain the best level for identifying the water bodies, while the colour value was automatically set to 0.2. The compactness/smoothness parameter for water identification was adjusted to values of 0.7/0.3 (Table 7.17). Results of TerraSAR-X HH texture image segmentation show that the bodies of water are segmented with a high level of identification and are discriminated well from other objects. Figure 7.21 shows a part of the segmented image in which can be seen a well-segmented water body.

Segmentation was also applied to a TerraSAR-X HH image without texture variables; this step was performed with the Radarsat-2 HH image so that the two results could be compared. The parameters of scale and composition of homogeneity were set to the same values as for those of the TerraSAR-X texture image presented in Table 7.17 because they provided similar results. The segmented image produced from the original TerraSAR-X products indicates that the image is able to discriminate water bodies from other land cover features.

Table 7.17: Segmentation parameters of TerraSAR-X HH texture image (*data-range* and *mean*) variables

Scale Level	Scale Parameters	Colour/Shape Factor	Compactness/Smoothness
1	10	0.2/0.8	0.7/0.3

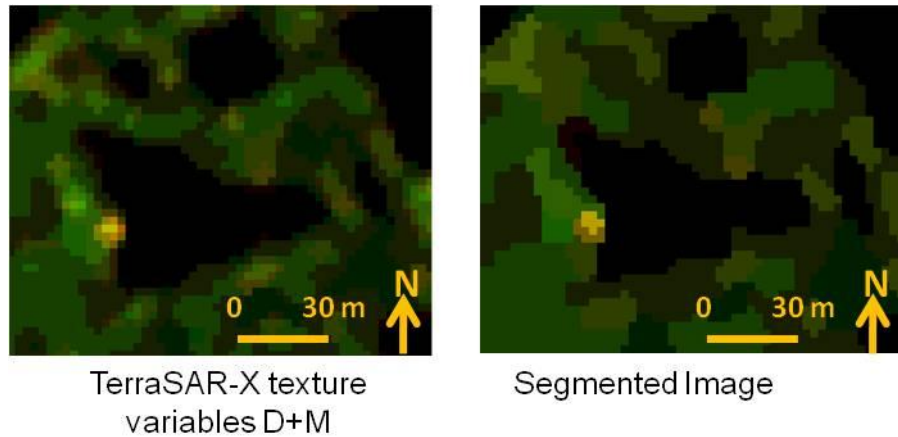


Figure 7.21: TerraSAR-X HH texture image (*data-range* and *mean*) before and after segmentation

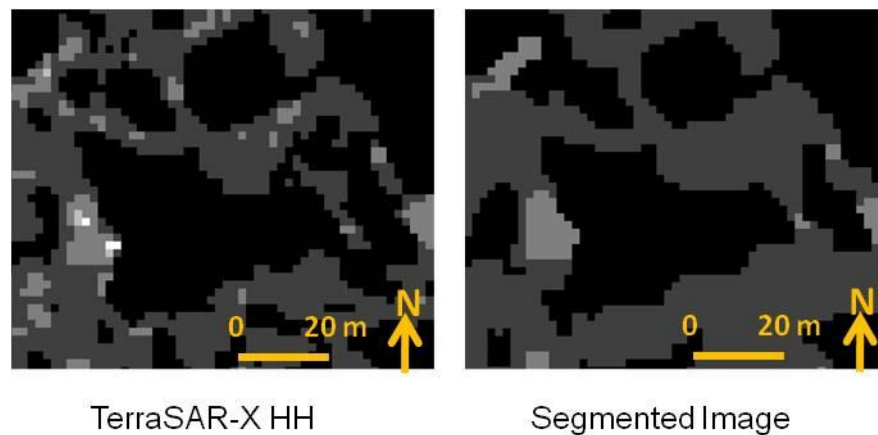


Figure 7.22: TerraSAR-X HH original image (non-texture image) before and after segmentation

7.4.2 Image Object-Oriented Classification

The object-based image classification approach based on the spectral and contextual information inherent in image objects generated from image segmentation process was discussed in section 7.4.1 (Malambo, 2009). Classification of the segmented objects is the second stage of the contextual analysis and takes full advantage of the information on the image objects (i.e. spectral values, shape and texture information). The ‘assign class’ algorithm was used instead of class description, because active classes contain exactly one class. This step provides valuable classification results (Definiens, 2006). Each class was defined by a nearest-neighbour classifier. The nearest-neighbour classifier is based on given sample objects or training areas that are typical representatives of a class. The procedure of nearest-neighbour classification in the Definiens software is similar to that described for supervised classification (see section 7.3.2).

Four classes (*Water*, *Wetland*, *Grassland* and *Builtup/Trees*) were established for the nearest-neighbour classification and categorized similar to the classes of the maximum likelihood classification (Section 7.3.2.1). Prototype segment samples of training areas for each class were selected randomly from the image objects by using the sampling tool in the Definiens software. Selection of samples was based on knowledge of the study area and high-resolution images from Google Earth (Section 7.3.2.1). Samples were selected according to feature value and signature and were compared with other classes. Various tools were used to verify that the selected samples were the most suitable ones. For the samples of training signatures, separability can be visually verified in the sample editor. The separability of classes can be checked via the feature space plot to ensure a satisfactory level, as shown in Figure 7.23.

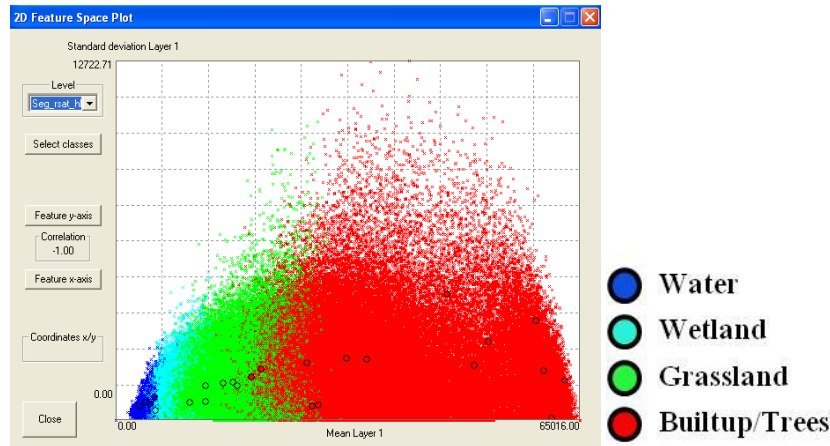


Figure 7.23: Checking signatures separability using Definiens 2D feature space plot for training classes

After establishing the desired classes and assigning suitable samples to the classes, classification was performed. Object-oriented classification was implemented for the two SAR sensors using non-texture HH images and the *occurrence data-range* and *mean* texture images. Reasons for this selection were discussed in Section 7.3.2. Contextual classified images were subjected to an accuracy assessment with the use of an error matrix. The error matrix was based on reference samples selected randomly from the image objects. The user accuracy, producer accuracy, overall accuracy and Kappa Index of Agreement (KIA) of classified images were also computed.

7.4.2.1 Object-Oriented Classification of Radarsat-2 HH and TerraSAR-X HH Images

Visual examination of the object-based classification results for Radarsat-2 HH texture images (Figure 7.24) demonstrated that water bodies are distinguished well compared to other land cover types. Classified images of the texture image and the original image both identified water bodies very well. The classified images therefore appear similar to one another in terms of delineating the *Water* class with only very few differences. The statistical results presented in the error matrix in Table 7.18 used for the accuracy assessment show very high overall accuracy for both types of classified images. Results of the accuracy assessment of the classified image without texture variables show an overall accuracy of 92.3%, while with texture variables the overall accuracy improved to 94.2%. The KIA, which reflects the agreement percentage between the classified

image and the reference data, is 0.8881 and 0.9138 for the original and the texture images, respectively, indicating a very good classification (see Table 7.18). Producer and user accuracy of *Water* class for both classified images reached 100%, except for the original image, which has a user accuracy of 80%. These highly accurate results for water object classification indicate that the proposed approach of contextual classification for water bodies is suitable for water identification. Furthermore, the contextual analysis shows that the Radarsat-2 HH ultrafine original image without texture variables is capable of classifying *Water* class to a high level of accuracy.

The classified images from the TerraSAR-X HH displayed very high discrimination between the land cover classes, particularly for the *Water* class. The homogeneity of water-body shape is well defined and distinguishable even with the classified single X-band image (Figure 7.25). The object-oriented classification error matrix results indicate that the *Water* class is highly accurate (100%) in terms of producer and user accuracy when classifying both types of images (Table 7.19). The classified original image provided an overall accuracy of 90.9%, and upon classifying the texture image this improved to 97.2% (Table 7.19). The KIA of the classified original image computed an agreement of 0.8713, while with the classified texture image the KIA improved to 0.9593. The very high accuracy of the classified images from the TerraSAR-X Stripmap along with the visual assessment results indicate that contextual classification is more credible than other traditional classification methods. Moreover, water body mapping can be implemented to very high accuracy by applying the proposed approach for the TerraSAR-X Stripmap imagery.

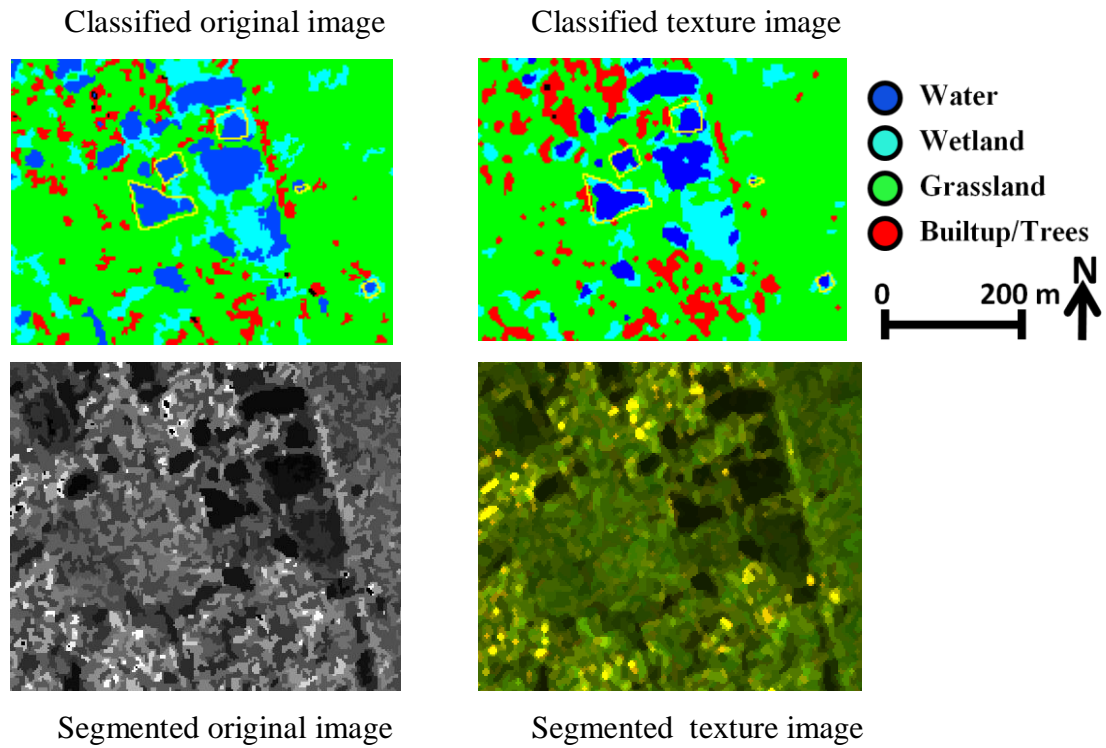


Figure 7.24: Comparison of object-oriented classification between original image and texture image (*occurrence data-range and mean*) of Radarsat-2 HH, along with the segmented images

Table 7.18: Confusion matrix comparison between texture image and non-texture image contextual classification - Radarsat-2 HH

Classes		Original Image		Texture Image	
	Overall Accuracy	92.3%		94.2%	
	KIA	0.8881		0.9138	
		Prod. Acc.%	User Acc.%	Prod. Acc.%	User Acc.%
<i>Water</i>	100.00	80.00	100.00	100.00	
<i>Wetland</i>	50.00	100.00	100.00	100.00	
<i>Grassland</i>	100.00	100.0	100.00	100.00	
<i>Builtup/Trees</i>	94.44	100.0	94.21	100.00	

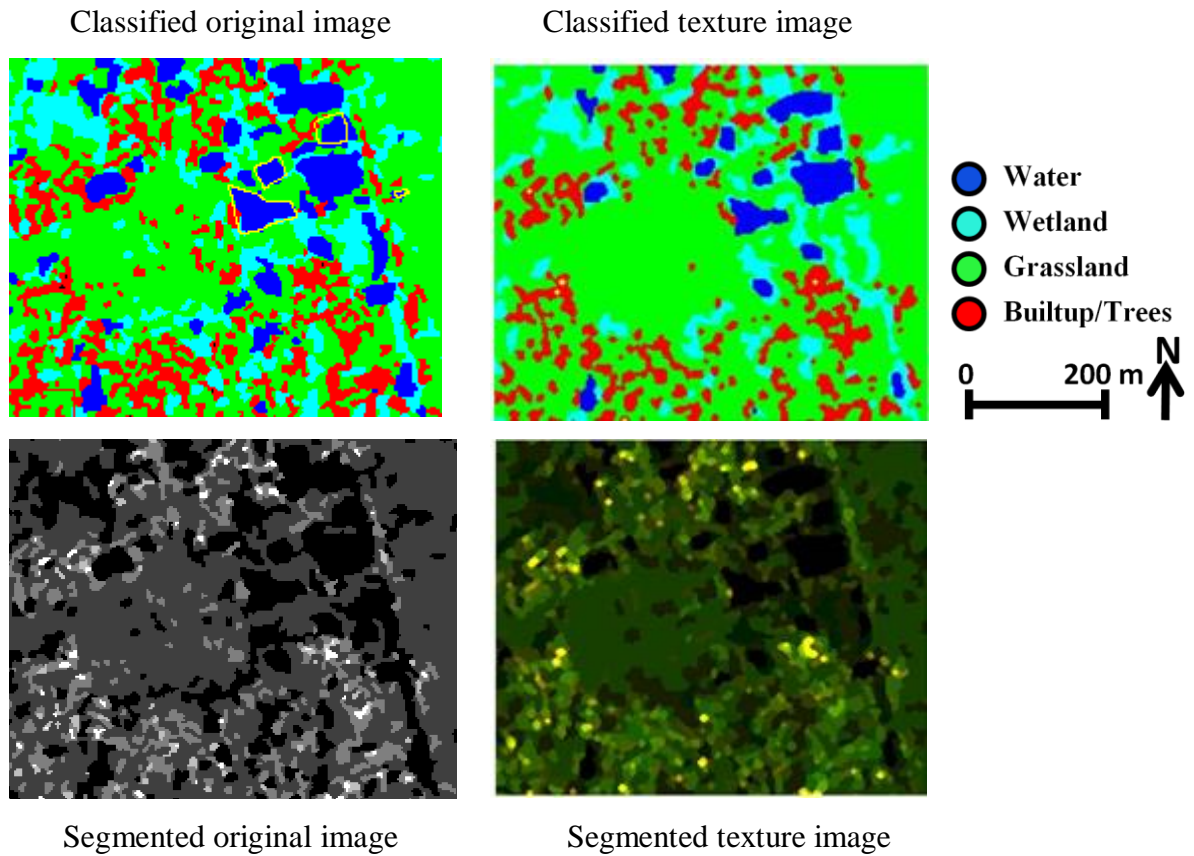


Figure 7.25: Comparison of object-oriented classification between original image and texture image (*occurrence data-range and mean*) from TerraSAR-X HH, along with the segmented images

Table 7.19: Confusion matrix comparison between texture image and non-texture image contextual classification - TerraSAR-X HH

Classes		Original Image		Texture Image	
	Overall Accuracy	90.9%		97.2%	
	KIA	0.8713		0.9593	
		Prod. Acc.%	Prod. Acc.%	User Acc.%	User Acc.%
<i>Water</i>		100.00	100.00	100.00	100.00
<i>Wetland</i>		100.00	100.00	100.00	100.00
<i>Grassland</i>		100.00	100.00	100.00	100.00
<i>Builtup/Trees</i>		80.00	100.00	94.21	100.00

7.5 Comparison between Radarsat-2 and TerraSAR-X

A comparison between SAR sensors was conducted in order to demonstrate their relative advantages for flood mapping. The SAR images used in this study have no distortion before performing geocorrection other than a slight translational offset which occurred to the west direction. Results of geocorrection showed that Radarsat-2 images were shifted by 46 m and TerraSAR-X by 8 m. This means that improvements of TerraSAR-X raw images quality in terms of pixel position accuracy in relation to the map projection might help in reducing the efforts required for geocorrection.

A visual assessment for spatial sizes of water bodies was conducted by measuring a number of water bodies with different sizes obtained from density sliced classification of the *water* class from both SAR sensors. The water body sizes were compared to the dGPS data in order to determine the degree of similarity. Table 7.1 shows measurements of the water body examples. From the comparison, both sensors give almost similar sizes of water bodies for sizes more than 3000 m² while water bodies less than 1300 m² the TerraSAR-X is better with around 100 m² compared to the same water body in the dGPS data.

A visual comparison of the supervised classification images was performed between occurrence and co-occurrence within Radarsat-2 HH images and also between classified images of Radarsat-2 and TerraSAR-X classified images. The comparison between image classifications before and after applying the median 3×3 window filter indicates an improvement in image classification for the two sensors' images after using the mean filter (see Tables 7.4, 7.5, 7.10, and 7.11). Image classification with co-occurrence of three variables shows that *water* class can easily be delineated with a high level of identification similar to the occurrence of two variables (section 7.3.3.2) (Table 7.9).

The visual comparison of the supervised classification maps between the two sensors indicates that Radarsat-2 HH has good homogeneity and discrimination in *water* class but the TerraSAR-X HH has better homogeneous appearance and identification of the *water* class over the Radarsat-2 (see Figures 7.12 and 7.15). Accuracy of water classification is high in both sensors. However, the user's accuracy of *water* class of the Radarsat-2 HH is 94.30% while TerraSAR-X HH image classification achieved higher

user's accuracy (98.78%) (See Table 7.25). The overall accuracy and Kappa Coefficient of the Radarsat-2 and TerraSAR-X are almost similar to each other with 90.41% - 0.8521 and 91.52% - 0.8828 respectively. The user's accuracy of the other classes has much similarity except *grassland* class in Radarsat-2 computed better (93.03%) than TerraSAR-X (89.70%). The *wetland* class in TerraSAR-X computed better (84.74%) than Radarsat-2 (73.49%) (see Table 7.25). The *water* class has been confused with *wetland* class in both sensors' classified images. In Radarsat-2 the *wetland* confusion estimated 11.4% which might interpret the reason for the bias which occurred on the user's accuracy which decreased to 94.30%. This result is lower than that of the TerraSAR-X (98.78%) which has very low confusion around 2.0% (see Tables 7.5 and 7.10).

Image segmentation which is the first stage of the contextual classification was applied to SAR images. Segmentation parameters of each sensor's image vary. While the scale parameters of Radarsat-2 imagery is (100), it is (10) with images of TerraSAR-X for non-texture image. Parameters of colour/factor of both sensors were close to each other and found to be 0.3/0.7 and 0.2/0.8 for Radarsat-2 and TerraSAR-X respectively (See Tables 7.16 and 7.17). The object-based classification implemented in the e-cognition environment achieved very high accuracy for both SAR products (see Tables 7.18 and 7.19).

The comparison between Radarsat-2 and TerraSAR-X products shows that both sensors have to some extent similar capability for mapping floods. However, TerraSAR-X appears to be more effective in flood detection than Radarsat-2. One of the reasons for this difference might be because of the wavelength differences in which the contrast ratio between water and the land features is less with longer wavelength (Drake and Shuchman, 1974). Table 7.20 outlines some results of the comparison between the two sensors.

Table 7.20: A brief comparison between images of Radarsat-2 and TerraSAR-X for water detection using HH polarisation, 3m, and high incidence angles.

	Radarsat-2	TerraSAR-X	Reference
Position accuracy of WB location	46 m shifting	8 m shifting	Figure 6.6
Water volume scattering (visual comparison)	Less	More	Appendix 8.1
WB Spatial size delineation compared to dGPS	Poorer	Better	Table 7.1
Supervised classification (water user accuracy)	94%	98%	Sections 7.3.3 and 7.3.4
e-cognition classification (water user accuracy)	1.0	1.0	Section 7.4

7.6 Area Estimation

An important aspect of flood extent mapping is to generate reliable estimates of the area affected. Despite this, many published mapping studies fail to include any quantitative assessment of the quality of flood area estimates. A study by Powell et al (2004) reviewed 26 per reviewed papers on mapping and concluded that only four included randomly selected reference data from high resolution imagery and/or field data but that three of these used fewer than 50 reference sample points and the fourth does not include an error matrix. To help address such concerns and to quantify bias in water area estimation and to assess the precision of the area mapping, the validation data were aggregated into two classes water and non-water and presented in error matrix form for both Radarsat-2 ultrafine and TerraSAR-X Stripmap and spotlight imagery. The overall accuracy summarised by the prevalence statistic is greater than 0.928 or 93% agreement for all three sensors, see tables 7.21 to 7.23. This is a very high figure, better than one would expect from automated classification of optical multispectral remotely sensed data, and is almost certainly explained by the distinctive backscatter response of water compared with other floodplain surfaces.

Table 7.21 Error matrix for Radarsat-2 HH ultrafine Data

Radarsat-2	Image Class	Reference Data			
Occurrence		Water	Non-water	Total	User Accuracy
	Water	2614	158	2772	94.30%
	Non-water	336	10705	11041	96.96%
	Total	2950	10863	13813	
Producer Accuracy		88.61%	98.55%		96.42 %

Table 7.22 Error matrix for TerraSAR-X Stripmap Data

TerraSAR-X	Image Class	Reference Data			
Occurrence		Water	Non-water	Total	User Accuracy
	Water	2747	34	2781	98.78%
	Non-water	203	7352	7555	97.31%
	Total	2950	7386	10336	
Producer Accuracy		93.12%	99.54%		97.71 %

Table 7.23 Error matrix for TerraSAR-X spotlight Data

TerraSAR-X – spotlight	Image Class	Reference Data			
Occurrence		Water	Non-water	Total	User Accuracy
	Water	5866	179	6045	97.04%
	Non-water	662	5018	5680	88.35%
	Total	6528	5197	11725	
Producer Accuracy		89.86%	96.56%		92.83 %

The error matrix for the assessment of the Radarsat-2 HH ultrafine data (table 7.20) has a total of 13,813 sampled reference pixels giving a total of 105,525 m² analysed. The study area is 204 km² which represents approximately 0.18% of Bangladesh's floodplain land area. This means that 0.05% of study area is used as reference data divided among water bodies, wetland, woodland and urban area.

The data from the error matrices are used to calculate bias and precision. Bias measures the difference between expected and actual map class and can be calculated from the

distribution of predicted positive and predicted negative pixels taken from the map and reference data. The precision of the area estimate can be calculated for a given confidence limit by calculating variance provided that there is a sufficiently large sample. The equations used to calculate bias and variance are given below.

Φ = area to be estimated

x_i = random sample element

E = Expected value

$$\text{Bias}(\Phi) = E[\Phi] - \Phi = \frac{\text{predicted positive} - \text{predicted negative}}{n}$$

$$\text{Variance}(\Phi) = \frac{1}{n(n-1)} \sum_{i=1}^n (\bar{x}_i - x_i)^2$$

Foody (2010) discusses the impact of imperfect ground reference data and demonstrates the impacts it can have on reported Producer's accuracy. While this study does not allow an error value to be attributed to the reference data every effort was made to ensure these are separate from the training data, selected randomly and collected as carefully as possible.

7.6.1 Flood Area Estimates

There are a number of ways that flood area can be estimated from remotely sensed image maps. The simplest is a probability-based approach using a simple random sampling (SRS) estimator. The advantage of the SRS estimator is that it is simple, intuitive and unbiased. A variation on SRS that is used in forest area mapping and can be usefully applied for estimating flood area, uses a model-assisted difference estimator (McRoberts 2010). The estimate assumes that the sample is randomly selected and unbiased.

The reference data described in the sampling design (section 5.6.1) is randomly sampled which allows a probability-based inference approach to be applied. This approach assumes (1) that samples are selected randomly; (2) that the probability of sample

selection can be estimated; (3) that the sampling fraction is proportional to the total population. Despite randomisation, there are several possible sources of bias that include:

1. Selecting sample areas from the random sample for convenience or because of availability of suitable reference data;
2. The reference data may be of variable quality and that quality may not be distributed randomly;
3. Operator bias could be present either in the distribution of errors in the output maps and also in the selection and interpretation of the reference data.

Although, the expectation is that probability-based estimators are unbiased, this cannot be assumed. An elegant approach that combines the advantages of simple random sampling with model-based estimators is the model-assisted difference estimator (McRoberts 2010; McRoberts *et al.* 2010a; McRoberts *et al.* 2010b). A model-assisted estimator uses map data to make an initial inference but uses the probability-based sample to validate the result. In this analysis the model-assisted difference estimator has been applied since the area of water can be calculated easily from the classified output. Bias and Variance are estimated from the probability-based sample as presented in tables 7.20-7.22.

7.6.1.1 Radarsat-2 HH Data and TerraSAR-X HH Data

At the 95% confidence level, the estimate of water area, based on the model-assisted stratified sampling design is $34.58 \pm 1.31 \text{ km}^2$ for Radarsat-2 products and $35.98 \pm 1.22 \text{ km}^2$ for TerraSAR-X. Since the water mapping was carried out when the country was not subject to flooding, it is possible to use the model-assisted estimator to predict the total land area of water in the country. Making the assumptions that the total land area of Bangladesh is $147,570 \text{ km}^2$ and of that $110,678 \text{ km}^2$ is floodplain similar in characteristics to the study area, then the model-assisted estimator predicts that $18,761 \text{ km}^2$ or 12.71 % of the country consists of water land cover with regard to the Radarsat-2 data while it is $19,520 \text{ km}^2$ or 13.23 % in terms of the TerraSAR-X data. This compares with a figure of $10,090 \text{ km}^2$ or 6.8% taken from the Bangladesh Bureau of Statistics. This is a predicted estimation based on the results obtained from the study area by using the model-assisted difference estimator. Results of the estimation can be verified by

cross-checking it with new statistics, if available, from the Bangladesh Bureau of Statistics or other governmental authorities. Appendix 6.1 shows more details about water area estimation for Bangladesh using Radarsat-2 and TerraSAR-X data. Note the similarities and differences between the different data sets seen in the Tables 7.24 and 7.25.

Table 7.24: Summary of water area estimates for the 204 km² study area comparing mapped areas and areas estimated from a model-assisted difference estimator

Sensor	Area in km ²	Confidence Interval (at 95% CL) km ²	% Water
Radarsat-2 HH	34.58	1.31	16.95
TerraSAR-X	35.98	1.22	17.64
Difference	1.4	0.09	0.69

The overall accuracy (prevalence) is very high which ranges from 92 %-97% of the pixel and object classification methods for both SAR sensors. At the 95% confidence limit, the Stripmap TerraSAR-X data has a confidence interval of 12.15 km², the ultrafine Radarsat-2 13.13 km² and the spotlight TerraSAR-X 20.18 km². Therefore, the data product that provides the highest level of mapping precision is the HH polarized Stripmap data from TerraSAR-X, see table 7.25.

Table 7.25: Comparison of sensors for water area estimation

	Radarsat-2		TerraSAR-X		
Date of acquisition	30-01-2009		20-01-2009		07-04-2009
Pixel size	3 m		3 m		1.5 m
Incidence angle	39 degrees		39-41 degrees		
Look direction	Right		Right		Right
Polarization	HH		HH		HH
Product beam mode	Ultrafine		Stripmap		VHR spotlight
Frequency	C-band		X-band		X-band
Mapping technique	ENVI – per pixel	Definiens – object-based	ENVI – per pixel	Definiens – object-based	ENVI – per pixel
Bias	-0.01289	+	-0.01635	+	-0.04119
Variance	2.589*10 ⁻⁶	+	2.218*10 ⁻⁶	+	6.118*10 ⁻⁶
Producer's Accuracy	0.886	1.0	0.931	1.0	0.899
User's Accuracy	0.943	1.0	0.988	1.0	0.970
Overall Accuracy (Prevalence)	0.964	0.942	0.997	0.970	0.928
Study area % Water	16.95		17.64		
Based on 95 % CL Confidence Interval km ²	1.31	+	1.22	+	2.02

+ Not reported by software

7.7 Summary

This chapter has proposed a methodology for texture and contextual analysis and presented results using Radarsat-2 and TerraSAR-X images using various mapping techniques. The density slice method based on levels of radar backscatter differences was used for mapping water bodies to assess the ability to identify water using different polarizations for the two SAR sensors. The results indicate that unsupervised classification using ISODATA and K-Means techniques appears to be unable to identify to a sufficient degree very small water bodies from the SAR data. Supervised maximum likelihood classification was used to successfully discriminate *Water* class from other land cover types using texture data with occurrence and co-occurrence variables. A median 3×3 window was applied to the texture images to ascertain any improvements it

may provide in water body area identification. The supervised classified images were assessed for accuracy with the use of a confusion matrix. Comparison of accuracy results of the classified images between Radarsat-2 and TerraSAR-X are summarised in Table 7.26. A contextual classification approach was used because its knowledge base includes shape, texture and the relational network of information in addition to the spectral information provided in an image. An error matrix was used for quantitative assessment of the contextual classified images.

Table 7.26: Comparison of accuracy assessment (in percentage) of Maximum-Likelihood classified image between both SAR sensors.

Classes		RSAT-2HH		TSX HH	
	Overall Accuracy	90.41		91.52	
	Kappa Coeff.	0.8521		0.8828	
		Prod. Acc.	User Acc.	Prod. Acc.	User Acc.
Water	88.61	94.30	93.12	98.78	
Wetland	85.24	73.49	92.40	84.74	
Grassland	94.49	93.03	93.63	89.70	
Built-up/Trees	83.35	89.26	84.93	90.64	

Textural and contextual analysis of the sensors' images using the proposed methodology provided a number of significant results:

1. Both C-Band Radarsat-2 and X-Band TerraSAR-X have HH and VV polarization beam modes. A comparison of polarization shows that HH yields higher mapping accuracies for both sensors.
2. Image texture variables provide additional quantitative information that helps to discriminate water bodies from other land cover types. Therefore, classified texture images achieved higher accuracy than images without texture variables.

Applying the median 3×3 window offers better identification and mapping of water bodies. Furthermore, water can easily be delineated to a high level of precision with the selected texture variables: occurrence *data-range* and *mean* for products of both sensors and *co-occurrence mean*, *variance* and *contrast* for Radarsat-2 products.

- 3 C-Band Radarsat-2 and X-Band TerraSAR fine beam modes with a similar spatial and radiometric resolution of 3 m yield similar results with small differences, indicating that the SAR response of water is not strongly affected by radar frequency.
- 4 Supervised statistical classification using at least two texture variables and HH polarized SAR data provides homogeneous and separable land cover classes with high accuracy. Note the main source of confusion occurs between water and wetland; other land cover classes are well separated from water.
- 5 The classified image from the spotlight HH (1.5 m resolution) appears to provide more detailed information regarding very small water bodies compared to the Radarsat-2 ultrafine and TerraSAR-X Stripmap data. However, the spotlight imagery has a limited swath coverage of (5×10 km) that may limit its operational application during extensive flood events. Also, the area estimates from spotlight data are less precise than equivalent Radarsat-2 and TerraSAR-X Stripmap products.
- 6 Contextual classification within Definiens software has the advantage of providing additional context information for defining a class, such as spectral values, spatial features and object shapes. Object-oriented classification with texture images is therefore well suited for mapping water bodies. However, the results also indicate that by using object-oriented classification with the original SAR images without texture variables, water bodies may also be mapped to very high accuracy. Consequently, the proficiency of object-oriented classification for non-textured SAR images may reduce the effort and time required for flood mapping.

- 7 Published water area estimates for Bangladesh suggest that approximately 6.84% of the country is open water. The results from this study suggest that this figure may be an underestimate. In the floodplain area under study, Radarsat-2 maps 16.95 % of the area as open water and TerraSAR-X maps 17.64 % as open water.

Chapter Eight:

THE POTENTIAL APPLICATIONS OF NEW SAR DATA FOR FLOOD DISASTER MANAGEMENT

8.1 Introduction

The SAR data used in this study were acquired from the German TerraSAR-X and the Canadian Radarsat-2 satellites, which were launched in June 2007 and December 2007 respectively at the outset of this research project. Since then a new era of high spatial resolution space-borne SAR systems has begun. The lack of assessments of the new high resolution radar satellite systems' products for mapping water areas necessitates the need for this type of study for better exploitation of such systems to support flood disaster management. Thus, this thesis is one of the first studies to attempt to perform an empirical assessment of the capabilities of high spatial resolution SAR imagery for water body mapping and to carry out a comparative evaluation between X-band TerraSAR-X and C-band Radarsat-2 systems in order to establish which performs best for mapping small water bodies.

The evaluation of the high resolution Radarsat-2 and TerraSAR-X products conducted in this thesis, along with the optimal methods for SAR image processing for water body mapping developed (chapters 5, 6, 7), were aimed to be used for mapping flood area in order to support flood disaster management and ,for water management purposes. The methods allowed mapping with high accuracy the water extent (section 7.3). Selecting the right SAR system parameters in addition to the appropriate processing methodology and high accuracy classification procedure will certainly improve the quality of flood mapping products.

Since using actual floods for assessing the accuracy of the high resolution SAR system for water extent detection is difficult (section 2.5), mapping small water bodies was an appropriate alternative investigation method for implementing the research objectives (section 1.2). As a result, the approaches used for water body mapping derived from this study might be applicable to flood area mapping.

8.2 Current Operational Applications of SAR Satellite Data for Flood Risk Management

Applications of remote-sensing information have increasingly demonstrated its effectiveness in providing support in all phases of the disaster management cycle (Bessis et al., 2004; Adams & Huyck, 2005; Ito, 2005; Gitas et al., 2008; De Groeve & Riva, 2009; Joyce et al., 2009a; Guha-Sapir et al., 2011). Applications can take various types, including urban vulnerability assessment, preparation of damage maps for emergency impact areas, monitoring of potentially hazardous regions and dealing with disaster impacts (Verstappen, 1995). Well-documented examples demonstrate successful applications of remotely sensed data in supporting disaster management, particularly for response efforts (The Disaster Charter, 2010). Table 8.1 lists some potential ways of using remote-sensing data to support activities in the various phases of disaster management.

Table 8.1: Potential ways of using remote sensing to support disaster management phases (adapted from: Lewis, 2009).

Disaster Phase	Mitigation	Preparedness	Response	Recovery
Cyclone	Risk modelling; vulnerability analysis.	Early warning; long-range climate modelling.	Identifying escape routes; crisis mapping; impact assessment; cyclone monitoring; storm surge predictions.	Damage assessment; spatial planning.
Drought	Risk modelling; vulnerability analysis; land and water management planning.	Weather forecasting; vegetation monitoring; crop water requirement mapping; early warning.	Monitoring vegetation; damage assessment.	Informing drought mitigation strategies.
Earthquake	Building stock assessment; hazard mapping.	Measuring strain accumulation.	Planning routes for search and rescue; damage assessment; evacuation planning; deformation mapping.	Damage assessment; identifying sites for rehabilitation.
Fire	Mapping fire-prone areas; monitoring fuel load; risk modelling.	Fire detection; predicting spread/direction of fire; early warning.	Coordinating fire-fighting efforts.	Damage assessment.
Flood	Mapping flood-prone areas; delineating flood plains; land-use mapping.	Flood detection; early warning; rainfall mapping.	Flood mapping; evacuation planning; damage assessment.	Damage assessment; spatial planning.
Landslide	Risk modelling; hazard mapping; digital elevation models.	Monitoring rainfall and slope stability.	Mapping affected areas.	Damage assessment; spatial planning; suggesting management practices.
Volcano	Risk modelling; hazard mapping; digital elevation models.	Emissions monitoring; thermal alerts.	Mapping lava flows; evacuation planning.	Damage assessment; spatial planning.

8.2.1 Current Capacity of Using SAR Satellites for Flood Disaster Management by Space-Based Initiatives

Most important factors controlling the production of SAR flood maps are the reliability of the information content, the usability of the product, and the efficiency of the delivery of data in order to help manage the impact of events. The use of SAR systems for mapping floods is applicable to emergency planning; the identification of flood warning areas and evacuation routes, search and rescue; and the prediction of the impacts of changes on flood extents. The potential operational capacity of SAR systems has been demonstrated in a range of products used to map flood events by a number of space-based initiatives relevant to disaster management. For example, the Disaster Charter facilitates access to satellite data (i.e. SAR systems) for disaster management (i.e. floods) (see section 2.4). Satellite images obtained from Radarsat-2 and TerraSAR-X have been made available via the Disaster Charter for a number of recent flood events.

Every year the Disaster Charter has supported numerous activations responding to a range of major disasters (floods, earthquakes, landslides, wildfires, wind storms, volcanic eruptions, ocean storms and wave surges). For example, during 2009 the Disaster Charter was activated 18 times for flood disasters, which is the highest recorded number of activations for any type of disaster in that year. Figure 8.1 shows the number of activations by hazard type for 2009, highlighting the fact that flooding tends to be the most frequently occurring natural disaster.

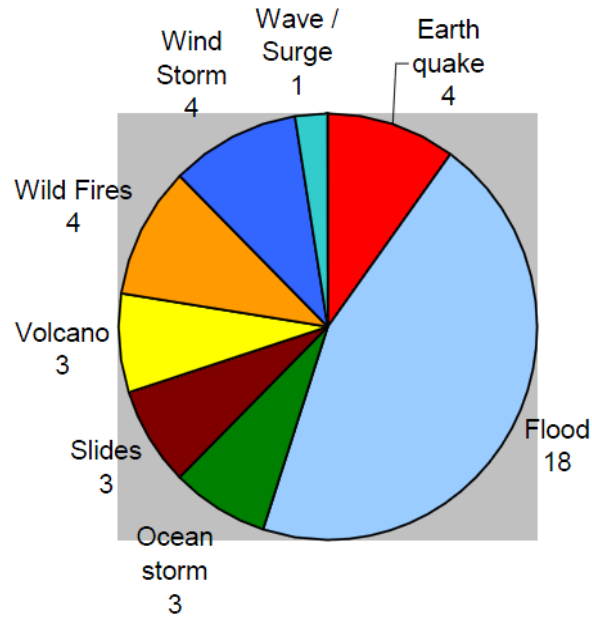


Figure 8.1: Number of activations of the Disaster Charter by hazard type in 2009; note that the highest number (18) of activations occurred for flooding (adapted from: Disaster Charter, 2010).

The remote-sensing imagery delivered for the Disaster Charter have been acquired from optical and radar sensors. For example, the total number of SAR data products delivered during 2009 was 362 (with 122 ex-archive and 240 new acquisitions) from the ENVISAT, Radarsat, ALOS and TerraSAR-X satellites (Disaster Charter, 2010) (Figure 8.2).

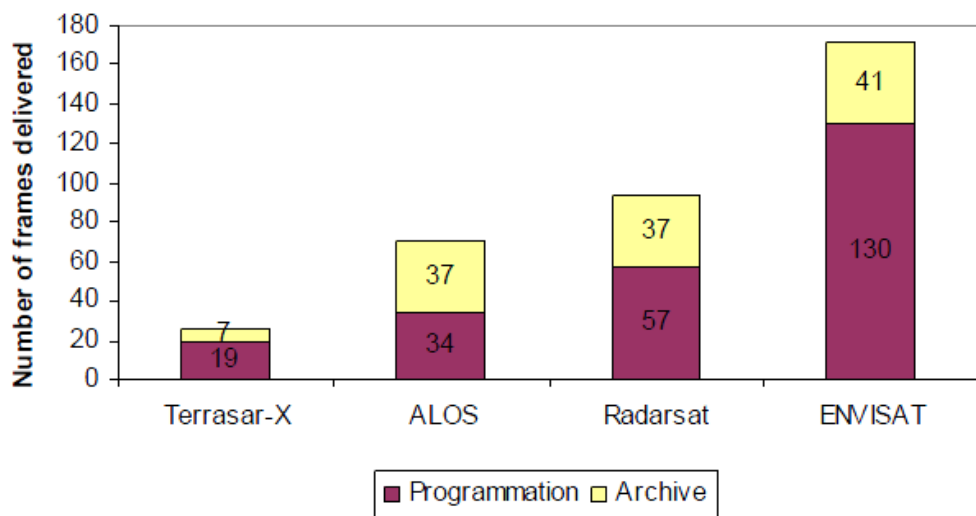


Figure 8.2: SAR data consumption during 2009 by quantity of archive and new-acquisition data (adapted from: Disaster Charter, 2010).

An example of an activation of the Disaster Charter for supporting flood disaster is the 2010 Colombia flood. Several days of continuous heavy rainfall caused widespread flooding in the country. According to official figures, 2.1 million people were affected, 279 people died, several thousand homes were destroyed and 300,000 were damaged, and around 150,000 hectares of crops were destroyed (OCHA, 2010). The Colombian government declared a state of emergency and set up a Crisis Room to coordinate the emergency response activities with the cooperation of UN agencies to provide technical assistance (Reliefweb, 2010).

The Disaster Charter was activated for data acquisition on 6 December 2010 (Disaster Charter call ID 347) by request from the Federal Emergency System of Argentina. The national space agency of Argentina (CONAE) worked as project management (Disaster Charter, 2010). A number of satellite images were provided by the Canadian Space Agency (CSA), Japan Aerospace Exploration Agency, China National Space Administration and the United States Geological Survey. A number of images were provided by the Radarsat-2, ALOS PALSAR, JERS-1 SAR and SPOT5 satellites, while data processing and the production of change detection maps were produced by CONAE (Disaster Charter, 2010). Figure 8.3 shows an example of a flood extent map of the affected region delivered for the flood-relief efforts and produced by CONAE. The map production was based on Radarsat-2 imagery acquired on 9 December 2010 for flood detection and archived imagery from Radarsat-1 acquired on 7 April 2010 for the pre-flood situation, while LANDSAT Thematic Mapper imagery was used as reference, obtained on 29 January 2010. The flood map illustrated in the figure was produced in 1:350,000 scale using a change detection method to generate the map by applying colour composition. Blue denotes the Radarsat-1 image showing pre-flood water bodies, and red indicates the Radarsat-2 image displaying the flood extent.

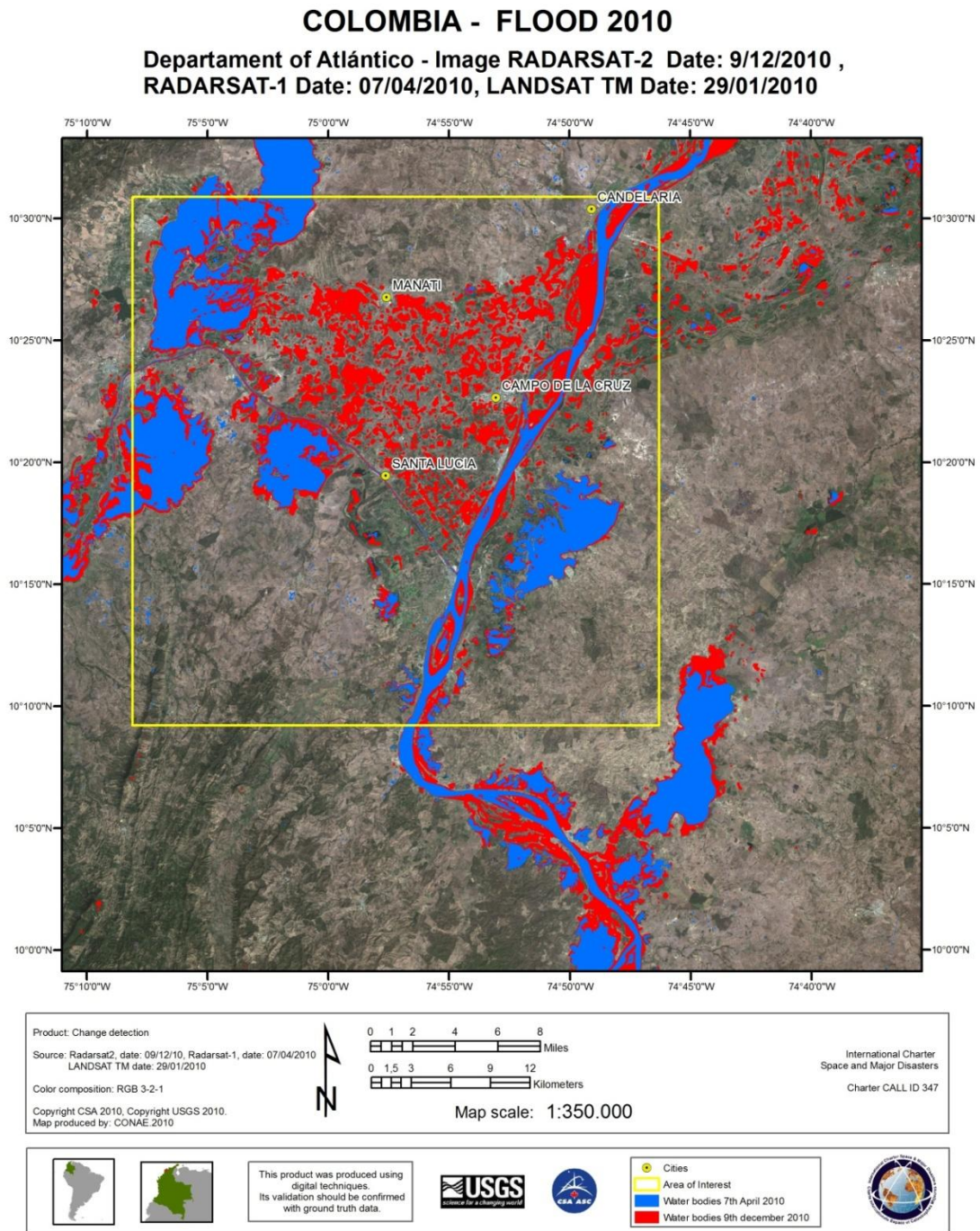


Figure 8.3: Colombia flood 2010. Colour code: blue – water bodies, 7 April 2010 (Radarsat-1); red – water bodies, 9 December 2010 (Radarsat-2) (source: Disaster Charter, 2010).

Although, numerous space-based data can be delivered through international initiatives for disaster management, there are still problems encountered using SAR data. These include image costs, satellite tasking, data acquisition, data processing and integration

to GIS for map generation, analysis, and interpretation. Lack of training in using SAR imagery is another issue to be overcome. The high costs of SAR imagery may limit its usefulness for a number of poor countries affected by disasters. Although the support given by the Disaster Charter for delivering free of charge space-based data, the Disaster Charter activation requests are only supplied for major disasters. Processing SAR products requires advanced skills for producing detailed flooded area maps with appropriate analysis and interpretation usable for the end-users. Agencies that cooperate with the Disaster Charter perhaps use simplistic methods for mapping flood extent. In addition, it is not always clear how data have been processed which calls into question the reliability of the resulting maps.

High spatial and temporal resolution remotely sensed data is necessary for mapping and monitoring flood extent and flood damage assessment rapidly in order to support effective flood risk management and to assist in immediate efforts towards emergency response. A single satellite does not have the ability to provide imagery quickly enough to be of use for immediate response, because of insufficient overpass frequency. A solution to this problem is to acquire data from a constellation of satellites (Sarti et al., 2001; Joyce et al., 2009a; Naval Gund, 2009). Multiple SAR satellites travelling on the same orbital plane will increase the revisit rate and will be more supportive in flood risk management. Examples of constellations of satellites carrying radar sensors are the Italian X-band COSMO-SkyMed (CONstellation of small Satellites for Mediterranean basin Observation), the Canadian Radarsat mission, and the Sentinel-1 from European Space Agency (ESA). COSMO-SkyMed is composed of four small satellites equipped with high-resolution X-band SAR sensors. The COSMO-SkyMed supplies products for a variety of applications, some of which are for risk management (COSMO-SkyMed, 2007). The Canadian C-band Radarsat Constellation Mission (RCM) includes three satellites planned to be launched in 2014 and 2015 and can be expanded to include additional satellites. Imaging modes and spatial resolution of RCM will be similar to those of Radarsat-2 (CSA, 2010). The Sentinel-1, planned for launch in 2013, is based on a constellation of two C-band SAR satellites (ESA, 2011).

The need for rapid disaster response based on satellite remote sensing has initiated a number of research projects aimed at developing onboard image processing technology for extracting the required information from images (Yuhaniz and Vladimirova, 2009;

Yuhaniz et al., 2007). The onboard system is composed of two main image processing functions: image compression and autonomous image analysis and selection. Several experimental satellite missions with onboard image processors have been launched, such as UoSat-5, BIRD, PROBA, TiungSAT-1, FEDSAT, and Techsat21 (Yuhaniz et al., 2007). Examples of possible onboard applications include detection of flooding, volcanic activity and fires. The onboard NASA EO-1 flood change detection algorithm using optical images was developed to downlink science data only when change occurs (Ip et al., 2006). Another onboard flood monitoring application using an automatic change detection system with multispectral images has been developed at the Surrey Space Centre (Yuhaniz et al. 2007). Based on tile-by tile change detection and a fuzzy logic inference algorithm, Yuhaniz and Vladimirova (2009) have developed an onboard system which achieved good accuracy for flood detection. Onboard processing technology developments have also extended to onboard UAVSAR investigations for disaster monitoring fire and hurricane induced disturbances over forests (see for example, Muellerschoen et al., 2008).

8.3 The Potential Operational Applications of the Developed Methods in the Phases of Flood Disaster Cycle

Maps and thematic analysis derived from space-based information, particularly SAR satellite imagery, can support those dealing with disasters during all phases of the disaster cycle (Voigt et al., 2007). SAR images can be considered to be a significant source of information in supporting flood disaster management in terms of identifying potential flood areas, rapid mapping and monitoring flood events and aiding flood damage assessment (Chesworth, 2006). Determining the most appropriate satellite data to use in terms of spatial resolution is very important, particularly in the response phase. For example, satellite imagery at low or medium spatial resolution with large area coverage is suited to providing a quick overview at the macro-scale of an area affected by widespread hazards such as flooding (Messner, 2007). In contrast, flood disaster assessment at the meso- and micro-scale requires high-resolution SAR satellite imagery for regional and local flood management that can provide more detailed data down to single buildings. The significant advantages of using satellite imagery for flood risk management can be extended to all phases of the disaster management cycle (see

Section 2.3) and according to the requirements of each phase, rather than focusing on one phase (i.e. response) (Joyce et al., 2009b).

Therefore, the methods developed and used in this thesis using the high resolution Radarsat-2 ultrafine and TerraSAR-X stripmap products for mapping water bodies, can be used for operational applications in all the phases of the flood disaster management cycle. Two main types of data product might be produced from the new SAR imagery: 1) detailed local-scale maps which may support the production of flood risk assessment maps, updating aspects of flood, vulnerability mapping and assisting with the hydrological assessment of flood plains; and 2) overview maps at the regional scale to better understand the general situation of the flood area extent and so identify areas at most risks for flooding.

The following sections highlight how SAR satellite imagery can be used to support efforts in all phases of the disaster cycle: pre-flood mitigation and preparedness; response to floods; and post-flood recovery (Figure 8.4).

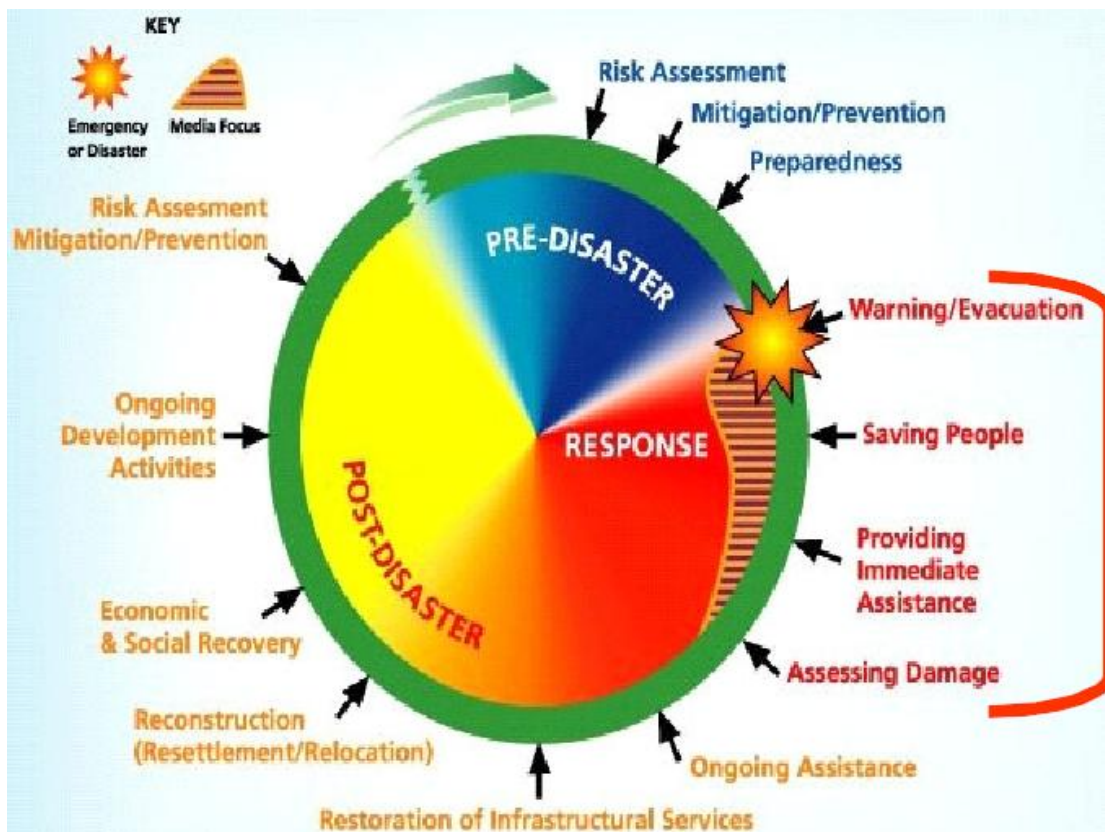


Figure 8.4: Phases of flood disaster management cycle (Adapted from: Platzeck, 2009).

8.3.1 Pre-Flood Mitigation and Preparedness

The potential applications of radar data in the phase of pre-flood mitigation and preparedness may take several forms. Mapping vulnerable land use and flood-prone areas is important for identification of flood hazards and updating vulnerability aspects of flood prone areas. During this phase SAR satellite images can be used for monitoring changes in river configuration and bank erosion based on the frequent satellite revisits, and multi-date satellite data can be used to map the poorly drained areas (Bhanumurthy et al., 2010). Accordingly, adequate measures for constructing flood defences and strengthening embankments can be identified. In addition, monitoring the progress of a flood from its inception by using SAR products derived from the proposed methods obtain from repeat-pass new SAR sensors can assist the development of early-warning systems. Moreover, the high accuracy of water body mapping derived from this research might support hydrologic models that can assist in predictions of potential flood extent and forecasting.

Monitoring hydrological changes over time during the phase before a flood using the new high resolution SAR imagery will assist in flood forecasting and the potential flood risks. Mapping water bodies in this phase will also help during flood events in terms of differentiating actual floods from permanent or semi-permanent water bodies, necessary to assess the potential impact of events. For example, mapping water bodies showing the distribution of water bodies used for aquaculture, reservoirs or other purposes would allow the impact of a flood event to be properly evaluated. Figure 8.5 illustrates an example of the potential use of very high resolution spotlight TerraSAR-X HH for inventory of very small water bodies that might assist flood impact assessment during the phase of flood disaster response.

Seasonality is another concern that must be considered when comparing before and after flood event imagery. Having good quality resource data on water bodies is very important to help differentiate established water bodies from floods. Figure 8.6 illustrates an example application of the developed methods to differentiate water bodies from flooding. In addition to the information required about the extent of damage of the current disaster, the information about the risk associated with potential future disasters (i.e. water contamination) is also needed. In order to assess these risks,

it is often necessary to have detailed information about pre-existing water bodies (i.e. locations, sizes etc). Drinking water contamination, which is a major risk associated with flood events, can be minimized if the potential risk is well recognised (WHO, 2005). In Bangladesh, for example, water bodies are important for drinking water, agriculture and for livestock. During a major flood, if the water is contaminated, then it might be possible to determine how many people might be affected based on population data. Floods may increase the potential for communicable diseases by contamination of the water bodies (Du et al., 2010). Therefore, mapping water bodies before flooding will also help assessment of water contamination (i.e. chemical or diseases) and the impact on people during flood that rely on static water bodies. This information may assist in providing immediate health needs for a flood affected community.

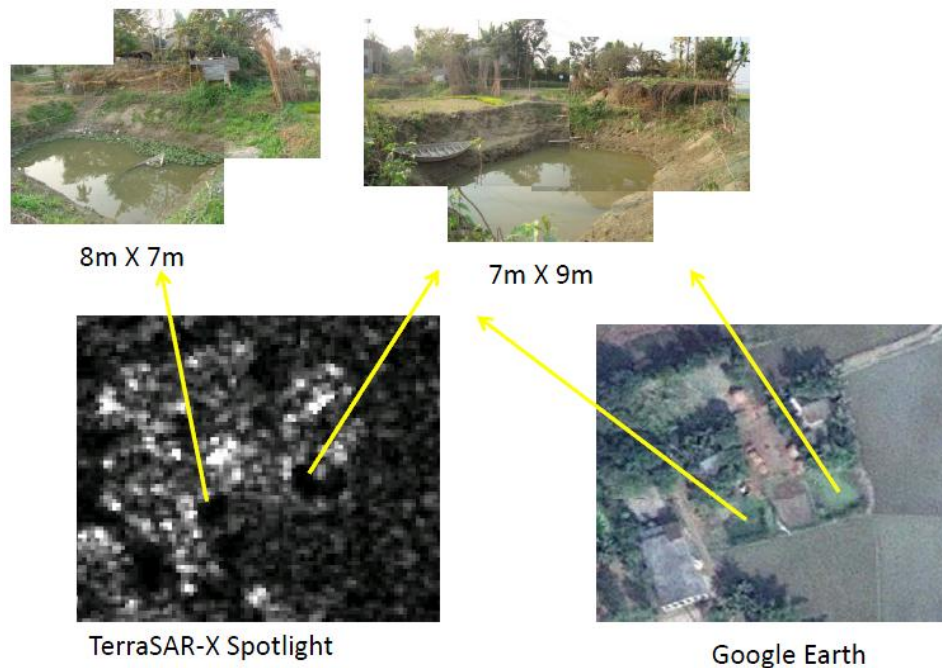


Figure 8.5: Potential use of TerraSAR-X spotlight HH for mapping very small water bodies will assist during flood disaster in terms of flood impact assessment. The example is extracted from the study area.

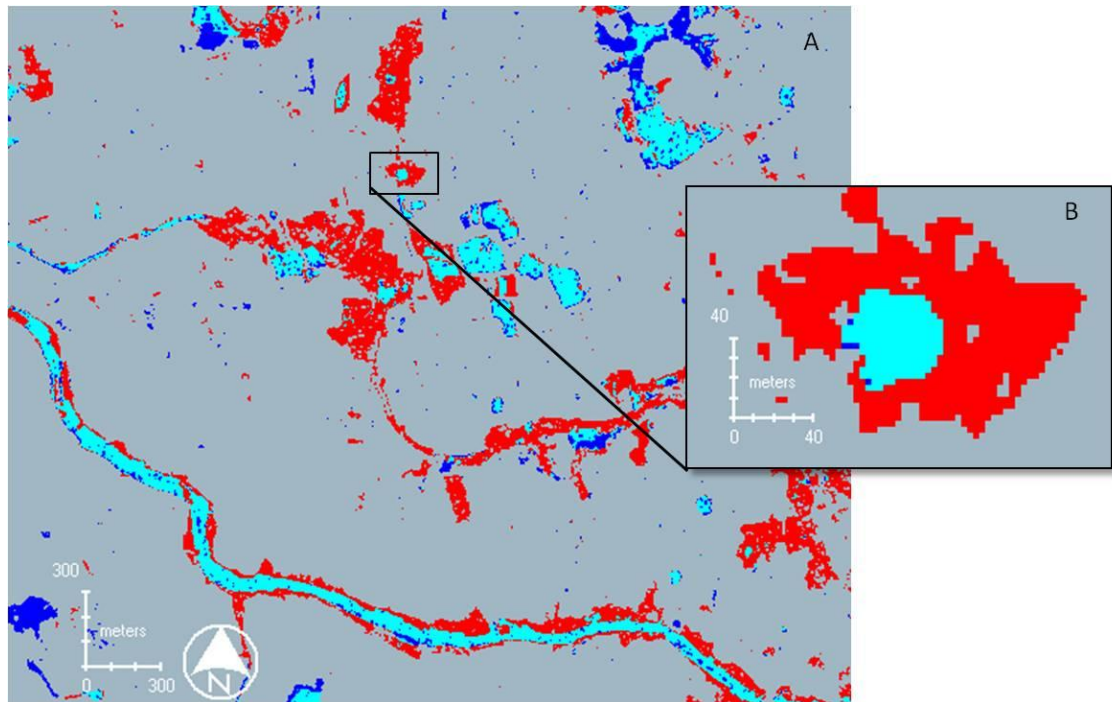


Figure 8.6: An example of discrimination between permanent water bodies and flooding extracted from TerraSAR-X HH imagery of the study area. In the zoomed in area (B) a permanent water body is shown in cyan and after flooding in red colour, showing the significance of the proposed methods. Blue (only before) and Grey (background).

8.3.2 Response to Floods

During the response phase delivering detailed and accurate remote sensing information of areas affected by floods can be essential in providing effective assistance for reducing the impacts of a flood disaster. Maps derived from SAR satellite images can be used for regional large-scale flood risk mapping, and detailed maps at the local scale for affected areas can be generated. Detailed-level flood maps include information about submerged buildings, roads and other physical infrastructures. These may take the form of, for example, mapping and monitoring flood extent, flood damage assessment and producing maps for evacuation and search and rescue operations.

In order to provide rapid and accurate flood maps during flood disasters this thesis proposed a number of methods and procedures to assist with flood area mapping. These methods can be used by those who are working to deliver accurate and timely mapping derived from remote sensing information. Figure 8.7 illustrates an outline of the optimal water mapping methodology which can be specified in three main categories: SAR data

specifications; producing overview (regional scale) flood maps and detailed (local scale) flood maps. Acquisition of the appropriate SAR products is the first stage for mapping flood extent successfully. This does not exclude using other auxiliary data such as geographical information and optical data. The appropriate SAR data parameters are the HH ultrafine Radarsat-2 and HH stripmap TerraSAR-X with high incidence angle (i.e. 39°-42°). Second, an overview flood map at the regional scale to enable disaster managers to achieve an overview of the situation required rapid processing and analysis of satellite imagery can be generated. Therefore, in this stage a backscatter density slicing technique should be performed with the use of *mean* texture filter and threshold value ranges 0.0-5000 for Radarsat-2 and 0.0-80 for TerraSAR-X products (e. g. using ENVI software packages). Third, a detailed flood map at a large scale (i.e.1:20,000) could be produced, based on image classification using a maximum likelihood supervised classification with occurrence texture filters of Data range and Mean for both SAR sensors. Object-based classification is another alternative method using e-cognition software (i.e. Definiens) for segmentation parameters specification and contextual classification as illustrated in Figure 8.7 for both SAR sensors.

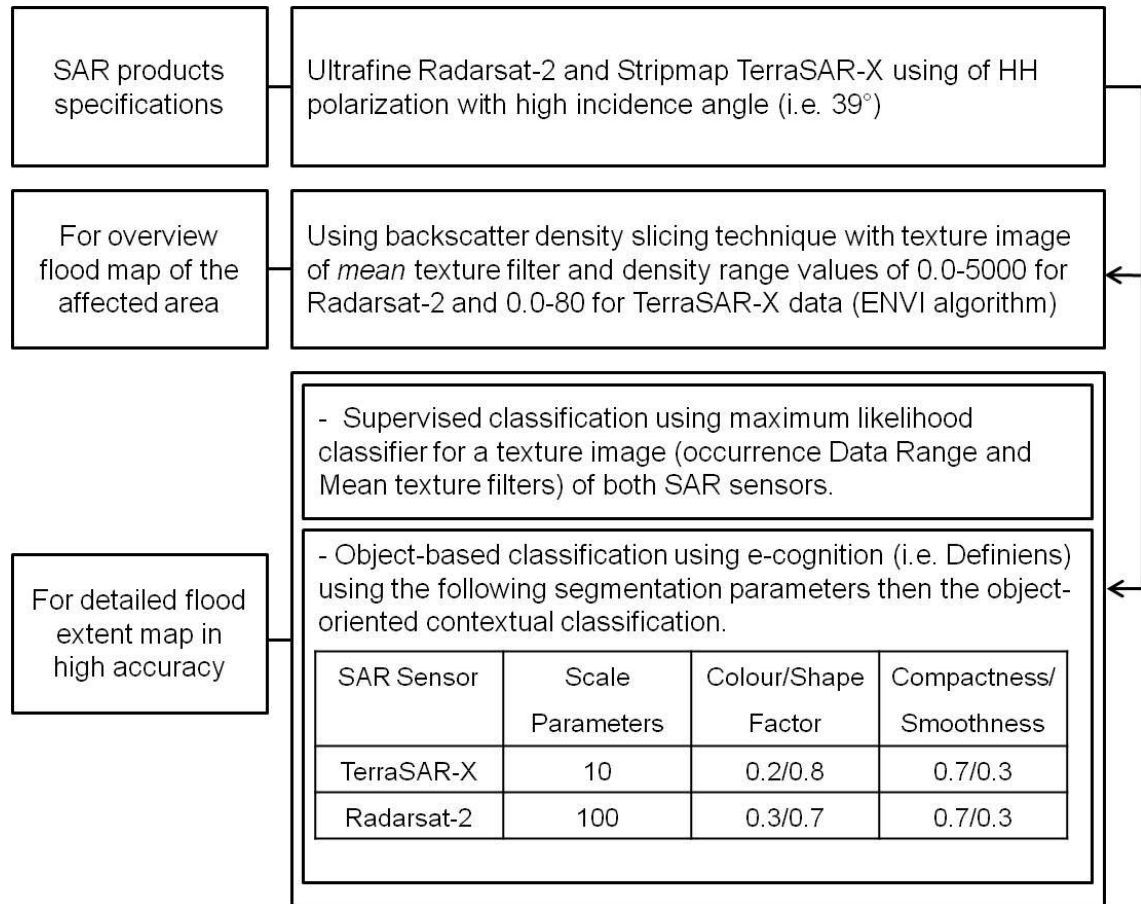


Figure 8.7: Outline of the water area mapping proposed methods for operational flood disaster applications for flat topography areas.

An example of the application of flood extent map generation according to the outline methods mentioned above can be employed in a flood disaster. The pre-disaster imagery obtained from archived SAR data can be used to extract the water body class before the occurrence of the flood event. This layer of pre-disaster water bodies can then be overlaid with the flood extent map derived from the water classification. The new map product is a water surface change detection map derived from the post classification change detection method. Figure 8.8 shows an example of change detection flooding (in red colour) during the wet season in the study area while the water bodies before the wet season is in blue.

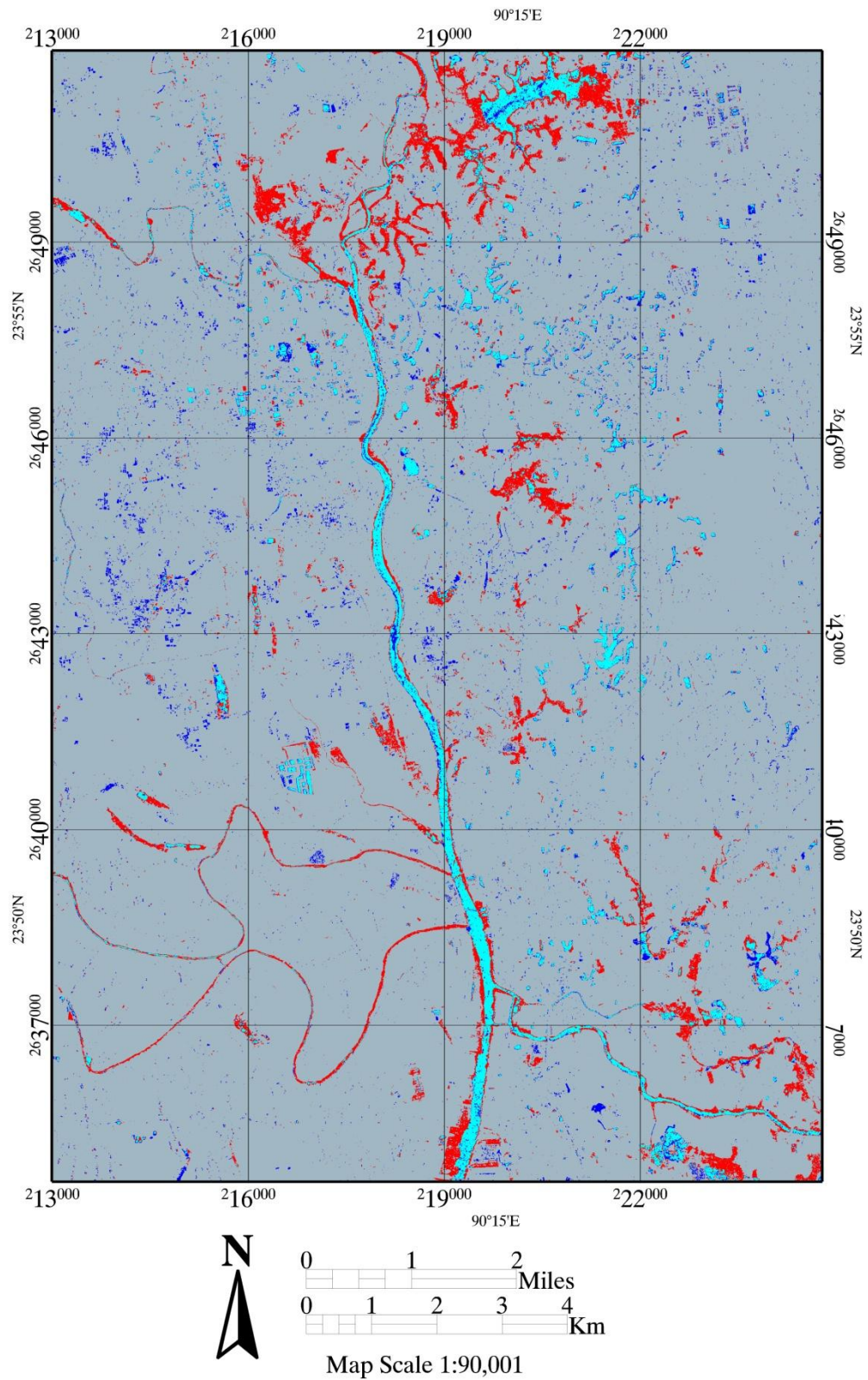


Figure 8.8: Changes detection using TerraSAR-X HH showing flooding in red. Colour code: Blue- WBs before; Red- WBs after; Cyan-no change; Grey- background.

In order to demonstrate the facilitation of stakeholder access to high quality information during a major flood event, a water class layer of the study area derived from image classification has been prepared to *mash-up* in Google Earth (Figure 8.9). This shows how easily maps can be disseminated via web services, which may be used for flood operational applications.

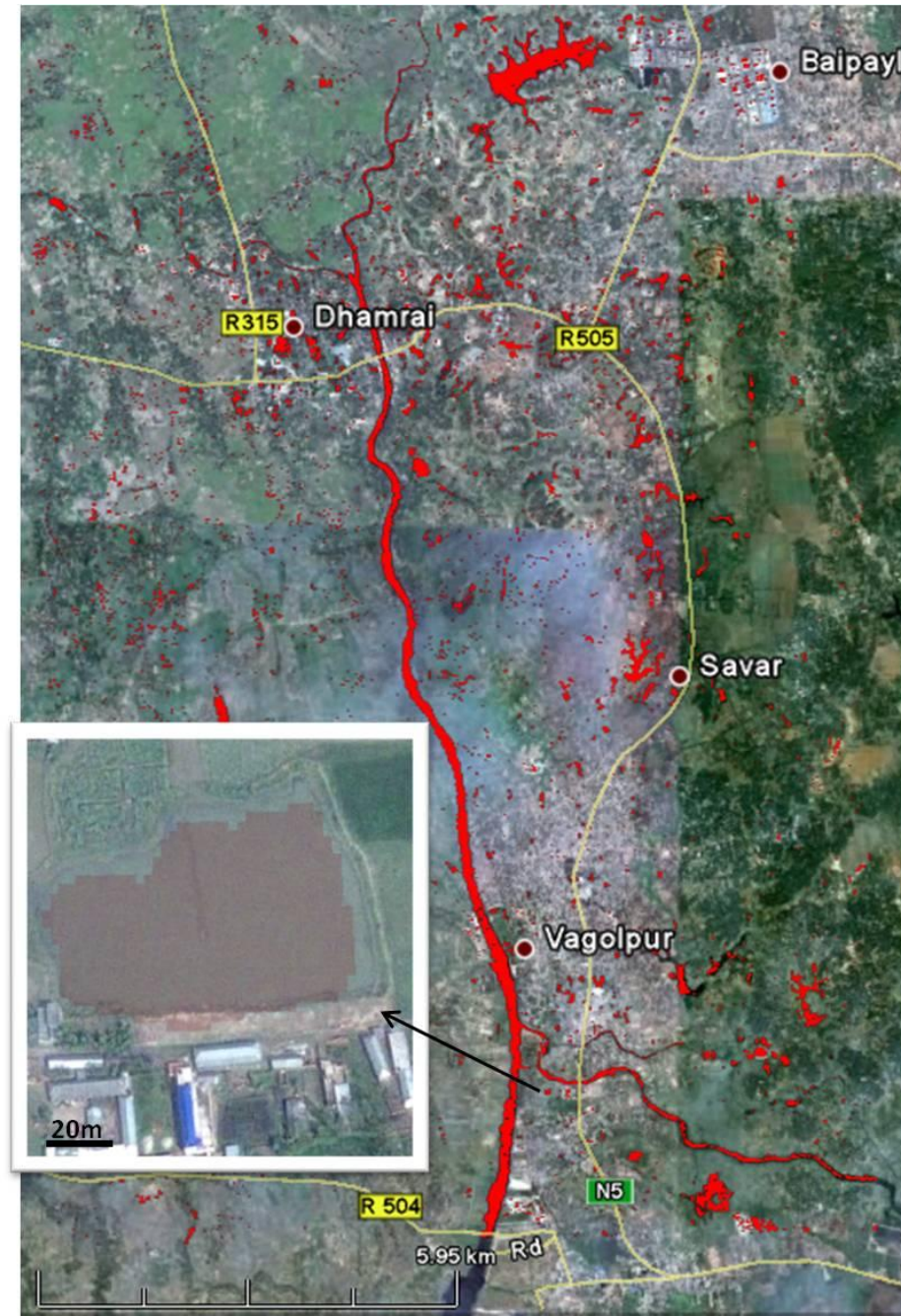


Figure 8.9: An example of *water* class layer of the study area (in red) produced from the developed methods and mashup in the Google Earth. Note the water body zoomed in (the white rectangle) showing the water layer in transparent red colour presenting the ability of the proposed water area mapping method.

8.3.3 Post-Flood Recovery

During the recovery process remote-sensing data can be collected on multiple occasions in order to monitor post-flood restoration in terms of the identification of areas vulnerable to flood hazards, and accordingly, to carry out rehabilitation and reconstruct physical infrastructure. Acquiring SAR imagery regularly after a flood disaster will allow monitoring of recovery activities and restoration of damaged areas (Shibayama et al., 2008). Moreover, applications of SAR satellite imagery can be extended to assist activities for debris removal and strengthening and reconstructing flood defences.

Flood damage assessment maps for the affected areas obtained from new SAR systems during the response phase can be used to support recovery planning and assist restoration infrastructural services for the short and long term. In the short term, the derived flood extent maps from SAR imagery will help in decision-making for identifying invulnerable sites for transitional shelters for re-housing people. While in the long term, permanent solutions for housing may be derived, allowing for example relocation of settlements that become vulnerable to the impact of future floods. Moreover, in the post-flood phase, sustained flooding may increase the potential of communicable diseases. Mapping flooded areas and the distribution of these areas particularly those among settlements might assist the healthcare planning. Furthermore, the usefulness of mapping flood area extent could be extended to be used for insurance and compensation purposes. Claiming for compensation due to areas affected by floods might be verified and supported by information derived from implementing the proposed methods due its high spatial accuracy.

8.4 Summary

The evaluation of the high resolution Radarsat-2 and TerraSAR-X products conducted in this thesis along with the optimal methods for SAR image processing for water body mapping developed were aimed to be used for mapping flood area in order to support flood disaster management. Since using actual floods for assessing the accuracy of the high resolution SAR system for water extent detection is difficult, mapping small water bodies was an appropriate alternative method for implementing the research objectives.

As a result, the developed methods used for water body mapping derived from this study might be applicable to be used for flood area mapping.

Two main types of data product might be produced from the new SAR imagery: 1) detailed local-scale maps that may support the production of flood risk assessment maps, updating aspects of flood, vulnerability mapping and assisting with the hydrological assessment of flood plains; and 2) overview maps at the regional scale to better understand the general situation of the flood area extent and so identify areas at most risks for flooding. Applications of the developed methods can be used for operational applications in all the phases of the flood disaster management cycle: pre-flood mitigation and preparedness; response to floods; and post-flood recovery

During a pre-flood phase, monitoring the progress of a flood using multi-date SAR products derived from the proposed methods can assist the development of early-warning systems. Mapping water bodies in this phase might assist in several aspects:

- The support of hydrologic models that can assist in predictions of potential flood extent and forecasting.
- The differentiation between actual floods and permanent or semi-permanent water bodies, to assess the potential impact of events.
- The assessment of water contamination (i.e. chemical or diseases) and the impact on people during flood that rely on static water bodies.

For the response phase and in order to provide rapid and accurate flood maps, an outline of the recommended optimal water mapping methods and procedures are as follows:

- SAR products specifications: HH polarization of Radarsat-2 ultrafine and TerraSAR-X stripmap with high incidence angle.
- For overview flood map of the affected area: using backscatter density slicing technique with texture image of *mean* texture filter and density range values of 0.0-5000 for Radarsat-2 and 0.0-80 for TerraSAR-X data using the ENVI algorithm.
- For detailed flood extent map in high accuracy: supervised classification using maximum likelihood classifier for a texture image with occurrence *Data Range* and *Mean* texture filters for both SAR sensors and also using as alternative

method the e-cognition object-based classification for the contextual classification.

During the post-flood phase, the proposed methods can be applied for different applications such as:

- Mapping flooded areas can assist strengthening and reconstructing flood defences and for debris removal during the post-flood phase.
- Flood damage assessment maps obtained during the response phase can also be used to support recovery planning and assist restoration infrastructural services.
- Mapping flooded settlements, which would assist the healthcare planning regarding the potential of communicable diseases.
- Mapping flood area extent for the post-disaster phase, which could be to be used for insurance and compensation purposes.

Chapter Nine:**CONCLUSIONS AND DIRECTIONS FOR FUTURE STUDY****9.1 Conclusions**

This thesis investigates the potential use of high resolution SAR remote sensing for detecting small water bodies by using multiple sensors through the examination of the ability of Radarsat-2 and TerraSAR-X data to separate water from other land cover types. There is extensive literature on SAR remote sensing and its applications in delineation of flooding. However, there is little documentation on the techniques associated with the applications of high resolution SAR remote sensing for detailed mapping and in particular for the detection of small water bodies. Mapping small water bodies is important for the potential of SAR for flood extent mapping. The importance of assessing high resolution SAR remote sensing data products with regard to the proposed research project is that, because flooding is an increasing problem, this technique will facilitate the use of the high resolution SAR data in the operational applications of flood risk management and water resource management.

Findings of this study emphasized the effectiveness of the new SAR imagery to add new information not available from optical systems. Cost is an issue for routine (i.e. non-disaster situation) use of SAR imagery but this cost may be out weighted by the good quality of mapping and also it is a low cost when compared to ground survey or air photo survey as a per unit.

Image texture variables from Radarsat-2 and TerraSAR-X provide valuable quantitative information that helps to discriminate water bodies from other land cover types. Therefore, classified texture images achieved higher accuracy than images without texture variables (improved from 86.9% to 90.4%-Radarsat-2 and from 87.3% to 91.5%-TerraSAR-X). Applying the median 3×3 window filter offers better identification for water bodies. Furthermore, the bodies of water can easily be delineated to a high level of identification with the selected texture image via either occurrence or co-occurrence variables.

The most effective image processing technique for mapping appears to be supervised classification using at least two texture variables and HH polarized SAR data. This technique provides homogeneous and separable land cover classes and in particular high overall accuracy as summarised by the prevalence statistic for water classification (96.42 %-Radarsat-2 and 97.71 %-TerraSAR-X). Results of object-oriented classification with texture images show very high accuracy (1.0- for both sensors) at mapping water bodies. However, the results also indicate that by using object-oriented classification with the original SAR images without texture variables, land covers may also be mapped to high overall accuracy (92.2%-Radarsat-2 and 91%-TerraSAR-X). Consequently, the proficiency of object-oriented classification for non-textured SAR images may reduce the effort and time required for flood mapping. A comparison of HH and VV polarization of both C-Band Radarsat-2 and X-Band TerraSAR-X beam modes shows that HH yields higher mapping accuracies for both sensors.

Pre-flood assessment using Radarsat-2 and TerraSAR-X SAR imagery during monsoon period will better estimate aquaculture resources, help quantify impacts of flood events, and will assist in supporting flood risk and water resources management. Flood maps derived from this study are in high accuracy for water extent detection (i.e. 93%) and with detailed information (i.e. can detect water area down to 150 m²), and can be easily disseminated via the web such as by Google Earth *Mash-up*.

9.2 Main Findings

The main findings derived from this research are the following:

1. Radarsat-2 ultrafine and TerraSAR-X stripmap co-polarized data map 85-95% of man-made water bodies within the study area.
2. The most suitable occurrence texture variables for Radarsat-2 products were *data range*, *mean* and *variance*, while for TerraSAR-X products, only the *data range* and *mean* texture filters showed good performance. The co-occurrence texture variables of *mean*, *variance*, *dissimilarity* and *contrast* were found to show the best performance in calculating water texture regions for Radarsat-2.
3. C-Band Radarsat-2 and X-Band TerraSAR-X fine beam modes with a similar spatial and radiometric resolution of 3 m yield similar results with small differences, indicating that the SAR response of water is not strongly affected by

frequency. Moreover, results demonstrate that small water bodies, down to areas of 150m² can be identified routinely from ultrafine Radarsat-2 and stripmap TerraSAR-X beam modes backscatter and backscatter texture data.

4. The overall accuracy of the water area estimation of the study area derived from the prevalence statistic is greater than 0.928 or 93% agreement for Radarsat-2 ultrafine and TerraSAR-X stripmap products. This is a very high figure, better than one would expect from automated classification of optical multispectral remotely sensed data.
5. The expected benefits of the thesis are:
 1. Improved rapid assessment of small water bodies that can easily be integrated into local and national planning processes;
 2. Assistance in supporting water resources management; and
 3. Helping to inform the choice of image products best suited for flood risk management and flood response.

9.3 Directions for Future Study

Since the aim of this study is to evaluate the ability of the high resolution SAR remote sensing data to accurately mapping water bodies and flood extent, and consequently interesting findings have been derived from this evaluation, however the research project is challenging. The recent advance in SAR systems technology needs to be accompanied by studies to demonstrate applications in order to adequately exploit their capabilities and also direct the future SAR development particularly in the field of mapping water areas and flood disaster management. There are a number of recommendations for future research and applications.

1. Operational application of the derived image processing in an actual flood event is important to understand its ability with regard to the actual time requirement for processing and delivering flood maps directly to the disaster response teams. This is essential in terms of understanding to what extent the proposed methods practically satisfied the end users requirements.
2. Although the international disaster agencies play a significant role in facilitating delivering space-based data for disaster response, there are still problems

encountered achieving rapid and satisfactory satellite-based information. Therefore, looking at standardization of SAR image processing for mapping floods to become more routine and may be used by International disaster agencies (i.e. the Disaster Charter, UN-SPIDER) and the proposed methodology in this thesis may be useful in this area.

3. Results derived from this study show high accuracy of water body maps without fusing other data with SAR imagery. However, integrating optical and SAR data for flood mapping along with DEMs data specifically the high resolution DEM products from TanDEM-X might add more information. For example, integrating high resolution DEMs with SAR data would help to mask regions in built-up areas in order to separate non-water dark areas from water bodies and also to identify water levels.
4. Monitoring flood events (e.g. rainfall caused from monsoon) require data acquisition over several weeks. Therefore improving data processing workflow to allow SAR repeat coverage to keep pace with a flood as it develops is necessary in flood risk management.
5. The potential of new polarimetric SAR data (i.e. Radarsat-2) on mapping floods needs to be investigated. The cross-polarized data have different interactions with properties and land cover types. This might be useful for mapping floods particularly in vegetated and urban areas.
6. Further studies are required to assess the accuracy of trees/woodland classification as a separate *class* using the new SAR systems, and more investigations are needed to identify how accurately trees/woodland among urban areas can be distinguished from buildings.
7. The delay in delivering flood maps to the response teams in the ground may be due to a number of problems, such as tasking SAR sensors for data acquisition, time consuming when acquiring raw SAR data and then allocate data to operators and teams for image processing and water classification. Further research should be carried out to study the potential of onboard SAR satellite

image processing for flood change detection and testing the proposed methods of image processing for automatic flood mapping for rapid flood.

8. The potential of UAVs (Unmanned Ariel vehicles) in disaster management need to be more exploited and countries may need to think about the potential of this technology. Further research need to be conducted to develop methods for operational use of UAVs particularly UAVs equipped with SAR sensors. The onboard image processing technology mentioned above needs also more investigations to be integrated in the UAVs (i.e. Muellerschoen et al., 2008).

9. In order to support a timely access to earth observation data (i.e. SAR products), there is a need to an international Earth observation knowledge portal (i.e. UN-SPIDER) offering a 'one stop shopping' for using space-based data for flood disaster management. This can be done for example by providing the portal mentioned above the remote sensing products (i.e. SAR products) of specific flood disaster from agencies who have collaboration with the (i.e. UN-SPIDER). Therefore, teams of disaster management and humanitarian relief from authorities and organizations can easily and timely access to appropriate and value-added space-based products and flood risk maps without struggling with the bulk of non value-added satellite data uploaded to several websites.

References

- Abrahams, J., 2001. Disaster management in Australia: the national emergency management system. *Emergency Medicine*, 13(2), 165–173.
- Adam, N., Eineder, M., Yague-Martinez, N. and Bamler, R., 2008. TerraSAR-X high resolution SAR-interferometry – Proceedings of EUSAR, Friedrichshafen, Germany.
- Adams, B.J., and Huyck, C.K., 2005. The emerging role of remote sensing technology in emergency management. In: C. Taylor and E. VanMarcke, eds., 2005, *Infrastructure risk management processes: natural, accidental, and deliberate hazards*, ASCE Council on Disaster Risk Management, Monograph No. 1, May 2005, The American Society of Civil Engineers.
- Ahmed, A.M.M. and Roy, K. 2007. Utilization and conservation of water resources in Bangladesh. *Journal of Developments in Sustainable Agriculture*. 2(1), 35-44.
- Ahtonen, P. and Hallikainen, M. 2005. Automatic detection of water bodies from spaceborne SAR images. *International Geoscience and Remote Sensing Symposium*, 6: 3845-3848.
- Al-Khudhairi, D.H.A., Caravaggi, I. and Glada, S., 2005. Structural damage assessments from Ikonos data using change detection, object-oriented segmentation, and classification techniques. *Photogrammetric Engineering and Remote Sensing*, 71, 825–37.
- Allenbach, B., Andreoli, R., Battiston, S., Bestault, C., Clandillon, S., Fellah, K., Henry, J.B., Merer, C., Seius, H., Tholey, N., Yesou, H., and Fraipont, P., 2005. Rapid EO disaster mapping service: added value, feedback and perspectives after 4 years of Charter. *Geoscience and Remote Sensing Symposium, IGARSS'05. Proceedings IEEE International*, 25–29 July 2005.
- APFM, 2004. *Technical Support Unit. World Meteorological Organization. Associated Programme on Flood Management (APFM)*. [Online] available at: <www.unwater.org> [Accessed April 2011].
- Arzandeh, S. and Wang, J. 2002. Texture evaluation of RADARSAT imagery for wetland mapping. *Canadian Journal for Remote Sensing*, 28(5), 653-666.
- Baghdadi, N. Bernier, M. Gauthier, R. and Neeson, I., 2001. Evaluation of C-band SAR data for wetlands mapping. *International Journal of Remote Sensing*, 22(1), 71-88.
- Baghdadi, N., Zribi, M., Loumagne, C., Ansart, P. and Anguely, T.P. 2008. Analysis of TerraSAR-X data and their sensitivity to soil surface parameters over bare agricultural fields. *Remote Sensing of Environment*, 112, 4370-4379.
- BBS, 1999. Statistical Year Book of Bangladesh, 1998. Bangladesh Bureau of Statistics (BBS), Dhaka

- BBS, 2006, Statistical Yearbook of Bangladesh 26th edition. Bangladesh Bureau of Statistics (BBS).
- BBS, 2009, Statistical Yearbook of Bangladesh 28th edition. Bangladesh Bureau of Statistics (BBS).
- Bailly, J.S., Arnaud, M., and Puech, C.2007. Boosting: a classification method for remote sensing. *International Journal of Remote Sensing*, 28(7), 1687–1710.
- Bakimchandra, O., 2006. *Reconstruction of the 2003 Daya River flood, using multi-resolution and multi-temporal satellite imagery*. PhD thesis, The International Institute for Geo-information Science and Earth Observation, Enschede, The Netherlands.
- Banko, G., 1998. *A review of assessing the accuracy of classifications of remotely sensed data and of methods including remote sensing data in forest inventory. Interim report IR-98-081*. International Institute for Applied Systems Analysis, Austria.
- Barry, R.G. and Chorley, R.J. 1998. *Atmosphere, weather and climate*. Routledge, London and New York.
- Belliss, S.E., Pairman, D. and McNeill, S.J. 1998. Use of Radarsat data to map landslide erosion in steep landforms. Application Development and Research Opportunity (ADRO) Final Symposium, 13–15 October, Montreal, Quebec, Canada, Electronic Proceedings.
- Berardino, P., Fornaro, G., Lanari, R. and Sansoti, E., 2002. A new algorithm for surface deformation monitoring based on small baseline differential SAR interferometry. *IEEE Transactions on Geoscience and Remote Sensing*, 41, 2375–83.
- Bessis, J.L., Bequignon, J., Mahmood, A., 2004. The International Charter “Space and Major Disasters” initiative. *Acta Astronautica*, 54(3), 183–190.
- Bhanumurthy, V., Manjusree, P., Srinivasa, Rao, G., 2010. Flood disaster management. In remote sensing applications, Roy, P.S., Dwivedi, R.S., Vijayan, D., (eds). National Remote Sensing Centre, India.
- Brammer, H., 1994. The agroecology of Bangladesh’s floodplains. *Asia Pacific Journal on Environment and Development*, 1(2), 1–20.
- Brammer, H., 1995. Floods, flood mitigation and soil fertility in Bangladesh. *Asia Pacific Journal on Environment and Development*, 2(1), 13–24.
- Brisco, B. Touzi, R. van der Sanden, J.J. Charbonneau, F. Pultz, T.J. and D’Iorio, M. 2008. Water resource applications with Radarsat-2 – a preview, *International Journal of Digital Earth*, 1(1), 130-147.
- Brivio, P.A., Colombo, R., Maggi, M., and Tomasoni, R. 2002. Integrating of remote sensing data and GIS for accurate mapping of flooded areas. *International Journal of Remote Sensing*, 23(3), 429-441.
- Bruijn, K.M., 2004. Resilience and flood risk management. *Water Policy*, 6(1), 53–66.

- Campbell, B.A, 2002. *Radar remote sensing for planetary surfaces*. Cambridge University Press.
- CCRS, 2008. Fundamentals of remote sensing applications-tutorial. Canada Centre for Remote Sensing. [Online] available at: <www.ccrs.nrcan.gc.ca/resource/tutor/fundam/chapter5/14_e.php> [Accessed July 2008].
- CCRS. Canada Centre for Remote Sensing (CCRS). [Online] available at: <<http://www.ccrs.nrcan.gc.ca/>> [Accessed November 2010].
- CCRS, 2011. *Fundamentals of Remote Sensing*. Canada Centre for Remote Sensing (CCRS). [Online] available at: <www.ccrs.nrcan.gc.ca/resource/index_e.php#tutor> [Accessed March 2011].
- CEGIS, 2003. *Analytical framework for the planning of integrated water resources management*. Centre for Environment and Geographic Information Services, December 2003, version 2.0, Dhaka, Bangladesh.
- CERF, 2008. Annual report of the humanitarian / resident coordinator on the use of CERF grants. Narrative Reports 2008. The Central Emergency Response Fund (CERF), United Nations. [Online] available at: <<http://ochaonline.un.org/FieldReports/CERF/NarrativeReports2008/tabid/5513/language/en-US/Default.aspx>> [Accessed August 2011].
- Chen, P. Liew, S. C. and Lim, H. 1999. *Flood detection using Multitemporal Radarsat and ERS SAR data*. [Online] available at: <www.gisdevelopment.net/aars/acrs/1999/ps6/ps6044.asp> [Accessed July 2010].
- Cheng, P. and Toutin, T., 2010. Radarsat-2- Automated High Accuracy Geometric Correction and Mosaicking without Ground Control Points. GEOInformatic. [Online] available at: <www.pcigeomatics.com/pdfs/RADARSAT-2data.pdf> [Last accessed November 2011].
- Chesworth, S., 2006. A new era of spaceborne SAR and its contribution to disaster management and damage mitigation. *4th International Workshop on Remote Sensing for Disaster Response*, September 25~26, 2006, Cambridge, UK.
- Chunxia, X., Jixiana, Z., Guomana, H., Zhenga, Z., Jiaoa, W., 2008. Water body information extraction from high resolution airborne SAR image with technique of imaging in different directions and object-oriented. *The International Archives of the Photogrammetry, Remote Sensing and Spatial Information Sciences*. Vol. XXXVII. Part B7. Beijing 2008.
- CIA, 2011. Bangladesh map. The World Fact Book. [Online] Available at: <www.cia.gov/library/publications/the-world-factbook/geos/bg.html> [Accessed June 2011].
- Cityriskpedia, 2001. Dhaka. [Online] available at: <<http://www.cityriskpedia.com/?title=Dhaka>> [Accessed March 2011].

- Congalton, R.G. 1991. A review of assessing the accuracy of classifications of remotely sensed data. *Remote Sensing of Environment* 37(1), 35-46.
- Congalton, R.G. and Green, K. 1998. Assessing the accuracy of remotely sensed data: principles and practices. Boca Raton, FL: CRC Press.
- Congalton, R.G. and Green, K. 2009. Assessing the Accuracy of Remotely Sensed Data: principles and practices. Taylor and Francis Group, LLC.
- COSMO-SkyMed, 2007. *System description and user guide, doc. no: ASI-CSM-ENG-RS-093-A*, 4 May 2007. [Online] available at: <www.cosmo-skymed.it/docs/ASI-CSM-ENG-RS-093-A-CSKSysDescriptionAndUserGuide.pdf> [Accessed April 2011].
- CRED, 2011. *2010 disasters in numbers*. Centre for Research on the Epidemiology of Disasters (CRED). [Online] available at: <www.cred.be/publications?order=field_year_value&sort=desc> [Accessed August 2011].
- Crichton, D., 1999. The risk triangle. In: J. Ingleton, ed., 1999, *Natural disaster management*, London: Tudor Rose, pp. 102–103.
- CSA, 2007. Radarsat-2: Applications. Canadian Space Agency (CSA). [Online] available at: <www.asc-csa.gc.ca/eng/satellites/radarsat2> [Accessed July 2011].
- CSA, 2010. *Radarsat constellation*. Canada Space Agency. [Online] available at: <www.asc-csa.gc.ca/eng/satellites/radarsat/default.asp> [Accessed April 2011].
- Dagestad, K.F., Johannessen, J., Kerbaol, V., Collard, F., Kudryavtsev, V., and Akimov, D., 2005. Marine monitoring of the South and East China seas based on Envisat ASAR. In: H. Lacoste, ed., *Proceedings of the 2005 Dragon Symposium (SP-611)*, 27 June – 1 July 2005, Santorini, Greece.
- Dasgupta, S., Huq, M., Khan, Z.H., Masud, Md.S., Ahmed, M.M.Z., Mukherjee, N. and Pandey, K., 2011. Climate Proofing Infrastructure in Bangladesh- The Incremental Cost of Limiting Future Flood Damage. *The Journal of Environment & Development*, 20(2) 167–190.
- Definiens, 2006. Definiens Professional 5. *Reference Book. Version 5.0.6.1*. [Online] available at: <<http://www.definiens.com/>> [Accessed October 2009].
- De Groeve, T., and Riva, P., 2009. Early flood detection and mapping for humanitarian response. In: *Proceedings of the 6th International ISCRAM Conference - Gothenburg, Sweden, May 2009* J. Landgren and S. Jul, eds.
- Dellepiane, S. Bo, G. Monni, S. and Buck, C. 2000. SAR images and Interferometric coherence for flood monitoring. *Proceedings of Geoscience and Remote Sensing Symposium*, 6: 2608 – 2610.
- Demirkesen, A.C., Evrendilek, F., Berberoglu, S., Kilic, S. 2007. Coastal Flood Risk Analysis Using Landsat-7 ETM+ Imagery and SRTM DEM: A case study of Izmir, Turkey. *Environ Monit Assess*, 131, 293–300.

Dewan, A., Islam, M.M., Kumamoto, T., Nishigaki, M., 2007. Evaluating flood hazard for land-use planning in Greater Dhaka of Bangladesh using remote sensing and GIS techniques. *Water Resource Management*, 21, 1601–1612.

DLR, 2008. TerraSAR-X Ground Segment. Basic product specific document. Cluster applied remote sensing. TX-GS-DD-3302, Issue 1.5, 24/02/2008, pp 103.

DLR, 2009. TerraSAR-X mission brochure. TerraSAR-X, D-GB, July 2009.

DLR, 2010. TerraSAR-X Ground Segment. Basic product specific document. Cluster applied remote sensing. TX-GS-DD-3302, Issue 1.7, 15/10/2010, pp 109.

DLR, 2011a. TanDEM-X - A New High Resolution Interferometric SAR Mission. [Online] available at: <www.dlr.de/hr/en/desktopdefault.aspx/tabid-2317/3669_read-5488/> [Accessed June 2011].

DLR, 2011b. TerraSAR-X system configuration. [Online] available at: <www.dlr.de/dlr/en/desktopdefault.aspx/tabid-10381/569_read-432/> [Accessed July 2011].

Dobson, M.C., Pierce, L.E, and Ulaby, F.T., 1998. *Evaluation of SAR sensor configurations for terrain classification and forest biophysical retrievals*. [Online] available at: <<http://www.eecs.umich.edu/amazon/sensor%20.pdf>> [Accessed May 2009].

eCognition Professional 4 User Guide, 2004. Definiens Imaging.

Epler, N., and Leitgab, M., 2011. UN-SPIDER: supporting disaster management from space. *Earthzine: an online magazine for earth observations*. [Online] available at: <www.earthzine.org/2011/03/09/un-spider-supporting-disaster-management-from-space> [Accessed April 2011].

ERDAS Field Guide, 2009. [Online] available at: <www.erdas.com/Libraries/Tech_Docs/ERDAS_Field_Guide.sflb.ashx> [Accessed 2009].

ESA, 2008. Radar Image Interpretation. TIGER Initiative: principles of remote sensing. [Online] available at: <[www.tiger.esa.int/ Training Cds/cd_01/ content _2/sez_2_2/pg2_2_06.htm](http://www.tiger.esa.int/Training/Cds/cd_01/content_2/sez_2_2/pg2_2_06.htm)> [Last accessed November 2011].

ESA, 2011. ESA's Sentinel satellites: Sentinel-1. European Space Agency (ESA). [Online] Available at: <[www.esa.int/ esaLP/ SEMBRS4KXMF_ LPgmes_ 0.html](http://www.esa.int/esaLP/SEMBRS4KXMF_LPgmes_0.html)> [Last accessed November 2011].

European Commission, 2004. Flood risk management: flood prevention, protection and mitigation. *COM/2004/0472 final*. [Online] available at: <[http://eur-lex.europa.eu/LexUriServ/LexUriServ.do?uri =COM:2004:0472:FIN:EN:PDF](http://eur-lex.europa.eu/LexUriServ/LexUriServ.do?uri=COM:2004:0472:FIN:EN:PDF)> [Accessed April 2011].

- Evans, T.L., Costa, M., Silva, T.S.F., Telmer, K, 2010. Using PALSAR and RADARSAT-2 to map land cover and inundation in the Brazilian Pantanal. Anais 3º Simpósio de Geotecnologias no Pantanal, Cáceres, MT, 16-20 de outubro 2010 Embrapa Informática Agropecuária/INPE, 485 -494.
- FAO, 2000. Bangladesh flood prone areas map. Bangladesh Agricultural Research Council. BARC/UNDP/FAO GIS Project, BGD/95/006, July 2000.
- FAO, 2011. Food and Agriculture Organization Gateway reports. [Online] available at: <www.apipnm.org/swlwpnr/reports/y_sa/z_bd/bd.htm> [Accessed February 2011].
- FAO/WFP, 2008. Crop and Food Supply Assessment Mission to Bangladesh, 28 August, 2008. [Online] available at: <<http://foodsecurityatlas.org/bgd/country/Publications>> [Accessed February 2011].
- FEMA. 2011a . *National Response Framework resource centre*. Federal Emergency Management Agency (FEMA). [Online] available at: <www.fema.gov/emergency/nrf/glossary.htm#E> [Accessed April 2011].
- FEMA. 2011b. *Disaster information*. Federal Emergency Management Agency (FEMA). [Online] available at: <www.fema.gov/hazard/flood/index.shtm> [Accessed April 2011].
- Floods Directive, 2007. *Floods Directive 2007/60/EC of the European Parliament and of the Council of 23 October 2007 on the assessment and management of flood risks*. [Online] available at: <<http://eurlex.europa.eu/LexUriServ/LexUriServ.do?uri=OJ:L:2007:288:0027:0034:EN:PDF>> [Accessed April 2011].
- FLOODsite, 2008. *Methods to determine probability, consequences and risk 2*. Floodsite Project. [Online] available at: <www.floodsite.net/juniorfloodsite/html/en/student/thingstoknow/geography/methods2.html> [Accessed August 2011].
- FLOODsite, 2009. *Language of risk, project definitions, Report T32-04-01*, 2nd ed., April 2009. [Online] available at: <www.floodsite.net> [Accessed April 2011].
- Foody, G.M. 2002. Status of land cover classification accuracy assessment. *Remote Sensing of environment*, 80(2): 185-201.
- Foody, G.M. 2010. Assessing the accuracy of land cover change with imperfect ground reference data. *Remote Sensing of Environment*, 114 (10): 2271-2285.
- Frazier, P.S. and Page, K.J., 2000. Water Body Detection and Delineation with Landsat TM Data. *Photogrammetric Engineering & Remote Sensing*, 66(12), 1461-1467.
- Freeman, T., 1996. *What is image RADAR?* Jet Propulsion Laboratory. [Online] available at: <<http://shouthport.jpl.nasa.gov/>> [Accessed November 2010].
- Gagnon, L. and Jouan, A., 1997. Speckle filtering of SAR images - A comparative study between complex-wavelet-based and standard filters. SPIE Annual Meeting: Wavelet Applications in Signal and Image Processing, (SPIE #3169), San Diego.

- Garg, A. Han, W.J. Hwang, J.H. Kim, J.E. and Halsnaes, K., 2007. From vulnerability to resilience: The challenge of adaptation to climate change. Case studies from Bangladesh Brazil, China, India, South Africa and Korea. A joint publication of KEI and UNEP Risø Centre.
- GDRC, 2008. *The disaster management cycle*. Global Development Research Centre (GDRC). [Online] available at: <www.gdrc.org/uem/disasters/1-dm_cycle.html> [Accessed April 2011].
- Gebhardt, S., Gstaiger, V., Huth, J., Wehrmann, T., Kunzer, Schmidt, M., and Dech, S., 2008. Simple image processing techniques for near-real time inundation monitoring using TerraSAR-X imagery.
- Gernhardt, S., and Bamler, R., 2010. Towards deformation monitoring of single buildings - persistent scatterer interferometry using TerraSAR-X very high resolution spotlight data. synthetic aperture radar (EUSAR), 2010 8th European Conference on 7-10 June 2010.
- Gianinetto, M. and Villa, P., 2006. Monsoon flooding response: a multi-scale approach to water-extent change detection. Proceedings of ISPRS Mid-term Symposium, from Pixels to Process, 8-11 May 2006. Kerle, N. and Skidmore, A.K. (eds).
- Gillespie, T.W., Chu, J., Frankenberg, E., and Thomas, D., 2007. Assessment and prediction of natural hazards from satellite imagery. *Progress in Physical Geography* 31(5), 459–470.
- Gilard, O., and Givone, P., 1997. Flood risk management: new concepts and methods for objective negotiations. *International conference on destructive water*, Anaheim CA, ETATS-UNIS, 293, 145–155.
- Gimeno, M. and San-Miguel-Ayanz, J., 2004. Evaluation of Radarsat-1 data for identification of burnt areas in Southern Europe. *Remote Sensing of Environment*, 92, 370–75.
- Gitas, I.Z., Polychronaki, A., Katagis, T., and Mallinis, G., 2008. Contribution of remote sensing to disaster management activities: A case study of the large fires in the Peloponnese, Greece, *International Journal of Remote Sensing*, 29(6), 1847–1853.
- Globe SAR, 2008. GlobeSAR-2 RADAR remote sensing training package. educational recourse for radar remote sensing. Canada Centre for Remote Sensing. Natural Resources Canada.
- GOFC-GOLD, 2010. A sourcebook of methods and procedures for monitoring and reporting anthropogenic greenhouse gas emissions and removals caused by deforestation, gains and losses of carbon stocks in forests remaining forests, and forestation. GOFC-GOLD Report version COP16-1, (GOFC-GOLD Project Office, Natural Resources Canada, Alberta, Canada).
- Gregg, C.E., and Houghton, B.F., 2006. Natural hazards. In: D. Paton and D. Johnston, eds., *Disaster resilience: an integrated approach*, Springfield: Charles C. Thomas Publishers Ltd, pp. 19–39.

- Grenier, M., Labrecque, S., Benoit, M., Allard, M., 2008. Accuracy assessment method for wetland object-based classification. Proceedings of GEOBIA, 2008 - Pixels, Objects, Intelligence: GEOgraphic Object Based Image Analysis for the 21st Century. pp. 285–289.
- Gu, Y.X., Rose, W.I., Schneider, D.J., Bluth, G.J.S. and Watson, I.M., 2005. Advantageous GOES IR results for ash mapping at high latitudes: Cleveland eruptions 2001. *Geophysical Research Letters*, 32, L02305.
- Guffanti, M., Mastin, L. G., Schneider, D. J., Tupper, A., 2010. Science in support of aviation-risk management since the April 2010 Eruption of Eyjafjallajökull, Iceland. American Geophysical Union, Fall Meeting 2010.
- Guha-Sapir, D., Vos, F., Below, R., Ponserre, S., 2011. Annual disaster statistical review 2010: The Numbers and Trends. Brussels: CRED.
- Guha-Sapir, D., Rodriguez-Llanes, J.M., and Jakubicka, T., 2011. Using disaster footprints, population databases and GIS to overcome persistent problems for human impact assessment in flood events. *Natural Hazards*. [Online] available at: <<http://www.springerlink.com/content/1227186406747440>> [Accessed April 2011].
- Hansen, M.H., Madow, W.G. and Tepping, B.J., 1983. An evaluation of model-dependent and probability sampling inferences in sample surveys. *Journal of the American Statistical Association* 78, 776– 760.
- Haralick, R.M., Shanmugam, K., and Dinstein, I., 1973. Textural features for image classification. *IEEE Transactions on Systems, Man and Cybernetics*, 3(6), 610–621.
- Hasan, K., Martin, T.C. Shireen, S.A. and Choudhury, A.M 1998. Dynamics of monsoonal flooding in Bangladesh using Radarsat imagery. Proceedings of the Final Symposium: Radarsat Advanced Data Research Opportunity (ADRO). Montreal, Canada.
- Hassan, Q.K., Martin, T.C., Hasan, K., Hassan, A., Ali, M.S., 1999. Evaluation of filtering and classification techniques for floodplain land use/cover mapping using Radarsat SAR Data. Proceedings of the Asian Association of Remote Sensing (AARS), 1999. [Online] available at: <www.a-a-r-s.org/acrs/proceeding/ACRS1999/Papers/LU99-5.htm> [Accessed 2010].
- Henderson, F. M., 1995. Environmental factors and the detection of open surface water using X-band RADAR imagery. *International Journal of Remote Sensing*, 16: 2423-2437.
- Henderson, F.M. and Lewis, A.J., 1998. Principles and application of imaging RADAR. manual of remote sensing, third edition, Vol. 2. Published in cooperation with the American Society for Photogrammetry and Remote Sensing. John Wiley and Sons. Canada.
- Henderson, F.M., and Lewis, A.J., 2008. Radar detection of wetland ecosystem: a review. *International Journal of Remote Sensing*, 29(20), 5809–5835.

- Henry, J.-B., Chastanekt, P., Fellah, K., and Desnos, Y.-L., 2006. Envisat multi-polarized ASAR data for flood mapping. *International Journal of Remote Sensing*, 27(10), 1921–1929.
- Herrera-Cruz, V. and Koudogbo, F., 2009. TerraSAR-X rapid mapping for flood events. Proceedings of the *International Society for Photogrammetry and Remote Sensing (Earth Imaging for Geospatial Information)*, Hannover, Germany, 170–175.
- Hess, L.L., Melack, J.M., and Simonett, D.S., 1990. Radar detection of flooding beneath the forest canopy: a review. *International Journal of Remote Sensing*, 5, 1313–1325.
- Hossain, A.N.H.A., 2003. *Integrated flood management, case study: Bangladesh flood management*. The Associated Programme on Flood Management. World Meteorological Organization and Global Water Partnership.
- Howard, W.B., 1999. Higher quality photos and images boost demand for accurate ground control. *The Magazine of Earth Observation Magazine*, 8, 7.
- Huang, G.M., Guo, J.K., Lv, J.G., Xiao, Z., Zhao, Z., and Qiu, C.P., 2004. Algorithms and experiment on SAR image orthorectification based on polynomial rectification and height displacement correction. *Proceedings of ISPRS*, 12–23 July 2004, Istanbul, Turkey.
- Huda K.M.S., 2004. *Detection monitoring and management of small water bodies: a case study of Shahjadpur Thana, Sirajgonj District, Bangladesh*. PhD thesis, Durham University.
- Huda, K.M.S., Atkins, P.J., Donoghue, D.N.M.D., and Cox, N.J., 2010. Small water bodies in Bangladesh. *Area*, 42(2), 217–227.
- Huq, M., 2000. Approach to zoning for the water plan. In: A.A. Rahman, S. Huq and G.R. Conway, eds. 2000. *Environmental aspects of surface water systems of Bangladesh*. Dhaka: University Press Ltd. Ch. 3.
- IAEM, 2007. *Principles of emergency management*. International Association of Emergency Managers (IAEM). [Online] available at: <www.iaem.com> [Accessed April 2011].
- IFI, 2008. *About the International Flood Initiative*. International Flood Initiative (IFI). [Online] available at: < http://www.ifi-home.info/About-IFI.html > [Accessed April 2011].
- Infoterra, 2011. TerraSAR-X Satellite and Mission. Infoterra-An EADS Astrium Company. [Online] available at: <www.infoterra.de/terrasar-x-satellite> [Accessed June 2011].
- Ip, F., Dohm, J.M., Baker, V.R., Dogget, T., Davies, A.G., Castano, R., Chien, S., Cichy, B., Greeley, R., Sherwood, R., Tran, D. and Rabideau, G., 2006. Flood detection and monitoring with the Autonomous Sciencecraft Experiment onboard EO-1. *Remote Sensing of Environment*, 101, pp. 463–481.

- ISPRS, 2008. International Society for Photogrammetry and Remote Sensing (ISPRS). [Online] available at: <<http://www.isprs.org/>> [Accessed April 2008].
- Islam, M.D., and Sado, K., 2000. Development of flood hazard maps of Bangladesh using NOAA-AVHRR images with GIS. *Hydrological Sciences-Journal-des Sciences Hydrologiques*, 45(3).
- Islam, S.A.K.M., Haque, A., Bala, K.S., 2008. *Hydrological aspects of flood 2007. Final report, R 03/ 2008*, May 2008. Institute of Water and Flood Management. Bangladesh University of Engineering and Technology, Dhaka-1000, Bangladesh.
- Ito, A., 2005. Issues in the implementation of the International Charter on Space and Major Disasters. *Space policy*, 21, 141–149.
- Jackson, C.R. and Apel, J.R. (edit.) 2004. Synthetic Aperture Radar Marine User's Manual. Department of Commerce, NOAA, USA.
- Jensen, J.R., 2005. Thematic information extraction: pattern recognition – a remote sensing perspective. *Prentice Hall series in geographic information science*. Keith C. Clarke, series ed. 3rd ed. Ch. 9, pp. 337–406.
- Joyce, K.E., Belliss, S.E., Samsonov, S.V., McNeill, S.J. and Glassey, P.J., 2009. A review of the status of satellite remote sensing and image processing techniques for mapping natural hazards and disasters. *Progress in Physical Geography* 33(2), 183–207.
- Joyce, K.E., Dellow, G.D. and Glassey, P.J., 2008a: Assessing image processing techniques for mapping landslides. *Proceedings of IEEE International Geoscience and Remote Sensing Symposium, Boston, MA 2*, 1231–34.
- Joyce, K.E., Dellow, G.D. and Glassey, P.J., 2008b: Methods for mapping landslides in New Zealand using satellite optical remote sensing. 14th Australasian Remote Sensing and Photogrammetry Conference, electronic proceedings.
- Joyce, K.E., Belliss, S.E., Samsonov, S.V., McNeill, S.J., and Glassey, P.J., 2009a. A review of the status of satellite remote sensing and image processing techniques for mapping natural hazards and disasters. *Prog Phys Geogr*, 33, 183–207.
- Joyce, K.E., Wright, K.C., Samsonov, W.S., and Ambrosia, V.G., 2009b. Remote sensing and the disaster management cycle. In: G. Jedlovec, ed., 2009, *Advances in Geoscience and Remote Sensing*, Vukovar, Croatia: In-Teh, pp. 317–346.
- JPL, 2008. Imaging RADAR. NASA Jet Propulsion Laboratory (JPL), [Online] available at: <<http://southport.jpl.nasa.gov/>> [Accessed July 2008].
- JPL, 2011. Jet Propulsion Laboratory. SEASAT. [Online] available at: <www.jpl.nasa.gov/missions/missiondetails.cfm?mission=Seasat> [Accessed June 2011].
- Karszenbaum, H., Grings, F., Ferrazzoli, P., Tiffenberg, J., Jacobo, J., Kandus, P., Pratolongo, P. and Parmuchi, G., 2004. ASAR Multitemporal and Dual Polarization

- Observations of Wetland Marshes. Proceedings of the Envisat and ERS Symposium, 6-10 September 2004, Salzburg, Austria.
- Kerle, N., Froger, J.L., Oppenheimer, C. and de Vries, B.V., 2003. Remote sensing of the 1998 mudflow at Casita volcano, Nicaragua. *International Journal of Remote Sensing*, 24, 4791–816.
- Kerle, N., and Oppenheimer, C., 2002. Satellite remote sensing as a tool in Lahar disaster management. *Disasters*, 26(2), 140–160.
- Khan, M., Iqbal, M., and Mahboob, S., 2004. A wind map of Bangladesh. *Renewable Energy*, 29(5), 643–660.
- Khan, M.S., 2000. Multiple use of ponds. In: A.A. Rahman, S. Huq and G.R. Conway, eds. 2000. *Environmental aspects of surface water systems of Bangladesh*. Dhaka: University Press Ltd. Ch. 14.
- Khan, M.A.H., 1990. Environmental aspects of surface water development projects in Bangladesh in AA Rahman et al ed, *Environment and Development in Bangladesh*, Vol 2, University Press Ltd, Dhaka.
- Komwong, K. and Simking, R., 2006. ALOS PALSAR and Radarsat Applications on Flash Flood Detection in the Lower North of Thailand. Asian Conference on Remote Sensing(ACRS), 2006. Asian Association of Remote Sensing (AARS).
- Kwoun, O.I., Lu, Z., Neal, K. and Wicks, C., 2006. Quiescent deformation of the Aniakchak Caldera, Alaska, mapped by InSAR. *Geology*, 34, 5–8.
- Leeuwen, H. V., Martin, T., Haque, I., Hassan, A., Werle, D. and Tittley, B., 1997. Flood Monitoring Study in the Jamuna and Amp Ganges Floodplain in Bangladesh Using ERS-1. 3rd ERS Symposium. Florence, Italy.
- Lee, J.-S., Grunes, M.R. and Pottier, E., 2001. Quantitative comparison of classification capability: Fully polarimetric versus dual- and single-polarization SAR, *IEEE Transactions on Geoscience and Remote Sensing*, 39(11), 2343-235.
- Lewis, S., 2009. Remote sensing for natural disasters: facts and figures. *The Science and Development Network*. [Online] available at: <www.scidev.net/en/new-technologies/remote-sensing-for-natural-disasters-1/features/remote-sensing-for-natural-disasters-facts-and-figures.html> [Accessed April 2011].
- Li, J., Chen, W. and Touzi, R., 2007. Optimum Radarsat-1 Configuration for Wetlands discriminations: a Case Study of the Mer Bleue Peat Bog . *Canadian Journal of Remote Sensing*, Vol. 33, Suppl. 1, pp. S46-S55.
- Liew, S. C., 2001. Principles of remote sensing. Space View of Asia, 2nd edition. The Centre for Remote Imaging, Sensing and Processing (CRISP) at the National University of Singapore. Online tutorial. Available at: <www.crisp.nus.edu.sg/~research/tutorial/rsmain.htm> [Accessed April 2008].

- Lillesand, T.M., Kiefer, R.W. and Chipman, J.W., 2004. Remote sensing and image interpretation. John Wiley and Sons, Inc.
- Li, P., and Shenghui, F., 2003. SAR image classification based on its texture features. *Geo-Spatial Information Science*. 6(3), 16–19.
- Li, J. and Chen, W., 2005. A rule-based method for mapping Canada's wetlands using optical, radar and DEM data. *International Journal of Remote Sensing*, 26, 5051–5069.
- Lira-Chavez, J., 1995. Texture processing, analysis, and coding in synthetic aperture radar images. *Proceedings of SPIE*, 2564, 98.
- Livingstone, C.E., Sikaneta, I., Gierull, C., Chiu, S. and Beaulne, P., 2005. Radarsat-2 System and Mode Description. In *Integration of Space-Based Assets within Full Spectrum Operations* (pp. 15-1 – 15-22). Meeting Proceedings RTO-MP SCI-150, Paper 15. Neuilly-sur-Seine, France: RTO.
- Lo, C.P. and Quattrochi, D.A., 2003. Land-use and land-cover change, urban heat island phenomenon, and health implications- a remote sensing approach. *Photogrammetric Engineering & Remote Sensing*, 69 (9), 1053–1063.
- Logan, T., Guritz, R., Macmahan, J., Li, S., Olmsted, C., Carsy, F., Shindle, M., Groves, J., and Haug, S., 1996. Synthetic aperture radar (SAR) image processing technique for large scale terrestrial applications. *CUG, Spring Proceedings*.
- Luscombe, B. W; Hassan, H., 1992. Applying remote sensing technologies to natural disaster risk management : Implications for developmental investments. Washington, D.C.; International Astronautical Federation.
- Lu, X., Wang, J., Wang, Z. and Sun, H., 2009. Flooded Area Detection using Multi-temporal TerraSAR-X data. Synthetic Aperture Radar, 2009. APSAR 2009. 2nd Asian-Pacific Conference on 26-30 Oct. 2009.
- MacDonald Dettwiler and Associates (MDA), 2008. *Radarsat-2 product format definition*.
- Mahmood, A., Bessis, J.L., Bequignon, J., and Venkatachary, K.V., 2002. An overview of the International Charter "Space and Major Disasters". *Geoscience and Remote Sensing Symposium, 2002. IGARSS. IEEE International*, 2, 771–773.
- Malambo, L.M., 2009. A region based approach to image classification. *Applied Geoinformatics for Society and Environment conference*. [Online] available at: <www.applied-geoinformatics.org/index.php/agse/conference2009/paper/view/101/4> [Accessed February 2011].
- Matgen, P., Schumann, G., Henry, J.B., Hoffmann, L., and Pfister, L., 2007. Integration of SAR-derived river inundation areas, high-precision topographic data and a river flow model toward near real-time flood management. *International Journal of Applied Observation and Geoinformation*, 9, 247–267.

- Mather, P.M., 2004. *Computer processing of remotely sensed images: an introduction*. 3rd ed. John Wiley & Sons.
- Matsuoka, M. and Yamazaki, F., 2005. Building damage mapping of the 2003 Bam Iran Earthquake using Envisat/ASAR intensity imagery. *Earthquake Spectra* 21, S285.
- Martinez, J.-M. and Toan, T. L., 2007. Mapping of flood dynamics and spatial distribution of vegetation in the Amazon floodplain using multitemporal SAR data. *Remote Sensing of Environment*, 108, 209-223.
- Martinis, S. Twele, A. and Voigt, S., 2009. Towards operational near real-time flood detection using a split-based automatic thresholding procedure on high resolution TerraSAR-X data. *Natural Hazards and Earth System Sciences*, 9, 303–314.
- Martinis, S., 2010. Automatic near real-time flood detection in high resolution X-band synthetic aperture radar satellite data using context-based classification on irregular graphs. Dissertation, LMU München: Faculty of Geosciences.
- Mason, D.C., Speck, R., Devereux, B., Schumaa, G.J., Neal, J.C. and Bates, P.D., 2010. Flood detection in urban areas using TerraSAR-X. *IEEE Transaction on Geoscience and Remote Sensing*, 48(2), 882-894.
- McCandless, S. W. and Jackson, C. R., 2004. Principles of Synthetic Aperture Radar (Chapter 1). Ed. Jackson, C. R. and Apel, J. R. Synthetic Aperture Radar Marine User's Manual. Sponsored by the NOAA/NESDIS, Office of Research and Applications. [Online] available at: <www.sarusersmanual.com/> [Accessed July 2008].
- McMillan, A., Morley, J.G., Adams, B.J., and Chesworth, S., 2006. Identifying optimal SAR imagery specifications for urban flood monitoring: a Hurricane Katrina case study. *Fourth International Workshop on Remote Sensing for Disaster Response*, 25–26 September 2006, Magdalene College, University of Cambridge.
- McRoberts, R.E., 2010. Probability- and model-based approaches to inference for proportion forest using satellite imagery as ancillary data. *Remote Sensing of Environment*, 114, 1017-1025.
- McRoberts, R.E., Tomppo, E.O., Naesset, E., 2010b. Using remotely sensed data to construct and assess forest attribute maps and related spatial products. *Scandinavian Journal of Forest Research*, 25 (4), 368-381.
- McRoberts, R.E., 2010. Advances and emerging issues in national forest inventories. *Scandinavian Journal of Forest Research*, 25 (4), 340-367.
- MDA, 2009. Radarsat-2 product description. MacDonald, Dettwiler and Associates (MDA). RN-SP-52-1238, Issue 1/6: Nov. 2, 2009.
- MDA, 2007. Polarization options. RS-2 polarization options 2007-aug-1 (2).doc. MDA Geospatial Services.
- Merz, B., and Thielen, A.H., 2004. Flood risk analysis: concepts and challenges. *Österreichische Wasser- und Abfallwirtschaft*, 56(3/4), 27–34.

- Messner, F., 2007. Evaluating flood damages: guidance and recommendations on principles and methods, *FLOODSite Report Number T9-06-01*. [Online] available at: <<http://www.floodsite.net/default.htm>> [Accessed May 2011].
- Mirza, M.M.Q., 2003. Three recent extreme floods in Bangladesh: a hydro-meteorological analysis. *Natural Hazards* 28(1), 35–64.
- Mitri, G.H., and Gitas, I.Z., 2004. A performance evaluation of a burned area object based classification model when applied to topographically and non-topographically corrected TM imagery. *International Journal of Remote Sensing*, 25(14), 2863–2870.
- MoEF, 2009. Bangladesh Climate Change Strategy and Action Plan 2009. Ministry of Environment and Forests, Government of the People’s Republic of Bangladesh, Dhaka, Bangladesh, xvii, 76pp.
- Molak, V. (ed.), 1997. *Fundamentals of risk analysis and risk management*. Boca Raton: Lewis Publishers.
- Morena, L.C., James, K.V. and Beck, J., 2004. An introduction to the Radarsat-2 mission. *Can. J. Remote Sensing*, 30(3), 221–234.
- Mroz, M. and Mleczko, M., 2008. Potential of TerraSAR-X Stripmap Data in Early and Rapid Agricultural Crops Mapping. [Online] available at: <http://sss.terrasar-x.dlr.de/papers_sci_meet_3/paper/LAN0167_mroz.pdf> [Accessed July 2009].
- Muellerschoen, R., Yunling, Y., Chien, S., and Saatchi, S., 2008. Real-Time Autonomous Disturbance Detection and Monitoring System with L-Band UAVSAR. Radar Conference, 2008. RADAR '08. IEEE.
- Nath, R.K. and Deb, S.K., 2010. Water-body area extraction from high resolution satellite images-an introduction, review, and comparison. *International Journal of Image Processing*, 3(6), 353-372.
- Navalgund, R., 2009. Disaster management needs satellite “constellations”. *The Science and Development Network*. [Online] available at: <www.scidev.net/en/new-technologies/remote-sensing-for-natural-disasters-1/opinions/disaster-management-needs-satellite-constellations--1.html> [Accessed April 2011].
- Nico, G. Pappalepore, M., Pasquariello, G., Refice, A. and Samarelli, S., 2000. Comparison of SAR amplitude vs. coherence flood detection methods- a GIS application. *International Journal of Remote Sensing*, 21(8): 1619-1631.
- Nichol, J., 2005. Remote Sensing of Urban Heat Islands by Day and Night. *Photogrammetric Engineering & Remote Sensing*, 71(5), 613–621.
- Nichol, J. and Wong, M.S., 2005b. Satellite remote sensing for detailed landslide inventories using change detection and image fusion. *International Journal of Remote Sensing*, 26, 1913–26.

- Norman, S., 2004. Focus on recovery: a holistic framework for recovery. In: *NZ Recovery Symposium Processing*, 12–13 July, 2004, S. Norman, ed., Ministry of Civil Defence and Emergency Management, Wellington.
- NRCAN, 2007. Radarsat-2 Technical Specifications. Canada Centre for Remote Sensing, Natural Resources Canada (NRCAN). [Online] available at: <www.nrcan.gc.ca. > [Accessed June 2011].
- Oberstadler, R., Hönsch, H., and Huth, D., 1997. Assessment of the mapping capabilities of ERS-1 SAR data for flood mapping: a case study in Germany. *Hydrological Processes*, 11(10), 1415–1425.
- Ongsomwang, S., 2006. Thematic map accuracy assessment. Digital Image Analysis and Interpretation. [Online] available at: <<http://geoinformatics.sut.ac.th/sut/vicha/vicha.htm#RS>> [Accessed July 2011].
- Oppenheimer, C., 1996. Crater lake heat losses estimated by remote sensing. *Geophysical Research Letters*, 23, 1793–96.
- Paradella, W.R., Oliveira, C.G., Luiz, S., Cecarelli, I.C.F., Cottini, C.P., Okida, R., 2005. Operational use of RADARSAT-1 fine stereoscopy integrated with Landsat-5 thematic mapper data for cartographic application in the Brazilian Amazon. *Canadian Journal of Remote Sensing*, 31(2), 139-148.
- Perry, R.W., and Lindell, M.K., 2003. Preparedness for emergency response: guidelines for the emergency planning process. *Disasters*, 27(4), 336–50.
- Petak, W.J., 1985. Emergency management: a challenge for public administration. *Public Administration Review*, 45(1), 3–7. [Online] available at: <www.jstor.org/stable/3134992?seq=4> [Accessed April 2011].
- Pitz, W. and Miller, D., 2010. The TerraSAR-X satellite. *IEEE Transactions on Geoscience and Remote Sensing*, 48:2, February 2010.
- Plate, E.J., 2002. Flood risk and flood management. *Journal of Hydrology*, 267, 2–11.
- Platzeck, G., 2009. International Charter - Space and Major Disasters. UN COPUOS Fifty-Second Session June 2009, technical presentations. [Online] available at <www.oosa.unvienna.org/oosa/COPUOS/2009/presentations.html> [Accessed September 2011].
- Powell, R.L., Matzke, N., de Souza, C., Clark, M., Numata, I., Hess, L.L., Roberts, D.A., 2004. Sources of error in accuracy assessment of thematic land-cover maps in the Brazilian Amazon. *Remote Sensing of Environment*, 90(2), 221-234.
- Pugnaghi, S., Gangale, G., Corradini, S. and Buongiorno, M.F., 2006. Mt Etna sulfur dioxide flux monitoring using ASTER-TIR data and atmospheric observations. *Journal of Volcanology and Geothermal Research*, 74–90.
- Quarantelli, E.L., 1997. Ten criteria for evaluating the management of community disasters. *Disasters*, 21(1), 39–56.

- Rashid, Haroun Er., 1991. *Geography of Bangladesh*, University Press Limited, Dhaka.
- Radoux, J., Defourny, P., Bogaert, P., 2006. Comparison of Pixel- and Object-Based Sampling Strategies for Thematic Accuracy Assessment. International Conference GEOBIA 2008 Pixels Objects Intelligence GEOgraphic ObjectBased Image Analysis for the 21st Century. The International Society for Photogrammetry and Remote Sensing.
- Reliefweb, 2010. *Colombia: floods 2010 – situation report #10*, 17/12/2010. [Online] available at: <<http://reliefweb.int/node/378002>> [Accessed May 2011].
- Rees, W.G., 2001. *Physical principles of remote sensing*. 2nd ed. Cambridge University Press.
- Reza, A., 2000. Use of aquatic weeds: Water hyacinth. In: A.A. Rahman, S. Huq and G.R. Conway, eds. 2000. *Environmental aspects of surface water systems of Bangladesh*. Dhaka: University Press Ltd. Ch. 15.
- Richards, J.A., 1993. *Remote sensing digital image analysis: an introduction*. 2nd ed. Berlin: Springer-Verlag.
- Riendeau, S and Grenier, C., 2007. Radarsat-2 antenna. Aerospace Conference, 3-10 March, 2007 IEEE
- Rosin, P.L. and Hervas, J., 2005. Remote sensing image thresholding methods for determining landslide activity. *International Journal of Remote Sensing*, 26, 1075–92.
- Rott, H. and Nagler, T., 2006. The contribution of radar interferometry to the assessment of landslide hazards. *g*, 37, 710–19.
- Rothery, D.A., Coppola, D. and Saunders, C., 2005. Analysis of volcanic activity patterns using MODIS thermal alerts. *Bulletin of Volcanology*, 67(6), 539-556.
- Ronan, K.R., and Johnston, D.M., 2005. *Promoting community resilience in disasters: the role for school, youth, and families*, New York: Springer.
- Ruecker, G. and Siegert, F., 2000. Burn scar mapping and fire damage assessment using ERS-2 SAR images in east kalimantan, Indonesia. *International Archives of Photogrammetry and Remote Sensing*, Vol. XXXIII, Part B7. Amsterdam 2000, 1286-1293.
- SAFER, 2011. Services and Application for Emergency Response (SAFER). *Home page*. [Online] available at: <http://safer.emergencyresponse.eu/site/FO/scripts/myFO_accueil.php?lang=EN> [Accessed March 2011].
- SARMAP, 2007. The SAR-Guide Book, SARscape, Swezerland, ITT. www.ittvis.com/portals/0/pdfs/envi/SAR_Guidebook.pdf, Accessed: March 2011.
- Sarti, F., Inglada, J., Landry, R., and Pultz, T., 2001. Risk management using Remote Sensing data: moving from scientific to operational applications, Presented at the X SBSR April 23–27, 2001 (Brazil).

- Sayers, P., Hall, J., Dawson, R., Rosu, C., Chatterton, J., and Deakin, R., 2002. *Risk assessment of flood and coastal defences for strategic planning (RASP) – a high level methodology*. [Online] available at: <www.rasp-project.net/RASP_defra2002_Paper_Final.pdf> [Accessed April 2011].
- Sandholt, I., Nyborg, L., Fog, B., Lo, M., Bocoum, O. and Rasmussen, K., 2003: Remote sensing techniques for flood monitoring in the Senegal River Valley. *Danish Journal of Geography*, 103, 71–81.
- Sandholt, I., Fog, B., and Fensholt, R., 2001. *Flood monitoring in the Senegal River valley: first results based on SAR PRI data*.
- Sanyal, J., and Lu, X.X., 2004. Application of remote sensing in flood management with special reference to monsoon Asia: a review. *Natural Hazards*, 33(2), 283–301.
- Schmidt, K.S., and Skidmore, A.K., 2003. Spectral discrimination of vegetation types in a coastal wetland. *Remote Sensing of Environment*, 85 (1), 92–108.
- Schulze, D., Zink, M., Krieger, G., Boer, J., Moreira, A., 2009. TANDEM-X Mission Concept and Status. Frascati: FRINGE 2009.
- Schmitz, M., Lohmann, P., Kuehn, F., 2007. Landcover Mapping of Bandah Aceh, Indonesia, using Optical and SAR Satellite Imagery. ISPRS Hanover Workshop 2007: High-Resolution Earth Imaging for Geospatial Information.
- Schumann, G., Baldassarre, G.D., Bates, P.D., 2009. The Utility of Spaceborne Radar to Render Flood Inundation Maps Based on Multialgorithm Ensembles. *IEEE Transactions on Geoscience and Remote Sensing*, 47(8), august 2009.
- Schroder, M., Bennartz, R., Schuller, L., Preusker, R., Albert, P., Fischer, J., 2002. Generating cloudmasks in spatial high-resolution observations of clouds using texture and radiance information. *International Journal of Remote Sensing*, 23, 4247–4261.
- Selg, F., 2009. *About UN-SPIDER*. [Online] available at: <www.un-spider.org/about> [Accessed April 2011].
- Sentinel Asia, 2011. *Sentinel Asia Web*. [Online] available at: <<https://sentinel.tksc.jaxa.jp/sentinel2/topControl.action>> [Accessed April 2011].
- Sertel, E., Kaya, S. and Curran, P.J., 2007. Use of semivariograms to identify earthquake damage in an urban area. *IEEE Transactions on Geoscience and Remote Sensing*, 45, 1590–94.
- Seiler, R., Schmidt, J., Diallo, O. and Csaplovics, E., 2009. Flood monitoring in a semi-arid environment using spatially high resolution radar and optical data. *Journal of Environmental Management*, 90(7), 2121-2129.
- Short, N.M., 2008. Online Remote Sensing Tutorial. [Online] available at: <<http://rst.gsfc.nasa.gov/>> [Accessed April 2008].

- Shibayama, T., Nonaka, T., Takagishi, S., Sasagawa, T., 2008. Acquiring images regularly after disaster, it is possible to monitor recovery and restoration status of the damaged areas. The International Archives of the Photogrammetry. *Remote Sensing and Spatial Information Sciences*. Vol. XXXVII. Part B8. Beijing.
- Sivanpillai, R., Miller, S.N., 2010. Improvements in mapping water bodies using ASTER data. *Ecological informatics* 5(1):73-78.
- Song, Y-S. Sohn, H-G., Park, C-H., 2007. Efficient Water Area Classification Using Radarsat-1 SAR Imagery in a High Relief Mountainous Environment. *Photogrammetric Engineering & Remote Sensing*, 73(3), 285–296.
- Soria-Ruiz, J., Fernandez-Ordoñez, Y., Woodhouse I.H., 2010. Land-cover classification using radar and optical images: a case study in Central Mexico, *International Journal of Remote Sensing*, 31(12), 3291-3305.
- Solbo, S., Malnes, E., Guneriussen, T., Solheim, I., Eltoft, T., 2003. Mapping surface-water with Radarsat at arbitrary incidence angles. Geoscience and Remote Sensing Symposium, 2003. IGARSS '03. Proceedings. 2003 IEEE International, 21-25 July 2003.
- Songer, T., 1999. Epidemiology of disasters. University of Pittsburgh, US. [Online] available at: <www.pitt.edu/~epi2170/lecture15/index.htm> [Accessed July 2011].
- Srivastava, H.S., Patel, P., Sharma, Y., Navalgund, R.R., 2009. Large-Area Soil Moisture Estimation Using Multi-Incidence-Angle Radarsat-1 SAR Data. *Geoscience and Remote Sensing, IEEE Transactions*, 47(8), 2528 – 2535.
- Stramondo, S., Bignami, C., Chini, M., Pierdicca, N. and Tertulliani, A., 2006. Satellite radar and optical remote sensing for earthquake damage detection: results from different case studies. *International Journal of Remote Sensing*, 27, 4433–47.
- Streutker, D.R., 2002. A remote sensing study of the urban heat island of Houston, Texas. *International Journal of Remote Sensing*, 23(13), 2595-2608.
- Stehman, S.V., 2009. Sampling designs for accuracy assessment of land cover. *International Journal of Remote Sensing*, 30 (20), 5243-5272.
- Stehman, S.V. and Czaplewski, R.L., 1998. Design and analysis for thematic map accuracy assessment: fundamental principles. *Remote Sensing of Environment*, 64:331–344.
- Staples, G.C., 2005. Radarsat-2: Program Overview and Applications. Anais XII Simpósio Brasileiro de Sensoriamento Remoto, Goiânia, Brasil, 16-21 abril 2005, INPE, p. 4501-4506.
- Strahler, A., Boschetti, L., Foody, G.M., 2006. Global land cover validation: Recommendations for evaluation and accuracy assessment Of Global Land Cover Maps, Report of Committee of Earth Observation Satellites (CEOS) - Working Group on Calibration and Validation (WGCV), European Communities, Luxembourg.

- Stumpf, P., 2010. *Space Aid*. [Online] available at: <www.un-spider.org/spaceaid> [Accessed April 2011].
- Stumpf, P., 2011. *Space Application Matrix*. [Online] available at: <www.un-spider.org/space-application-matrix> [Accessed April 2011].
- Szekiela, K., 1988. *Satellite Monitoring of the Earth*. John Wiley and Sons.
- Terunuma, T., Nishida, K., Amada, T., Mizuyama, T., Sato, I. and Urai, M., 2005. Detection of traces of pyroclastic flows and lahars with satellite synthetic aperture radars. *International Journal of Remote Sensing*, 26, 1927–42.
- The Disaster Charter [International Charter on Space and major Disasters], 2000. *Charter on cooperation to achieve the coordinated use of space facilities in the event of natural or technological disasters*, Rev. 3 (25/4/2000). [Online] available at: <www.disasterscharter.org/web/charter/charter> [Accessed April 2011].
- The Disaster Charter [International Charter on Space and major Disasters], 2010. *9th annual report, January–December 2009*. [Online] available at: <www.disasterscharter.org> [Accessed April 2011].
- The Disaster Charter [International Charter on Space and major Disasters], 2011. *Home page*. [Online] available at: <www.disasterscharter.org> [Accessed April 2011].
- Thielen, A.H., Apel, H., Kreibich, H., and Aronica, G., 2007. Comparison of different approaches for flood damage and risk assessment. *Perception of uncertainty in water management by stakeholders and researchers*, Prague, 14–16 May 2007.
- The World Bank, 2010. Bangladesh: Economics of Adaptation to Climate Change Study. [Online] available at: <<http://climatechange.worldbank.org/content/bangladesh-economics-adaptation-climate-change-study>> [Accessed June 2011].
- Tholey, N., Clandillon, S., and de Fraipont, P., 1997. The contribution of spaceborne SAR and optical data in monitoring flood events: examples in northern and southern France. *Hydrological Processes*, 11, 1409–1413.
- Tingsanchali, T., and Karim, F.M., 2005. Flood hazard and risk analysis in the southwest region of Bangladesh. *Hydrological Processes*, 19, 2055–2069.
- Trevett, J. W., 1986. *Imaging RADAR for Resources Surveys*. Chapman and Hall.
- Tralli, D.M., Blom, R.G., Zlotnicki, V., Donnellan, A. and Evans, D.L., 2005. Satellite remote sensing of earthquake, volcano, flood, landslide and inundation hazards, *ISPRS Journal of Photogrammetry and Remote sensing*, 59(4), 185–198.
- Tsutsui, K., Rokugawa, S., Nakagawa, H., Miyazaki, S., Cheng, C.T., Shiraishi, T. and Yang, S.D., 2007. Detection and volume estimation of large-scale landslides based on elevation-change analysis using DEMs extracted from high-resolution satellite stereo imagery. *IEEE Transactions on Geoscience and Remote Sensing*, 45, 1681–96.

- Uchida, H. and Ando, K. 2007. Characteristics of Paddy Fields and Irrigation in the Dry Season in a Village of Bangladesh. *The Japan Agricultural Research Quarterly (JARQ)* 4: 4, 267-272.
- UGS COSMO-SkyMed, 2011. About COSMO-SkyMed. [Online] available at: <<http://www.cosmo-skymed.it/en/index.htm>> [Accessed June 2011].
- UK Planning Portal, 2010. *Policy statement 25: development and flood risk*. [Online] available at: <www.planningportal.gov.uk> [Accessed April 2011].
- Ulaby, F.T., and Batlivala, P.P., 1976. Optimum radar parameters for mapping soil moisture. *Geoscience Electronics, IEEE Transactions*, 14(2), 81–93.
- UNDP, 2004. A global report: Reducing disaster risk: A challenge for development. [Online] available at: <www.undp.org/bcpr> [Accessed June 2011].
- Unlu, A., Kapucu, N., and Bahadir Sahin, B., 2010. Disaster and crisis management in Turkey: a need for a unified crisis management system. *Disaster Prevention and Management*, 19(2), 155–174.
- UNISDR, 2002. *Guidelines for reducing flood losses*. UN International Strategy for Disaster Reduction [UNISDR]. [Online] available at: <www.unisdr.org/eng/library/isdr-publication/flood-guidelines/isdr-publication-floods.htm> [Accessed April 2008].
- UNISDR, 2005. *Hyogo Framework for Action 2005–2015: building the resilience of nations and communities to disasters*. UN International Strategy for Disaster Reduction [UNISDR]. [Online] Available at: <www.unisdr.org/eng/hfa/hfa.htm> [Accessed April 2011].
- UNISDR, 2009. *Terminology on disaster risk reduction*. UN International Strategy for Disaster Reduction [UNISDR]. [Online] available at: <www.unisdr.org/we/inform/terminology> [Accessed April 2011].
- UN Office for the Coordination of Humanitarian Affairs (OCHA). *Home page*. [Online] available at: <<http://reliefweb.int/node/378002>> [Accessed May 2011].
- UN Office for Outer Space Affairs [UNOOSA], 2007. *United Nations Platform For Space-based Information for Disaster Management and Emergency Response*. [Online] available at: <www.oosa.unvienna.org/oosa/SpaceLaw/gares/index.html#ARES_61_110> [Accessed April 2011].
- UN Office for Outer Space Affairs [UNOOSA], 2010. *Technical advisory support activities carried out in 2010 in the framework of the United Nations Platform for Space-based Information for Disaster Management and Emergency Response*. A/AC.105/985, 14 December 2010. [Online] available at: <www.unoosa.org/oosa/en/unspider/index.html> [Accessed April 2011].
- UN-SPIDER Portal, 2011. *Space application matrix*. [Online] available at: <www.unspider.org/space-application-matrix> [Accessed April 2011].
- UNU, 2004. *United Nations University Newsletter*, 32, July–August.

- UNHCR, 2004. UN Cartographic Section, *Map of Bangladesh*, January 2004, No. 3711 Rev. 2. [Online] available at: <www.unhcr.org/refworld/docid/4607a26c2.html> [Accessed June 2011].
- Verstappen, H.Th., 1995. Aerospace technology and natural disaster reduction. *Advances in Space Research*, 15(11), 3–15.
- Voigt, S., Kemper, T., Riedlinger, T., Kiefl, R., Scholte, K., and Mehl, H., 2007. Satellite Image Analysis for Disaster and Crisis-Management Support. *IEEE Transactions on Geoscience and Remote Sensing*, 45 (6), JUNE 2007.
- Waring, R.H., Way, J., Hunt Jr., E.R., Morrissey, L., Ranson, K.J., Weishampel, J.F., Orem, R. and Franklin, S.E., 1995. Imaging radar for ecosystems studies. *BioScience*, 45: 715-723.
- Wazed, A., 1991 *Bangladesher Nadimala* (Rivers of Bangladesh, in Bangla), Dhaka.
- WFP, 2011. World Food Program (WFP). *Food security atlas for Bangladesh*. [Online] available at: <<http://foodsecurityatlas.org/bgd/country>> [Accessed February 2011].
- WHO, 2005. Flooding and communicable diseases fact sheet - Risk Assessment and Preventive Measures. World Health Organization. [Online] available at: <www.who.int/hac/techguidance/ems/flood_cds/en/> [Accessed August 2011].
- Wolf, J., 2009. Coastal flooding: impacts of coupled wave-surge-tide models. *Natural Hazards*, 49, 241–260.
- Yamazaki, F., 2007. *Remote sensing and GIS*. Department of Urban Environment Systems, Graduate School of Engineering, Chiba University.
- Yang, C., Zhou, C., and Wan, Q., 1999. Detecting the flood extent with Radarsat SAR data and image fusion. *20th Asian Conference of Remote Sensing*. Hong Kong, 22–25 November 1999.
- Ye, X., 2008. *Characterizing the spatial distribution of giant pandas in China using MODIS data and landscape metrics*. MSc thesis, The International Institute for Geo-information Science and Earth Observation, Enschede, The Netherlands. [Online] available at: <www.itc.nl/library/papers_2008/msc/gem/xingpingye.pdf>. [Accessed 2010].
- Yuhaniz, S., Vladimirova, T., Gleason, S., 2007. An intelligent decision-making system for flood monitoring from space. In Proceedings of ECSIS Symposium on Bio-inspired, Learning, and Intelligent Systems for Security (BLISS 2007), 9–10 August 2007, Edinburgh, UK, pp. 65–71.
- Yuhaniz, S.S. and Vladimirova, T., 2009. An onboard automatic change detection system for disaster monitoring, *International Journal of Remote Sensing*, 30(23), 6121-6139.

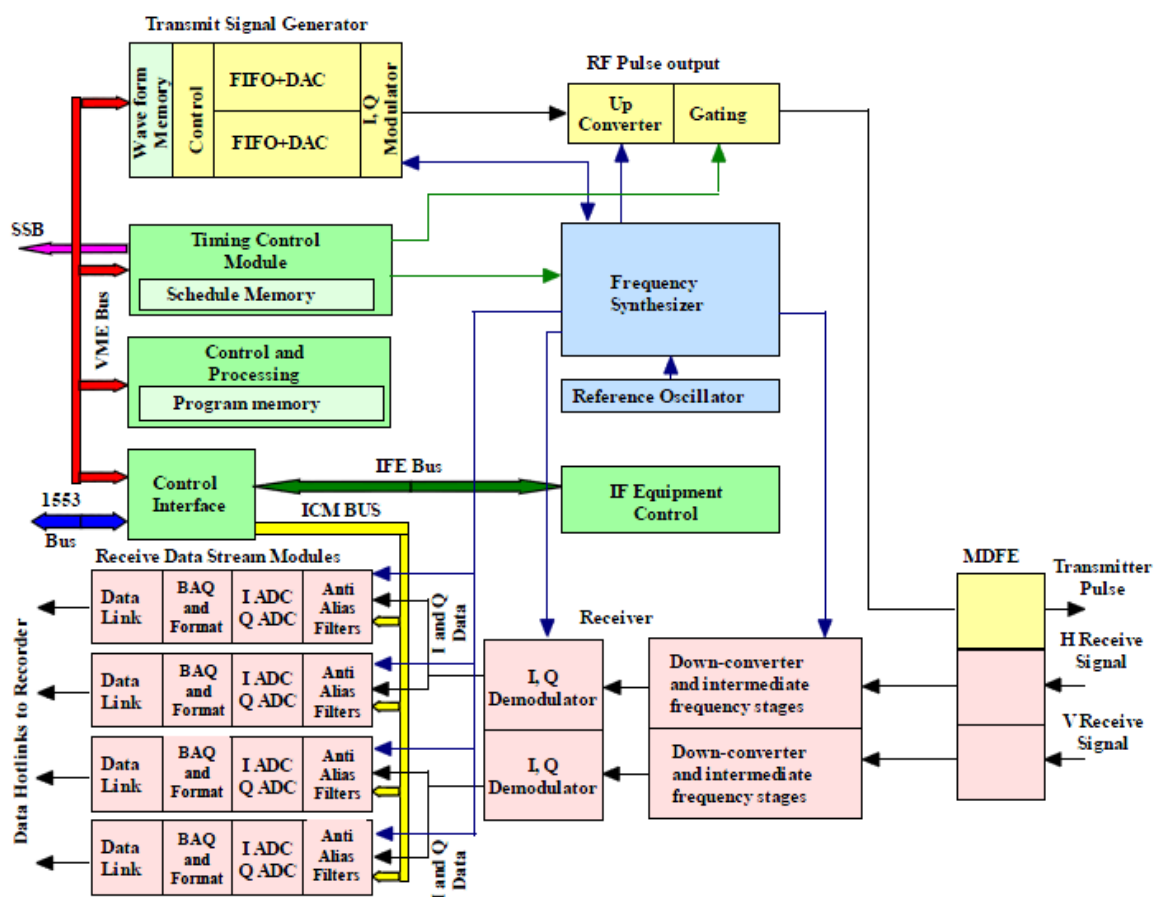
Zaitchik, B., Macalady, A.K., Bonneau, L.R. and Smith, R.B., 2006. Europe's 2003 heat wave: A satellite view of impacts and land-atmosphere feedbacks. *Int. J. Climatol.*, 26(6), 743–769.

Zehner, C., (Ed.), 2010. Monitoring Volcanic Ash from Space. Proceedings of the ESA-EUMETSAT workshop on the 14 April to 23 May 2010 eruption at the Eyjafjöll volcano, South Iceland. Frascati, Italy, 26 27 May 2010. ESA-Publication STM-280. doi:10.5270/atmch-10-01.

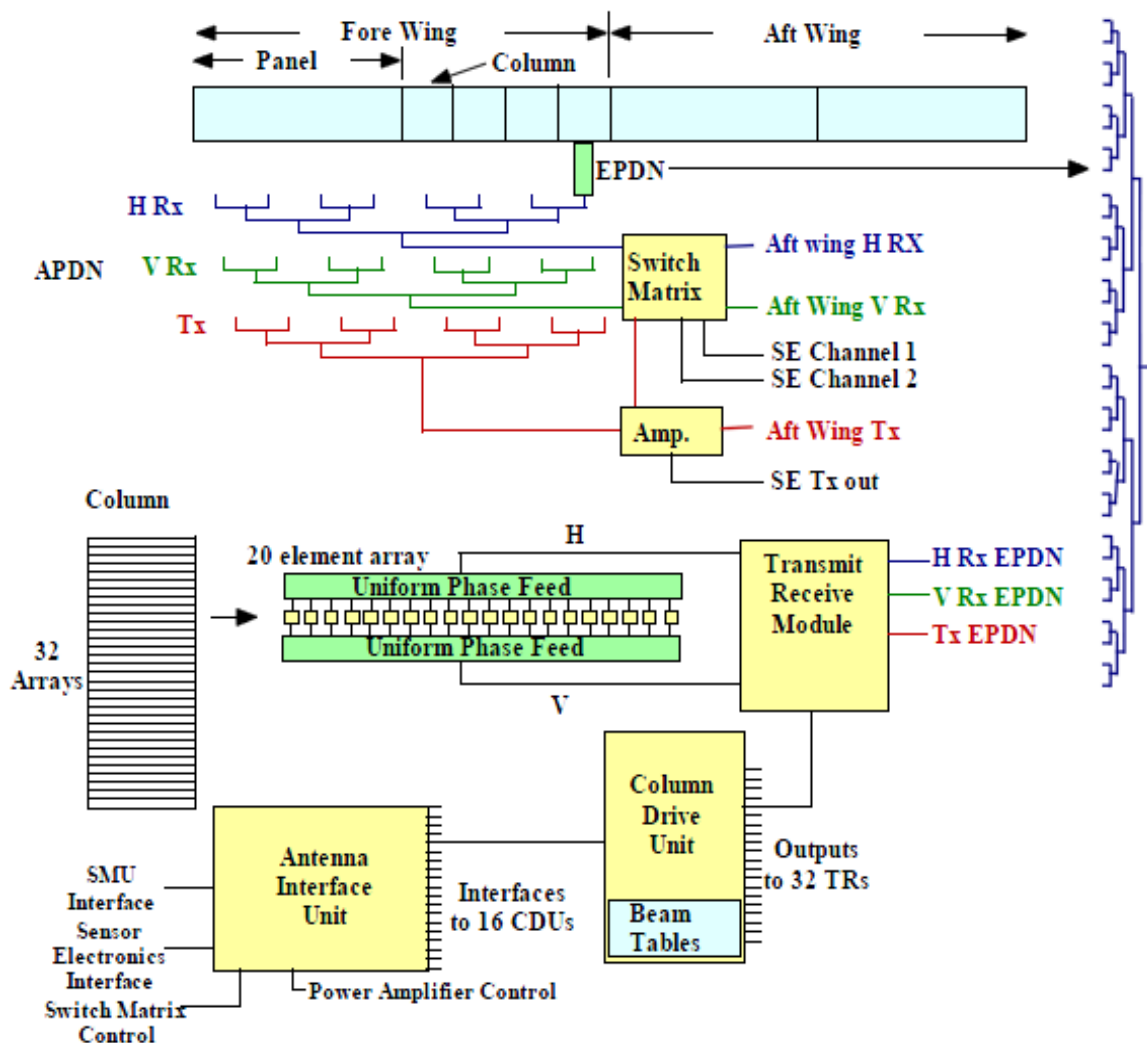
Appendices

Appendix 3.1:

Radarsat-2 sensor electronics sub-system and antenna subsystem diagrams



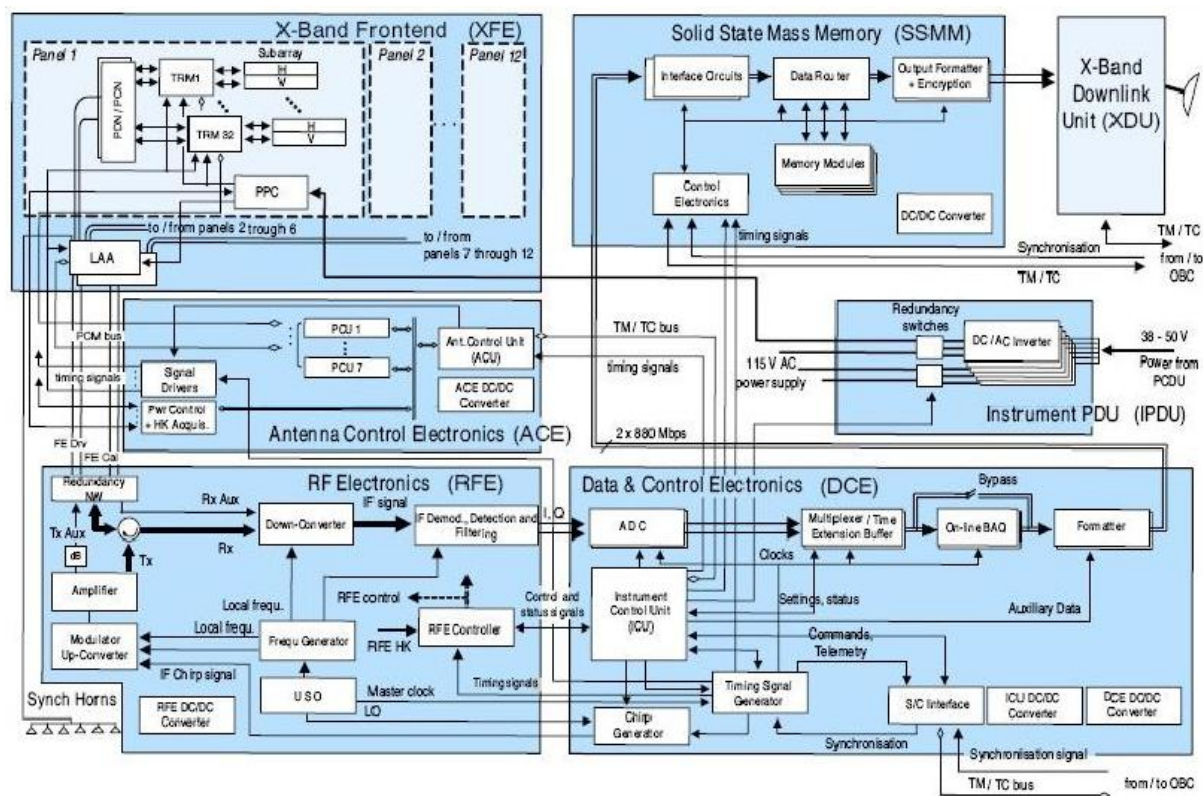
Radarsat-2 sensor electronics sub-system (adapted from Livingstone et al., 2005)



Radarsat-2 antenna subsystem (adapted from Livingstone et al., 2005)

Appendix 3.2:

TerraSAR-X instrument functional block diagram and antenna panel



TerraSAR-X instrument functional Unit block diagram (Source: DLR, EADS)



TerraSAR-X antenna panel (source: Miller et al., 2006)

Appendix 5.1:

A follow-up water body data sheet

Area name:
Date:
Time:

Site ID (from Pro):	Site description (from Pro):	File name (from Pro):	
WB type:	Size: Small – Medium – Large	Water colour: clear-stained	Photo: () Time:
Water depth: <input type="checkbox"/> more than 1 m <input type="checkbox"/> 1 m to 0.5 m <input type="checkbox"/> less than 0.5m	Distance of dGPS from water edge: (m)		
Comments:			
WB Drawing			
			N ↑

┌──────────┐ 10 m

Appendix 6.1:

Follow-up table for SAR data processing

SAR sensor		Texture analysis variables	RADARSAT-2			TerraSAR-X			
Product			HH(1)	HH(2)	VV	HH(1)	HH(2)	VV	HH spotlight
Georeference transformation									
Geocorrection (dGPS)									
CP error									
Subset image									
			Data range						
		Mean							
		Variance							
		Entropy							
		Skewness							
Texture Filters	Occurrence measures	Mean							
		Variance							
		Entropy							
	Co-occurrence measures	Mean							
		Variance							
		Homogeneity							
Contrast									
	Dissimilarity								
	Entropy								

		Second moment																
		Correlation																
Training samples signature																		
Unsupervised classification																		
Supervised classification (texture)																		
Object-based classification	Segmentation																	
	Classification																	
Accuracy assessment																		

Appendix 7.1:**Water area estimation for Bangladesh using Radarsat-2 and TerraSAR-X****Bangladesh**

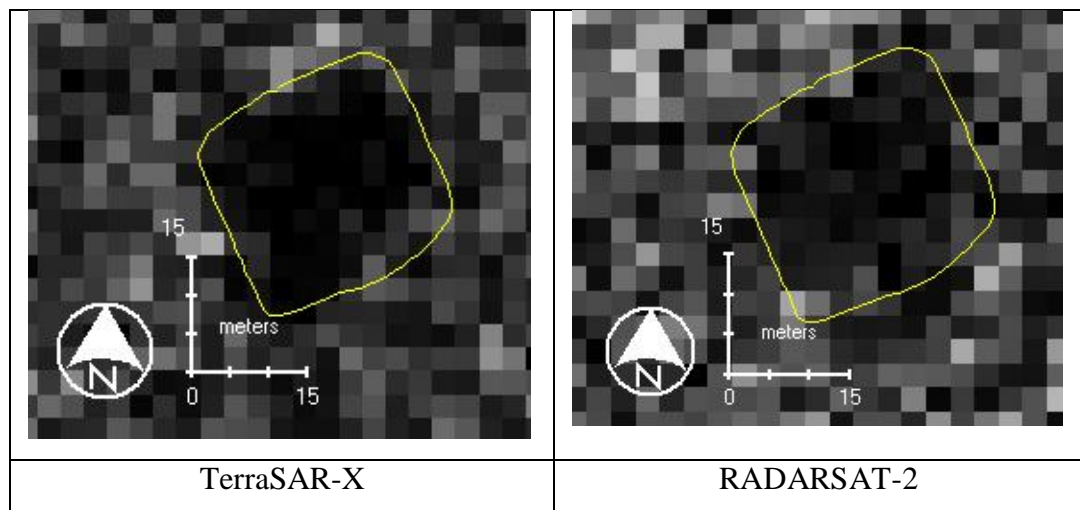
Area in km ²	147570	km ²	from Bangladesh Bureau of Statistics
Area of water in Bangladesh	10090	km ²	from Bangladesh Bureau of Statistics
Percent area of water in Bangladesh	6.837	%	
Area prone to flooding all Bangladesh	110678	km ²	from Wikipedia

Radarsat-2

Mapped % of water in study area	16.95	%	
Estimated area of water in Bangladesh	18761	km ²	
Estimated % area of water in Bangladesh	12.71	%	

TerraSAR-X

Mapped % of water in study area	17.64	%	
Estimated area of water in Bangladesh	19520	km ²	
Estimated % area of water in Bangladesh	13.22	%	

Appendix 8.1:**Visual comparison of WB volume scattering**

Visual comparison of WB volume scattering away of original SAR imagery HH 3m between TerraSAR-x and Radarsat-2 products.